Autothermal Reforming of Bio-oil Model Compounds

Tande Lifita Nguve

Submitted in accordance with the requirements for the degree of
Doctor of Philosophy

The University of Leeds
School of Chemical and Process Engineering

February 2018

The candidate confirms that the work submitted is his own, except where work which has formed part of jointly-authored publications has been included. The contribution of the candidate and the other authors to this work has been explicitly indicated below. The candidate confirms that appropriate credit has been given within the thesis where reference has been made to the work of others.

Tande, L. N. and Dupont, V (2016) Autothermal reforming of palm empty fruit bunch bio-oil: thermodynamic modelling. AIMS Energy, 4 (1). pp. 68-92. ISSN 2333-8326.

This publication is based entirely on the work contained in Chapter 4 of this thesis. The Candidate was principal researcher and author. The co-author contributed with comments and edits on the whole paper

Dupont, V., Yun, H. A. H., White, R. & Tande, L. N. High methane conversion efficiency by low temperature steam reforming of bio-feedstock. REGATEC 2017, 4th International Conference on renewable Energy gas Technology, 22-23 May 2017 2017 Pacengo (Verona), Italy. 25-28.

This publication contains some results presented in Chapter 5 of this thesis. The Candidate was a co-author only.

Acknowledgements

I would like to express my heartfelt gratitude and appreciation to my supervisor Dr Valerie Dupont. This work was made possible thanks to her invaluable support, guidance and motivation and also her willingness to always make time to listen and discuss my ideas.

I want to thank all my friends and colleagues who contributed in one way or the other in helping me complete this project; especially Dr Oluwafemi Omoniyi, Dr Gurav Nahar, Dr Zaheer Abbas, Dr Hafizah Yun, Dr Zainab Ibrahim Adiya, Erik Resendiz, Oliver Grasham, and Robert Bloom. Special thanks to Sergio Ramirez for all the extra help and training he provided for XRD analysis and catalyst preparation.

I want to also acknowledge the help and support provided by the technicians and staff of SCAPE and LEMAS; especially Dr Adrian Cunliffe, Carine Alvarez, Stuart Micklethwaite and Dr Zabeada Aslam.

Finally and most importantly, my deepest gratitude goes out to my entire family; especially my mother, Ms Clara Mbua, my father Dr Amos N. Ngongi, and my brothers Makuna, Dibussi, Fayeofori and Elive. My love to my wife Enanga, for accepting to come over to live with me in England, and to my lovely children Mosima and Mojoko.

Abstract

The potential of hydrogen and syngas production by autothermal reforming (ATR) of bio-oil was examined by performing thermodynamic equilibrium, process modelling and experimental studies. Model 'bio-compounds' typically found in bio-oil were studied either individually or as mixtures in order to understand the various phenomena and factors controlling and influencing the ATR process. Thermodynamic equilibrium analysis of ATR was performed on a moisture free (mf) bio-oil obtained from the fast pyrolysis of palm empty fruit bunch (PEFB), a significant agricultural waste of the palm oil industry. Feed stream conditions of ATR are characterised by the molar steam feed to the molar carbon feed ratio (S/C), and the oxygen equivalence ratio Φ (feed fuel-oxygen ratio divided by combustion-stoichiometric fuel-oxygen ratio). The bio-oil was modelled as a mixture of acetic acid, phenol, levoglucosan, palmitic acid and furfural. The maximum hydrogen yield obtained was about 12 wt% of the dry bio-oil at (S/C) of 1 and increased to about 18 wt% at S/C = 4. Equilibrium studies also revealed that carbon (in the form of graphite) can only exist in equilibrium at S/C = 1 and oxygen equivalence ratio $\Phi < 0.3$. The design and simulation of a process involving the production of pure H_2 from solid, wet PEFB was carried out. Sensitivity analysis revealed that a maximum S/C = 3 is recommended for any optimal design using ATR for hydrogen production. Depending on the actual process configuration, hydrogen efficiencies (ratio of the lower heating value of hydrogen produced on the lower heating value of the input fuel) obtained varied from 43% to 57% while overall process efficiencies (total energy output from process divided by total energy input to process) ranged from 45 to 65%. Experiments of ATR of acetic acid conducted at conditions of S/C of 1 – 3 and air equivalence ratio λ (feed air-fuel ratio divided by combustion-stoichiometric fuel-air ratio) of 0.34 – 0.37 were performed using two conventional nickel catalysts ('Ni-Al' and 'Ni-CaAl'). Acetic acid conversions > 90% were obtained compared to an equilibrium value of 100%, with H_2 production also at about 90% of the expected equilibrium value. The ATR of acetic acid, 2-butanone, furfural, m-cresol and their mixture was also examined in a packed bed reactor using powder rhodium on alumina ('Rh-Al') catalysts prepared in-house. High fuel conversions were obtained with values of 98, 98, 95, 81 and 90 % for acetic acid, 2-butanone, furfural, m-cresol and their mixture respectively, thus close to the equilibrium value of 100%. Compared to Ni-Al, the Rh-Al catalyst

showed excellent resistance to coke formation with only 0.8 wt% coke deposit formed per mass of catalyst compared to 14.7 wt% for the nickel catalyst for acetic acid ATR experiments performed under similar conditions. ATR experiments were also carried out using a formulated PEFB bio-oil surrogate as feed. Rh-Al catalyst performed slightly better than the ceria doped RhCe-Al catalyst with a bio-oil conversion of 84 and 87 % at S/C ratio = 2.2, $\lambda = 0.318$ and S/C = 3, $\lambda = 0.391$ respectively compared to 83 and 85% for the ceria doped RhCe-Al catalyst. However, H_2 production was slightly higher on the RhCe-Al catalyst with a H_2 yield of about 83% of the equilibrium value compared to 80% obtained for the Rh-Al catalyst. Finally, ATR experiments were carried out using two rhodium monoliths, with and without ceria on alumina washcoat, denoted as ‘R-M’ and ‘RC-M’ (on cordierite honeycomb structure). Acetic acid conversion varied only slightly from 91 to 92% as the S/C ratio was increased from 1 to 3 for the R-M monolith. The ceria doped RC-M monolith on the other hand showed initial lower conversions but improved from 85% to 95%, as the S/C molar ratio was varied from 1 to 3. The hydrogen yield obtained for both monoliths of 6.2 and 6.3 wt% for R-M and RC-M respectively was well short of the equilibrium value of 7.2 wt% of the acetic acid feed.

Table of Contents

List of Tables

List of Figures

Abbreviations

AFC	alkaline fuel cell
AFR	air to fuel ratio
ASU	air separation unit
ATR	autothermal reforming
BET	Brunauer-Emmett-Teller
BF	bio-feedstock
BM	biomass
BO	bio-oil
BO-RX	Boudouard reaction
BPT	back-pressure turbine
CEA	Chemical Equilibrium with Applications
CET	condensing extraction turbine
C-GS	carbon gasification
CHNS	carbon, hydrogen, nitrogen and sulphur
CO-OX	carbon monoxide oxidation
COX	complete oxidation
DEC	decomposition
DFT	Density Functional Theory
DTG	derivative thermogravimetry curve
ESP	Electrostatic Solid Separator
FFB	fresh fruit bunch
FWF	fresh water feed
GC	gas chromatograph
GHSV	gas hourly space velocity
HGI	Hardgrove Grindability Index
HHV	higher heating value
HICE	hydrogen internal combustion engines
H-OX	hydrogen oxidation
HPWS	high pressure water scrubber
IC	inorganic carbon
IUPAC	International Union of Pure and Applied Chemistry
LCA	lifecycle assessment

LHV	lower heating value
MCFC	molten carbonate fuel cell
MEN	methanation of C(s)
ME-SR	methane steam reforming
mf	moisture free
MMT	million metric tonnes
MTOE	million ton oil equivalent
NCG	non-condensable gases
NDIR	non-dispersive infrared
Ni-Al	18 wt.% NiO/Al_2O_3 catalyst
Ni-CaAl	15 wt.% $NiO/CaO-Al_2O_3$ catalyst
NPOC	non-purgeable organic carbon
PAFC	phosphoric acid fuel cell
PAPS	pyrolysis and autothermal reforming process with hydrogen separation by pressure swing adsorption
PAPS-BT	PAPS using back pressure turbine
PAPS-CT	PAPS using condensing extraction turbine
PAWS	pyrolysis and autothermal reforming process with hydrogen separation by high pressure water scrubber
PAWS-BT	PAWS using back pressure turbine
PAWS-CT	PAWS using condensing extraction turbine
PEFB	palm empty fruit bunch
PEFC	polymer electrolyte fuel cell
PEMFC	proton exchange membrane fuel cell
POX	partial oxidation
PR-BM	Peng-Robinson equation of state with Boston-Mathias modification
PSA	pressure swing adsorption
PSD	particle size distribution
PTSA	pressure-temperature swing adsorption technology
RC-M	1 wt.% Rh - 3 wt.% $Ce/\gamma-Al_2O_3$ washcoat on cordierite monolith
Rh-Al	1wt.% $Rh/\gamma-Al_2O_3$ catalyst
RhCe-Al	1 wt.% Rh – 3 wt.% $Ce/\gamma-Al_2O_3$ catalyst
R-M	1wt.% $Rh/\gamma-Al_2O_3$ washcoat on cordierite monolith
SOFC	sulphur oxide fuel cell

SR	steam reforming
SSC	specific steam consumption, kg/kWh
STEAM-TA	steam table property method
TC	total carbon
TGA	thermogravimetric analysis
TIC	total inorganic carbon
TOC	total organic carbon
TPD	tons of per day
WGS	water gas shift
WPA	water pump around
wt	weight

Nomenclature

$(\dot{P}^{+})/(\dot{P}^{-})$	net power/electricity generated or demanded by the process (MW)
$(\dot{Q}^{+})/(\dot{Q}^{-})$	net het produced or required by the process (MW)
$\dot{H}_{pr}$	is the required process heat MW;
$\dot{H}_{re}$	residual heat recovered from cooling the dryer exit stream, MW;
$\dot{m}$	mass flow, kg/h
W_{i}	isentropic mechanical (turbine) work (MW)
A_j	pre-exponential factor
C_W	isentropic work of compression, kW
$\dot{E}$	total electrical energy demand, MW
E_j	activation energy
P	pressure, N/m^2
P_W	pump power, kW
S_T	specific steam consumption of the turbine, kg/kW-h
$\dot{W}$	total mechanical work generated, MW
X_i	conversion
Y_{H_2}	hydrogen yield (wt.%, mol%, or mol H_2/mol C)
a_{ji}	number of gram atoms of element *j* per gram mole of species *i*
b_j^o	number of gram atoms of element *j* in a reaction mixture
k_c	rate constant
$\dot{m}$	mass flow rate, kg/s
n_i	number of moles of species
$\dot{n}_i$	molar flow, mol/s
p_0	saturation pressure, Pa
v	specific volume of the gas, m^3/kg
$\dot{v}$	molar volume, m^3/mol
$\dot{V}$	volumetric flow rate, m^3/s
v_m	amount of adsorbed gas forming the monolayer, ml
y_i	mole fraction
z_{jo}	mass fraction of volatiles from component j
C_w	concentration of carbon atoms
ΔG_i^0	standard Gibbs free energy of formation, kJ

Φ_i	Lagrangian multiplier
α_j	mass fraction of component j
$\eta_{H_2(BM)}$	hydrogen efficiency (biomass as input fuel)
$\eta_{H_2(BO)}$	hydrogen efficiency (bio-oil as input fuel)
η_{H_2O}	water conversion efficiency
η_{BM}	biomass to bio-oil conversion efficiency
η_T	turbine isentropic efficiency
η_{pr}	overall process efficiency
μ_i	chemical potential of species
h	specific enthalpy, kJ/kg
H	enthalpy, kW
R	universal gas constant, 8.314 J/mol·K
s	specific entropy, kJ/kg.K
S	specific surface area, m^2/g
T	temperature, K
V	volume, m^3
λ	air equivalence ratio
λ_{opt}	optimum equivalence
λ_w	wavelength
ϕ	oxygen equivalence ratio
A	cross sectional area, m^2
G	Gibbs free energy, kJ
M	module (for methanol synthesis)
N	Avogadro’s number
S	selectivity (%)
c	BET constant
d	spacing between diffracting planes
g	Gibbs free energy per gram of reaction mixture, kJ/g
m	mass, g or kg
$\boldsymbol{n'}$	polytropic index
n	reaction order or integer
t	time, s
ΔP	pressure differential across the pump, N/m^2

η	pump efficiency
θ	incident angle

Chapter 1 Introduction

1.1 Biomass and sustainability

The last two decades have witnessed growing concerns over the continued use of fossil fuels as the world primary energy resource. Significant amount of research and published literature clearly points to the fact that the development of alternative energy sources is a sound sustainable solution and benefits the environment (Demirbas, 2011, Chattanathan et al., 2012). One major issue associated with the use of fossil fuels is the emission of greenhouse gases and the role they play in global warming (Naik et al., 2010). These greenhouse gases, together with other pollutant gases, are produced during the combustion of fossil fuels and include CO_2, SO_2 and NO_x (Ni et al., 2006). Biomass, which can be defined generally as any biological material obtained from a living or recently living organism (plant or animal) or simply as all organic material that stems from plants (including trees and crops), algae and animal manure, is being considered as an alternative to fossil fuel since it is abundant and can be readily accessed and processed sustainably (Demirbas, 2001a). Though the combustion of biomass/biofuel generates CO_2, it is considered a carbon near-neutral process since the CO_2 released during combustion is the same CO_2 absorbed by plants when synthesising carbohydrates during photosynthesis. Some fossil CO_2 emissions may occur when acquiring and handling biomass such as during soil conditioning via synthetic fertilisers and biomass transport and storage with conventional vehicles and refrigeration. One other major drawback with the use of fossil fuel is the fact that it is a finite source of energy and existing world reserves are known to be depleting very fast due to increase in world demand (Chattanathan et al., 2012, Wu et al., 2008). According to the June 2016 BP Statistical review of world energy, fossil fuels (petroleum, coal and natural gas) account for more than 86 % of commercially traded fuels which corresponds to 11,306 MTOE (Million Ton Oil Equivalent). Meanwhile, modern renewables only account for about 3% of commercially traded fuels; with 22% of this derived from biofuels (ethanol and biodiesel) and the rest from solar, wind, geothermal and biomass (BPp.l.c, 2016). Direct combustion of traditional biomass still accounts for 9% (about 1,183 MTOE based on 2016 estimates) of world primary energy supply representing 65% of world renewable energy consumption (Lauri et al., 2014, REN21, 2015).

Some reasons accounting for the low share of biomass as a primary source of energy are its low energy content (when fresh and wet), bulkiness, and the low efficiency associated with direct combustion processes. The net energy available from combusted biomass can range from about 8 MJ/kg for green wood, 20 MJ/kg for dry plant matter, to 55 MJ/kg for bio-methane (Demirbas, 2001a). Typical electrical, thermal and mechanical efficiencies for biomass combustion processes range from 20 – 40 % (Demirbas, 2001a, Ni et al., 2006, Doherty et al., 2010). By using different technologies based on physical, chemical, thermal or biological methods, it is possible to convert biomass into heat energy, electricity, solid fuels, liquid fuels (bio-oil, biodiesel and ethanol) and gas fuels (Chang et al., 2011). These different biomass conversion technologies all have their advantages and disadvantages.

Chemical industries rely on fossil feedstock not only for fuel production but also for the production of chemicals, plastics, fertilisers etc. Unlike other alternative sources of energy like wind, solar and tidal energy, biomass presents a better option due to its complex organic nature which can serve as feedstock, either directly or indirectly after processing, for the production of multiple bio-based chemical products (Czernik and Bridgwater, 2004a, Kamm et al., 2006).

1.2 Types of biomass/biofuel

Biomass has been used by humans as a source of energy (heating) for many centuries. According to Ni et al., 2006, biomass can be divided into four categories:

a) Energy crops: which include herbaceous energy crops, woody energy crops, industrial crops, agricultural crops and aquatic crops.

b) Agricultural residues and waste: crop waste and animal waste.

c) Forestry waste and residues: mill wood waste, logging residues, trees and shrub residues.

d) Industrial and municipal wastes: municipal solid waste, sewage sludge and industry waste.

More than 80% of biomass resource is obtained from the forestry industry and is used directly as fuelwood or converted to charcoal or black oil (see Figure 1.1).

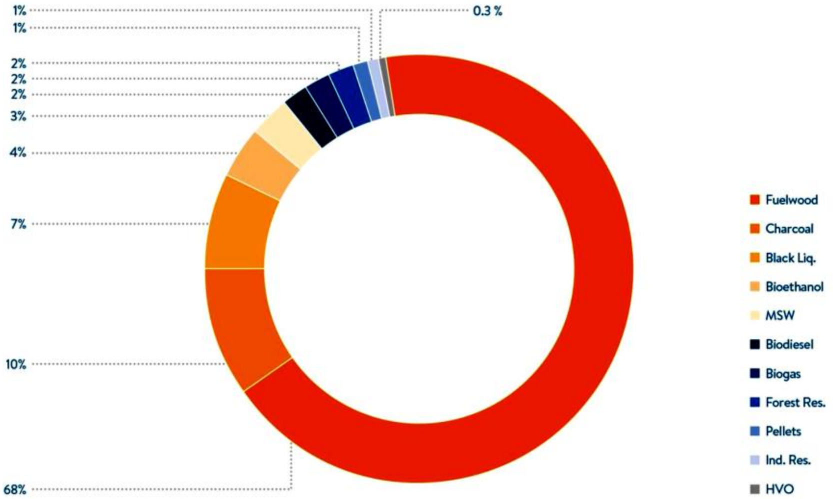

MSW: municipal solid waste

Figure 1.1 Primary energy supply of biomass resources globally in 2013 (WBA, 2016)

However, the share of biogas and liquid biofuels has witnessed average annual growth rates leading to an increase of 11.2% and 15.6% respectively to their 2000 values (Bart et al., 2010). This increase in production can be associated to favourable government legislation, tax incentives and even government subsidies. For example in May 2003, the European Union (EU) outlined the Biofuels Directive (EU Directive 2003/30/EC). This directive required member states to increase the use of biofuels to a minimum of 2% of total liquid fuel consumption by 2005 and to 5.75% by 2010 (Di Lucia and Kronsell, 2010). The EU Biofuel directive was followed by the Energy Tax Directive 2003/96/EC which laid out the frame work for the taxation of energy products and provided the much welcomed tax relief needed to achieve the targets of the Biofuel Directive (Bart et al., 2010). The EU reinforced its commitment to increase the share of biofuels in transportation by imposing obligatory targets for their consumption in the 2009 directive, 2009/28/EC, which also set a quota of at least 10% biofuels in the total gasoline and diesel consumed by 2020 (Skogstad, 2016, Pacesila et al., 2016).

Different process technologies exist for the conversion of biomass into useful products. As shown in Figure 1.2, biomass conversion processes can be divided into four main categories: Thermochemical, biological, chemical and physical conversions. All these processes combine to form a wide range of different products collectively referred to as either biofuels or bio-materials (bio-chemicals).

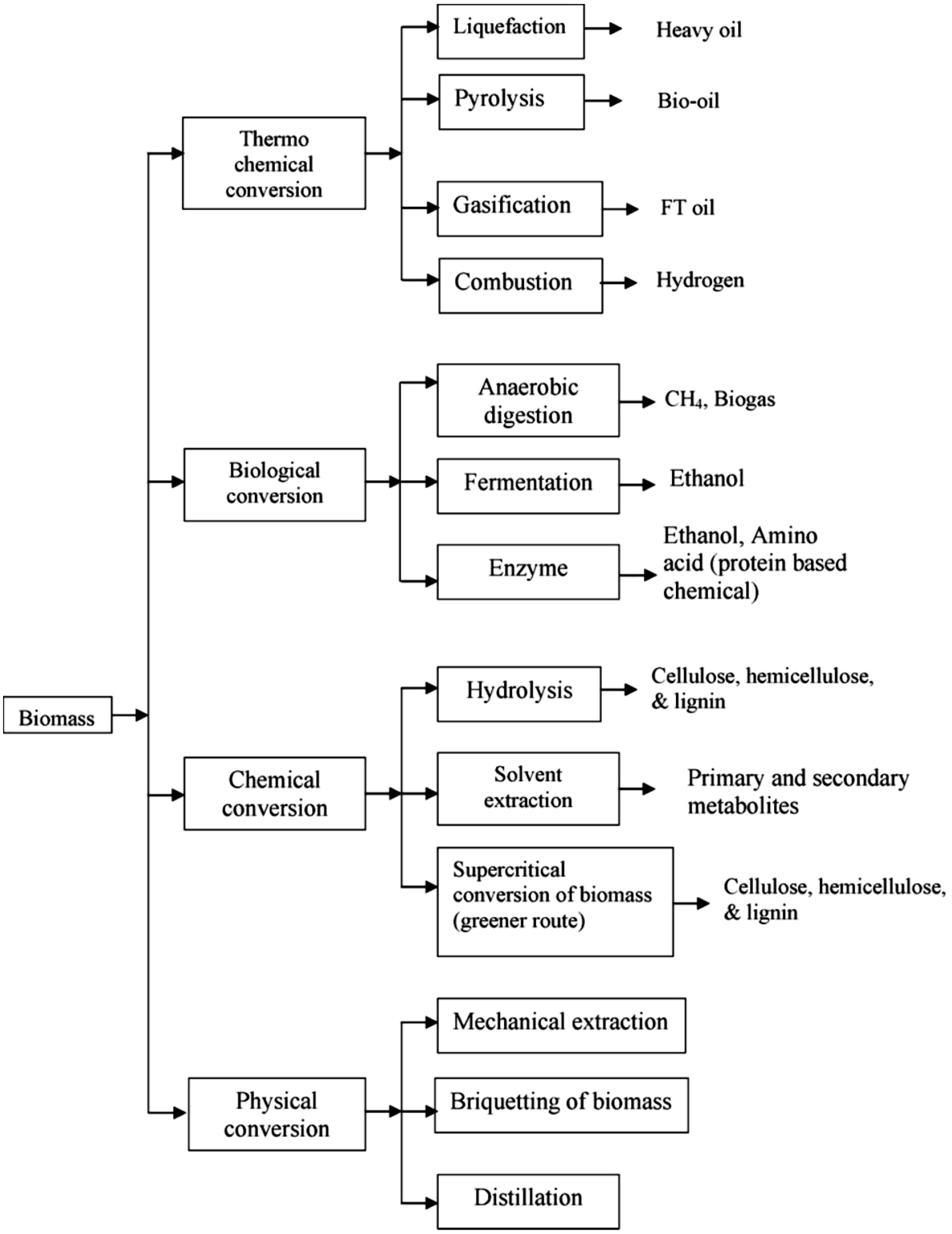

FT: Fischer Tropsch

Figure 1.2 Biomass conversion processes (Naik et al., 2010)

Bio-oil (which is an example of a biofuel) is obtained from biomass through a thermochemical process called pyrolysis (see Figure 1.2). Hydrogen can then be produced from this bio-oil either by reforming or partial oxidation.

1.3 Hydrogen Production

1.3.1 Global production

Hydrogen has been gaining ground as a promising alternative to reduce global dependence on fossil fuels (Kalinci et al., 2009). This is due to the fact that hydrogen is seen as a clean and abundant source of energy whose production, especially from renewable sources, can guarantee energy sufficiency for years to come. Hydrogen is an energy carrier and, just like electricity, it has to be produced before it can be used. With an energy density of 122 MJ/kg, hydrogen has the highest energy density of all fuels (Hou et al., 2009a). As a comparison, 9.5 kg of hydrogen is sufficient to replace 25 kg of gasoline (Parthasarathy and Narayanan, 2014). This advantage in energy density is somewhat overturned by the very low density of hydrogen causing it to occupy four times more volume than gasoline with the same energy (Balat, 2008).

Unlike natural gas and coal, free hydrogen gas does not occur significantly in nature and is mostly found in an oxidised state in water and in reduced form in hydrocarbons and organic molecules. Global hydrogen production is currently estimated at 7.2 EJ per year (about 667 billion m^3/year), of which about 96% of is from fossil fuels with natural gas alone accounting for 48% of hydrogen production as shown in Figure 1.3 (Voldsund et al., 2016).

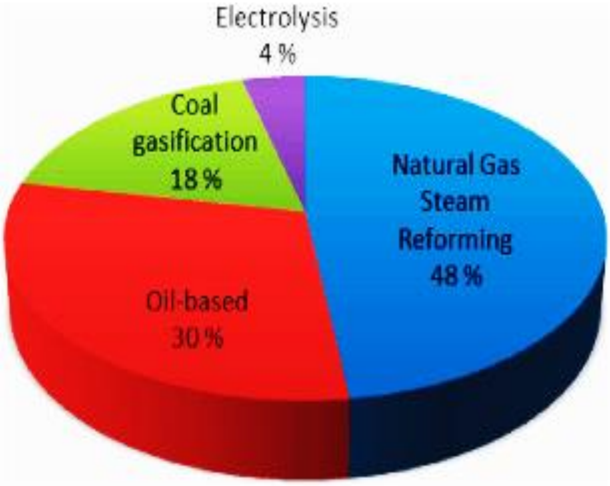

Figure 1.3 Shares of production sources of hydrogen (Voldsund et al., 2016).

1.3.2 Hydrogen from biomass

Hydrogen can be produced from biomass either directly or indirectly, via chemical intermediates, by thermochemical or bio-chemical (biological) processing. Biological processing requires very specific biomass feedstocks, usually starch or sugar derivatives, which are converted to simpler molecules and finally upgraded to hydrogen using either gasification or reforming (Naik et al., 2010). Thermochemical processing on the other hand, allows for a wide range of biomass feedstock to be processed, producing an even more extensive range of products. Thermochemical conversion processes tend to be fast, cost effective and have higher overall efficiencies when compared to biological conversion processes (Parthasarathy and Narayanan, 2014). This work focuses on thermochemical conversion processes. Two main thermochemical processing routes exist for the production hydrogen from biomass. The first route proceeds by biomass gasification to syngas followed by direct reforming of the gaseous mixture produced. Alternatively, the biomass undergoes pyrolysis which is then followed by reforming of the pyrolysis vapour or liquid pyrolysis oil depending on the type of pyrolysis method employed. Hydrogen yield from biomass thermochemical processing ranges typically from 12 to 18 wt% of the biomass feed (on dry basis) depending on the actual process used (Demirbas, 2001b). Biomass gasification is usually carried out at temperatures ranging between 600 – 1000 °C with steam or air producing a predominantly gaseous stream with small quantities of char and ash (Balat, 2009, Demirbaş, 2002). The general equation for biomass gasification is given in Eq. 1.1.

$$\text{Biomass} + H_2O\ (\text{or Air}) \rightarrow CO, CO_2, H_2O, H_2, N_2\ CH_4, C_xH_y, \text{tar, char, ash} \quad 1.1$$

Conceptually, any gasifier can be divided into four main reaction zones (Balat, 2009, Demirbaş, 2002): drying zone (up to 100 °C), pyrolysis zone (200 – 500 °C), combustion or oxidation zone (700 – 1000 °C) and reduction zone (800 – 1000 °C). In the drying zone, moisture is liberated from the biomass without causing any further decomposition. Biomass decomposition is initiated in the pyrolysis zone during which volatiles such as water and acetic acid together with gases like CO, CO_2, and light hydrocarbons are released accompanied by the formation of tar. In the presence of air or pure oxygen, a combustion zone exist in which all the oxygen present reacts with combustible compounds to form CO_2 and H_2O. Finally, a series of gas phase chemical reactions take place in the absence of O_2 in what is termed the reduction zone leading to the formation of CO, CO_2, H_2, H_2O. The actual composition of the gas obtained from the gasifier depends on the prevailing feed conditions especially on the amount of air, oxygen or steam used as given in Table 1.1. Steam gasification yields a syngas with the highest heating value mainly due to its high CH_4 content and negligible N_2 content. Apart from the different gasification conditions presented in Table 1.1, biomass properties such as surface area, size, moisture content, volatile matter and carbon content also affect the gasifier syngas composition. Pure hydrogen can be obtained by first sending the gasifier output gas into a water gas shift reactor followed by a hydrogen purification unit (see Chapter 2).

Table 1.1 Comparison between gasification processes using either air, oxygen or steam (Parthasarathy and Narayanan, 2014)

	Air gasification	**Oxygen gasification**	**Steam gasification**
Product heating value, MJ/Nm^3	4 – 6	10 – 15	15 – 20
Products	CO, H_2, Water, CO_2, HC, Tar, N_2	CO, H_2, HC, CO_2	H_2, CO, CO_2, CH_4, light HC, tar
Average product gas composition	H_2 – 15%, CO – 20%, CH_4 – 2%, CO_2 – 15%, N_2 – 48%, H_2:CO = 0.75	H_2 – 40%, CO – 40%, CO_2 – 20%, H_2:CO = 1	H_2 – 40%, CO – 25%, CH_4 – 8%, CO_2 – 25%, N_2: 2%, H_2:CO = 1
Reactor temperature, °C	900 – 1100	1000 – 1400	700 – 1200
Cost	Cheap	Costly	Medium

HC: Hydrocarbon

Hydrogen production from biomass by pyrolysis will be reviewed and presented in detail in Chapter 2. Table 1.2 summarises the advantages and limitations of producing hydrogen from biomass (Demirbas, 2006).

Table 1.2 Main advantages and limitations of biomass to hydrogen (Demirbas, 2006)

Advantages
Use of biomass reduces CO_2 emissions
Crop residues conversion increases the value of agricultural output
Replacing fossil fuels with sustainable biomass fuel
Costs of getting rid of municipal solid wastes
Limitations
Seasonal availability and high costs of handling
Non-total solid conversion (char formation) and tars production
Process limitations: corrosion, pressure resistance and hydrogen aging

Eventual the feasibility of producing hydrogen from biomass is ultimately controlled by the cost of the final hydrogen product.

1.4 Uses of hydrogen

Using hydrogen as a fuel is still at an early stage of technological development and so most of the hydrogen produced globally is still used as feedstock for some well-established chemical and petrochemical processes. In 2016, almost 50% of hydrogen produced (330 billion m^3) was used for the production of ammonia, 37% was consumed by refineries, 6.5 % was used for methanol synthesis and the remaining 6.5% was used to manufacture other chemicals (Voldsund et al., 2016). Global hydrogen production has witnessed steady growth over the last decade. This increase in production has been driven by a need to satisfy the growing demands of the major hydrogen consumers. For example increase demand for agrochemicals and ammonia fertilisers to meet the food needs of a growing world population; the increasing demand for refining heavier and higher sulphur content crude oil to meet up with strict environment regulations; and finally increase use of hydrogen as a transportation fuel (Levin and Chahine, 2010, Arregi et al., 2016, Behera et al., 2013).

1.4.1 Ammonia production

As mentioned previously, about 50% of hydrogen produced is used for the synthesis of ammonia. Ammonia is produced industrially by the Haber-Bosch process during which hydrogen reacts with nitrogen at high pressures (200 – 500 bar) and high temperatures (400 – 500 °C) in the presence of iron promoted catalysts (Tanabe and Nishibayashi, 2013). About 180 million metric tonne (MMT) of ammonia was produced in 2014 most of which was used to produce fertilisers either as salts, solutions or anhydrous solids (Gellings and Parmenter, 2016).

1.4.2 Petroleum industry

The second major consumer of hydrogen is the petroleum refinery industry where it used mainly for hydrotreating and hydrocracking processes. During hydrocracking, high molecular heavy gas oils are converted into light distillates such as kerosene, diesel and naphtha by using hydrogen to initiate cracking (carbon-carbon scissions) and hydrogenation reactions. The aim is to produce refined fuels with smaller molecules and higher H/C ratios (Ramachandran, 1998). Long et al. (2011) identified hydrocracking as the prime consumer of hydrogen in a refinery, accounting for about 84% of total hydrogen consumption. Hydrotreating processing on the other hand involves the removal of undesirable components from different petroleum fractions by selectively reacting them with hydrogen. These undesirable components included but not limited to sulphur, nitrogen, olefins and aromatics. Light petroleum fractions such as naphtha undergo hydrotreating as a pre-treatment measure to reduce their sulphur content before moving into catalytic reforming units to avoid catalyst poisoning. While heavier fractions ranging from jet fuel to heavy vacuum gas oils are usually hydrotreated to meet strict product quality specifications (Gruia, 2008). Other hydrogen consuming processes that can exist in a refinery include lubricant plants, isomerization process, and petrochemical processes that are integrated with the refinery hydrogen network (Rabiei, 2012).

1.4.3 Petrochemical industry

More than 10% of hydrogen produced globally is used either directly or indirectly in synthesis of several important bulk (commodity) chemicals. Most of this hydrogen is used for the synthesis of methanol. The hydrogen for methanol synthesis is obtained as part of the syngas produced after methane steam reforming or coal gasification. The hydrogen and carbon monoxide in the syngas are reacted over a catalyst at high temperatures and pressures to from methane according to Eq. 1.2.

$$CO + 2H_2 \rightleftarrows CH_3OH \qquad (\Delta H_{298} = -91 kJ/mol) \qquad 1.2$$

Figure 1.4 shows the fraction of global methanol consumption by product and industry.

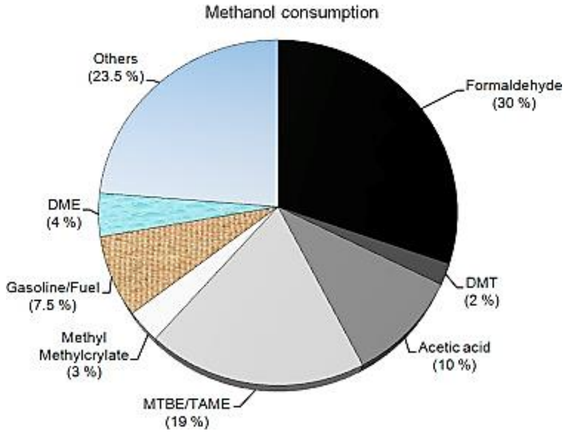

Figure 1.4 Methanol consuming industries (Ali et al., 2015)

Most of the methanol produced is used by the petrochemical industry in the production of formaldehyde, methyl tertiary butyl ether (MTBE), aromatics, ethylene, dimethyl ether (DME), acetic acid and other chemicals such as butyraldehyde, butanediol, tetrahydrofuran, hexamethylene and cyclohexane (Ali et al., 2015, Ramachandran, 1998). Methanol is also used in the transportation industry either directly by blending with gasoline are indirectly as a reactant in the production of biodiesel (Pérez-Fortes et al., 2016).

1.4.4 Other uses

Hydrogen is widely used in the food industry in the hydrogenation of fats and oils to produce margarine and butter. Hydrogenation of oils is carried out in the presence of a metal catalyst and leads to the reduction of the double bonds in unsaturated fatty acids to single saturated bonds by the reaction with hydrogen gas (Tarrago-Trani et al., 2006). Hydrogenation leads to an increased melting point and enhanced resistance to oxidation thus improving the shelf-life of the final product (King et al., 2001).

In the metallurgical industry, hydrogen is used to reduce metals to their oxides. It is also used as an O_2 scavenger during heat treatments such as annealing and furnace brazing to form water (Ramachandran, 1998). In the Sherritt Gordon Process, it is used as a reducing agent to precipitate nickel from nickel sulphate solution in the presence of ammonia (Ramachandran, 1998). Hydrogen also finds very useful applications in the electronics and glass making industries.

1.4.5 Fuel cell

Coupled to the ‘traditional’ demands for hydrogen is the growing need to use it as an energy carrier in small stand-alone fuel cell units. Hydrogen fuel cells are units which convert the chemical energy of hydrogen directly into electrical and thermal energy. A fuel cell consists of a pair of electrodes and an electrolyte like a regular battery. However, a fuel cell is fundamentally different from a battery in that the species consumed during the electrochemical reactions have to be continuously replenished (Ellis et al., 2001, Williams, 2011). One major advantage of fuel cells is that they produce water and heat as the only by-products. Figure 1.5 illustrates the basic components of a fuel cell.

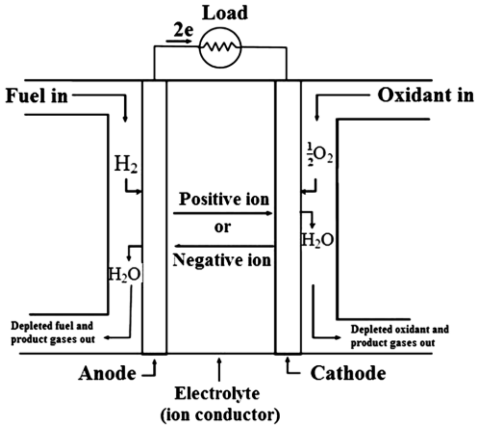

Figure 1.5 Schematic representation of a single fuel cell (EG&G Technical Services Inc, 2004)

In a fuel cell, a fuel such as hydrogen enters the anode while an oxidant (usually air) is supplied to the cathode. The anode and cathode are both separated by a selectively conductive electrolyte. At the anode, the fuel is oxidized, producing electrons which travel through the external circuit to the cathode where they cause the oxidant to reduced (Ellis et al., 2001). Conduction through the electrolyte can occur either from the anode to cathode or from the cathode to anode depending on the electrolyte’s composition and this constitutes the fundamental difference amongst different fuel cells types (Larminie and Dicks, 2003, Williams, 2011).

There are five main types of hydrogen fuel cells divided into two main categories: low-temperature fuel cells and high-temperature fuel cells. The low-temperature fuel cells are the polymer electrolyte fuel cell (PEFC) also called the proton exchange membrane fuel cell (PEMFC), the alkaline fuel cell (AFC), and the phosphoric acid fuel cell (PAFC). The high-temperature fuel cells are the molten carbonate fuel cell (MCFC) and the sulphur oxide fuel cell (SOFC). These fuel cells all operate under different conditions with the high-temperature ones showing more flexibility in feedstock and catalyst requirements. Meanwhile, the low-temperature ones are easy to manage with better efficiencies but at the same time require expensive catalysts and have a very low tolerance to impurities such as CO. Table 1.3 provides a summary of some properties and differences existing amongst the various types of fuel cells.

Overall, fuel cells show higher efficiencies and better flexibility when compared to conventional internal combustion engines and power generators.

Table 1.3 Summary properties of the different types of fuel cells (Larminie and Dicks, 2003, EG&G Technical Services Inc, 2004).

FC	**PEMFC**	**AFC**	**PAFC**	**MCFC**	**SOFC**
Electrolyte	Hydrated Polymeric Ion Exchange Membranes.	Mobilized or immobilised KOH in asbestos matrix.	Immobilised liquid H_3PO_4 in SiC.	Immobilised liquid molten carbonate in $LiAlO_2$	Ceramics
Electrodes	Carbon	Transition metals	Carbon	Nickel and Nickel Oxide	Perovskite and perovskite / metal cermet
Catalyst	Platinum	Platinum	Platinum	Electrode Material	Electrode Material
Operating Temp , °C	40 – 80	65°C – 220	205	650	600 – 1000
Charge Carrier	H^+	OH^-	H^+	CO_3^-	O^-
Efficiency	53-58%	60%	32-38%	45-47%	35-43%
External reformer use	Yes	Yes	Yes	No, for some fuels	No, for some fuels and cell designs
External shift conversion	Yes, plus purification to remove CO traces	Yes, plus purification to remove CO& CO2	Yes	No	No
Prime cell components	Carbon Based	Carbon based	Graphite based	Stainless Based	Ceramic
Product heat management	Process Gas + Liquid Cooling Medium	Process Gas + Electrolyte Circulation	Process Gas + Electrolyte Circulation	Internal Reforming + Process Gas	Internal Reforming + Process Gas
Power, kW	1 – 250	10 – 100	50 – 1000	1 – 1000	1 – 3
Application	Combined heat and power (CHP), transportation	Military and space	Distributed generation (DG)	Electric utility, large distributed generation	Electric utility & large scale DG

1.4.6 Combustion

Apart from its use in fuel cells, hydrogen can be combusted directly in some internal combustion engines known as hydrogen internal combustion engines (HICE). These engines work almost similarly to sparked-ignited gasoline engines (Gupta and Pant, 2008). Hydrogen’s suitability for transportation is assured by its excellent fuel properties such as wide flammability limit range (4 to 75% by volume), high flame velocity, a high octane number (130), and no toxicity or ozone-forming potential (Balat, 2010). One major concern with HICE is premature ignition and knock which is usually caused by hot spots in the combustion chamber as a result of hydrogen’s lower ignition energy, wider flammability range, and shorter quench (Gupta and Pant, 2008).

1.5 Research scope

This project covers the production of H_2 and syngas from a renewable source, bio-oil, obtained after the fast pyrolysis of a biomass waste such as palm empty fruit bunch (PEFB), which is a by-product of the palm oil industry. Specifically, it covers the autothermal reforming (ATR) of bio-oil by considering various bio-oil model compounds, using both powder/particulate catalysts (18 wt% NiO/Al_2O_3, 15 wt% NiO/CaO/ Al_2O_3, 1 wt% Rh/γ-Al_2O_3 and 1 wt% Rh–3 wt% Ce/γ-Al_2O_3) and low pressure drop monolithic catalysts (1 wt% Rh/γ-Al_2O_3 and a 1 wt% Rh–3 wt% Ce/γ-Al_2O_3). Initial ATR experiments are performed on single bio-oil model compounds selected to represent some of the main chemical structures found in PEFB bio-oil i.e. acetic acid (carboxylic acids), 2-butanol (alcohols), furfural (furans) and m-cresol (phenolics). A more complex bio-oil surrogate, consisting of formaldehyde, acetaldehyde, 2-butanone, acetic acid, water, furfural, creosol, phenol, guaiacol, catechol, palmitic acid and levoglucosan, is formulated to achieve similar composition and properties to that of the PEFB bio-oil and also tested in ATR experiments. Thermodynamic equilibrium analysis was carried out using NASA Lewis Research Centre’s CEA (Chemical Equilibrium with Applications) software to determine the influence of the main process factors on the ATR of bio-oil and most importantly to determine if hydrogen or syngas production is determined by the actual chemical composition of the bio-oil or its molar elemental composition. The thermodynamic analysis is also used to determine the major reactions contributing to the ATR process and explore how this affects the choice of catalyst. A detailed mechanistic and kinetic study is out of the scope of this project. A process flowsheet design and steady state process simulation is carried out using the Aspen Plus software to explore the feasibility of producing pure H_2 from PEFB by way of pyrolysis of the as-received wet biomass and autothermal reforming of the pyrolysis bio-oil. This design includes measures to bolster overall process efficiency such heat integration and combined heat and power generation, and caps off with a sensitivity analysis to determine the effect of different process factors on the process efficiency.

1.5.1 Aim

A survey of existing literature reveals that most studies on biofuel autothermal reforming have been limited to bio-ethanol and bio-methanol as feedstocks. There exists a knowledge gap on experimental and process feasibility studies involving autothermal reforming of bio-oil for the production of hydrogen. The aim of this research project is to bridge this knowledge gap by providing experimental and process modelling evidence to support the claim that palm empty fruit bunch (PEFB) derived bio-oil stands as a viable alternate feedstocks for the production of hydrogen by autothermal reforming.

1.5.2 Objectives

To accomplish the aim mentioned above, the project was set out to achieve the following objectives:

1. Perform thermodynamic equilibrium analysis to determine the influence of the main process factors affecting the ATR of a moisture free bio-oil using a mixture of bio-oil model compounds. Also, determine if the equilibrium syngas composition is influenced by either the actual chemical composition of the bio-oil mixture or its molar elemental composition.
2. Based on thermodynamic equilibrium results, propose a reaction mechanism detailing the individual contributions, to product gas composition, of the main reactions taking place during bio-oil ATR; and by so doing determine how this can affect the eventual choice of catalyst.
3. Formulate, prepare and characterise a bio-oil surrogate with similar composition and properties to an actual PEFB derived bio-oil; and used this bio-oil surrogate in process design and experimental studies.
4. Carry out a detailed design and simulation of a process converting fresh PEFB to pure H_2 using the Aspen Plus software. Perform a process optimisation to improve the overall process efficiency by including, in the design, elements of an efficient heat integration network and a combined heat and power generation unit.
5. Perform ATR experiments on a bench scale packed bed reactor using individual bio-oil model compounds and a few powder catalysts. This experiments should provide insights into the variation in feed conversion, H_2 yield, product distribution and coke formation when different bio-oil model compounds and catalysts are used. Also, compare the performance of two commercially available Ni based catalysts to a prepared rhodium (Rh) based catalyst.
6. Study the ATR of the formulated bio-oil surrogate in a packed bed reactor and determine the influence of varying feed conditions and catalyst on the H_2 yield and product distribution. The experiments should compare the performance of

two Rh based catalyst: a monometallic catalyst and a cerium (Ce) promoted catalyst.

7. Carry out the ATR of the bio-oil surrogate and a bio-oil model compound (acetic acid) in a monolithic reactor and determine how similar/or dissimilar the results obtained compare to those from the packed bed reactor experiments.

Chapter 2 Literature Review

2.1 Biomass Pyrolysis : Case of Palm Empty Fruit Bunch (PEFB)

2.1.1 Introduction

Due to its complex organic nature, biomass can serve as feedstock, either directly or indirectly after processing, for the production of multiple bio-based chemicals and energy products (Czernik and Bridgwater, 2004b, Kamm et al., 2005). Biomass can be valorised by pyrolysis to produce bio-oil which is a dark brown, polar, high-density and viscous organic liquid containing a complex mixture of oxygenated compounds such as sugars, carboxylic acids, phenols, esters, ketones, aldehydes and benzenoids (Jacobson et al., 2013, Mantilla et al., 2014, Czernik et al., 2007).

Many different biomass materials have been investigated as potential sources of bio-oil and other pyrolysis by-products. One such biomass is palm empty fruit bunch (PEFB) which is obtained after oil extraction at palm oil mills. The oil palm industry alone is estimated to generated annually over 200 million metric tonnes (MMT) of solid biomass residue most of which is used either as manure or as a cheap source of renewable energy (Pirker et al., 2016, Aghamohammadi et al., 2016, Ooi et al., 2017). As an estimate, for every tonne of palm oil produced from a fresh fruit bunch (FFB), approximately 1 tonne of PEFB, 0.7 tonne of palm fibres, 0.3 tonne of palm kernels and 0.3 tonne of palm shells are generated (Chang, 2014). These different biomass residues are obtained at various stages of the palm oil production process. Figure 2.1 shows a flow diagram for the production of crude palm oil and kernel oil and approximate biomass residues formed assuming 1000 kg of fresh fruit bunch as starting feed.

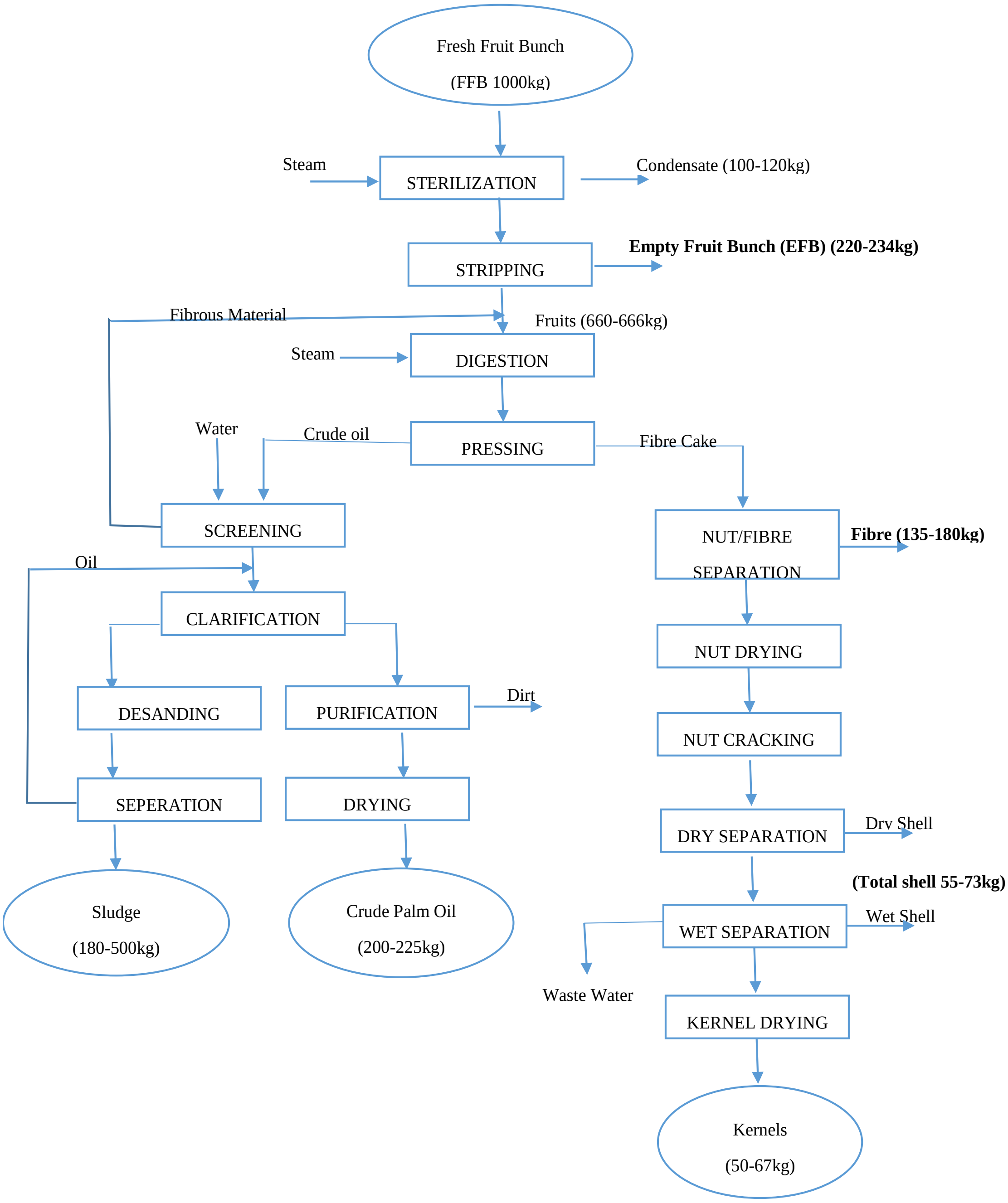

Figure 2.1 Schematic flow diagram for palm oil and kernel extraction showing approximate range of mass outputs from 1000 kg of FFB (Reproduced from (*Obibuzor et al., 2012*)

Pyrolysis is the thermal decomposition of biomass in the absence of oxygen at temperatures ranging from 400 ºC to 600 ºC (Bridgwater, 2012). The result of this decomposition is the production of mostly vapours, aerosols and solid char (Abdullah and Gerhauser, 2008). Biomass composition influences the yield and composition of bio-oil obtained after pyrolysis. The proximate analysis of PEFB given in Table 2.1 reveals that the volatile matter in PEFB accounts for about 70 to 80 wt% and this translates directly to how much 'organic' content is present thereby influencing bio-oil yield (Abnisa et al., 2013).

Table 2.1: Properties of PEFB fibres (Chang, 2014)

Properties	**Values**
Moisture (%)	2.40-14.28
Proximate analysis (%[a])	
Volatile matter	70.03-83.86
Fixed carbon	8.97-18.30
Ash	1.30-13.65
Ultimate analysis (%[b])	
C	43.80-54.76
H	4.37-7.42
O[c]	38.29-47.76
N	0.25-1.21
S	0.035-1.10
Chemical composition (%[a])	
Cellulose	23.7-65.0
Hemicellulose	20.58-33.52
Lignin	14.1-30.45
Extractive	3.21-3.7

a Weight percent on a dry basis.
b Weight percent on a dry and ash-free basis.
c By difference

The actual yield and composition of the bio-oil is determined by the fraction of cellulose, hemicellulose and lignin content in the biomass and the pyrolysis process conditions. Bio-oil can be produced by fast or flash pyrolysis, slow pyrolysis and solvolysis of solid biomass feedstock (Isahak et al., 2012).

2.1.2 Types of pyrolysis

2.1.2.1 Fast pyrolysis

The main process parameters used to distinguish between the different pyrolysis methods are temperature, rate of biomass heating and vapour residence time. Low temperatures and long vapour residence times favour the production of a solid residue (charcoal). Meanwhile, moderate and high temperatures coupled with short or long residence times tend to favour conversion to non-condensable gas or liquid depending on the actual values used (Bridgwater, 2012). Typical conditions required for fast pyrolysis are a dry feedstock (< 10% moisture), small particle size (< 3 mm), short residence times (0.5 – 2 s), moderate temperatures (400 – 500 °C), and rapid quenching of pyrolysis vapours (Isahak et al., 2012). The major components of biomass (cellulose, hemicellulose and lignin) degrade at different rates and by way of different mechanisms when subjected to thermal treatment. Once decomposed, these components form primary products, some of which undergo secondary gas phase reactions, whose yields depend on time allowed and reigning temperature and this is followed by cooling and collection (Bridgwater, 1999). Many studies have been carried out to understand the thermochemical conversion of biomass into bio-oil with authors focusing on process parameters such as pre-treatment of biomass, particle size of feedstock, reaction temperature, reactor type, choice of catalyst and reaction time. Depending on the actual process conditions and the presence or absence of catalyst, bio-oil yield from PEFB fast pyrolysis can range from 30-70 wt% of the solid feedstock, with non-condensable gases and solid char formed as co-products (Abdullah and Gerhauser, 2008, Sulaiman and Abdullah, 2011, Vasiliou et al., 2013, Auta et al., 2014). In a study carried out by Mantilla et al. (2014), PEFB pyrolysis experiments were conducted in a fixed-bed reactor at temperatures ranging between 460 – 600 ºC, gas residence time 16 – 80 s and particle size < 0.5 mm, as well as 0.5–1.4 mm. The maximum yield of bio-oil of 48.4 wt% was obtained at a temperature 540 ºC, gas residence time of 31 s and particle size < 0.5 mm. Their study concluded that temperature was the most significant parameter, of the three considered, in determining the bio-oil yield. Abdullah et al. (2010b) studied the fast pyrolysis of PEFB using a fluidised bed system for which the reactor temperature was varied from 400 to 600 ºC, the residence time between 0.79 – 1.32 s, and particle size diameters (with corresponding ash content) were < 150 μm (8.49 %), 150–250 μm (7.46 %), 250–300 μm (6.70 %) and 355–500 μm (4.83%). They obtained optimum bio-oil yields at a pyrolysis temperature of 450 ºC, retention time of 1.02 s and for the particle size 355 – 500 μm with the lowest ash content. The somewhat high ash content of PEFB (rich in potassium) particularly reduces the yield in bio-oil resulting in the need for pre-treatment options before pyrolysis. Abdullah and Gerhauser (2008) were able to demonstrate that by washing PEFB feedstock with distilled water before pyrolysis, the yield in bio-oil (organic phase) obtained rose to 61.3 wt% which was significantly higher than that the 34.7 wt% obtained for the unwashed PEFB.

2.1.2.2 Slow pyrolysis

Slow pyrolysis, also referred to as carbonization, has been used by mankind for thousands of years to produce charcoal. It involves the use of moderate heating rates with long residence times to produce char with yields ranging from 20 – 40 % (Libra et al., 2014, Kirubakaran et al., 2009). Unlike most traditional processes where the gas and vapour produced are not recovered, industrial processes use a closed kiln fired using recovered pyrolysis gases (Libra et al., 2014). The slow heating rate and long vapour residence time causes secondary cracking of primary products leading to an increased yield of char which is considered the main product (Jahirul et al., 2012). However, slow pyrolysis can be used as a means to produce both char and recoverable bio-oil. In such cases, low heating rates, 5 – 7 K/min, coupled with temperatures ranging between 400 – 500 °C and residence times of about 5 – 30 minutes are used (Bridgwater, 2003, Goyal et al., 2008). Experimental studies involving the slow pyrolysis of various biomass feedstocks have so far focused on determining the influence of heating rate, temperature, residence time and use of an inert purge gas such as nitrogen on the char, bio-oil and gas yields. Beis et al. (2002) performed slow pyrolysis experiments in a fixed bed reactor using safflower seeds to determine influence of pyrolysis temperature, heating rate, particle size and purge gas flow rate on the pyrolysis product yields and chemical composition. They obtained a maximum bio-oil yield of 44% for a reactor temperature of 500 °C, particle size range of 0.425 – 1.25 mm, heating rate of 5 °C/min, and N_2 flow rate of 100 cm^3/min. Their results showed that increasing the temperature and heating rate leads to an overall reduction in the char yield; and reducing the particle size to 1.25 mm resulted in an increase in bio-oil yield at 500 °C at a constant heating rate of 5 °C/min. In another study, Khor et al. (2009a) performed slow pyrolysis of PEFB in a pilot scale kiln with a heating rate of 5 °C/min. The PEFB fibres were dried and heated to 600°C for a total duration of 2 hours. Pyrolysis product yield obtained was 24.8% char, 62.3% of condensates and 12.9% gas. Producing bio-oil by slow pyrolysis presents some tough challenges as the long residence time results in extended secondary gas phase reactions which ultimately affect bio-oil yield and quality. Also, the long residence time and low heat transfer impose the need for extra energy input (Jahirul et al., 2012).

2.1.2.3 Solvolysis

Solvolysis, or hydrothermal liquefaction, is the use of highly pressurised solvent (usually at pressures > critical pressure of solvent) such as water, methanol, ethanol or mixture of water and organic solvent to cause the decomposition of biomass to yield bio-oil at mild temperatures, usually below 400 ºC (Chang, 2014, Akhtar and

Amin, 2011). Typical solvolysis temperatures range from 300 – 400 °C with corresponding pressures of 50 – 200 bar depending on the solvent used, and residence times from 10 to 60 minutes (Xiu and Shahbazi, 2012). A few studies have been carried out to determine the influence of different solvents and catalysts on the production of bio-oil by solvolysis of PEFB. Akhtar et al. (2010), studied the alkaline catalysed liquefaction of PEFB in a batch reactor operating under mild conditions of 270 °C and 20 bars for 20 minutes. They investigated the effect of different catalysts such as NaOH, KOH and K_2CO_3 on PEFB solvolysis with water as solvent. The highest bio-oil yield of about 67 wt% was obtained with K_2CO_3 catalyst with a concentration of 1 M.

Table 2.2 summarises the main differences between the three pyrolysis methods.

Table 2.2 Comparing the different biomass pyrolysis methods (Xiu and Shahbazi, 2012, Bridgwater, 2003)

Process	Temperature, °C/ Pressure, bar	Residence time, s	Product distribution (wt. %)			Comments
			Bio-oil	Char	Gas	
Fast	450 – 500 / 1 (high heating rate)	10 – 20	50-75	12-20	13-30	High bio-oil yield with poor fuel properties. Low capital cost
Slow	400 / 1 (low heating rate)	5 – 30 min	30	35	35	Poor bio-oil yield and slow process
Solvolysis	300 – 400 / 50 – 200	1 – 5	20-60	15-35	15-25	Better quality bio-oil obtained with high heating value

2.1.3 Fast pyrolysis process

In the last two decades, a lot of research and process developments have focused on understanding and optimising the fast pyrolysis process. Unlike the more traditional slow pyrolysis (carbonisation) process, fast pyrolysis is an advanced process which has to be carefully controlled to give high yields of liquid (Bridgwater et al., 1999, Abdullah et al., 2010b). A typical fast pyrolysis process begins with feed preparation which involves drying and grinding, followed successively by the pyrolysis reaction, solid char separation and liquid bio-oil collection. According to Bridgwater (2003), to obtain bio-oil yields of up to 75% on a dry feed basis, the fast pyrolysis process must have the following essential features:

- very high heating and heat transfer rates at the reaction interface, which usually require a finely ground biomass feed,

- carefully controlled pyrolysis reaction temperature of around 500 °C and vapour phase temperature of 400–450 °C,
- short vapour residence times, typically less than 2 s,
- rapid cooling of the pyrolysis vapours to give the bio-oil product.

2.1.3.1 Feed preparation

Biomass feedstock drying and milling are two very important treatment operations that greatly influence the final quality and yield of bio-oil obtained in a fast pyrolysis process.

Drying reduces the moisture content of the biomass and this has a concomitant effect in lowering the final moisture content of the bio-oil produced. Water is produced during fast pyrolysis and in order to maintain bio-oil moisture at an acceptable level (below 25 %), biomass moisture needs to be below 15 % (Jahirul et al., 2012). It is however recommended that biomass should be dried to less than 10 % for fast pyrolysis (Bridgwater et al., 1999). This is because bone-dry biomass still produces bio-oil with a moisture content of 12 – 15 % (Ringer et al., 2006). High moisture content reduces the calorific value of bio-oil and also poses problems affecting bio-oil stability, viscosity, pH, corrosiveness, and other liquid properties (Bridgwater et al., 1999). Drying also helps to improve heat transfer during pyrolysis as any moisture in the feed becomes a heat sink and competes directly with the heat available for pyrolysis (Ringer et al., 2006).

Biomass grinding is also a crucial feed preparation step as a small particle size is necessary in order to satisfy the heat transfer requirements needed to ensure rapid pyrolysis reactions during fast pyrolysis (Jahirul et al., 2012). An average particle size of 2 mm is recommended, especially for processes using fluidised bed reactors, for an efficient fast pyrolysis process (Isahak et al., 2012, Bridgwater, 1999). This is because biomass has a very poor thermal conductivity (0.1 W/mK along the grain, 0.05 W/mK cross grain) and the use of small-sized particles facilitate gas-solid heat transfer thereby fulfilling the requirements for rapid heating and high liquid yields (Bridgwater et al., 1999). The use of a small particle size helps to overcome the insulating effect of the char formed during pyrolysis which hinders the rate at which heat is transferred inside surrounded particles (Ringer et al., 2006). Several studies have shown that an increase in particle size reduces the bio-oil yield during fast pyrolysis (Abdullah et al., 2010b, Ruengvilairat et al., 2012). This decrease in bio-oil yield can be attributed to poor heat transfer and significant increase in cracking and secondary reactions (Scott and Piskorz, 1984). Apart from facilitating rapid heat transfer and pyrolysis reaction, particle size reduction also enhances solid (char) separation and collection of the bio-oil (Bridgwater, 2012).

2.1.3.2 Pyrolysis reactions

The actual pyrolysis of the dried and ground biomass takes place in a suitable reactor where the following steps occur (Babu, 2008):

a) Heat transfer from a heat source, leading to an increase in temperature of the biomass inside the reactor.
b) Initiation of pyrolysis reactions, leading to the release of volatiles and the formation of char.
c) Release of volatiles, resulting in heat transfer between the hot volatiles and cooler biomass particles.
d) Condensation of some of the volatiles in the cooler parts of the feed to produce char.
e) Autocatalytic secondary pyrolysis reactions due to gas/solid and solid/solid interactions.

Heat transfer plays a very important role in determining the success of a fast pyrolysis process. Heat transfer occurs in a pyrolysis reactor in two steps. Firstly, from the heat source to the reactor heat transfer medium which could be the solid wall in ablative reactors or gas in entrained flow reactors. Secondly, from the heat transfer medium to the biomass (Bridgwater et al., 1999). Heat transfer occurs by means of conduction, convection or radiation depending on the reactor design and mobile phases involved. Different reactor designs have been proposed which meet the heat transfer requirements needed for a fast pyrolysis process. These reactors can be grouped into the following categories: fluidised bed, transported bed, circulating fluid bed, ablative (vortex and rotating blade), rotating cone and vacuum reactors (Ringer et al., 2006). Figure 2.2 shows two conceptual fast pyrolysis processes, one integrated with a fluid bed reactor and the other with a rotatory cone reactor. A detailed description of these different reactors types can be found in Bridgwater and Peacocke (2000) and Ringer et al. (2006).

In the reactor, the heat transferred to the surface of the biomass particles is then conducted inside the particle causing an initial release of moisture present in the particle. This is followed by the pre-pyrolysis and main pyrolysis reactions (Babu, 2008). The pre-pyrolysis stage is characterised by the release of volatiles such as acetic acid which flow out of the particles through pores and participate in the heat transfer process.

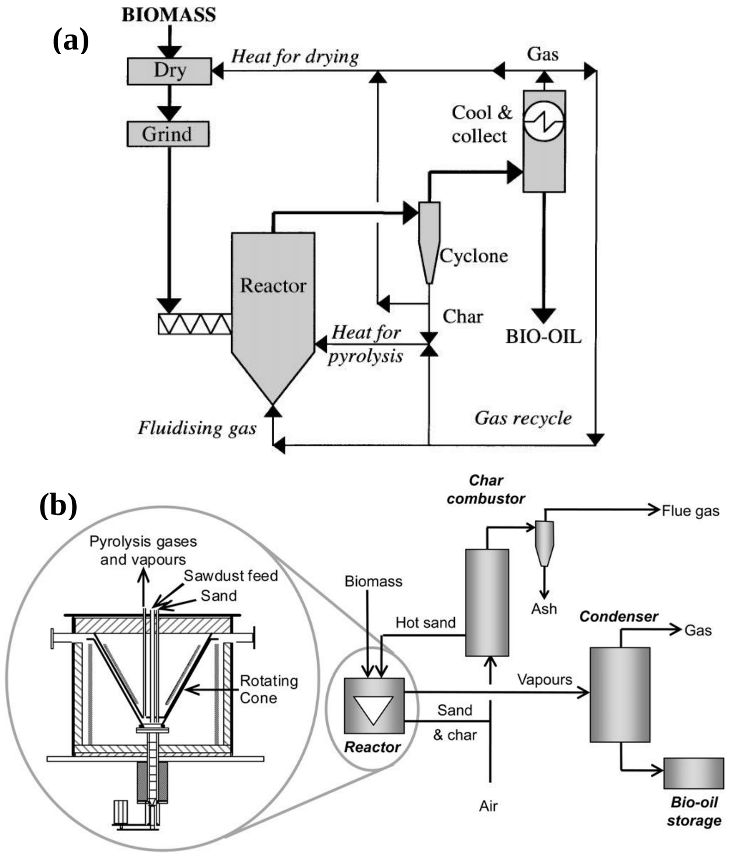

Figure 2.2 Fast pyrolysis process. a) Process using a fluid bed reactor. b) Process with a rotating cone reactor. (Bridgwater et al., 1999, Bridgwater, 2012).

The major components of biomass, i.e. cellulose, hemicelluloses, and lignin, all undergo thermal degradation with varying reaction mechanisms and reaction rates. The complexity of biomass pyrolysis is further compounded by the fact that these components and their products interact with each other during the process (Kan et al., 2016). Figure 2.3 shows the building blocks for cellulose, hemicellulose and lignin. The rate of decomposition of each component depends on factors such as reactor type, temperature, particle size and heating rate; with hemicellulose decomposing first followed closely by cellulose and finally lignin (Babu, 2008). The main reactions taking place during pyrolysis include dehydration, depolymerisation, isomerization, aromatisation, decarboxylation, and charring (Kan et al., 2016).

Hemicellulose is the name given to a group of macromolecules formed by the polymerisation of monosaccharides such as glucose, mannose, arabinose, xylose, and galactose. It is the second most abundant component of biomass after cellulose and decomposes between 200 and 300 °C. Hemicellulose decomposition begins with scission of less stable bonds at 200 °C leading to the formation water, CO_2, methanol, and formic acid.

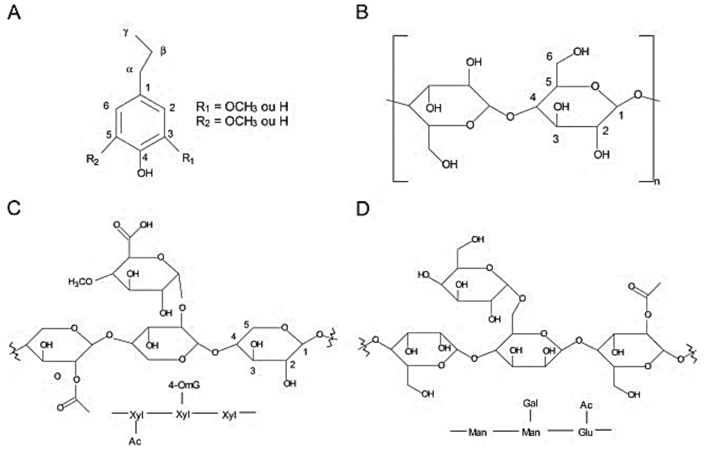

Figure 2.3 Chemical structures of biomass constituents. (A) lignin unit; (B) Cellulose unit; (C) Partial structure of xylan (hemicellulose); (D) partial structure of glucomannan (Xyl: xylopyranose, 4-OmG: 4-O-methylglucuronic acid, Man: mannopyranose, Glu: glucopyranose, Gal: galactopyranose, Ac: acetyl). (Collard and Blin, 2014).

The fragmentations of acetyl substituents of hemicellulose structures, which represent more than 10 wt% of its mass, also occurs at about 200 °C and leads to the production of acetic acid (Collard and Blin, 2014). It has been suggested that most of the acetic acid liberated from wood during pyrolysis is attributed to deacetylation of the hemicellulose (Mohan et al., 2006). Heating up to 300°C causes rapid depolymerisation of hemicellulose leading to the formation of anhydrosugars such as levoglucosan, levomannosan, and levogalactosan. Some of these pyran structures are converted to more stable furan rings, leading to the formation of compounds such as 5-hydroxymethylfurfural, 5-methylfurfural and furfural (Collard and Blin, 2014).

Cellulose is a macromolecule made up of over 5000 glucose units. The thermal degradation of cellulose, like hemicellulose, occurs within a narrow temperature range of 240 and 350 °C. Cellulose pyrolysis is known to give rise to more volatiles and less char than hemicellulose. Among the different biomass components, cellulose pyrolysis has been studied extensively. Several mechanisms and kinetic models have been proposed to explain the decomposition of cellulose and the reactions leading to the formation of the different products. One such model is the Waterloo-mechanism which is widely accepted as a simplified representation of cellulose pyrolysis (Figure

2.4). A similar mechanism has been proposed by Lin et al. (2009) in which the onset of cellulose decomposition is characterised by the formation oligosaccharides with lower molecular units and further heating results in further bond breaking until only the anhydro-monosaccharide, levoglucosan remains (Figure 2.5).

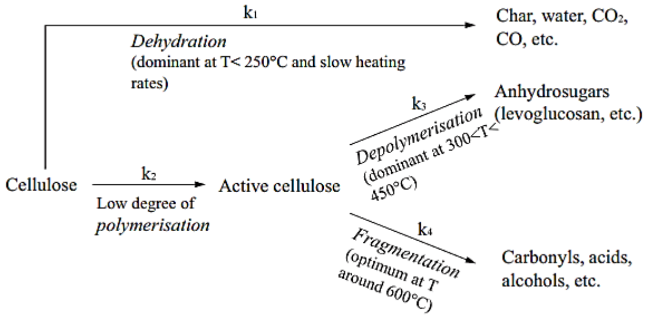

Figure 2.4 Waterloo-mechanism of primary decomposition of cellulose (Radlein et al., 1991)

The levoglucosan formed can undergo dehydration and isomerisation reactions to form other anhydrosugars such as levoglucosenone, and 1,6-anhydro-β-D-glucofuranose (Figure 2.5).

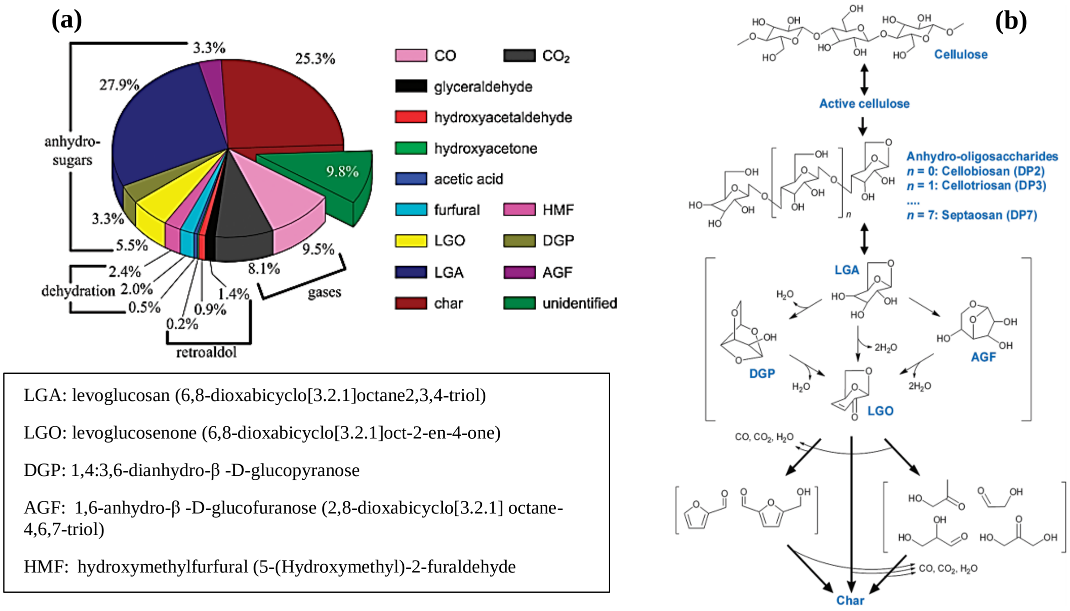

LGA: levoglucosan (6,8-dioxabicyclo[3.2.1]octane2,3,4-triol)

LGO: levoglucosenone (6,8-dioxabicyclo[3.2.1]oct-2-en-4-one)

DGP: 1,4:3,6-dianhydro-β -D-glucopyranose

AGF: 1,6-anhydro-β -D-glucofuranose (2,8-dioxabicyclo[3.2.1] octane-4,6,7-triol)

HMF: hydroxymethylfurfural (5-(Hydroxymethyl)-2-furaldehyde

Figure 2.5 Cellulose pyrolysis. a) Product yields. b) Proposed Mechanism. (Lin et al., 2009)

These anhydrosugars can react further by dehydration, fragmentation and retroaldol condensation reactions to form compounds such as furfural, hydroxymethyl-furfural, hydroxyacetone, glycolaldehyde and glyceraldehyde. Carbon monoxide and carbon dioxide are formed from decarbonylation and decarboxylation reactions (Lin et al., 2009).

Lignin on the other hand decomposes between 250 and 500 °C. This decomposition temperature range is wider than that for hemicellulose and cellulose making lignin to have an apparent thermal stability during pyrolysis (Kan et al., 2016, Bridgwater, 1999). Lignin is a three-dimensional, highly branched, polyphenolic substance with no exact structure consisting of an irregular array of bonded "hydroxy-" and "methoxy" substituted phenyl units (Mohan et al., 2006). Initial lignin decomposition starts at about 250 °C with the release of volatiles formed from the breakup of alkyl side chains, e.g. propyl side chains, and methoxy substituents on aromatic rings (Collard and Blin, 2014). Depending on the actual location of the hydroxyl group on the lateral propyl chains, C–C bond fragmentation may lead to the formation of formaldehyde, CO and CO_2 (Liu et al., 2008). Increasing the temperature to 400 °C causes the release of other compounds such as CH_4, methanol, acetaldehyde, acetone, and acetic acid; together with substituted phenolic compounds such as p (or m)-cresol, guaiacol and syringol (Collard and Blin, 2014).

As the major biomass components decompose as described above, a solid polycyclic aromatic residue, called char, is formed as a result of increased reticulation and thermal stability caused by ongoing intra/inter-molecular rearrangement reactions (Pastorova et al., 1994, Collard et al., 2012). Benzene structures appear at about 300 °C from dehydrated pyran rings obtained from hemicellulose and cellulose decomposition. These benzene structures, together with the phenolic structures obtained from lignin decomposition become more condensed and crosses linked as temperature is increased to 500 °C accompanied by the release of more water and other non-condensable gases such as H_2, CO, CO_2 and CH_4 (McGrath et al., 2003, Shen et al., 2010, Collard and Blin, 2014). On a dry basis, the char production from the pyrolysis of cellulose, hemicellulose and lignin is estimated to be 10 – 15 wt% , 20 – 30 wt% and 30 – 50 wt% respectively (Hosoya et al., 2007, Qu et al., 2011).

2.1.3.3 Char removal

Char is catalytically active and is responsible for promoting pyrolysis vapour cracking reactions (Jahirul et al., 2012). Its presence in bio-oil has been shown to accelerate ageing and aggravate instability issues (Bridgwater, 2003). Ideally, char can be separated from the hot vapours leaving the pyrolysis reactor by using a cyclone. This however has a serious limitation as cyclones are known to be ineffective in recovering fine particles (below 2-3 microns) which eventually end up in the bio-oil (Ringer et al., 2006). Other char separation methods have been developed and tested with each having varying degrees of success. One such method is the use of a modified bag-house filter to separate char form the pyrolysis vapour by hot gas filtration. This technique is able to produce a high quality bio-oil with very little residual char but comes with a loss of 10 – 15% of the initial liquid yield as a result of vapour cracking caused by char accumulation on the surface of the filter (Scahill et al., 1997, Ringer et al., 2006). There are also problems with the sticky nature of fine char and disengagement of the filter cake from the filter (Bridgwater, 2003). Alternative techniques such as in-bed vapour filtration and rotary particle separation have been proposed but also show some limitations due to the complex interaction between char and pyrolytic liquid which results in a gel-like phase that rapidly blocks the filter (Jahirul et al., 2012).

2.1.3.4 Bio-oil recovery

Pyrolysis vapour product is quite unstable and usually requires rapid quenching in order to preserve the future bio-oil components which may otherwise crack to permanent gases or polymerise to form char (Ringer et al., 2006). The vapour is actually not just a gas mixture but a combination of true vapour, micron sized droplets and polar molecules (Bridgwater et al., 1999). Pyrolysis vapours form aerosols upon cooling thereby complicating the liquid collection processes. Column and venturi scrubbers have both been used for bio-oil recovery and have proved very effective for large scale processing. Quenching is achieved in such scrubbers by using either previously collected bio-oil or an immiscible organic solvent. However, some of the bio-oil remains as aerosols and additional collection can be achieved using electrostatic precipitators (Peryoga et al., 2014).

2.1.3.5 Bio-oil composition

The bio-oil recovered after fast pyrolysis is a dark brown mixture with a moisture content usually between 15 – 35 wt% comprising hundreds of organic compounds such as acids, alcohols, ketones, aldehydes, phenols, sugars, furans, alkenes, nitrogen compounds and miscellaneous oxygenates (Kan et al., 2016). Solid char and metals from ash may also be present bio-oil. The actual composition of bio-oil depends on the biomass feedstock used and the entire pyrolysis process employed as described above i.e. drying, particle size, reactor type, heat transfer rate, pyrolysis temperature, vapour residence time and bio-oil recovery method. Table 2.3 summarises the PEFB bio-oil composition as reported by several authors.

Table 2.3 Summary of PEFB bio-oil composition obtained in literature

	(Sulaiman and Abdullah, 2011)	**(Kim et al., 2013)**	**(Abdullah et al., 2010b)**	**(Sukiran et al., 2009)**	**(Pimenidou and Dupont, 2012)**	**(Khor et al., 2009a)**
Pyrolysis temperature (ºC)		480		500		600
Reactor	Fluidised	Fluidised		Fluidised		Kiln
Moisture	7.9	0	7.90	18.74	24.30	5.2
Proximate analysis (%)						
Volatile matter					84.3	
Fixed carbon					11.3	
Ash				0.65	2.43	0.1
Solids						
Ultimate analysis (%)						
C	69.35	58.65	69.35	49.80	45.23	68.26
H	9.61	7.02	9.61	7.98	6.53	8.02
O	20.02	30.14	20.02	40.29	47.03	21.57
N	0.74	2.74	0.74	1.93	8.5×10^{-3}	2.02
S		<0.1			0.0611	0.03
H/C molar ratio		1.436		1.92		1.41
O/C molar ratio		0.39		0.61		0.24
HHV (MJ kg^{-1})	36.06	24.9	36.06	21.41	19.8	31.44
LHV (MJ kg^{-1})					18.4	
TAN KOH (mg kg^{-1})		110		76		102.9
pH				3		3.6

2.1.3.6 Bio-oil uses and upgrade

Bio-oil can be used directly as fuel in combined heat and power applications or it can serve as a source for the extraction of selected chemicals (Ringer et al., 2006). For heat and power generation, bio-oil can be burned directly in oil fired burners or in medium and slow conventional diesel engines (Jahirul et al., 2012). So far, a few chemicals with potential industrial and economic applications have shown recoverable potential from bio-oil. These includes polyphenols for producing resins, levoglucosan, hydroxyl-acetaldehyde, fertilisers, wood preservatives, and range of flavourings and essences for the food industry (Goyal et al., 2008, Bridgwater et al., 1999).

Bio-oil can be upgraded via chemical and catalytic means to a product closer to conventional hydrocarbon fuels. The aim is to achieve full deoxygenation and at the same time increase its heating value and reduce its viscosity. This can be done by either hydrotreating or catalytic vapour cracking over zeolites (Isahak et al., 2012). Both techniques however do not have wide industrial application due to concerns with catalyst stability and the high costs involved (Bridgwater and Peacocke, 2000).

A lot of focus recently has been on the thermochemical processing of bio-oil to H_2 or syngas; and eventual synthesis of transportation fuels and other hydrocarbons from the syngas produced using Fischer Tropsch synthesis (Jahirul et al., 2012, Bridgwater, 2012).

2.2 Hydrogen production by thermochemical processes

2.2.1 Hydrogen production from fossil fuels

2.2.1.1 Steam Reforming

2.2.1.1.1 Steam reforming process

Steam reforming (SR) is a process widely established in the chemical and petrochemical industries. It involves the conversion of hydrocarbons with steam into a mixture of hydrogen and carbon monoxide (synthesis gas or 'syngas') (Salhi et al., 2011). The general steam reforming reaction for a hydrocarbon is given in Eq. 2.1.

$$C_nH_m + nH_2O \rightarrow nCO + (n + \tfrac{1}{2}m)H_2 \qquad 2.1$$

This reaction is endothermic and usually requires a lot of external heat. Steam reforming is therefore an energy intensive process with reformers designed to optimize heat exchange alongside huge capital investments for heat recovery units (Dybkjaer, 1995b). The main hydrocarbon feedstocks used are natural gas and naphtha. Industrially, steam reforming of methane is carried out at pressures of 1.4 – 4.0 MPa and temperatures in the range of 750 – 900 ºC (Jonga et al., 2009). Despite high pressures being thermodynamically unfavourable to the reaction, their wide spread use allow for more economic and compact plants. The mixture of methane and steam is first preheated and then passed over a catalyst bed (in the reformer) where it converts to carbon monoxide and hydrogen (Eq. 2.1). The reformer exit stream is typically composed of hydrogen, carbon monoxide, carbon dioxide, steam and methane. To obtain essentially pure hydrogen, the product stream from the reformer has its CO shifted in water gas shift reactors where the reaction given by Eq. 2.2 takes place. Shifting is often carried out in two stages ('high temperature' and 'low temperature' CO shift) with cooling in between, then the CO_2 and H_2 rich gas mixture is sent to a pressure swing adsorption (PSA) unit where the off gasses (unreacted CO and CH_4, CO_2 and 15 -20% of the total H_2) are recycled to a furnace for burning in order to supply the reformer with heat (see Figure 2.2). Typically, the molar steam to carbon ratio (S/C) used is about 3 but can be varied over a wide range depending on the desired composition for the product gases (Lutz et al., 2003). The WGS reaction is usually carried out in the presence of a copper catalyst at low temperatures (210 – 330 °C) to ensure complete conversion of carbon monoxide (Choi and Stenger, 2003, Li et al., 2000). The relatively low temperatures are required for the WGS reaction to proceed to the right since it is an exothermic reaction.

$$CH_4 + H_2O \rightleftarrows CO + 3H_2 \qquad \Delta H^{\theta}_{298} = 206\ \text{kJ/mol} \qquad 2.2$$

$$CO + H_2O \rightleftarrows CO_2 + H_2 \qquad \Delta H^{\theta}_{298} = -41\ \text{kJ/mol} \qquad 2.3$$

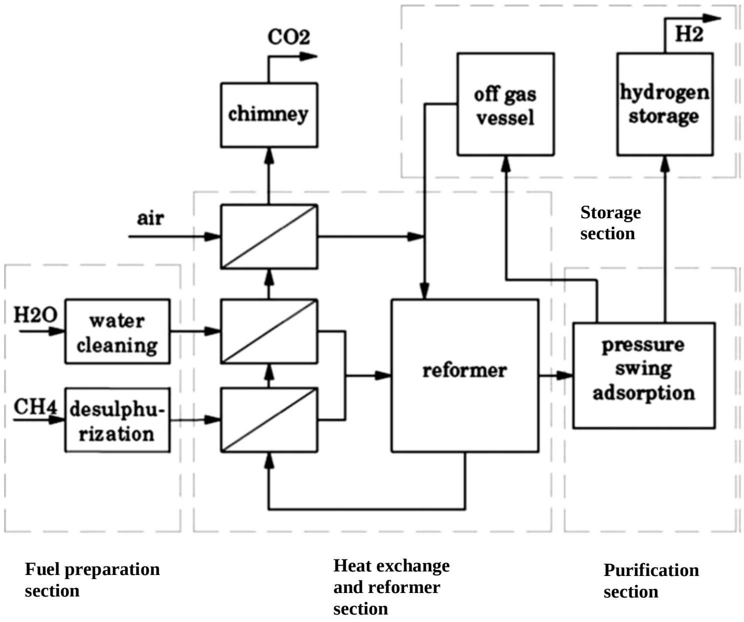

Figure 2.6 Steam reforming of methane (de Jong et al., 2009).

Steam reforming can be carried out in several different types of reactors with the main types being adiabatic pre-reformers, tubular or primary steam reformers, and various types of heat exchange reformers (Aasberg-Petersen et al., 2011).

Apart from the Eq. 2.2 and 2.3, other side reactions take place during steam reforming including methanation, dry reforming, Boudouard reaction and various equilibrium controlled carbon gasification reactions (Xu and Froment, 1989). This reactions are listed in Table 2.4.

2.2.1.1.2 Steam reforming catalysts

Catalysis plays a very important role in steam reforming. Even though the choice of catalyst depends on operating conditions and feedstock, some catalysts have been identified to be generally very suitable. Nickel has been identified as the most suitable metal for steam reforming of hydrocarbons and it is mostly supported on refractory alumina, Al_2O_3, ceramic magnesium aluminate, $MgAl_2O_4$, cerium oxide, CeO_2, and zirconium oxide, ZrO_2 (Ming et al., 2002). Other noble metals, especially group VIII transition metals, have been shown to exhibit very good catalytic activity (Aasberg-Petersen et al., 2011). It has been demonstrated by several authors that Ru and Rh are the most active steam reforming catalyst, with Ir, Pt, Pd and Re being less active (Rostrup-Nielsen, 1993, Jones et al., 2008). Even though Rh and Ru have the highest activity for steam reforming, nickel-supported catalysts are still widely used because of their low cost (Liu et al., 2009).

The choice of metal support is known to affect the steam reforming process as some of them participate in the reaction mechanisms involved especially in the rate determining steps. In one study, Wang and Gorte (2002) carried out steam reforming of various hydrocarbon fuels and demonstrated that using 1wt% Pd/ceria gave higher H_2 selectivity and CO_2/CO ratio than 1wt% Pd/Al_2O_3. They concluded that ceria plays an important role in the steam reforming process.

2.2.1.2 Partial Oxidation

2.2.1.2.1 Partial oxidation reactions

Steam reforming remains the preferred process for the production of synthesis gas from methane and other hydrocarbons but there is a growing interest in alternative methods such as partial oxidation (POX) and autothermal reforming (ATR) (Heitnes et al., 1995, Melchiori et al., 2014). The interest in these alternative processes is because SR provides H_2/CO ratios too high for the Fischer–Tropsch process and methanol synthesis (Asencios et al., 2012) and also because SR is a very capital and energy-intensive process in which superheated steam, higher than stoichiometric value, is used to avoid carbon deposition (Melchiori et al., 2014). POX involves the reaction of a hydrocarbon feedstock with oxygen to yield a mixture of carbon dioxide, carbon monoxide and water. The POX of methane is shown in Eq. 2.4.

$$CH_4 + \frac{1}{2}O_2 \rightleftarrows CO + 2H_2 \qquad \Delta H^{\theta}_{298} = -22.6 \text{ kJ/mol} \qquad 2.4$$

The POX reaction is slightly exothermic and, as a result, rather hard to control especially in large-scale reactors (Asencios et al., 2012). This can lead to the formation of hot spots and zones of instability which can reduce catalyst performance by causing catalyst sintering and support degradation (Dedov et al., 2015). Partial oxidation can be catalytic or non-catalytic. The non-catalytic partial oxidation occurs at high temperatures (normally ranging between 800 and 950 ºC) to achieve hydrocarbon conversion. During non-catalytic partial oxidation, soot is always formed and can be removed in a separate soot scrubber system downstream to the partial oxidation reactor (Aasberg-Petersen et al., 2001b). In catalytic partial oxidation, the reactants are premixed and all chemical conversion takes place in a catalytic reactor. Eq. 2.7 represents an ideal reaction and, in practice, it is somewhat impossible to avoid further oxidation of CO and H_2 (Aasberg-Petersen et al., 2001b).

Table 2.4 Summary of reactions occurring during methane partial oxidation

Name	Reaction	SN
Oxidation	$CH_4 + 2O_2 \rightarrow CO_2 + 2H_2O$	1
Partial Oxidation	$CH_4 + \frac{1}{2}O_2 \rightarrow CO + 2H_2$	2
Partial Oxidation	$CH_4 + O_2 \rightarrow CO_2 + 2H_2$	3
Water Gas Shift	$CO + H_2O \leftrightarrows CO_2 + H_2$	4
Steam Reforming	$CH_4 + H_2O \leftrightarrows CO + 2H_2$	5
CO_2 (dry) Reforming	$CH_4 + CO_2 \leftrightarrows 2CO + 2H_2$	6
CO Reduction	$CO + H_2 \leftrightarrows C + H_2O$	7
Methane Decomposition	$CH_4 \leftrightarrows C + 2H_2$	8
Boudouard Reaction	$2CO \leftrightarrows CO_2 + C$	9
CO Oxidation	$CO + \frac{1}{2}O_2 \leftrightarrows CO_2$	10
Hydrogen Oxidation	$H_2 + \frac{1}{2}O_2 \leftrightarrows H_2O$	11

As shown in Table 2.4, there are at least 10 other reactions that play an important role in the partial oxidation of methane and so the resulting product composition is determined by the thermodynamics of all possible species (Enger et al., 2008a). It has been proposed that catalytic POX of methane occurs via two possible mechanisms which are the direct route and the indirect route. In the direct mechanism, methane decomposes to elemental carbon and hydrogen and adsorbs on the catalyst surface. The adsorbed carbon reacts with oxygen on the catalyst surface to form CO which then desorbs together with H_2. In the indirect mechanism, partial oxidation of methane occurs by means of a sequence of reactions consisting of total combustion of some of the methane (during which all oxygen in consumed) followed by steam reforming and CO_2 'dry' reforming of the remaining methane coupled with the water gas shift reaction (Bharadwaj and Schmidt, 1995, Heitnes et al., 1995). For the indirect mechanism, adsorbed carbon (from methane) reacts with adsorbed oxygen to form CO and this further reacts with more oxygen to form CO_2 which then desorbs. H_2O is formed when adsorbed ‘H’ is first oxidised to ‘OH’ which reacts further with another adsorbed ‘H’ to produce H_2O. The resulting CO_2 and H_2O desorb and then re-adsorbed in another region of the catalyst bed where reforming reactions take place (Smith and Shekhawat, 2011b).

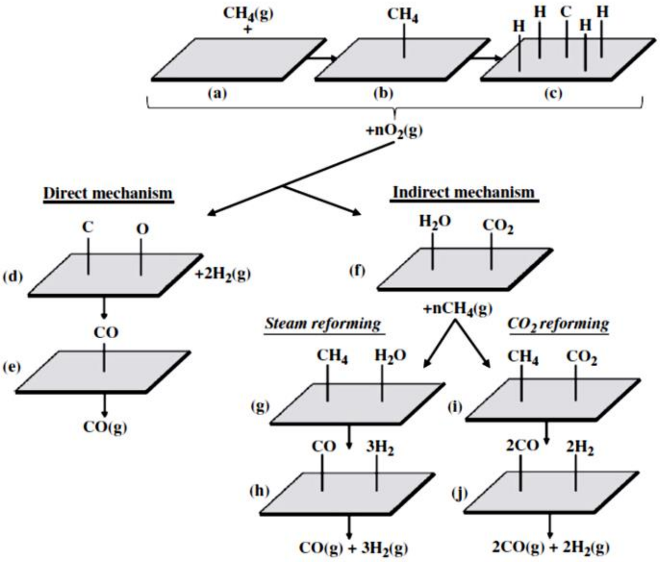

Figure 2.7: Diagram comparing the direct and indirect mechanism for the CPOX of methane (Smith and Shekhawat, 2011b)

The reaction mechanisms for the catalytic POX of higher hydrocarbons and oxygenates are more complex than those described above for methane due to the numerous side reactions that can occur including those from cracking intermediates.

2.2.1.2.2 Partial oxidation catalysts

The most widely used catalysts for POX are transition metals like Ni, Co, Cu and Fe. Noble metals like Pt, Pd, Rh, Ru and Ir can also be used but this is limited by their high cost (Larimi and Alavi, 2012). Different catalysts have been used in the POX of hydrocarbons especially methane with nickel based catalysts being the most common (Silva et al., 2009, Enger et al., 2009a, Enger et al., 2009b). In a study carried out by Heitnes et al. (1995) on the POX methane using 5 wt% Ni monolith and 5 wt% Pd monolith as catalyst, it was demonstrated that Ni impregnated monolith possessed better catalytic properties than Pd with a H_2 selectivity of 93 compared to 87 for the

Pd catalyst. The different catalysts used have been shown to favour either the direct mechanism or the indirect mechanism during POX. For example, Tavazzi et al. (2007) carried out the partial oxidation of CH_4 and C_3H_8 on 2 wt% Rh/α-Al_2O_3. They obtained a syngas with about a 1% variation in composition for each component as predicted by equilibrium and proposed an indirect mechanism model to explain their results.

2.2.1.3 Autothermal Reforming

2.2.1.3.1 Autothermal reforming overview

Autothermal reforming (ATR) is the process of using steam and oxygen to convert a fuel into a mixture of H_2 and CO. ATR is therefore a process combining both POX and SR reactions (Martin and Wörner, 2011). Autothermal reactors are designed to couple the endothermic SR reaction with the exothermic POX reaction so as to obtain thermoneutral (adiabatic) or slightly exothermic system (Kolios et al., 2000). Apart from SR and POX reactions, autothermal systems also harbour reactions for coke formation, coke gasification, WGS, methanation and most of the other side reactions mentioned in Table 2.4 (Martin and Wörner, 2011). The overall reaction occurring during the autothermal reforming of a hydrocarbon is given in reaction Eq. 2.5.

$$C_nH_m + aO_2 + bH_2O \rightarrow cH_2 + dCO + eCO_2 + fCH_4 \qquad 2.5$$

The coefficients c, d, e, and f depend on the amount of oxygen and steam (a and b) and also on the extent of side reactions like methanation, coke gasification, WGS, Boudouard reaction and decomposition.

There exist two types of autothermal reforming systems which have been studied so far. The first one has just a catalyst bed in which both partial oxidation and steam reforming reactions occur simultaneously. The second system is designed to have two separate sections, in the first section non-catalytic partial oxidation occurs using a burner and steam reforming reactions takes place in the catalyst bed (Zahedi Nezhada et al., 2009). Autothermal reforming systems based on the former are mostly useful for fuel cell applications while the latter is ideal for gas to liquid applications (Zahedi Nezhada et al., 2009).

Irrespective of the type of catalyst bed (fixed or a fluidized bed) used, product gas (syngas) composition is determined by the thermodynamic equilibrium at the exit temperature, which in turn is determined by the adiabatic heat balance (Rostrup-

Nielsen et al., 2002b). The synthesis gas produced can have molar H_2/CO ratios ranging from 1.5 to 3.5, depending on the feedstock used, suitable for synthetic fuel synthesis (Dybkjaer, 1995a). Another significant advantage of ATR over SR is that it can be stopped and started very rapidly (Holladay et al., 2009).

In order to maximize H_2 yield while reducing the competition between ATR reactions and unwanted side reactions, ATR reformers are operated at high temperatures (800 to 1200°C), and downstream WGS reaction is carried out at lower temperatures (<350 °C) (Nahar and Dupont, 2013).

Table 2.5: Comparison of reforming technologies

Technology	Advantages	Disadvantages
Steam reforming	- Most extensive industrial experience - Oxygen not required - Lowest process temperature - Best H_2/CO ratio for H_2 production	- Highest air emissions
Autothermal reforming	- Lower process temperature than POX - Low methane slip	- Limited commercial experience - Requires air or oxygen
Partial oxidation	- Decreased desulfurization requirement. - Low methane slip	- Low H_2/CO ratio - Very high processing temperatures - Soot formation/handling adds process complexity

In order for autothermal reforming to become a well-established industrial process for heavy fuel reforming, key issues such as mixing enhancement of reactants and development of durable catalyst resistant to carbon deposition, need to be resolved (Yoon et al., 2008). Table 2.5 compares the different reforming technologies.

2.2.1.3.2 Autothermal reforming catalysts

Catalysts used for ATR have to meet the same requirements as those used for SR and POX such as: be active and selective for major reactions involved in both the SR and the POX reaction sequences; and be robust and able to withstand the high temperatures needed for optimal H_2 yield without significant loss in activity (Haynes and Shekhawat, 2011). Most of the work carried out on ATR has been done with the same catalysts used for SR and catalytic POX. Ayabe et al. (2003) studied the ATR of methane and propane using several catalysts consisting of 2 wt% metal supported on alumina. They obtained an order of activity of Rh > Pd > Ni > Pt > Co which is similar to that reported for SR reactions i.e. Rh, Ru > Ni > Pd ~ Pt > Re > Co (Jones et al., 2008). The lower performance of the Ni catalyst compared to Pd during ATR was attributed to its preferential oxidation by the O_2 present in the input gas mixture.

2.2.2 Hydrogen production from oxygenates and bio-oil

2.2.2.1 Steam reforming of oxygenates

Even though bio-feedstocks can be easily obtained, their utilization as a source of industrial hydrogen is greatly limited due to their high oxygen content, complex nature, low heating value and degradation during storage (Trane et al., 2012, Garcia et al., 2000). Before SR can be carried out, most solid bio-feedstocks have to be converted first to a volatile state suitable to the catalytic reforming reactions (methane, bioethanol, biodiesel or bio-oil) before feeding to a reforming unit. Eq. 2.6 and 2.7 represent the steam reforming of bio-feedstocks.

$$C_nH_mO_k + (n - k)\ H_2O \rightarrow nCO + (2n + m - 2k)/2\ H_2 \qquad 2.6$$

$$C_nH_mO_k + (2n - k)\ H_2O \rightarrow nCO_2 + (2n + m/2 - k)/2\ H_2 \qquad 2.7$$

The complete SR reaction, Eq. 2.7, occurs when Eq. 2.6 is combined with Eq. 2.3 (WGS reaction). It is noteworthy that, given its mild exothermicity, the WGS reaction is favoured at temperatures well below those used for SR. It is therefore usual to find significant amount of CO in the reformer product stream. The product distribution is also influenced by methanation (reverse of Eq. 2.2) and thermal decomposition reaction (Eq. 2.8). Methanation reduces the amount of hydrogen produced (it is favoured at low temperature and high pressure) while thermal decomposition is responsible for coke formation (it is favoured by high temperature and low pressure).

$$C_nH_mO_k \rightarrow C_xH_yO_z + \text{gases} + \text{coke} \qquad 2.8$$

In practice, high temperatures are used to breakdown the hydrocarbon to CO, CO_2 and H_2; and a low temperature reactor is used to shift the product stream to the desired CO/H_2 ratio (Czernik et al., 2007).

Among oxygenated fuels, ethanol has received a lot of attention as a feedstock for hydrogen production via SR owing to its availability as a renewable fuel. A lot of ongoing research emphasis has been on catalyst development and on its application as a source of hydrogen for mobile fuel cells. The complete equation for the SR of ethanol (including WGS) is given in Eq. 2.9.

$C_2H_5OH + 3H_2O \rightarrow 2CO_2 + 6H_2$ 2.9

Liguras et al. (2003) investigated the catalytic performance of different loadings of noble metals (Rh, Ru, Pt, Pd) supported on Al_2O_3, MgO and TiO_2 on the SR of ethanol at a temperature range of 600 – 850 °C. Their results show that for the same metal loading, the selectivity towards H_2 production was in the order Rh > Ru ≈ Pt ≈ Pd. Ethylene and acetaldehyde are two undesirable by-products formed during ethanol SR as a result of dehydration and dehydrogenation reactions respectively. Liguras et al. (2003) reported very minute quantities of these two in their work with noble metal catalyst especially when the SR temperature was higher than 750 °C. Ni has been shown to be very active in promoting ethanol SR with high ethanol conversions obtained at temperatures as low as 450 °C. However, this is accompanied by significant quantities of ethylene especially if an acidic support such as Al_2O_3 is used. This results in rapid carbon accumulation on the catalyst leading to loss of activity and structural disintegration (Fatsikostas, 2004, Comas et al., 2004). A detail review of ethanol SR can be found in the work published Ni et al. (2007).

Methanol has been identified as potential source of H_2 for mobile fuel cell applications with substantial amount of research focused on catalyst development. The reaction for the complete SR of methanol is given in Eq. 2.10.

$CH_3OH(g) + H_2O(g) \rightarrow 3H_2 + CO_2$ 2.10

Methanol SR is also endothermic but unlike other fuels, optimal H_2 yield is achieved at temperatures below 300 °C. Takezawa and Iwasa (1997) performed SR of methanol at 220 °C using Cu, Ni, Rh, Pd, and Pt supported over MgO, La_2O_3, Nd_2O_3, MnO_2, Cr_2O_3, HfO, Nb_2O_5, $A1_2O_3$, SiO_2, and ZnO. The Cu-based catalysts and Pd/ZnO gave high H_2 selectivities when compared to the other supported catalysts. Results from several other studies confirm that Cu based catalyst are the most active for methanol SR and that the activity of these catalysts greatly depend on dispersion of Cu and the nature of the support used (Papavasiliou, 2004, Shen, 2002).

Other oxygenates that have received attention as potential sources for H_2 include glycerol and butanol. A review published by Nahar and Dupont (2014) (covers existing literature on the steam reforming of bio-feedstocks including ethanol, glycerol, butanol, bio-oil, biodiesel.

2.2.2.1.1 Steam reforming of bio-oil and model compounds

Unlike methane and other fossil fuels, the use of bio-oils as feedstock to produce hydrogen (or syngas gas) presents some tough challenges because of their very heterogeneous composition and thermal instability (Vagia and Lemonidou, 2007). The main challenge is the formation of coke due to dehydration and polymerisation reactions which can be mitigated by using excess steam, bio-oil blending and appropriate catalyst (Rennard et al., 2010). Due to the enormous variability in chemical composition that exists among bio-oils produced from different biomass sources (Hou et al., 2009b), most experimental and equilibrium studies have focused on using model compounds to simulate bio-oil feedstock SR, POX, and ATR.

Among these model compounds, acetic acid has received the most attention. Resende et al. (2015) performed thermodynamic and experimental studies on SR of acetic acid and the results obtained suggests the existence of two possible mechanisms. In one route, acetic acid is converted into adsorbed acetate species (CH_3COO^*) followed by decomposition into acetyl species (CH_3CO^*). The CH_3CO^* formed latter decomposes into CHx*and CO*, giving rise to reforming products and adsorbed carbon (see Figure 2.8). The other route involves the conversion of acetic acid to acetone, CO_2 and water at temperatures between 327 and 600 °C.

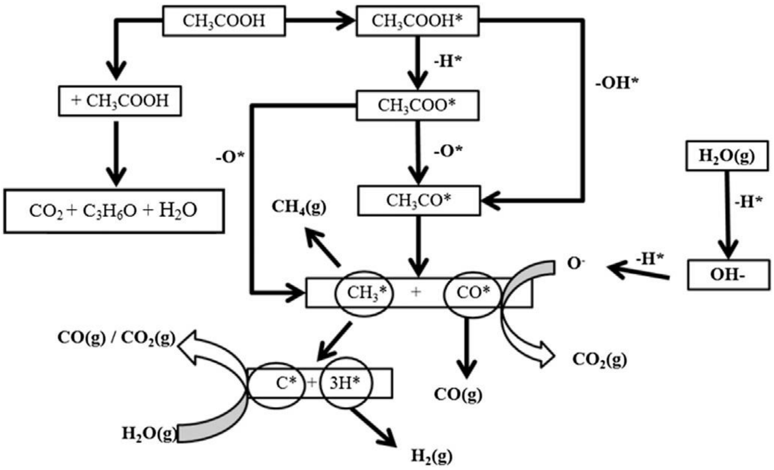

Figure 2.8 Proposed reaction mechanism for acetic acid SR (Resende et al., 2015).

The same catalysts used for the SR of methane, hydrocarbons and oxygenates mentioned previously have been used for the SR of bio-oil and bio-oil model compounds. Basagiannis and Verykios (2007a) performed a series of acetic acid SR experiments to determine the activity of different metals (Pt, Pd, Rh, Ru and Ni) and supports (Al_2O_3, La_2O_3/Al_2O_3, MgO/Al_2O_3 and CeO_2/Al_2O_3) and the influence of parameters such as the reaction temperature. Their results show that the Ni based catalysts have the best activity and highest selectivity toward hydrogen production at temperatures > 600 °C. The order of catalyst activity obtained was : 17% Ni/Al_2O_3 > 0.5% Rh/Al_2O_3 > 1% Ru/Al_2O_3 > 1% Pd/Al_2O_3 > 1% Pt/Al_2O_3. They determined that the amount of carbon deposited on each catalyst at 750 °C was inversely related to catalytic activity with the most over the poor Pd/Al_2O_3 catalyst and the least over the very active Ni/Al_2O_3 catalyst. With the knowledge that Ni based catalyst are very active in the SR of bio-oil model compounds, some researchers have focused on determining the influence of Ni metal loading and the effect of support on the SR activity. Wang et al. (2014) selected phenol, acetic acid and hydroxyacetone as bio-oil model compounds in their the SR experiments using different loadings of Ni/nano-Al_2O_3 catalyst. They obtained phenol, acetic acid and hydroxyl-acetone conversions up to 84.2%, 98.2% and 98.7% at 700 °C and S/C = 2 with corresponding H_2 yields of 69%, 87% and 97.2% respectively. Their results also show that acetic acid and hydroxyl-acetone conversions and H_2 yield increased for catalysts with higher Ni loadings. García-García et al. (2015a) performed SR experiments with cresol as a model bio-oil compound by using Ni based catalyst supported on both conventional and unconventional supports (α-Al_2O_3, γ-Al_2O_3, olivine sand, zircon sand, CeO_2-Al_2O_3, La_2O_3-Al_2O_3). At 600 °C, α-Al_2O_3 and olivine sand supported catalysts did not generate any gaseous reforming products. All six tested catalyst produced H_2 at 800 °C with total yield strongly dependent on the support used decreasing in the order γ-Al_2O_3 > CeO_2-Al_2O_3 > α-Al_2O_3 > La_2O_3-Al_2O_3 > olivine sand. This order in hydrogen selectivity change when catalysts initially used at 600 °C were reused at 800 °C. The new order in terms of decrease in H_2 production was CeO_2-Al_2O_3 > γ-Al_2O_3 > olivine sand > La_2O_3-Al_2O_3 > α-Al_2O_3. The improvement in the performance of the reused olivine sand supported catalyst at 800 °C was attributed to recrystallization causing an improvement in metal dispersion at high temperatures. They also noted that the use of ceria as a support modifier promoted coke gasification and reduced catalytic deactivation through coking. Other compounds such as cresol, acetone and ethylene glycol have also been used as model bio-oil compounds (Vagia and Lemonidou, 2007, Xie et al., 2011).

Some researchers have however focused on performing SR experiments using actual bio-oil or its aqueous fraction (Basagiannis and Verykios, 2007b, Remón et al., 2014, Zin et al., 2012). Wang et al. (1998) performed SR experiments using both whole and aqueous fraction of poplar bio-oil with commercial and research catalysts. Their screening experiments on process parameters such as temperature, molar steam to carbon ratio, gas hourly space velocity, and residence time revealed that temperature had the most significant effect on H_2 yield and product distribution. They reported that SR of bio-oil was rendered difficult due to its poor vaporisation causing the residual solid to block the feeding line and the reactor. This meant that a spray system had to be used to inject the bio-oil or its aqueous fractions into the reactor to avoid char formation prior to the actual SR reaction. For the bio-oil aqueous fraction, they were able to obtain conversions of up to 100 % for SR experiments performed with excess superheated steam (850 °C and S/C ratios greater than 20).

Catalyst coking and deactivation is a major concern when performing SR of bio-oil. Several studies have been carried in a bid to completely eliminate coke formation or prolong catalyst life during bio-oil SR. Garcia et al. (2000) performed SR of the aqueous fraction of poplar bio-oil on various Ni supported catalyst in an attempt to reduce coke formation and extend catalyst life. They implemented two strategies in order to achieve this goals. The first approach was to facilitate partial oxidation and other coke removal reactions by enhancing steam adsorption on the catalyst surface; this was achieved by using magnesium and lanthanum as promoters. The second strategy was to slow down the surface reactions leading to the formation of the coke precursors due to cracking, deoxygenation, and dehydration of adsorbed intermediates by using cobalt and chromium as additives. Their strategy proved successful as the prepared catalysts, $Ni/MgO-Al_2O_3$, $Ni/MgO-La_2O_3-Al_2O_3$, $Ni-Co/MgO-La_2O_3-Al_2O_3$, and $Ni-Cr/MgO-La_2O_3-Al_2O_3$, all gave better H_2 yields with improved coke resistance when compared to a reference Ni/Al_2O_3 catalyst for SR experiments performed at 825 °C and an S/C ratio of 4.92. Wu et al. (2008), on the other hand, proposed a method of reducing catalyst coking and deactivation by performing bio-oil SR experiments in a two stage fixed bed reactor using dolomite and Ni/MgO catalyst. They investigated the influence of temperature, S/C ratio and space velocity on gas product yield and selectivity of gaseous carbon products and H_2. While the first stage required high temperatures (> 850 °C) and high S/C (>12) to completely gasify the bio-oil, the second stage with the Ni catalyst had very little coke formation and required a S/C ratio of 2 or more and a reaction temperature of 800 °C to effectively convert any CH_4 present to H_2. Noble metals such as Rh and Ru have been demonstrated to have excellent activity as catalysts for bio-oil SR accompanied by a high resistance to coke induced deactivation. Table 2.6 obtained from Trane et al., (2012) shows a summary of catalysts and operating conditions used for the SR of bio-oil found in literature. It is clear from the table that nickel is the most extensively used catalyst with temperatures ranging from 600 – 1000 °C and typical steam to carbon (S/C) ratios between 2 and 10.

Table 2.6: Catalysts and operating conditions used for SR of bio-oils found in literature (Trane et al., 2012)

Type of oil	Metal	Content [wt%]	Support	Temp. [°C]	S/C [mole/mole]	$G_{C1}HSV^a$ [h^{-1}]	Y_{H2} [%St]	Bed type	Stability b [h]
Aq. poplar	Ni	15	Al_2O_3	825 – 875	5 – 11	62,300-126,000	87	Fixed	0.5
Aq. pine	Ni[c]			800 – 850	7 – 9	770 – 1000	89	Fluid	90
Hemicellose	Ni[c]			850	7 – 14.1	800 – 1000	77	Fluid	2.5
Glycerin	Ni[c]			850	2.1 – 2.7	1400	74	Fluid	-
Grease	Ni[c]			600 – 850	2.7 – 5	950 – 1100	82	Fluid	16
Hardwood	Ni[c]			850	5.8		80	Fluid	16
Hardwood	Ni[d]			850	5.8	-	90	Fluid	4
Saw dust	Ni	20	Dolomite	600 – 800	2 – 10	1.5 (W)	74	Fluid	5
Aq. Saw dust	Ni	20	Dolomite	800	6.5	1.5 (W)	74	Fluid	5
Aq. Beech wood	Ni[d]			300–1000	8.2	300 – 600	90	Fixed	5
Aq. Pine wood	Ni	28.5	Ca/MgAl	650	7.6	5400 – 800	-	Fluid	2
Saw dust	Ni	7.2	MgO	700 - 900	1 – 16	1.5 (W)	80	Fixed[e]	
Saw dust	Ni	15	γ-Al_2O_3	350 – 550	6.1	12,000	50	Fixed	
Saw dust	Ni	15	CNT	350 – 550	2 – 6.1	12,000	92.5	Fixed	6
Beech wood	Pt	1	$Ce_{0.5}Zr_{0.5}O_2$	700 – 780	2.5 – 10	0.6 – 2.5	70	Monolith	
Beech wood	Rh	1	$Ce_{0.5}Zr_{0.5}O_2$	700 – 780	2.5 – 10		52	Monolith	
Aq. Beech wood	Ru	5	$MgAl_2O_4$	550 – 800	7.2	3000-17000	60	Fixed	> 45
Beech wood	Pt	1	Al_2O_3	860	10.8	3090	40	Fixed	
Beech wood	Rh	1	Al_2O_3	860	10.8	3090	60	Fixed	
Beech wood	Pt	1	$CeZrO_2$	740 – 860	10.8	3090	70	Fixed	> 9[f]
Beech wood	Rh	1	$CeZrO_2$	860	10.8	3090	75	Fixed	
Model oil 1[g]	Ni	7.2	MgO	450 – 850	1 – 10	0.8 (W)	85	Fixed	8
Model oil 2[h]	Ni	7.2	MgO	450 – 850	1 – 10	0.8 (W)	85	Fixed	10
Aq. rice hull	Ni	5 – 12	CeO – ZrO	450 – 800	3.2 – 5.8	-	70	Fixed	0.5

a (W) indicates that the SV is WHSV (weight hourly space velocity, i.e. total mass flow rate divided by catalyst mass).

b Time for the conversion or YH2 to decrease 10% from its initial value. >X indicates that data in the article are shown for X hours, but the conversion have not decreased 10%.

c C11-NK from Sud-Chemie.

d NREL catalyst.

e 2-stage reactor with a guard bed.

f Autothermal conditions.

g Consisting of equal amounts of methanol, ethanol, acetic acid, and acetone on a weight basis.

h Consisting of equal amounts of furfural, phenol, catechol, and m-cresol on a weight basis.

2.2.2.2 Partial-oxidation of oxygenates

POX of oxygenates and other bio-feedstocks (such as biodiesel and bio-oil) is a growing area of research but much work still remains to be done. The general POX reaction of oxygenated biofuels is represented by Eq. 2.11 and can be slightly exothermic or endothermic (depending on the n/m ratio of the fuel). The presence of oxygen in the reactor feed can also lead to the complete oxidation (COX) of some of the input fuel. The COX reaction is represented by Eq. 2.12 which is very exothermic.

$$C_nH_mO_k + (n/2 - k/2)\ O_2 \rightarrow nCO + (m/2)\ H_2 \qquad 2.11$$

$$C_nH_mO_k + (n + m/4 - k/2)\ O_2 \rightarrow nCO_2 + (m/2)\ H_2O \qquad 2.12$$

Most studies carried out on the POX of oxygenates have centred on alcohols such as ethanol, methanol and glycerol with focus on catalyst activity, selectivity to syngas production and resistance to coke formation and deactivation. Liguras et al. (2004) examined the POX of ethanol using 13 wt% loadings of Ni/La_2O_3 supported over cordierite monoliths, mullite ceramic foams, zirconia–alumina ceramic foams and γ-Al_2O_3 pellets as catalysts. All the catalysts examined proved to be very active with ethanol conversions > 99 % reached for all experiments carried out at 600 °C and hourly space velocity of 5250 h^{-1}. H_2 selectivities up to 95% were obtained with the Ni/La_2O_3 washcoated on the cordierite monolith even after continuous operation for 70 hours. They also reported trace amounts of C_2H_4, C_2H_6 and acetaldehyde in experiments performed with this catalyst. Other metal such as Cu, Zn, Pd, and Au have been identified to promote POX of some oxygenates (Ou et al., 2008, Schuyten et al., 2009, Fixman et al., 2007, Rodrigues et al., 2009). Salge et al. (2005) studied the POX of ethanol using Rh, Rh-Ce, Pt, Pd, and Rh-Ru supported on ceramic foams. They concluded that ethanol adsorbs as an ethoxide specie on the Rh catalysts followed by complete decomposition to carbon, hydrogen and oxygen. These adsorbed species then undergo surface reactions together with previously adsorbed oxygen to produce H_2, CO, CO_2 and CH_4. The Rh-Ce catalyst was most active, attaining over 95 % ethanol conversion and 80 % H_2 selectivity (close to the equilibrium value of 82 %) at a back-face temperature of 810 °C and C/O ratio of 0.7. The order of catalyst activity in syngas production (hydrogen selectivity) was established to be Rh–Ce > Rh–Ru > Rh > Pd > Pt. One reason accounting for the poor performance of the Pd and Pt catalysts was that adsorbed ethoxides species tend to undergo dehydrogenation to form acetaldehyde on both surfaces thereby reducing syngas formation.

2.2.2.2.1 Partial oxidation of bio-oil and model compounds

Not very many studies have been carried out involving the POX of bio-oil to produce hydrogen or syngas. In one study carried out by Marda et al. (2009), synthesis gas was produce by non-catalytic POX of bio-oil derived from poplar wood. The temperature was varied from 625 to 850 ºC and oxygen to carbon molar ratio (O/C) from 0.7 to 1.6. They reported high yields of CO ranging between 50% and 70% (of the stoichiometric maximum possible from the bio-oil). Hydrogen yields were much lower, about 25% of the maximum possible, with bio-oil carbon to gas conversion between 85% and 95%. Rennard et al. (2010) on the other hand carried out POX of pine bio-oil (stabilised with 10 wt% methanol) using Rh-Ce monoliths. They obtained a bio-oil conversion of about 97% of the theoretical maximum at a reactor front-face temperature of 650 °C, C/O ratio of 0.71 and gas space hourly space velocity (methane equivalent) of about 14000 h^{-1}. Coke build up was a major issue at low O_2 feed flow (low O/C ratio) as it impaired reactor operation resulting to very low conversions.

2.2.2.3 Autothermal reforming of oxygenates

The overall reaction occurring during the autothermal reforming of oxygenated hydrocarbons is given in Eq. 2.13.

$$C_nH_mO_k + aO_2 + aH_2O \rightarrow cH_2 + dCO + eCO_2 + fCH_4 \qquad 2.13$$

Autothermal reforming of oxygenates has been suggested as a means to sustainably produce hydrogen from renewable biomass resources; especially as some of these compounds present attractive reforming properties, such as low boiling point, low processing temperature, and minimal amounts of catalyst contaminants (Haynes and Shekhawat, 2011). Methanol, ethanol and glycerol have all been suggested as potential fuels for hydrogen production by ATR as an alternative to the energy intensive steam reforming (Murcia-Mascarós et al., 2001, Liu and Lin, 2012, Fierro et al., 2003, Rennard et al., 2009). Most methanol ATR experiments have been reported with different variations of active and cost effective Cu-based catalysts combined with promoters such as Zn, Cr, Ce and Zr (Yong et al., 2013). The activity of these catalysts rely greatly on metal dispersion and reducibility of surface Cu (Haynes and Shekhawat, 2011). Chang et al. (2010) investigated the influence of the amount of Al_2O_3, CeO_2 and ZrO_2 on CuO/ZnO supported catalysts used for the ATR of methanol. They found out that all three metal oxides promoted CuO and ZnO dispersions. However, high loading of Al_2O_3 lowered the reducibility of the catalyst, due to the strong interaction between Al_2O_3 and CuO, thereby reducing the ATR activity of the prepared catalyst. They recommended a maximum Al_2O_3 loading of 10 wt% in order to ensure the stability and the mechanical strength of the catalyst. On the other hand, their results showed that CeO_2 increased the reducibility of the catalyst but at the same time reduced its ability to promote reforming reactions. Finally, ZrO_2 was found to improve the reducibility of the catalyst, and promoted the ATR reactions. Other studies on the ATR of methanol can be found in existing literature (Patel and Pant, 2007, Agrell et al., 2003).

The ATR of ethanol has been studied and proposed as an excellent alternative to produce hydrogen for stand-alone fuel cells for use in cars (Youn et al., 2008). Fierro et al. (2003) examined the ATR of ethanol over various Ni based catalysts for S/C ratio of 0.8 and O_2/C ratio of 0.34. In homogenous studies (i.e. no catalyst present), they were able obtain ethanol conversions as high as 95% at 700 °C with complete oxygen conversion obtained above 550 °C. Product selectivity was rather constant for temperatures higher than 500 °C with average values of 30, 50 and 18 % for H_2, CO and C_2H_4 respectively. Using a 20 wt% Ni/Al_2O_3 catalyst, the selectivity for H_2, CO, CO_2 and CH_4 obtained were 80, 55, 30 and 12 % respectively. They also showed that H_2 and CO selectivities increased while that of CH_4 and CO_2 decreased with no C_2 compounds produced as temperature was increased to 800 °C. Tests with bimetallic catalysts revealed that the addition of Cr, Zn and Fe decrease H_2 production at temperatures lower than 750 °C. While above this temperature the order of catalyst activity becomes Ni–Zn > Ni–Fe > Ni–Cr > Ni > Ni–Cu. Other authors have focused on the use of noble metals as catalysts for ethanol ATR with Salge et al. (2005) proposing the following order of activity, Rh > Pd > Pt. The addition of Ce to Rh based catalysts has been shown to increase H_2 selectivity and catalysts stability (Deluga et al., 2004, Salge et al., 2005).

2.2.2.3.1 Autothermal reforming of bio-oil and model compounds

Very few experimental studies have been carried out on the ATR of whole bio-oil or bio-oil fractions. The main challenge with using bio-oil as a feed for hydrogen production, as mentioned earlier, is the coking taking place on the hot reactor walls and catalyst surface. The presence of oxygen during ATR is an added advantage as it can be used to simultaneously burn-off any coke formed on the catalyst or reactor walls. Rennard et al. (2010) showed in their study that the presence of water during ATR helped to increase conversion and hydrogen yield under the same conditions used for POX. Czernik and French (2014) performed the ATR of oak, poplar, pine and lignin-free oak bio-oils using a noble metal catalyst (0.5% Pt/Al_2O_3). For ATR experiments carried out at 850 °C and space velocity of 2000 h^{-1}, they reported conversions of 70, 89, 86, and 89 % for the oak, poplar, and pine and lignin-free oak bio-oils respectively with corresponding H_2 yields of 8.5, 11.0, 10.5 and 3.0 g/100 g of bio-oil feed. Most of the unconverted carbon was a result of incomplete volatility which caused about 11 – 30 % of the initial bio-oil to form carbon deposits in the evaporator thereby affecting overall product yield.

2.3 Mechanisms of carbon (coke) formation

The risk of carbon formation is of great concern during the reforming of fuels since it can deactivate the catalyst and lead to a decrease in reforming efficiency and process stability (Yoon et al., 2008). Carbon formation can occur in three different forms: pyrolytic coke (collective description of various kinds of carbonaceous deposit), whiskers, and gum. Pyrolytic coke and whiskers occur mainly at high temperatures while gum formation is a problem at low temperatures (Rostrup-Nielsen et al., 2002b, Trane et al., 2012). Eq. 2.14 to 2.21 represent the different chemical reactions responsible for coke formation during SR, POX and ATR. CO reduction, Boudouard reaction, thermal decomposition and gum formation are all catalytic reactions and so depend on the type of catalyst used (Trane et al., 2012, Alstrup et al., 1998b, Trimm, 1999). Pyrolytic coke formation is a non-catalytic process and depends on the feedstock used and operating parameters such as feedstock mixing and reactor temperature (Yoon et al., 2009).

CO reduction:

$$CO + H_2 \rightleftarrows C_s + H_2O \qquad 2.14$$

Boudouard reaction:

$$2CO \rightleftarrows C_s + 2CO_2 \qquad 2.15$$

Thermal decomposition:

$CH_4 \rightleftarrows C_s + 2H_2$ 2.16

$C_nH_m \rightleftarrows nC_s + m/2\ H_2$ 2.17

$C_nH_mO_k \rightleftarrows (n - k)C_s + m/2\ H_2 + kCO$ 2.18

Pyrolytic coke:

$C_nH_m \rightarrow \text{olefins} \rightarrow \text{coke}$ 2.19

$C_nH_mO_k \rightarrow C_xH_yO_z + \text{gases} + \text{coke}$ 2.20

Gum:

$C_nH_m \rightarrow (CH_2)_n \rightarrow \text{gum}$ 2.21

Many studies have been carried out to understand the carbon formation mechanism during methane reforming. These studies have mostly focused on the identification of carbon type and morphology, nucleation and growth mechanisms, the influence of reaction conditions and catalyst structure, and parameter modifications to reduce carbon formation (Chen et al., 2007). As mentioned in previous sections, the mechanism for steam reforming of hydrocarbons proceeds via dissociative adsorption on the catalyst surface (Trimm, 1999). Eq. 2.22 – 2.26 show the steps for methane steam reforming on nickel catalyst. It begins with the separation and chemisorption of CH_3 and H species on active sites on the catalyst surface (Eq. 2.22). At sufficiently high temperatures, CH_3 is subsequently dehydrogenated stepwise to finally form adsorbed C and H species (Alstrup et al., 1998b). Adsorbed H atoms can then react to form hydrogen gas while adsorbed C reacts with adsorbed O to form carbon monoxide (Eq. 2.25 and 2.26 respectively).

$CH_4 + 2^* \rightleftarrows CH_3^* + H^*$ 2.22

$CH_4 + (5 - x)^* \rightleftarrows CH_x^* + (4 - x)H^*$ 2.23

$H_2O + 3^* \rightleftarrows O^* + 2H^*$ 2.24

$2H^* \rightleftarrows H_2 + 2^*$ 2.25

$C^* + O^* \rightleftarrows CO + 2^*$ 2.26

* is for an adsorption (active) site on the catalyst surface

$1 \leq x \leq 4$

A similar sequence of reactions can be used to describe steam reforming of higher hydrocarbons but their adsorption on the catalyst surface is faster (Yoon et al., 2009). The adsorption of carbon on catalyst is faster for higher hydrocarbons and it is found in practice that this results in an increased rate of carbon accumulation on the catalyst surface and so coking therefore becomes more pronounced (Trimm, 1999). All in all, the rate limiting step for methane SR is the dissociation of the hydrocarbon molecule (Eq. 2.22). Meanwhile for olefins and paraffins, the rate limiting step is the diffusion of carbon into the nickel crystal since their dissociation is very fast (Rostrup-Nielsen et al., 2002b).

According to Trimm (1997), the monoatomic carbon formed on the catalyst surface, referred to as C_α, is very reactive and can be easily gasified by reactions such as that given in Eq. 2.26 to form carbon monoxide. However, if an excess of C_α is formed or gasification is slow, then it can polymerize to form the less reactive C_β which may accumulate on the catalyst surface (resulting in encapsulation) or may dissolve in the nickel crystal (Figure 2.9).

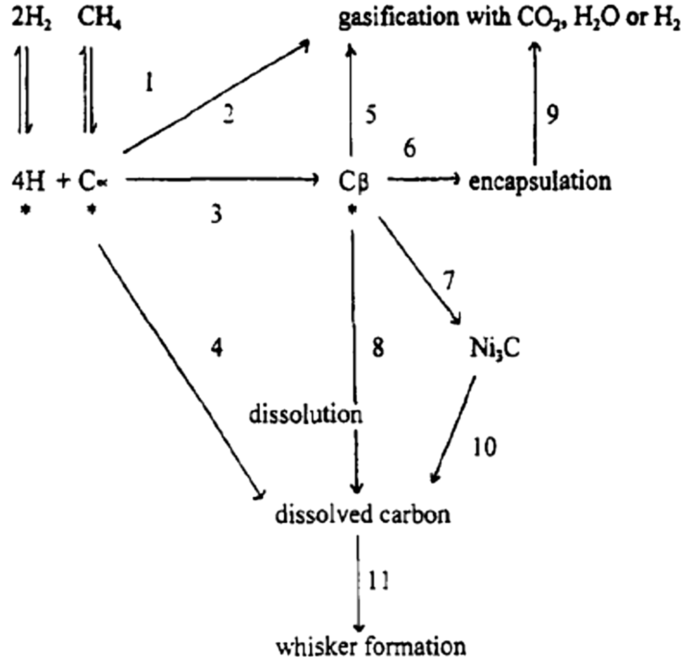

Figure 2.9 The proposed mechanism of steam reforming (Trimm D. L, 1997)

The dissolved carbon migrates through the nickel crystal and accumulates at the interface with the catalyst support leading to the formation of whiskers.

Evidence gathered so far indicates that there might not be a unique mechanism for the deposition of carbon since the resulting structure (morphology) depends on parameters such as type of hydrocarbon, type of catalyst used, catalyst particle size, and reforming temperature (Rostrup-Nielsen et al., 2002b). Whisker carbon, as shown in Figure 2.10, is characterised by long filamentous nanofibres (graphene tubes) which tend to be very destructive as they are formed on the metal/support interface (Aasberg-Petersen et al., 2011). Whiskers leave most of the catalyst surface free to catalyse reactions but their continued growth leads to catalyst disintegration and increase pressure drop in the system (Trane et al., 2012). Nucleation of carbon atoms and eventual growth to form whiskers occur faster on the more active step sites of nickel reflected by the kinetics shown in equation (2.24).

$$\frac{dC_w}{dt} = k_c(t - t_0) \qquad 2.27$$

Where

C_w is the concentration of carbon atoms,

k_c is the rate constant for the growth of the whisker

t is the time , and t_o is the induction time needed for nucleation to begin

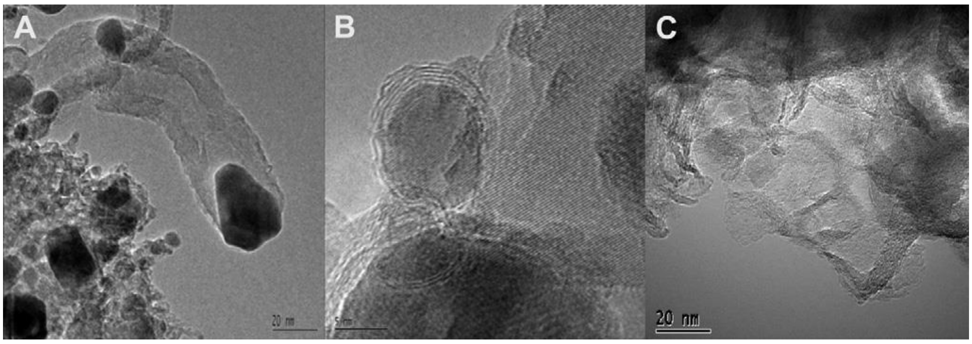

Figure 2.10 Electron microscopy images of whisker carbon (A), encapsulating carbon gum (B) and pyrolytic carbon on the $MgAl_2O_4$ support (C) of a Ni/$MgAl_2O_4$ reforming catalysts (Sehested, 2006).

Ideally, t_o should be infinitely long since after nucleation, the carbon growth rate becomes constant (Rostrup-Nielsen et al., 2002b). The only way for t_o to be infinitely long is to work under conditions in which carbon formation is not thermodynamically possible. This is indicated by the carbon limit of the given hydrocarbon feedstock and depends on the process temperature, steam/carbon ratio and oxygen/carbon ratio (for autothermal reforming). For a given feedstock and at given temperature, carbon will be formed below a given steam/carbon ratio given by A on Figure 2.11. This steam/carbon ratio reduces with increasing temperatures and can be pushed towards the thermodynamic limit B by using promoters like alkali metal.

The carbon limit can be pushed further to C by the use of noble metals and sulphur passivation (Alstrup et al., 1998a).

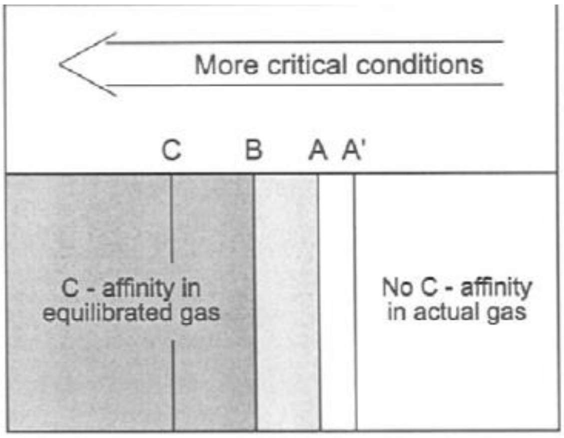

Figure 2.11 Carbon Limits: A' no affinity for actual gas; A real carbon limit; B principle of equilibrated gas; C sulphur passivation, noble metals (Alstrup et al., 1998a)

For higher hydrocarbons it is recommended to operate in conditions where the carbon limit shows no affinity for carbon formation (A'). This is because the carbon reactions are irreversible and the presence of paraffins, aromatics and oxygenates further complicates the process.

Sulphur and alkali reduce the risk of carbon formation by completely or partially blocking the most active (step) sites of Ni catalyst thereby preventing carbon nucleation from occurring. This reduces the activity of the catalyst and can cause other undesirable effects like sintering (Trane et al., 2012). This decrease in catalytic activity (turnover frequency) has to be weighed with the cost of carbon formation during the entire reforming operation.

Carbon growth is not energetically favourable before the carbon island (formed by nucleation) exceeds a critical size. Therefore working with smaller metal particle size can delay the growth phase. The minimum carbon island needed to initiate complete growth has been estimated by Density Functional Theory (DFT) calculations to be 25 A° and it is recommended to work with metal particles sizes less than 50 A° in diameter to minimise whisker formation (Rostrup-Nielsen et al., 2002b). It has been shown that for catalyst with small nickel crystals, about 7 nm, the temperature for the onset of whisker carbon formation is approximately 100°C higher than that for that large crystals (about 100 nm) (Rostrup-Nielsen et al., 2002b).

As explained earlier, pyrolytic coke formation is non catalytic and depends on the feedstock and process conditions. Longer chain hydrocarbons are more susceptible to thermal cracking than methane and this leads to the formation of ethylene which has been demonstrated to be a major coke initiator (Yoon et al., 2009, Yoon et al., 2008). Yoon et al. (2009) studied the effects of ethylene on carbon formation during the autothermal reforming of diesel and found that ethylene was produced in the absence of catalyst. They established that increasing S/C ratio and/or oxygen/carbon ratio reduced the amount of coke formed by favouring the effective decomposition of ethylene on the catalyst (oxidation) and also by favouring the forward directions of the WGS and coke removal gasification reaction (Eq. 2.28).

$$C + 2H_2O \rightleftarrows CO_2 + 2H_2 \qquad 2.28$$

Chapter 3 Materials and Methods

3.1 Introduction

This chapter presents a succinct description of the materials and methods used in the course of this research project. This include details of the experimental rig, gas analysis equipment, some properties of the model compounds used and also characterisation data of both supplied and prepared catalysts. Chapter 4 and 5 contain complete descriptions of the modelling method applied using the CEA equilibrium software and Aspen plus process simulator software both used to perform thermodynamic equilibrium analysis and process simulation respectively.

3.2 Experimental rig

The schematic and a picture of the packed bed reactor setup (experimental rig) used for ATR experiments are shown in Figure 3.1 and Figure 3.2 respectively. The rig consists of a down flow 316 stainless steel tube reactor with 10 mm internal diameter placed inside an electric tube furnace (Elite Thermal Systems TSV10/20/85 or TSV12/38/120) to provide external heating.

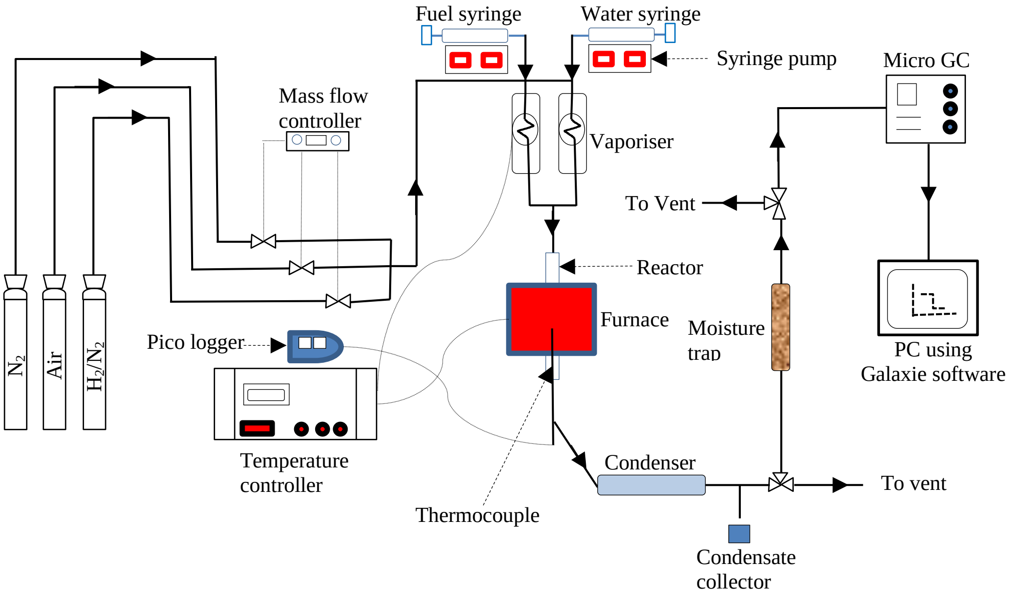

Figure 3.1 Schematic diagram of experimental rig

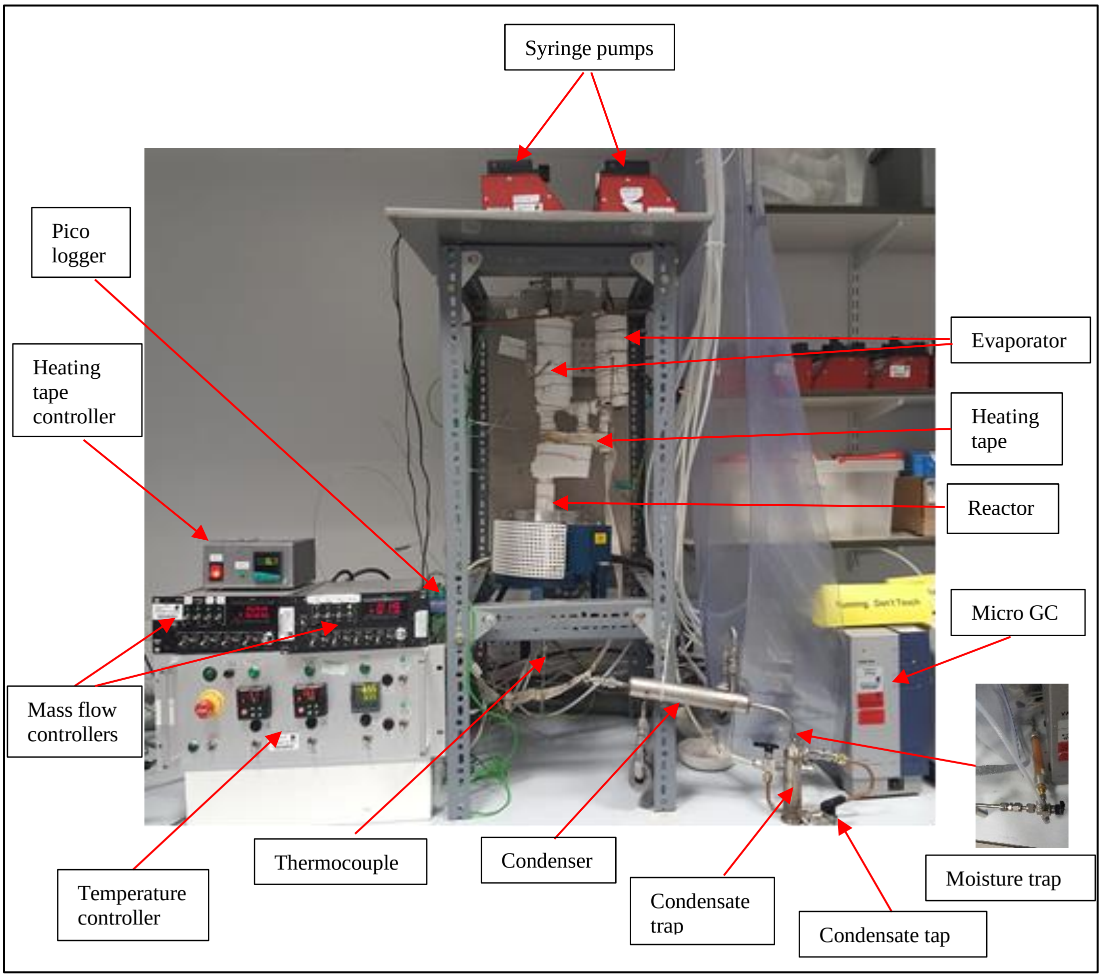

Figure 3.2 Picture of reactor setup and auxiliary equipment

The stainless steel reactor inlet is connected through a mixing cross connector to pipes leading from the fuel (bio-feedstock) vaporiser, water vaporiser and gas input. Water and liquid bio-feedstock are fed separately into the reactor by means of programmable syringe pumps supplied by New Era Pump System Inc (model NE-1000). Depending on the experiment, the N_2, H_2 or air flows are controlled separately using MKS mass flow controllers which employ thermal sensors for flow measurement together with a fast acting proportioning valve. A pico-logger console is used to monitor the temperature readings from various thermocouples placed at different points on the rig notably the two vaporisers and the bottom of the reactor. A heating tape is used to maintain the fuel, steam and gas temperature in the tubbing leading from the vaporisers to the reactor. A stainless steel condenser is used to cool down hot product gas leaving the reactor. This is achieved by using a 30 vol. % ethylene glycol/water mixture flowing counter clockwise from a chiller (Fisher Scientific 3016S) set at -2 °C. A tap is connected to the condenser trap to facilitate condensate removal and the cooled product gas is directed to flow to a silica gel moisture trap by means of a two way valve. The glass indicating moisture trap supplied by Agilent Technologies (model 5182-9411) is filled with orange silica gel pellets from Sigma Aldrich. An on-line micro gas chromatograph (GC) is attached at the end of the rig and used for gas analyses.

3.3 Micro GC

Dry product gas leaving the rig by way of the moisture trap was analysed using a micro gas chromatograph (Micro GC) supplied by Varian Instruments, UK (model CP 4900). The micro GC is equipped with two thermal conductivity detectors (TCD) and two columns which are a Molecular Sieve 5A plot column and Pora Plot Q column. The Molecular sieve 5A plot column (column 1) is 10 m long and is used for the analysis of permanent gases such as hydrogen, oxygen, nitrogen, methane, and carbon monoxide. The Pora Plot Q column (column 2) is used to detect carbon dioxide, methane, ethane, ethene, propane and propene. Both columns were tuned on argon as carrier gas. The micro GC is also fitted with two pre-columns both responsible for preventing unwanted condensate or moisture from entering the principal columns. For proper functioning, column 1 was operated with a backflush of 13 s in order to prevent CO_2, moisture and higher hydrocarbons from getting inside and blocking the pores of the molecular sieve. The total run time for gas analysis was about 3 minutes making it faster than other conventional gas analysis methods.

Figure 3.3 Micro GC Variant CP 4900

The Galaxie data acquisition software provided by the manufacturer was used to configure and operate the micro GC. The GC inlet sample line was maintained at 45°C with a sampling time lasting 20’s. The column temperatures were set to 100°C with a pressure of 100 kPa during analysis. An external standard method was used to calibrate the instrument by using different gas mixtures with known compositions. The different calibration plots used for gas identification and quantification are given in Appendix B. After each experiment, the columns were conditioned by heating to 180°C and maintained at this temperature overnight to get rid of any moisture which might have entered them.

3.4 Catalyst and catalyst preparation

3.4.1 Nickel catalysts

Two commercial grade nickel catalysts, 18 wt% NiO/Al_2O_3 and 15 wt% $NiO/CaO\text{-}Al_2O_3$, henceforth termed Ni-Al and Ni-CaAl respectively, were obtained as pellets of 11 and 16 mm diameter respectively from Twigg Scientific & Technical Ltd (UK). The catalysts were crushed and sieved to obtain a particle size of 0.355 – 1 mm before being used for reforming experiments.

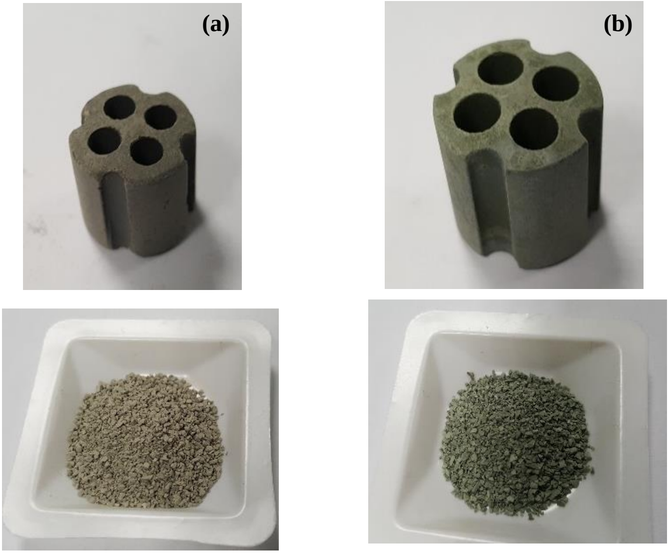

Figure 3.4 Catalyst pellets and crushed catalyst. (a) ‘Ni-Al’ = 18 wt% NiO/Al_2O_3. (b) ‘Ni-CaAl’ = 15 wt% $NiO/CaO\text{-}Al_2O_3$

3.4.2 Prepared Catalysts

A 1 wt% $Rh/\gamma\text{-}Al_2O_3$ catalyst (henceforth termed ‘Rh-Al’) and a 1 wt% Rh – 3 wt% $Ce/\gamma\text{-}Al_2O_3$ catalyst (henceforth termed ‘RhCe-Al’) were both prepared in-house by the author by wet impregnation and used for reforming experiments. $\gamma\text{-}Al_2O_3$ pellets (1/8") obtained from Alfa Aesar were crushed and sieved to a particle size ranging from 0.355 – 1 mm and used as support for catalyst preparation. Depending on which catalyst was being prepared, a known amount of rhodium (III) nitrate hydrate, ($Rh(NO_3)_3.xH_2O$ with ~36% rhodium), supplied by Sigma-Aldrich and cerium (III) nitrate hydrate, ($(Ce(NO_3)_3).xH_2O$ with x = 6-7), supplied by Alfa Aesar was dissolved in 50 ml of deionised water in a 500 ml beaker. The crushed γ-Al_2O_3 support was then added to the salt solution and the resulting slurry was slowly stirred using a magnetic stir bar on a hotplate stirrer maintained at 60 °C until most of the water was evaporated. In a typical preparation, 3 g of γ-Al_2O_3 was used with 0.0833 g of Rh salt for the 1 wt% Rh catalyst. Similar quantities where used for the RhCe-Al catalyst with the only difference being the addition of 0.279 g of Ce salt.

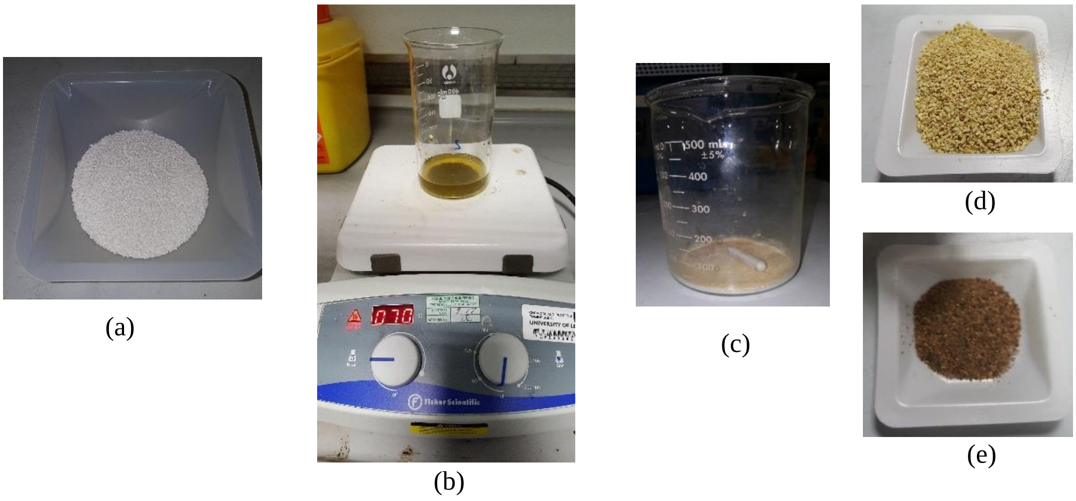
(a)
(b)
(c)
(d)
(e)

Figure 3.5 Prepared catalyst at various stages. (a) Crushed γ-Al_2O_3 with an average grain size of 677 μm. (b) Slurry of γ-Al_2O_3 in 50ml salt solution. (c) Solid recovered from dried slurry. (d) 'RhCe-Al' = Calcined 1 wt% Rh – 3 wt% Ce/γ-Al_2O_3. (e) 'Rh-Al' = Calcined 1 wt% Rh/γ-Al_2O_3

The partly wet solid obtained after heating on the hot plate was then dried overnight in a muffle furnace at 105°C (Lenton Thermal Design, LTF12/38/250). Using the same muffle furnace, the dried solid was calcined at 550 °C for 4 hours.

3.4.3 Monolithic catalysts

Two honeycomb monoliths, R-M (1wt% Rh/γ-Al_2O_3 washcoat on cordierite) and RC-M (1 wt% Rh - 3 wt% Ce/γ-Al_2O_3 washcoat on cordierite), provided by Twigg Scientific & Technical Ltd (UK) were used for acetic acid ATR experiments (Chapter 7). The monoliths were 42 mm long and featured a cell density of 400 cpsi (cells per square inch), corresponding to square channels of 1.21 mm sides and 62 cells per cm^2.

Typical wall and washcoat thicknesses range from 70 – 100 μm. Assuming a typical washscoat loading on the cordierite monolith of 15 wt% (Wei, 1975) and, based on a bulk density for the 400 cpsi cordierite monolith of 320 kg m^{-3} (Hayes and Kolaczkowski, 1997), the mass of Rh in both monoliths was estimated be 4.3 mg, compared to the 2 mg of Rh for the prepared powder catalysts (1wt% Rh/Al_2O_3, 1wt%Rh-3wt%Ce/Al_2O_3).

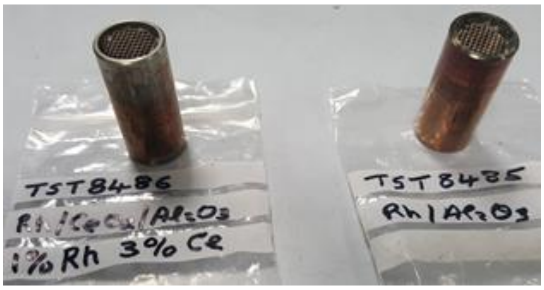

Figure 3.6 Monoliths used for ATR experiments. 1wt% Rh/γ-Al_2O_3 washcoat monolith on the right (R-M), 1 wt% Rh - 3 wt% Ce/γ-Al_2O_3 washcoat monolith on the left (RC-M).

3.5 Bio-oil model compounds

Several bio-oil model compounds were used as feedstock either individually or in a mixture for various experiments performed in the course of this study. Table 3.1 lists the various compounds used and their physical properties.

Table 3.1 Some physical properties and supplier information of the bio-oil model compounds

Compound	Molecular formula	Boiling point (K)	Density (g/cm^3)	Purity (%)	Water solubility	Supplier
Acetic acid	$C_2H_4O_2$	391	1.049	99	Very soluble	Sigma-Aldrich
m-cresol	C_7H_8O	284	1.034	99	2.35 g/100 ml @ 20 °C	Sigma-Aldrich
Formaldehyde	CH_2O	254	1.09	37	Very soluble	Santa Cruz Bio. Inc.
Acetaldehyde	C_2H_4O	293.2	0.785	99.5	Very soluble	Sigma-Aldrich
2-butanone	C_4H_8O	353	0.805	99.9	Soluble	Sigma-Aldrich
Furfural	$C_5H_4O_2$	434.7	1.16	99	Soluble	Sigma-Aldrich
Phenol	C_6H_6O	454.7	1.071	>98	84 g/1000 ml @ 20 °C	Merck Chemicals Ltd
Creosol	$C_8H_{10}O_2$	492.5	1.092	>98		Alfa Aesar
Guaiacol	$C_7H_8O_2$	478	1.129	>98	23.3 g/1000 ml @ 25 °C	Cayman Chemical Co.
Catechol	$C_6H_6O_2$	518.5	1.37	99	451 g/1000 ml @ 20 °C	Alfa Aesar
Palmitic acid	$C_{16}H_{32}O_2$	624	0.852	98	5×10^{-5}/1000 ml @ 20 °C	Fisher Scientific
Levoglucosan	$C_6H_{10}O_5$	657	1.69	99	Very soluble	Carbosynth Ltd

These compounds were selected so as to represent the various chemical families found in typical bio-oil (acids, ketones, sugars and furans) formed from pyrolysis of the three main components of biomass (see section 2.1.3.2).

3.5.1 Bio-oil surrogate formulation

Several authors agree that by grouping bio-oil compounds into chemical macro-families, the modelling of bio-oil reactions and other processes become easier (Branca et al., 2003, Ba et al., 2004). This makes it possible for the bio-oil to be considered as a simple mixture of few groups of compounds instead of the hundreds of compounds it actually contains. According to (Garcia-Perez et al., 2007), the understanding of this chemical families characterised by parameters such as boiling point and molar mass distribution could provide a realistic description of bio-oil behaviour. The thermal degradation of the individual chemical macro families present in the bio-oil is given by the Eq. 3.1 – 3.5 (Garcia-Perez et al., 2007).

$$\frac{d\alpha}{dt} = \sum_{j=1}^{N} z_{jo} \frac{d\alpha_j}{dt} \qquad 3.1$$

$$\alpha_j = \frac{m_{jo} - m_j}{m_{jo} - m_{j\infty}} \qquad 3.2$$

$$\frac{d\alpha_j}{dt} = A_j \exp\left(-\frac{E_j}{R \times T}\right)(1 - \alpha_j)^{nj} \qquad 3.3$$

$$\sum_{j=1}^{N} z_{jo} = 1 \qquad 3.4$$

$$z_{jo} = \frac{m_{jo} - m_{j\infty}}{m_{jo} - m_{j\infty}} \qquad 3.5$$

Where $\frac{d\alpha}{dt}$ is the instantaneous vaporisation rate; α_j, is the mass fraction of component j; z_{jo}, the mass fraction of volatiles from component j; A_j, the pre-exponential factor corresponding to the thermal degradation of component j; E_j, the activation energy for the thermal degradation of component j; n, is the reaction order; m, the mass of solid residue. The values for z_{jo}, A_j, E_j, and n, are obtained by curve fitting derivative thermogravimetry (DTG) data using a least-square regression analysis.

Using the above methodology presented in the work by Garcia-Perez et al. (2007), the thermogravimetric analysis (TGA) data of a palm empty fruit bunch (PEFB) bio-oil from a previous study by Pimenidou and Dupont (2012) was analysed. Firstly, the TGA curve was transformed to a DTG curve from which the possible number of macro chemical families was identified based on its shape (see Figure 3.7).

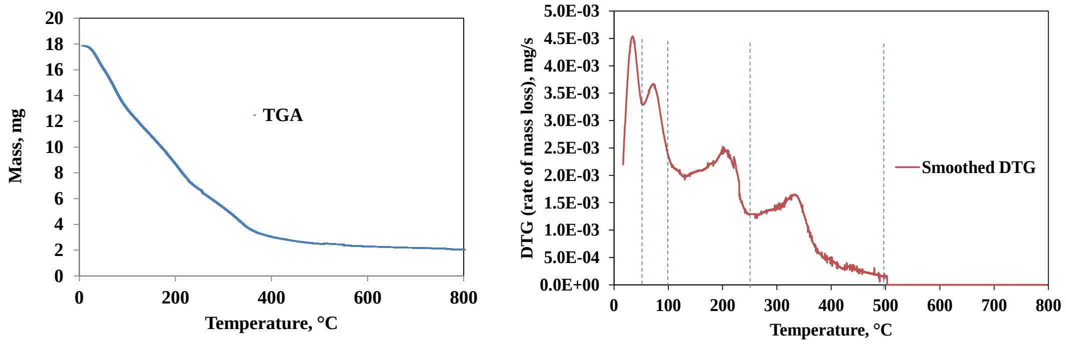

Figure 3.7 TGA curve and corresponding DTG curve from PEFB bio-oil (Pimenidou and Dupont, 2012)

Curve fitting was performed with MS Excel by using the solver function to minimise the sum of the difference between the squares of the actual DTG values and those predicted by the model. Initial values for the model were obtained by selecting approximate values E_j, A_j, n, and m which were then varied by the solver function to meet the minimisation criteria. Two constrains were included in the solver function (Eq 3.6 and 3.7).

$$\sum m_j = 1 \tag{3.6}$$

$$E_j, A_j \geq 0 \tag{3.7}$$

The fitted values obtained for A_j, E_j, and n do not have any real physical meaning (Garcia-Perez et al., 2007).

3.5.2 Bio-oil surrogate preparation

A Bio-oil surrogate was prepared by accurately measuring and mixing the different model compounds selected to represent the identified chemical macro-families in PEFB bio-oil. 500 g of bio-oil surrogate was taken as the basis for calculating the various quantities of individual bio-oil model compounds needed in the mixture based on their previously determined mass fractions. The surrogate was prepared by successively adding the different compounds into a 600 mL beaker placed on a hotplate stirrer with a magnetic stir bar set for mild stirring. The entire mixing process was performed in a fume cupboard while wearing appropriate personal protection equipment (PPE). Distilled water was the first component added to the empty beaker after which the remaining components were added based on their water solubility from the highest to the least soluble.

Table 3.2 Composition of bio-oil surrogate prepared on a 500 g basis

	Mass fraction	In 500 g solution	Purity (wt%)	Density (g/ml)	volume (ml)	Additional H_2O (ml)	Liquids (ml)	Solids (g)
Formaldehyde	0.083	41.48	50*	1.09	76.12	41.48	76.12	
Acetaldehyde	0.008	3.77	99.5	0.785	4.83	0.02	4.83	
2-butanone	0.008	3.77	99.9	0.805	4.69	0.004	4.69	
Acetic acid	0.075	37.71	99	1.049	36.31	0.38	36.31	
Water	0.238	119.09	100	1	76.37	0	76.37	
Furfural	0.136	67.88	99	1.16	59.11	0.69	59.11	
creosol	0.030	15.09	99	1.092	13.95	0.15	13.95	
Phenol	0.008	3.77	100	1.071	3.52	0		3.77
Guaiacol	0.121	60.34	100	1.129	53.45	0		60.34
Catechol	0.249	124.45	100	1.37	90.84	0		124.45
Palmitic acid	0.008	3.77	100	0.852	4.43	0		3.77
Levoglucosan	0.038	18.86	100	1.69	11.16	0		18.86
Total		**500**				**42.73**	**271.39**	**211.19**

* Methanol contained in the 37% formalin solution was considered as formaldehyde

Formaldehyde and acetaldehyde were added last due to their very high volatilities. This ensured that they dispersed in the final volume and stayed in solution. Table 3.2 shows the amounts of each bio-oil model compound plus water added to form the surrogate. With only water in the beaker, the hotplate was turned on and the temperature increased to 40 °C. This was followed by the successive addition of acetic acid, 2-butanone, furfural, levoglucosan, catechol, phenol, guaiacol, creosol and palmitic acid. The resulting mixture was stirred for 1 hour then transferred into a 600 ml sample bottle with a screw cap where it was stirred rapidly for 6 hours. The hotplate heat was then turn off and the mixture allowed to cool down to room temperature after which acetaldehyde and formaldehyde (supplied as formalin) were both poured rapidly into the sample bottled and sealed. The surrogate, still in the sealed sample bottle, was left on the hotplate in low stirring mode for 12 hours. The result was a homogenous mixture containing only very little specks of undissolved solids as seen in Figure 3.8.

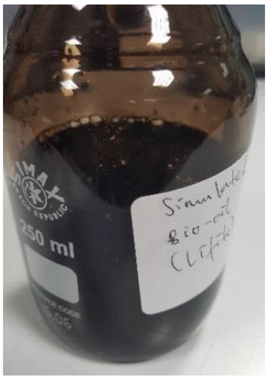

Figure 3.8 Prepared bio-oil surrogate

3.6 Solid Characterisation

3.6.1 Surface properties by N_2 adsorption/desorption

Nitrogen gas adsorption/desorption isotherm was used to determine the surface area, the pore volume, and the pore size distribution of fresh and used catalysts. A Quantachrome Nova 2200e instrument (Figure 3.9) was used for the analysis. Catalyst samples were degassed at 120°C under vacuum for 3 hours to remove any moisture or contaminants such as CO_2 or oils present before exposure to nitrogen vapour (the adsorbate) at 77 K. Small amounts of nitrogen are admitted stepwise into the evacuated chamber holding the solid sample and the partial pressure of the adsorbed gas determined using pressure sensors in the instrument. A plot of amount of adsorbed gas against its relative pressure is known as the adsorption isotherm.

The surface area of the solid sample is calculated by first determining the amount of adsorbate molecules needed to form a monolayer cover over the adsorbate surface and then multiplying this by the cross sectional area of the adsorbate. This is all achieved by applying the Brunauer-Emmett-Teller (BET) equation which is written as

$$\frac{p}{V(p_0-p)} = \frac{c-1}{V_m c}\left(\frac{p}{p_0}\right) + \frac{1}{V_m c} \qquad 3.8$$

Whence V is the quantity of adsorbed gas (could be expressed as a volume); V_m is the quantity of adsorbed gas forming the monolayer; p_0 and p are the saturation and equilibrium pressures of the adsorbed gas at the given adsorption temperature; and c is the BET constant and relates to energy.

Figure 3.9 BET analysis equipment

A plot of $\frac{p}{V(p_0-p)}$ against $\left(\frac{p}{p_0}\right)$ yields a straight line whose gradient and intercept values are used to determine V_m and c from Eq. 3.8.

The surface area of the adsorbent (expressed as specific surface area), S, is then calculated using the following equation:

$$S = \frac{V_m \times N \times A}{\dot{v} \times m} \qquad 3.9$$

In Eq. 3.9, N is the Avogadro's number; A is the cross sectional area of the adsorbate (N_2 in this case) and it corresponds to the area occupied by one adsorbate molecule in the monolayer; $\dot{v}$ is the molar volume of the adsorbate and m is the mass of adsorbate used for the analysis.

BET method provides a simplistic but reliable approach in determining surface area. It however makes some important assumptions such as

- The existence of a homogeneous surface.
- No lateral interactions between adsorbed molecules.
- Uppermost layer is in equilibrium with vapour phase.
- Heat of adsorption is associated with the formation of the first layer while the heat of condensation applies to the formation of subsequent layers.
- At saturation pressure, the number of layers becomes infinite.

3.6.2 X-Ray Powder Diffraction (XRD)

XRD is a technique used for phase identification of crystalline materials. This technique relies on X-ray diffraction which involves the constructive interference of monochromatic X-rays with a crystalline sample. The electrons present in atoms of the crystalline sample interact and scatter the incident radiation. This scattering (or diffraction) forms a circular pattern if the electrons (consequently the atoms) are arranged in a regular structure (crystal lattice). The occurrence of constructive interference and a diffraction pattern is governed by Bragg's law

$$n\lambda_w = 2d \sin\theta \qquad 3.10$$

In Eq. 3.10, n is any integer, λ is the wavelength of the beam, d is the spacing between diffracting planes, and θ is the incident angle. Diffraction occurs when the λ for X-ray has a similar order of magnitude as d for most crystals.

Figure 3.10 X-ray diffraction equipment

A Brucker D8 Advance diffractometer (Figure 3.10) was used for XRD analysis. Like all other diffractometers, it works by generating X-ray radiation from a cathode ray tube which is then filtered to produce monochromatic radiation, then collimated (concentrated) and directed towards the sample and the resulting pattern detected. This diffractometer uses Cu as anode material (target material) to generate Cu $K_{\alpha 1}$ radiation (λ = 1.54060 Å) and Cu $K_{\alpha 2}$ radiation (λ = 1.54443 Å) which are passed through a nickel filter. The crushed catalyst samples were placed in the sample holder and scanned at 2θ angles ranging from 20° to 80° at a rate of 0.0330 °/s. Constructive interference occurs when Bragg's law is satisfied and the detector records and converts the signal to a count which subsequently yields a corresponding peak. The Highscore Plus X'Pert software was used to process the output from the XRD.

3.6.3 Scanning Electron Microscopy – Energy Dispersive X-ray (SEM-EDX)

The morphology of used and fresh catalyst were examined using a Hitachi SU8230 high performance cold field emission scanning electron microscopy (CFE-SEM). The scanning electron microscope produces images of a sample by scanning the surface with a focused beam of electrons. These electrons interact the atoms in the sample generating signals containing data which reveal information of the surface's topography. The Hitachi SU8230 (Figure 3.11) was equipped with an Oxford Instruments Aztec Energy Dispersive X-ray (EDX) system with 80 mm^2 X-Max SDD detector.

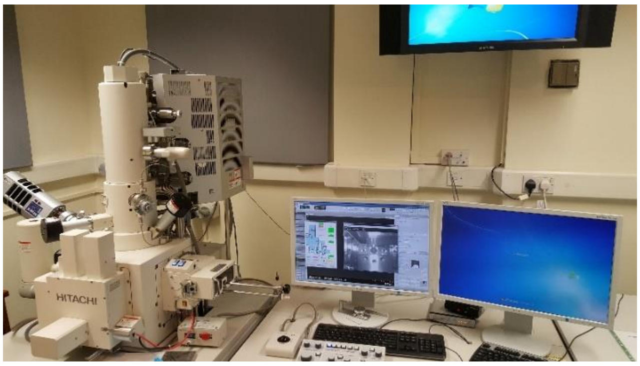

Figure 3.11 Cold field emission scanning electron microscopy, Hitachi SU8230

EDX system was used for elemental analysis and chemical characterization of the sample. This provided information on carbon deposition and dispersion of the active metals Ni, Rh and Ce on fresh and used catalyst surface. Sample preparation consisted of placing a small amount of ground catalyst on sticky carbon pads attached to stainless steel studs followed by coating with a 10 mm layer of iridium.

3.6.4 Transmission electron microscopy (TEM)

Transmission electron microscopy (TEM) imaging was performed on the fresh prepared catalyst using an FEI Titan3 Themis 300 equipped with an FEI Super-X 4-detector EDX system and a Gatan OneView 4K CMOS digital camera (Figure 3.12). TEM allowed detailed imaging of the prepared 1 wt% Rh/Al_2O_3 and 1wt% Rh-3 wt% Ce/Al_2O_3 catalyst making it possible to estimate the particle size and distribution of active metal particles on both catalysts. During TEM analysis, a beam of accelerated electrons is transmitted through a specimen to form an image which is magnified and focused on an imaging device.

Figure 3.12 TEM equipment on the left. Holey carbon film on Cu grid on the left

Catalyst samples were crushed and a very small amount dispersed in ethanol placed in a 10 ml glass vial. The vial was then placed in an ultrasonic agitation bath for 5 to

10 minutes. Using disposable pipettes, small amounts of the suspension were transferred to a Cu grid covered with a holey carbon film (holey carbon films on 400 mesh copper grid from Agar Scientific) and allowed to dry overnight at room temperature.

3.6.5 Elemental (CHNS) Analysis

The amount of carbon deposited on used catalyst was determined using a Thermo Scientific Flash 2000 Elemental Analyzer (Figure 3.13). A similar analysis was carried out on the bio-oil surrogate to establish its elemental composition. The equipment is designed to determine the carbon, hydrogen, nitrogen and sulphur (CHNS) content when present in a solid or liquid sample. Crushed solid samples were placed in small tin capsules and their mass adjusted to range between 8 – 11 mg. In the case of the bio-oil surrogate, only about 3 mg of sample was used. The tin capsule was then folded into a sphere to exclude any trapped air. Two tin capsules were prepared for each catalyst sample analysed. The folded tin capsules were placed inside an auto-sampler from where they were dropped into an oxidation reactor maintained at about 1000 °C. CHNS analysis was performed in batches of about 10 to 15 catalyst samples and also included about 3 mg of oatmeal (Oatmeal Organic Analytical Standard obtained from Elemental Microanalysis Ltd) used as standard for quality control.

Figure 3.13 CHNS equipment, Thermo Scientific Flash 2000

The tin capsule ignites in the reactor in the presence of excess oxygen producing a very hot flame of about 1800 °C capable of converting the desired elements into their combustible form (CO_2, H_2O, NO_2, and SO_2). Helium is used as a carrier gas and entrains the combustion products from the reactor into a GC column where they are separated and detected using a thermal conductivity detector. The detected amount is quantified based on previously established calibration curves. The amount of oxygen present in the bio-oil surrogate was calculated by the difference in mass.

3.7 Liquid Characterisation

3.7.1 Density

The densities for the mixture of four model compounds (acetic acid, 2-butanol, furfural and m-cresol) and the bio-oil surrogate were determined by accurately weighing out different volumes in a 10 mL measuring cylinder placed on an analytical balance with accuracy of ±0.00001. The density equation was applied for each volume and corresponding mass and the average of four values taken as the correct value.

3.7.2 Total Organic Carbon (TOC)

The total organic carbon (TOC) content of the condensate recovered after each experiment was determined by differential method using a Hach Lange IL 550 TOC/TIC analyser (Figure 3.14). The differential method was preferred to the non-purgeable organic carbon (NPOC) method as the amount of anticipated TIC (Total Inorganic Carbon) was very small and the presence of volatile organic compounds in the liquid condensate most likely. In the differential method, the Total Carbon (TC) and the Inorganic Carbon (IC) are measured separately while the TOC is obtained by subtracting the IC from the TC. For most analyses, 10 mL samples were prepared as 1:10 dilution of the initial condensate using deionised water. In cases were the condensate was coloured due to contamination by unreacted feed, 1:100 dilutions were preferred.

Figure 3.14 TOC analyser

The TOC analysis is performed by injecting about 100-500 μl aliquot of the diluted sample into the analyser’s reactor where it reacts with a 10 % phosphoric acid solution. Inorganic carbon such as $CaCO_3$ present in the sample reacts with this acid and is released from solution as CO_2 and transferred to the detector, which in this case is a non-dispersive infrared (NDIR) detector, to be measured. This corresponds to the TIC of the sample when corrected by the dilution factor used. Some of the remaining sample is then injected to a heated reactor at 800 °C where all the carbon present in the sample (TOC and TIC) combusts completely in the presence of pure O_2 and a platinum-rhodium catalyst to produce CO_2 and H_2O gas. The H_2O produced together with any other contaminant gas is removed by a moisture trap while the CO_2 passes on to the NDIR detector for measurement and the value obtained corresponds to the TC of the sample. TOC is then obtained by difference between the TC and TIC previously obtained.

3.7.3 Calorific Value

A Parr Instruments 6200 isoperibol oxygen bomb calorimeter (Figure 3.15) was used to determine the calorific value of the bio-oil surrogate. About 0.3 g of the bio-oil surrogate was placed in a previously weighed crucible and covered with 0.06 g of transparent adhesive tape (Sellotape®) which served as a spike to ensure ignition. The crucible was then mounted on a holder just below a fuse wire and then place inside a metallic bomb. The whole assembly was pressurised to 3 bar with pure oxygen and then placed in a bucket containing 2.0 L of deionised water located inside the instrument.

Figure 3.15 Bomb calorimeter

Upon ignition, the rise in temperature from the burning fuel caused an increase in temperature of the surrounding water which was measured by a high precision thermistor. The highest temperature achieved is recorder and used to calculated the gross calorific value of the bio-oil surrogate. A total of three measurements were performed and the average value used.

3.7.4 Flash Point

The flash point of the bio-oil surrogate was determined using a Setaflash Series 3 Plus Closed Cup Flash Model 33000-0 (Figure 3.16). A 2 ml liquid sample was loaded into the sample cup holder at an initial temperature of 22.1 °C. The test jet was lit and the shutter manually open to allow the flame to dip into the vapour above the liquid sample. The instrument made an audible beep each time the flame had to be place over the sample. This was repeated until the instrument displayed the word ‘FLASH’ and the corresponding flash point temperature.

Figure 3.16 Flash point equipment

Chapter 4 Thermodynamic Equilibrium Studies

All the results and discussions in this chapter have been published in an article found in the AIMS energy journal 2016, issue 1 (Tande and Dupont, 2016).

4.1 Introduction and bio-oil composition generation

Due to the enormous variability in chemical composition that exists among bio-oils produced from different biomass sources (Hou et al., 2009a), most thermodynamic equilibrium studies have focused on using model compounds to simulate bio-oil feedstock in SR, POX, and ATR studies. Among these model compounds, acetic acid has received the most attention (Resende et al., 2015, Wang et al., 2014, Latifi et al., 2014). Other compounds such as cresol, acetone and ethylene glycol have also been used (Vagia and Lemonidou, 2008b, García-García et al., 2015b, Wu and Liu, 2010a). Even when the same biomass feedstock is used, variations in pyrolysis process parameters lead to different bio-oil compositions.

Using information from existing literature, the moisture free (mf) elemental compositions of some PEFB bio-oils were determined. The results are summarized in Table 4.1. Mean elemental compositions were determined excluding the results from Pimenidou and Dupont (2012) due to the low H/C ratio and high O/C ratio.

Table 4.1 Moisture free (mf) PEFB bio-oil elemental composition (mol fractions)

Author	**C**	**H**	**O**	**H/C**	**O/C**
Pimenidou and Dupont (2012)	0.4099	0.4137	0.1730	1.0092	0.4220
Sukiran et al. (2009)	0.3575	0.5032	0.1274	1.4076	0.3565
Kim et al. (2013)	0.3506	0.5001	0.1353	1.4262	0.3858
Abdullah et al. (2010a)	0.3780	0.5654	0.0531	1.4955	0.1406
Khor et al. (2009b)	0.3983	0.5173	0.0743	1.2988	0.1865
Sulaiman and Abdullah (2011)	0.3774	0.5659	0.0531	1.4995	0.1407
Mean Elemental composition	**0.3724**	**0.5304**	**0.0886**	**1.4243**	**0.2381**

The mean over five mf elemental compositions obtained for PEFB bio-oil was $C_{0.3724} H_{0.5304} O_{0.0886}$ for which the nitrogen content was neglected. For this equilibrium analysis, acetic acid, phenol, levoglucosan, palmitic acid and furfural were selected as representative compounds since their presence in PEFB bio-oil has been repeatedly detected in significant amounts via GC-MS semi-quantitative analyses (Mantilla et al., 2014, Zin et al., 2012, Sembiring et al., 2015). Other authors have performed thermodynamic analysis of complex mixtures using mixtures of simpler compounds with the same molar elemental compositions. Zin et al. (2015) used mixtures of acetic acid, levoglucosan, vanillin and furanone to perform the thermodynamic analysis of pine bio-oil aqueous fraction steam reforming. Hanika et al. (2011) on the other hand used a mixture of glucose, vanillin, n-butyl-stearate, methionine and tri-ethyl-phosphate as representative compounds to simulate the partial oxidation of rape meal. Table 4.2 lists some physical properties of acetic acid, phenol, levoglucosan, palmitic acid and furfural.

Table 4.2 Physical properties of model compounds found in PEFB bio-oil

Properties	**Acetic acid**	**Phenol**	**Levoglucosan**	**Palmitic acid**	**Furfural**
Molecular formula	$C_2H_4O_2$	C_6H_6O	$C_6H_{10}O_5$	$C_{16}H_{32}O_2$	$C_5H_4O_2$
Heat of formation (gas) (kJ/mol)	-433	-95		-730	-149.6
Heat of combustion (liquid) (kJ/mol)	-874	-3058 (solid)	-2832 (solid)	-9977	-2339
Melting point (K)	289	314	455	336	237
Boiling point (K)	391	455	657	624	435
Flash point (K)	313	352	459	386	335
Density (@ 25°C) (g/cm^3)	1.043	1.0545 @45°C	1.688	0.8527@62°C	1.155

Using the Solver function in MS Excel, it was possible to generate five moisture free PEFB bio-oil mixtures with similar elemental composition by considering different possible mixtures of the five representative compounds mentioned above.

Table 4.3 Model PEFB bio-oils obtained using different combinations of acetic acid, phenol, levoglucosan, palmitic acid and furfural. BOSi stands for ‘bio-oil surrogate composition #i’. Target composition: $C_{0.3724}$ $H_{0.5304}$ $O_{0.0886}$

	BOS1	**BOS2**	**BOS3**	**BOS4**	**BOS5**
Name	mol (%)	mol (%)	mol (%)	mol (%)	mol (%)
Acetic acid	12.2	23.2	0.0	0.3	0.0
Phenol	35.1	45.2	36.0	65.3	12.2
Levoglucosan	2.2	0.3	8.6	16.4	0.0
Palmitic acid	20.0	16.3	21.6	17.5	25.5
Furfural	30.5	15.0	33.8	0.5	62.2
TOTAL	100.0	100.0	100.0	100.0	100.0
C	0.3724	0.3724	0.3724	0.3724	0.3740
H	0.5390*	0.5390*	0.5372	0.5390*	0.5374*
O	0.0886	0.0886	0.0904*	0.0886	0.0886
Maximum relative error* (%)	1.6	1.6	2	1.3	1.3

* Only the relative error (%) per element of a given mixture that yielded the maximum error is shown, .i.e. for BOS1,2,4 and 5, error on H, for BOS3, error on O.

The Solver function has been demonstrated by other authors to be a very versatile and useful tool in performing chemical engineering calculation (Lima da Silva et al., 2009, Lwin, 2000). The mf bio-oil mixtures were numbered BOS1-5. The relative error on the elemental composition for the different mixtures was less than 2% when compared to the mean elemental composition (see Table 4.3).

4.2 Solution method of CEA

Chemical Equilibrium with Applications (CEA) software developed by the National Aeronautics and Space Administration (NASA) was used to perform thermodynamic equilibrium calculations. The software determines the equilibrium properties of a reaction mixture by using the Gibbs free-energy-minimisation method based on a known pool of reactant and species, and user defined initial composition, temperature and pressure (Gordon and McBride, 1994).

This method takes into consideration the fact that the total Gibbs free energy of a reacting system reaches a minimum at equilibrium when varying the mixture composition at constant pressure and temperature.

For a given mixture with a *K* number of species, the Gibbs free energy can be written as:

$$G = \sum_{i=1}^{K} \mu_i n_i \qquad 4.1$$

Where G is the Gibbs free energy, μ_i is the chemical potential of species i and n_i the number of moles of species i. The condition of equilibrium is the minimisation of G. In order to find the n_i that minimize the value of G, it is necessary that the values of n_i satisfy certain constraints, one of which is the elemental mass balance given by

$$\sum_{i=1}^{K} a_{ji} n_i - b_j^o = 0 \qquad 4.2$$

or

$$b_j - b_j^o = 0 \qquad (j=1,\ldots,M) \qquad 4.3$$

Where a_{ji} are the number of gram atoms of element *j* per gram mole of species *i* and b_j^o is the number of gram atoms of element *j* in the reaction mixture.

Using Lagrangian multipliers, G can be written as

$$G = g + \sum_{j=1}^{M} \Phi_j (b_j - b_j^o) \qquad 4.4$$

Where Φ_j are Lagrangian multipliers and g the Gibbs free energy per gram of reaction mixture. Based on these equations, the condition for equilibrium can be expressed as:

$$G = \sum_{i=1}^{K} n_i \Delta G_i^0 + RT\sum_{i=1}^{K} n_i ln y_i + RT\sum_{i=1}^{K} n_i lnP \qquad 4.5$$

Where ΔG_i^0 is the standard Gibbs free energy of formation of species i, R is the universal gas constant, T is the temperature in Kelvin, y_i is the mole fraction of species i, and P is the total pressure.

The thermodynamic state for which the equilibrium composition is determined has to be specified by two intensive properties which, in principle, can be any combination of: temperature (T), pressure (P), specific enthalpy (h), specific entropy (s) and specific volume (v). In CEA, the “tp” setting is used for constant temperature and pressure processes, and the “hp” setting is used for constant pressure and enthalpy (adiabatic) processes. To solve Eq. 4.5, an iteration procedure is used with the Newton-Raphson method applied to solve for corrections to the initial estimates for composition, n_i, Lagrangian multipliers, moles of gaseous species and (when required) temperature, T (Gordon and McBride, 1994).

All inputs into the CEA software were based on a mf bio-oil feedstock with an arbitrary carbon moles number of 1500 (user-chosen). This carbon moles number was used to calculate the amount of water and oxygen needed for ATR based on the desired steam to carbon ratio (S/C) and amount of oxygen expressed as the oxygen equivalence ratio, Φ, as used to describe oxy-combustion processes (actual O_2 to fuel molar ratio divided by stoichiometric combustion O_2 to fuel molar ratio). All temperatures were entered in Kelvin (K) and pressures in atmosphere (atm).

Thermodynamic simulation executed in CEA generates an output file containing all the relevant thermodynamic properties and an equilibrium composition in mole fractions. To obtain the molar yields of equilibrium products, the mole fractions were converted to moles using a carbon balance. The total number of moles at equilibrium was determined using Eq. 4.6.

$$total\ moles = \frac{n_c}{\sum_{i=1}^{j} c_i x_i} \qquad 4.6$$

Where n_c is the number of initial (or input) moles of carbon in the feed, and in this case is equal to the chosen carbon number of 1500, j is the number of carbon containing species at equilibrium, and c_i and x_i are the carbon moles and mole fraction respectively of the chemical species i considered. Once the total moles of equilibrium species was determined, the equilibrium yields n_i of each species present were calculated using Eq 4.7.

$$n_i = x_i \times total\ moles \qquad 4.7$$

For each set of process condition considered, the overall performance was evaluated using critical factors such as hydrogen yield (Y_{H_2}, in wt% of the mf feed), and the percentage selectivity (S_i) to CH_4, CO and CO_2 (see equations 4.8 – 4.11).

$$Y_{H_2} = \frac{mass\ of\ H_2 at\ equilibrium}{initial\ mass\ of\ bio-oil} \times 100 \qquad 4.8$$

$$S_{CH_4} = \frac{moles\ of\ CH_4}{total\ moles\ of\ all\ carbon\ products} \times 100 \qquad 4.9$$

$$S_{CO} = \frac{moles\ of\ CO}{total\ moles\ of\ all\ carbon\ products} \times 100 \qquad 4.10$$

$$S_{CO_2} = \frac{moles\ of\ CO_2}{total\ moles\ of\ all\ carbon\ products} \times 100 \qquad 4.11$$

4.3 Modelling the global reactions of mf bio-oil ATR

It has been established in existing literature that several reactions are involved when biofuels (or organic fuels in general) undergo reforming to produce H_2 or syngas (Czernik et al., 2007, Haynes and Shekhawat, 2011, Smith and Shekhawat, 2011a, Nahar, 2010). In order to eventually optimise the ATR of bio-oil, it is helpful to devise a tool that can be used to predict the contribution of the different participating reactions. The CEA software determines equilibrium composition by applying numerical techniques which are independent of the actual reaction mechanisms taking place. To determine possible global reaction mechanisms, different sets of reactions where proposed and then tested to see how well they could fit the equilibrium yields obtained using CEA. Global reaction mechanism testing was performed algebraically using the Solver function in MS Excel. A mechanism was accepted as correct if predicted equilibrium concentrations with the proposed mechanism were close to actual equilibrium concentrations for all species with a relative percent error less than or equal to 1%.

As an example, suppose we propose a mechanism for ATR of bio-oil for which only three reactions, POX, SR, and WGS are assumed to occur. Then the following reactions can be written for the ATR of BOS1:

POX: $C_{0.3724}H_{0.5390}O_{0.0886} + 0.1419O_2 \rightarrow 0.3724CO + 0.2695H_2$ 4.12

SR: $C_{0.3724}H_{0.5390}O_{0.0886} + 0.2838H_2O \rightarrow 0.3724CO + 0.5533H_2$ 4.13

WGS: $CO + H_2 \rightarrow CO_2 + H_2$ 4.14

Let the moles of BOS1 (n_{BOS1}) consumed by POX and SR reactions be n_{POX} and n_{SR} respectively; and n_{WGS} the moles of carbon monoxide (CO) consumed by the WGS reaction. The general material balance equation for a particular species can be written as:

$$Input + Generation - Consumption = Output + Accumulation \qquad 4.15$$

Given that the calculations are performed for a system at equilibrium there is no accumulation term and the other terms will depend on the particular chemical species considered. Applying Eq 4.15 to our example, we can write the following equations to predict equilibrium concentration (in moles) of the chemical compounds involved:

$$n_{CO} = 0.3724\mathrm{n_{POX}} + 0.3724\mathrm{n_{SR}} - \mathrm{n_{WGS}} \qquad 4.16$$

$$n_{CO_2} = \mathrm{n_{WGS}} \qquad 4.17$$

$$n_{H_2} = 0.2695\mathrm{n_{POX}} + 0.5533\mathrm{n_{SR}} + \mathrm{n_{WGS}} \qquad 4.18$$

$$n_{BOS1} = \mathrm{n_{POX}} + \mathrm{n_{SR}} \qquad 4.19$$

The number of predicted chemical species has to be equal to the number of equations in order for system to produce a unique solution. This system consisting of 4 equations and 4 unknowns is entered in Excel such that

$$\begin{pmatrix} 0.3724 & 0.3724 & -1 \\ 0 & 0 & 1 \\ 0.2695 & 0.5533 & 1 \\ 1 & 1 & 0 \end{pmatrix} \begin{pmatrix} \mathrm{n_{POX}} \\ \mathrm{n_{SR}} \\ \mathrm{n_{WGS}} \end{pmatrix} = \begin{pmatrix} n_{CO} \\ n_{CO_2} \\ n_{H_2} \\ n_{BOS1} \end{pmatrix} \qquad 4.20$$

By substituting random values for n_{POX}, n_{SR}, and n_{WGS} into Eq. 4.20 it is possible to generate estimated equilibrium yields of CO, CO_2 and H_2 corresponding to an input moles of mf bio-oil (i.e. $n_{CO}, n_{CO_2}, n_{H_2}$ and n_{BOS1}). These calculated values are then compared to the actual (desired) equilibrium concentration values and the error between both sets of values determined. A solution is accepted if the errors for each species is below 1%, and the combined sum of errors is also below 5%.

Using the ATR equilibrium data generated by the CEA software, different combinations of reactions shown in Table 4.4 were tested using the methodology described above. Any number of the reactions given in Table 4.4 can occur during ATR of mf bio-oil. An acceptable mechanism should be able to account for all chemical species present at equilibrium and must contain equations which can represent the following processes (reactions): bio-oil degradation (consumption), oxygen consumption, steam consumption, carbon formation, methane formation, carbon removal and methane removal.

Table 4.4: List of all reactions considered during bio-oil ATR mechanism modelling

	Name	Abbreviation	Reaction
1	Partial oxidation	POX	$C_nH_mO_k + (n\text{-}k)/2\ O_2 \rightarrow nCO + m/2\ H_2$
2	Complete oxidation	COX	$C_nH_mO_k + (n+m/4–k/2)O_2 \rightarrow nCO_2 + m/2\ H_2O$
3	Steam reforming	SR	$C_nH_mO_k + (n\text{-}k)\ H_2O \rightarrow nCO + (2n+m\text{-}2k)/2\ H_2$
4	Decomposition	DEC	$C_nH_mO_k \rightarrow kCO + m/2\ H_2 + (n\text{-}k)\ C$
5	Water gas shift*	WGS	$CO + H_2O \leftrightarrow CO_2 + H_2$
6	Boudouard reaction	BO-RX	$2CO \rightarrow CO_2 + C$
7	Methanation of $C_{(s)}$	MEN	$C_{(s)} + 2H_2 \rightarrow CH_4$
8	Carbon gasification 1	C-GS1	$C_{(s)} + H_2O \rightarrow CO + H_2$
9	Carbon gasification 2	C-GS2	$C_{(s)} + 0.5O_2 \rightarrow CO$
10	Methane steam reforming	ME-SR	$CH_4 + H_2O \rightarrow CO + 3H_2$
11	Carbon monoxide oxidation	CO-OX	$CO + 0.5O_2 \rightarrow CO_2$
12	Hydrogen oxidation	H-OX	$H_2 + 0.5O_2 \rightarrow H_2O$

* The reverse of the water gas shift reaction (R-WGS) was used in some cases

4.4 Results and discussions

4.4.1 Sensitivity analysis and product distribution

The influence of the mf bio-oil chemical composition on hydrogen yield was investigated. ATR was performed on the five mf bio-oil mixtures considered in this study by varying S/C ratio and amount of oxygen. The amount of oxygen used during ATR was expressed in terms of the oxygen equivalence ratio, Φ, which in this case was defined as actual oxygen-fuel ratio (OFR) on the stoichiometric combustion oxygen-fuel ratio.

$$\Phi = \frac{OFR_{Actual}}{OFR_{Stoic}} \qquad 4.21$$

By substituting the mass of oxygen and bio-oil into Eq 4.21 and simplifying to obtain moles, the equivalence ratio can then be written as the ratio of actual moles of oxygen the reaction mixture to the stoichiometric moles of oxygen needed for stoichiometric combustion (complete oxidation-COX) of the bio-oil feedstock. This is written mathematically as

$$\Phi = \frac{Actual\ moles\ of\ O_2}{Stoichiometric\ moles\ of\ O_2 needed\ for\ COX} \qquad 4.22$$

The oxygen equivalence ratio was preferred over the more traditional O_2/C ratio (or O/C ratio) because it highlights the relative amount of oxygen in the system and indicates how far off the system is from complete oxidation (stoichiometric combustion). By dividing the moles of oxygen needed for the stoichiometric partial oxidation of the bio-oil with that needed for its stoichiometric complete oxidation (see Eq. 2.11 and Eq. 2.12) we can define the special value of equivalence ratio for stoichiometric partial oxidation, Φ_{POX} (equation 23).

$$\Phi_{POX} = \frac{Stoichiometric\ moles\ of\ O_2 needed\ for\ POX/moles\ of carbon\ in\ bio\text{-}oil}{Stoichiometric\ moles\ of\ O_2 needed\ for\ COX/moles\ of carbon\ in\ bio\text{-}oil} = \frac{\frac{n-k}{2}}{n+\frac{m}{4}-\frac{k}{2}} \qquad 4.23$$

Where n, m, and k are the moles of carbon, hydrogen and oxygen in one mole (or one ‘molecule’) of the bio-oil. Φ_{POX} was equal to 0.31 for all five bio-oil mixtures. Other equivalence ratios used in this study were obtained by considering 50%, 150%, and 200% of this value. Therefore for a given S/C ratio, the equivalence ratio considered were $\Phi = 0.15$, 0.31 (Φ_{POX}), 46, and 0.61 (corresponding to molar O_2/C ratios of 0.19, 0.38, 0.57, and 0.76).

For all five bio-oil mixtures, equilibrium hydrogen yield and product concentrations were the same for all ATR equilibrium conditions examined. The maximum standard error obtained when comparing mean hydrogen yields from all five bio-oil mixtures was 0.324, corresponding to a percent error of 3.1%. This was obtained for S/C ratio = 4 and $\Phi = 0.15$ (Figure 4.1). This implies that hydrogen yield and equilibrium product distribution is insensitive to exact bio-oil composition. The minimal variations in mean hydrogen yield observed were due to the slight difference in elemental composition among the bio-oil mixtures.

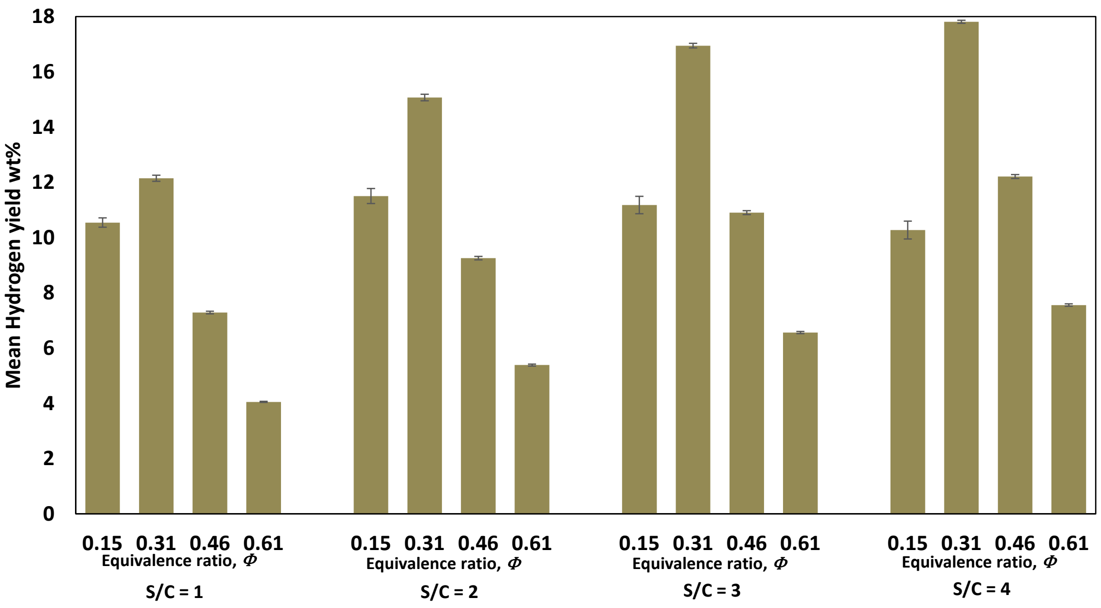

Figure 4.1 Mean hydrogen yield for all five bio-oil mixtures (BOS1-5) and standard error for $\boldsymbol{\Phi}$(0.15-0.61) and S/C (1-4)

These results imply that the mf bio-oil mixtures all undergo similar reactions when subjected to the same oxidizing conditions. Zin et al. (2015) also found that chemical equilibrium products from the SR of different mixtures of simulated aqueous fraction of pine bio-oil were the same. Table 4.5 shows the corresponding mean equilibrium temperatures and their standard deviations obtained during the ATR of the five bio-oil mixtures. The equilibrium temperatures are almost equal for similar conditions of steam and oxygen with the maximum percent error of 1.6% obtained for $S/C = 1$ and $\Phi = 0.30$. This provided further evidence that ATR proceeds with a similar mechanism for all bio-oil mixtures and the equilibrium product composition depends on the final equilibrium (exit) temperature.

Table 4.5 Mean temperatures (K) and standard deviations obtained during ATR of the five bio-oil mixtures (BOS1-5) considered in this study.

Equivalence ratio, Φ	S/C =1	S/C = 2	S/C = 3	S/C 4
$\Phi_1 \approx 0.15$	874 ± 4	804 ± 4	755 ±4	715 ± 4
$\Phi_2 \approx 0.31$	1204 ± 19	1043 ± 13	942 ± 10	871 ± 7
$\Phi_3 \approx 0.46$	1963 ± 19	1587 ± 14	1370 ± 11	1225 ± 9
$\Phi_4 \approx 0.61$	2521 ± 12	2079 ± 13	1773 ± 11	1566 ± 9

At constant S/C ratio, increasing the amount of oxygen (equivalence ratio) causes the exothermic oxidation reaction to become more favourable leading to an overall increase in the temperature of the system. On the other hand, increasing S/C ratio at constant Φ reduces the equilibrium temperature due to the high heat capacity of water which absorbs some of the surrounding heat without causing a temperature increase. Figure 4.2a shows the influence of the S/C ratio on the equilibrium hydrogen yield during the ATR of BOS2. BOS2 was used to discuss all remaining results because its composition is more realistic when compared to that of bio-oils found in published literature. As expected, the amount of equilibrium hydrogen increased with increase in S/C ratio. The maximum hydrogen yield obtained was about 12 wt% at S/C = 1 and increased to about 18 wt% at S/C = 4. This was due primarily to increase in water gas shift reaction whose equilibrium shifts to the right (towards forming more products) as more steam is introduced in the system.

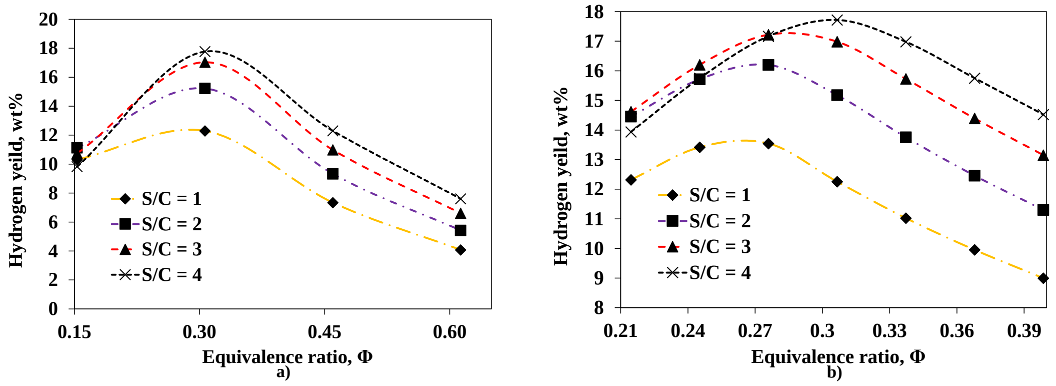

Figure 4.2: Influence of S/C ratio and the equivalence ratio on the amount of hydrogen produced during the ATR of BOS2. (a) Complete $\boldsymbol{\Phi}$ range 0.15-0.61, (b) Reduced $\boldsymbol{\Phi}$ scale (0.21-0.39)

For all S/C ratios, the maximum hydrogen yield was obtained at values of Φ close to Φ_{POX} (0.31) that is, when the amount of oxygen in the system was close to that needed for stoichiometric partial oxidation. A closer look (Figure 4.2b) reveals that at low S/C ratios (1 and 2), the maximum hydrogen yields occurred at equivalence ratio lower than Φ_{POX} ($\Phi \approx 0.27$) but attained this value at S/C = 4. Φ_{POX} is therefore an important parameter that can be used to determine the amount of oxygen to use during ATR in order to achieve maximum hydrogen yield.

4.4.2 Selectivity to carbon containing products

The influence of S/C ratio and amount of oxygen on the selectivity to carbon containing products is shown in Figure 4.3. Overall, as more steam is added, the product gas becomes increasingly rich in CO_2. In Figure 4.3a, solid carbon (in the form of graphite), CH_4, CO_2 and CO are all present at the lowest equivalence ratio considered in this study. The presence of carbon and methane is an indication of possible bio-oil thermal decomposition and Boudouard reaction that will take place under oxidant deficient conditions (Wu and Liu, 2010a). As more oxygen is added, carbon and CH_4 essentially become negligible and CO remains as the major product.

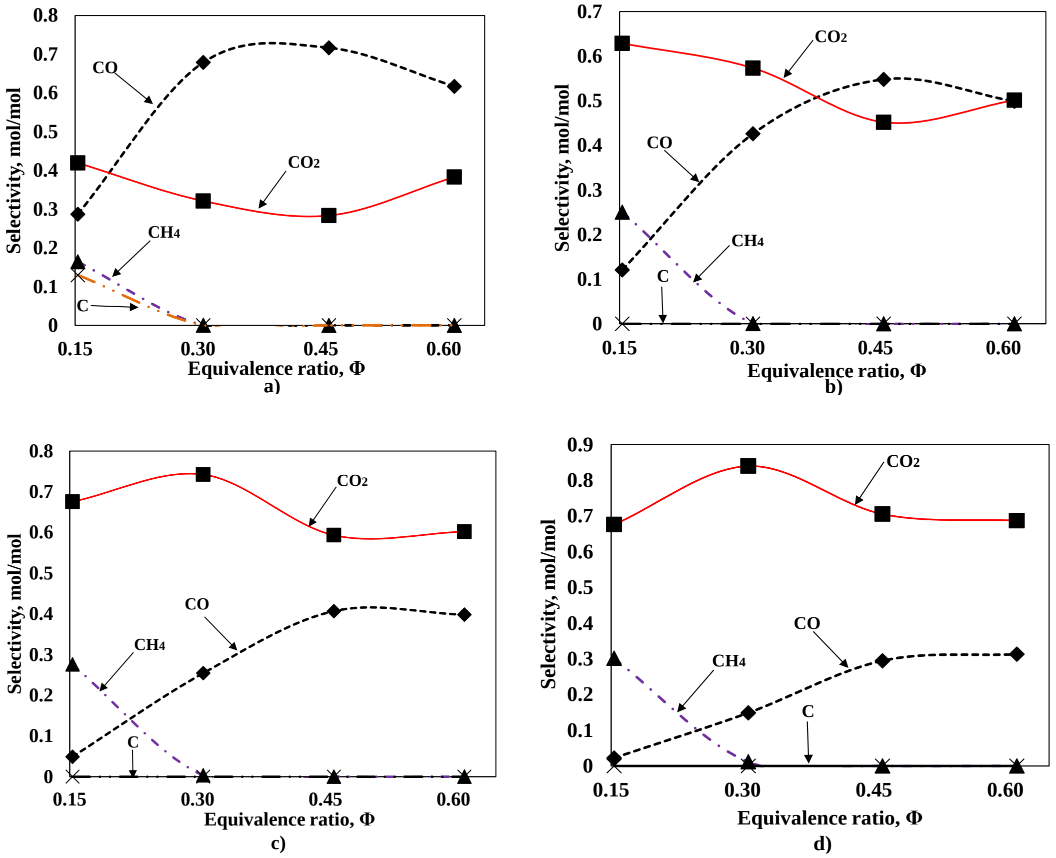

a)

b)

c)

d)

Figure 4.3 Influence of S/C ratio and O_2/C ratio on the selectivity of carbon and carbon containing products during the ATR of BOS2 at 1 atm. a) S/C = 1 b) S/C = 2 c) S/C = 3 d) S/C = 4

The decrease in carbon and CH_4 concentrations observed between $\Phi = 0.15$ and 0.30 in Figure 4.3a is due to carbon gasification and methane steam reforming respectively (reaction 8 and 10 on Table 4.4). Both reactions directly contribute in increasing the H_2 concentration and CO selectivity. The high CO content indicates that virtually no water gas shift reaction takes place under this process condition. The decrease in CO_2 concentration that occurs between $\Phi = 0.3$ and 0.45 is due to the reverse water gas shift reaction which become favourable at high temperatures (1204 – 1963 K). The slight increase in CO_2 observed $\Phi > 0.45$ is due to the bio-oil undergoing combustion (complete oxidation) producing CO_2 and H_2O. The same trends as just explained hold for Figure 4.3b-d. The main difference being that as the S/C ratio is increased to 2, 3, and 4, the water gas shift reaction becomes increasingly prominent, converting most of the CO in the system to CO_2.

4.4.3 Synthesis gas composition

Hydrogen or synthesis gas can be used as a primary feedstock in fuel cells or as feed for downstream chemical synthesis. Depending on the end use of the synthesis gas produced, the ATR process can be operated by choosing appropriate values for S/C ratio and amount of oxygen (*Φ*) to give the desired synthesis gas composition based on the downstream application (Enger et al., 2008b).

4.4.3.1 Fuel cell feed

As described in section 1.4.5, low-temperature fuel cells such as PEMFC, AFC, and PAFC operate at temperatures ranging between 370 – 473 K and use hydrogen as their only fuel source with very little tolerance for CO (< 20ppm for PEMFC) (Semelsberger et al., 2004, Pant and Gupta, 2008). For such fuel cells, the output gas from an autothermal reformer will have to be purified and all CO_2, CO and unreacted feedstock removed to give an essentially pure hydrogen stream. To reduce the cost of the downstream purification, the ATR process will have to be operated under conditions of maximum hydrogen yield for a given S/C ratio and amount of oxygen (see Figure 4.2). Purification can then be achieved by using either a CO_2 absorbent, pressure swing adsorption systems or catalytic preferential oxidation (Semelsberger et al., 2004, Dejong et al., 2009). The high-temperature fuel cells (MCFC and SOFC) on the other hand can operate at much higher temperatures ranging between 923 – 1273 K and show more flexibility in feedstock and catalyst requirements (Williams, 2011).

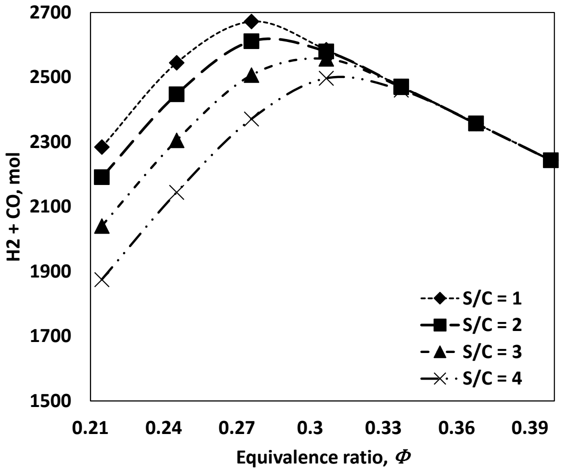

Figure 4.4 Influence of S/C ratio and *Φ* (amount of oxygen) on the total H_2 + CO obtained during ATR of BOS2 at 1 atm.

For these fuel cells, hydrogen competes with CO and even CH_4 as fuel source making the combined H_2 + CO from ATR an important parameter. Figure 4.4 shows the influence of Φ and S/C ratio on total H_2+CO yield. The maximum total H_2 + CO reduces as the S/C ratio is increased from 1 to 4. This happens because the formation of CH_4 becomes favourable at high S/C ratios and $\Phi < \Phi_{POX}$ (Figure 4.3). In the absence of methanation, the total H_2 + CO remains the same ($\Phi > 0.33$) due to the equal mole to mole ratio between H_2 and CO as one mole of CO converted to CO_2 via the water gas shift reaction gives one mole of H_2. Irrespective of the S/C ratio chosen, optimal yield for H_2 + CO is obtained at equivalence ratio approximately equal to Φ_{POX}.

4.4.3.2 Chemical synthesis feed

Synthesis gas is an important intermediate in the production of several important chemicals such as methanol, dimethyl ether, ammonia and liquid fuels (see section 1.4.3). These processes rely either on direct combination of reactants or Fischer-Tropsch (FT) chemistry and have different requirements in the amounts of H_2, CO and CO_2 in synthesis gas. A key parameter for such processes is the H_2/CO ratio whose variation for the ATR of PEFB is shown in Figure 4.5.

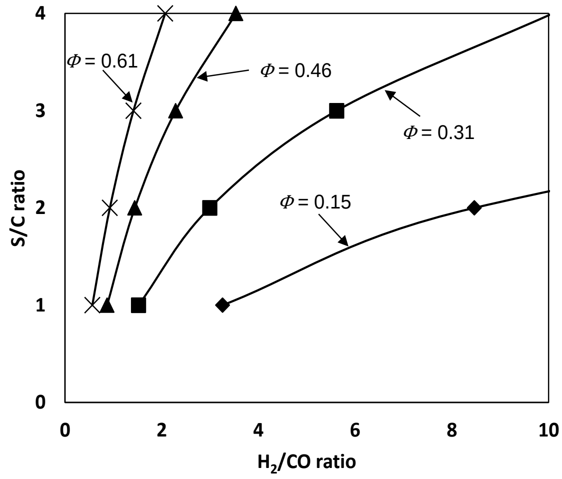

Figure 4.5 Plot of S/C ratio versus H_2/CO ratio at different values of $\boldsymbol{\Phi}$ during ATR of BOS2. Equilibrium simulation carried out at 1 atm. The maximum H_2/CO ratio shown is 10.

Gas-to-liquid (GTL) Fischer-Tropsch processes for which only H_2 and CO are reactants require a $H_2/CO \approx 2$ (Aasberg-Petersen et al., 2011, Wilhelm et al., 2001a). The synthesis gas in this case can be produced from an autothermal reformer operating with at different combinations of S/C ratios and Φ; at S/C = 1 , $\Phi \approx \Phi_{POX}$; at S/C =

2, $\Phi \approx 1.25\Phi_{POX}$; at S/C = 3, $\Phi \approx 1.5\Phi_{POX}$; and at S/C = 4, $\Phi \approx 2.0\Phi_{POX}$ (Figure 4.5). Synthesis of higher alcohols require H_2/CO = 1 (Rostrup-Nielsen et al., 2002a). In this case ATR process can be operated at a low S/C ratio (S/C ≤ 2) and equivalence ratio larger than the value required for stoichiometric partial oxidation, that is, $\Phi > \Phi_{POX}$ so as to avoid any carbon formation (Figure 4.3a). H_2, CO and CO_2 are all reactants in methanol, dimethyl ether and high temperature Fischer-Tropsch synthesis (Aasberg-Petersen et al., 2001a). For such processes, the synthesis gas is made to have the same stoichiometry as the final product with its composition expressed as shown in Eq 4.24.

$$M = \frac{H_2 - CO_2}{CO + CO_2} \qquad 4.24$$

M is called the module and is equal to 2 for methanol and dimethyl ether synthesis (Rostrup-Nielsen et al., 2002a, Aasberg-Petersen et al., 2001a). For this study, the maximum value of M was 0.7, obtained at $\Phi = \Phi_{POX}$ for all S/C ratios examined. This implies that for a process using ATR, the required value of M for synthesis feed can only be obtained either by addition of pure H_2 or removal of CO_2.

The explanations given in this section are simplified and meant to serve as a guide only. The eventual choice in process parameters will depend on other important factors like process scale and amount of product recycle (Rostrup-Nielsen, 2000).

4.4.4 Reaction mechanism

One advantage of using the Gibbs minimization energy is that a very large pool of chemical species is used to determine eventual equilibrium composition. The alternative will be to assume the prevailing reactions under the given process conditions and then use their equilibrium constants to determine equilibrium concentrations. The limitation of the latter is that fewer number of reactions and potential products are considered, compared to the number of species used by the Gibbs minimization method. Two main types of mechanisms were successful in accounting for equilibrium species obtained by the CEA software in the ATR of PEFB bio-oil. It should be noted that the word ‘mechanism’ is used in this case to described a system of dominant reactions accounting for equilibrium product distribution irrespective of the actual prevailing elementary reactions. The results presented are those obtained from using BOS2 as feedstock. Similar results were obtained for all five mf bio-oil mixtures considered in this study. All reactions in this section are identified using the reaction nomenclature and abbreviations listed on Table 4.4.

4.4.4.1 Partial oxidation (POX) or direct mechanism

The reactions considered for this mechanism were: bio-oil partial oxidation (POX), bio-oil steam reforming (SR), water gas shift reaction (WGS), Boudouard reaction (BO-RX), methanation of carbon (MEN), carbon gasification (C-GS1 and C-GS2), methane steam reforming (ME-SR), hydrogen oxidation (H-OX) and carbon monoxide oxidation (CO-OX).

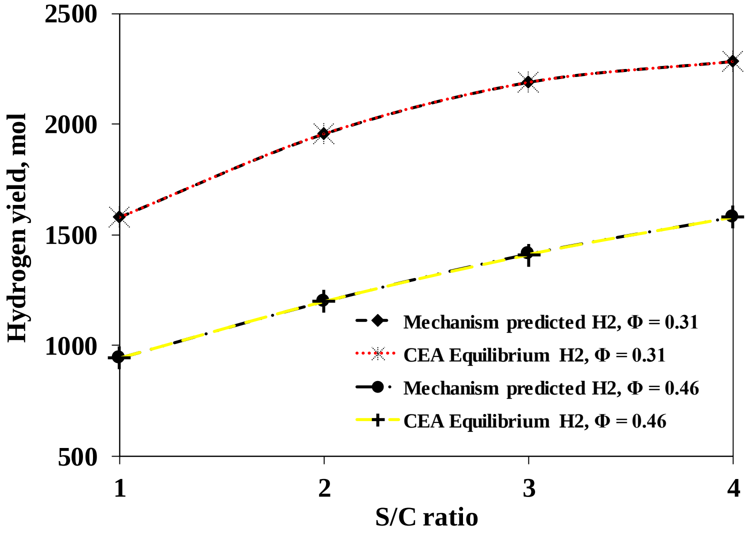

Figure 4.6 Comparing actual equilibrium hydrogen yield with predicted yield using POX based mechanism. Results shown for $\Phi = 0.31$ and 0.46

These reactions were used to fit equilibrium results obtained at S/C = 1 – 4 and $\Phi = 0.31$ and 0.46. Not all reactions listed above were involved at the same time for a given process condition. With a relative error less than 0.1% on individual molar production rates, it was impossible to distinguish between the mechanism-predicted and the equilibrium (‘actual’) values of H_2 yield as shown in Figure 4.6.

The contribution to hydrogen production by participating reactions for the POX mechanism is shown in Figure 4.7. By way of this mechanism, hydrogen production was primarily from POX, WGS and carbon gasification (C-GS1) reactions at $\Phi = 0.31$ and from POX and SR reactions at $\Phi = 0.46$.

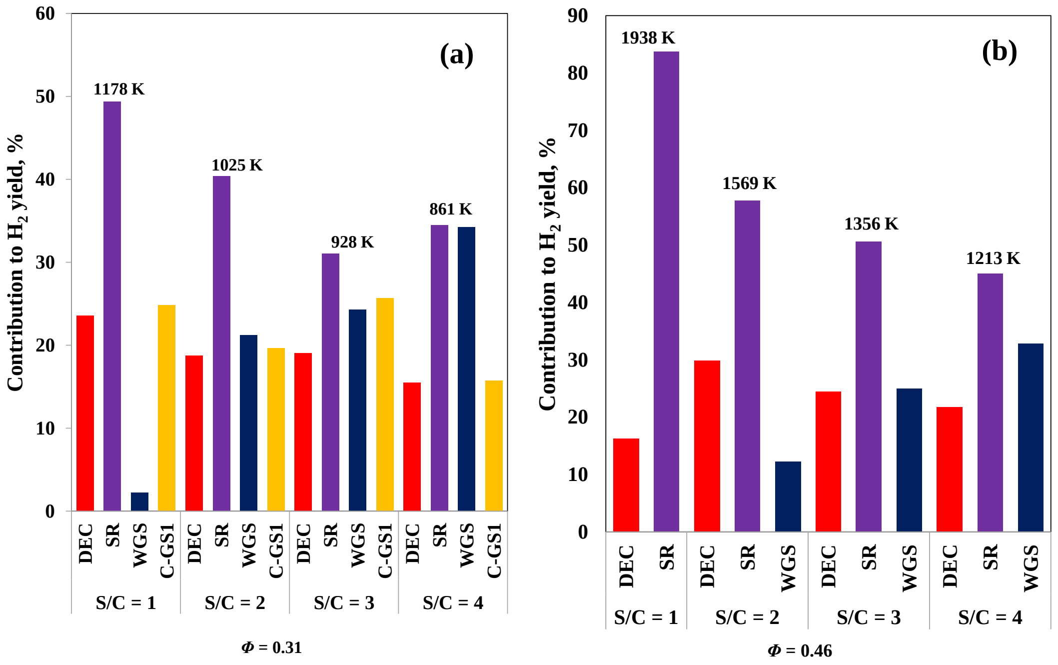

Figure 4.7 Percentage contribution to hydrogen production by participating reactions for the POX mechanism at autothermal temperatures given in the figure for each S/C. a) $\Phi = 0.31$. b) $\Phi = 0.46$. Temperature values (in K) for the different process conditions examined are included above their corresponding S/C ratios.

One interpretation of this mechanism is that under low oxygen content ($\Phi \leq \Phi_{POX}$), the bio-oil completely undergoes POX and more hydrogen is subsequently produced by the water gas shift reaction with no significant contribution from SR. Further production of hydrogen is achieved by the gasification of all solid carbon formed. Meanwhile at the intermediate oxygen equivalence ratio $\Phi = 0.46$ ($>\Phi_{POX}$), POX and SR were the only hydrogen producing reactions. For this mechanism, no significant hydrogen consumption occurred as methanation of carbon (MEN) was virtually zero. In the case of S/C = 1 and Φ = 0.46, H-OX and reverse WGS (R-WGS) reactions where responsible for H_2 consumption. Figure 4.8 shows how the amount of steam and oxygen influenced the bio-oil consuming reactions. Complete bio-oil consumption was assured only by POX at $\Phi = 0.31$. While POX and some SR were both involved in bio-oil consumption at $\Phi = 0.46$.

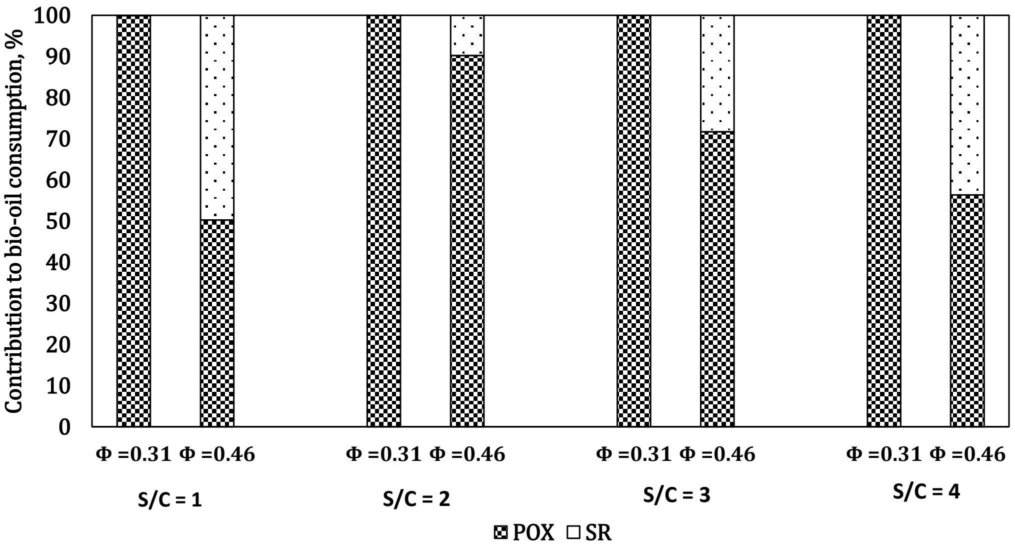

Figure 4.8 Influence of S/C ratio and oxygen on Bio-oil consuming reactions

Table 4.6 gives a summary of the different reactions that dominate in the POX mechanism at various temperature ranges. This table provides valuable information for the eventual choice of catalyst. For ATR carried out at temperatures below 1100 K, the catalyst should be very selective to POX and WGS. High temperatures typical of low S/C ratios and high oxygen content ($\Phi \gg \Phi_{POX}$) should always be avoided since it can lead to catalyst degradation.

Table 4.6 Summary of the POX mechanism for different temperature ranges. Only reactions which contribute to equilibrium products are included

	Temperature range		
	T < 1100 K	**1200 < T < 1600 K**	**T > 1800 K**
Steam content	S/C >2	2 < S/C < 4	S/C < 2
Oxygen content	$\Phi < \Phi_{POX}$	$\Phi > \Phi_{POX}$	$\Phi \gg \Phi_{POX}$
Reaction condition	Catalytic	Catalytic and homogenous	Homogenous
Reactions	POX, WGS, BO-RX, MEN, C-GS1	POX, SR, C-GS2 CO-OX	POX, SR, R-WGS, H-OX, CO-OX

Based on this mechanism, it can be said that at $\Phi \leq \Phi_{POX}$, actual SR reactions are minimal and the choice of catalyst should be based on the prevailing POX, WGS and C-GS1 reactions.

4.4.4.2 Complete oxidation (COX) or indirect mechanism

Another mechanism was validated for which complete oxidation (COX) was the dominant oxygen-consuming reaction. There was a near perfect agreement between the predicted hydrogen concentration and actual equilibrium hydrogen yield (Figure 4.9).

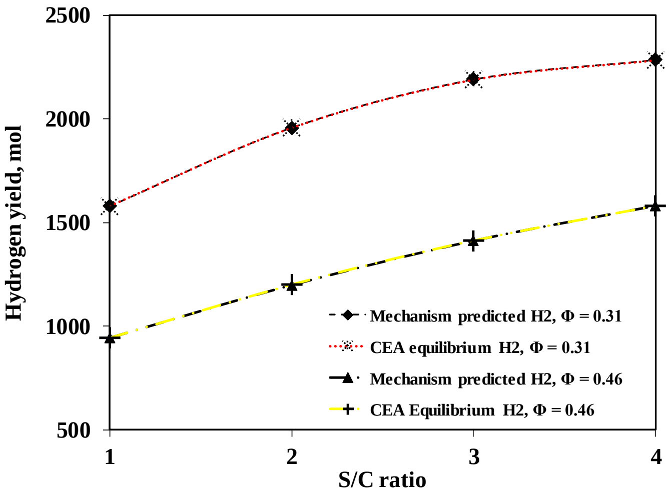

Figure 4.9 Plots of predicted hydrogen and actual equilibrium hydrogen showing near match with maximum relative error of 0.1% for the COX based mechanism. Results shown for Φ = 0.31 and 0.46

The reactions considered for this mechanism were bio-oil thermal decomposition (DEC), bio-oil complete oxidation (COX), bio-oil steam reforming (SR), WGS, reverse water gas shift (R-WGS), methane steam reforming (ME-SR), methanation of carbon (MEN), carbon gasification (C-GS1 and C-GS2), and hydrogen oxidation (H-OX), as shown in Figure 4.10.

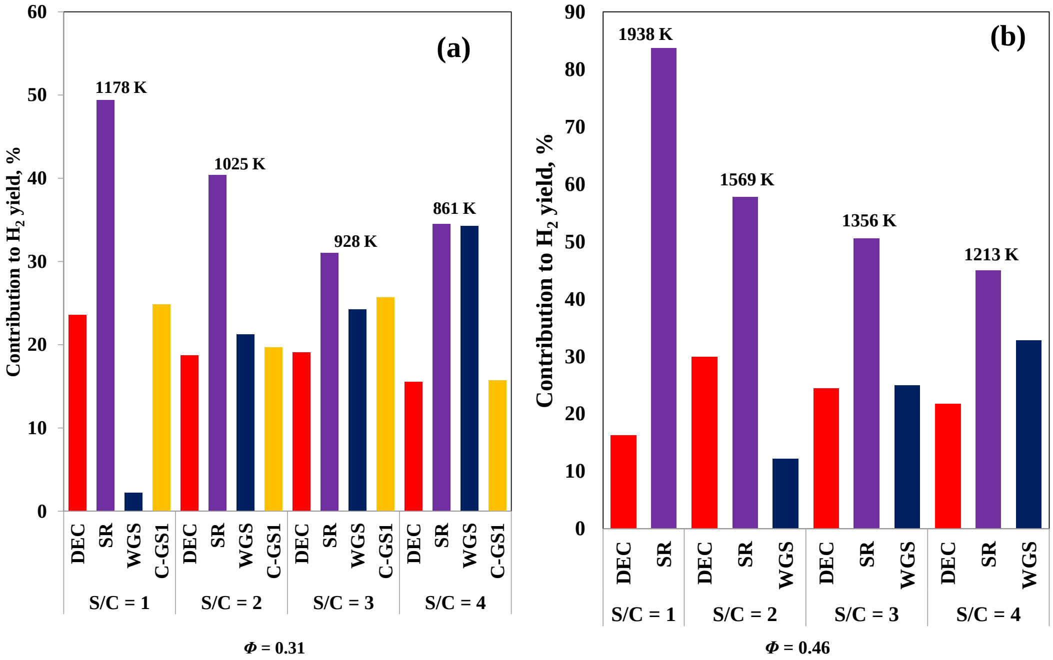

Figure 4.10 Percentage contribution to hydrogen production by participating reactions for the COX based mechanism at autothermal temperatures given in the figure for each S/C. a) Φ = 0.31. b) Φ = 0.46. Temperature values (in K) for the different process conditions examined are included above their corresponding S/C ratios.

At $\Phi = 0.31$, hydrogen production stemmed from DEC, SR, WGS and C-CG1. As expected more hydrogen was produced from WGS as the S/C ratio was increased from 1 to 4. A similar trend was observed at $\Phi = 0.46$ except for the fact that there was no C-GS1 reaction. Carbon formed at the higher equivalence ratio is removed via reaction with oxygen (C-GS2).

For this mechanism, bio-oil was consumed almost in the same proportion among COX, SR and DEC reactions independently of the amount of oxygen, as illustrated in Figure 4.11.

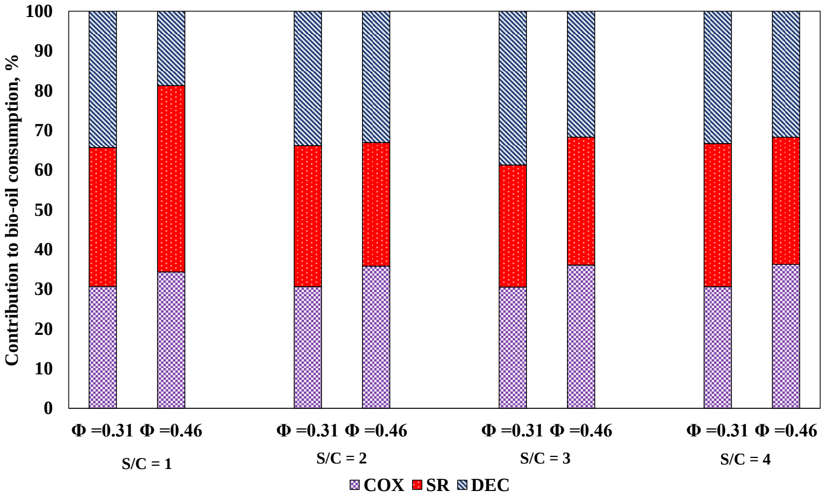

Figure 4.11 Influence of S/C ratio and oxygen on Bio-oil consuming reactions

This mechanism relies on gas phase decomposition and combustion which occur significantly at all ATR conditions examined. Table 4.7 gives a summary of the different reactions that dominate in the COX based mechanism at various temperature ranges.

Table 4.7 Summary of the COX mechanism for different temperature ranges. Only reactions which contribute to equilibrium products are included

	Temperature range		
	T < 1100 K	**1200 < T < 1600 K**	**T > 1800 K**
Steam content	S/C >2	2 < S/C > 3	S/C < 2
Oxygen content	$\Phi < \Phi_{POX}$	$\Phi > \Phi_{POX}$	$\Phi \gg \Phi_{POX}$
Reaction condition	Catalytic and homogenous	Catalytic and homogenous	Homogenous
Reactions	COX, DEC, SR, WGS, C-GS1,	COX, DEC, SR, C-GS1	COX, DEC, SR, R-WGS, C-GS2, H-OX

A suitable catalyst for this mechanism will have to be very selective for COX, DEC, SR and C-GS1, as well as offering high thermal stability, although at high Φ, all reactions are expected to become homogeneous (non-catalytic) due to high autothermal temperatures.

4.4.4.3 Comments on mechanisms

The POX (direct) and COX (indirect) mechanisms discussed above highlight the fact that there may be several routes leading to the formation of the desired H_2 and CO products during ATR. Such schemes are typical for systems where several reaction equilibria occur simultaneously (Enger et al., 2008a). For the POX mechanism to be realistic it has to be completely catalytic and an appropriate choice of catalyst can lead to the suppression of undesirable side reactions and products like carbon (coke). The COX based mechanism relies on homogenous oxidation and decomposition. Thermal decomposition accounts for about 30% of the bio-oil consumption and this can prove challenging to manage due to excessive carbon deposition on reactor walls and catalyst and can be difficult to completely eliminate by gasification (depending on type of carbon formed). In addition, it might be necessary to operate under conditions of $\Phi > \Phi_{POX}$ in order to compensate for heat loss and feed preheating (sensible heat) (Kumar et al., 1996).

4.5 Conclusion

This work demonstrates that ATR is in theory a viable process for the production of hydrogen-rich syngas from bio-oil. Using mf bio-oil mixtures with different compositions, it was established that hydrogen yield and concentration of other equilibrium products were insensitive to actual chemical composition. The molar elemental composition proved to be the determining factor for equilibrium hydrogen and syngas yield. The possibility of generating syngas with different H_2 and CO compositions by varying the S/C ratio and the equivalence ratio makes ATR of bio-oil a viable option for applications like fuel cells and chemical synthesis. Mechanisms were proposed to account for equilibrium product yields. A direct (or POX) mechanism was proposed in which H_2 was produced from POX, SR and WGS reactions. Results obtained for this mechanism show that ATR can be viewed as partial oxidation combined with WGS instead of the more traditional notion of exothermic oxidation coupled with endothermic SR. Another mechanism validated was the indirect (or COX) mechanism in which thermal decomposition accounted for about 30% of bio-oil consumption with hydrogen production assured by bio-oil decomposition, steam reforming, water gas shift and carbon gasification reactions.

The equilibrium calculations performed in this study do not take into consideration the kinetic aspects of the reactions involved and could prove unrealistic in real ATR reactors. The proposed mechanisms can only occur when equilibrium is attained for example working at low space velocities and high catalytic activity. Future work should therefore focus on kinetic studies and the influence of other process parameters like pressure and space velocity.

Chapter 5 Process Design and Simulation

5.1 Introduction

This chapter focuses on the use of palm empty fruit bunch (PEFB) as a source of hydrogen by means of a process design and simulation using the Aspen Plus software. PEFB biomass is produced as a main by-product in the oil palm industry. The Low bulk density of PEFB necessitates on-site processing, and pyrolysis provides a convenient and efficient way for long-term storage and distribution.

Several authors have proposed Aspen Plus simulation models for biomass pyrolysis and gasification to produce hydrogen rich syngas. Onarheim et al. (2015) developed fluidised-bed based models for pine and forest residue pyrolysis using Aspen Plus. An overall process efficiency of 69.3% was determined for pine residue pyrolysis, which was higher than the 55.8% obtained for the forest residue. Ward et al. (2014) developed a computational fluid dynamics model using Aspen plus to analyse and optimise the pyrolysis process of four types of biomass: shredded green waste, pine chips, wood and birch. They obtained a maximum bio-oil yield of 58% for shredded green waste. Doherty et al. (2013) performed an Aspen plus simulation of biomass gasification featuring a steam blown dual fluidised bed. The influence of key factors such as gasification temperature, biomass moisture, steam to biomass ratio, air to biomass ratio and steam temperature on syngas composition were investigated. Their study established that biomass moisture is the most important factor influencing the efficiency of the process. The process design proposed in this chapter includes PEFB biomass pyrolysis to produce bio-oil, followed by ATR of this bio-oil to obtain syngas which is then shifted and separated to give pure H_2. Influence of process factors such as S/C ratio and amount of air on hydrogen yield and syngas composition are investigated. An optimised heat exchange network including a combined heat power generation unit is proposed using pinch analysis.

5.2 Process Design

5.2.1 Process Description

Figure 5.1 shows a simplified process diagram for the production of syngas and eventual upgrading to hydrogen using fresh PEFB biomass as feedstock for a hydrogen production plant. The overall process consists of four main stages: pre-processing, pyrolysis, autothermal reforming (ATR) and purification. Fresh (wet) PEFB obtained from a near-by oil palm processing plant is chopped from an initial size of 400 mm to 15 mm. The chopped feedstock then has its moisture reduced from 40% to 10 % in a dryer before undergoing further size reduction in a mill to obtain an average of 2 – 3 mm particle size suitable for pyrolysis (Bridgwater, 2012).

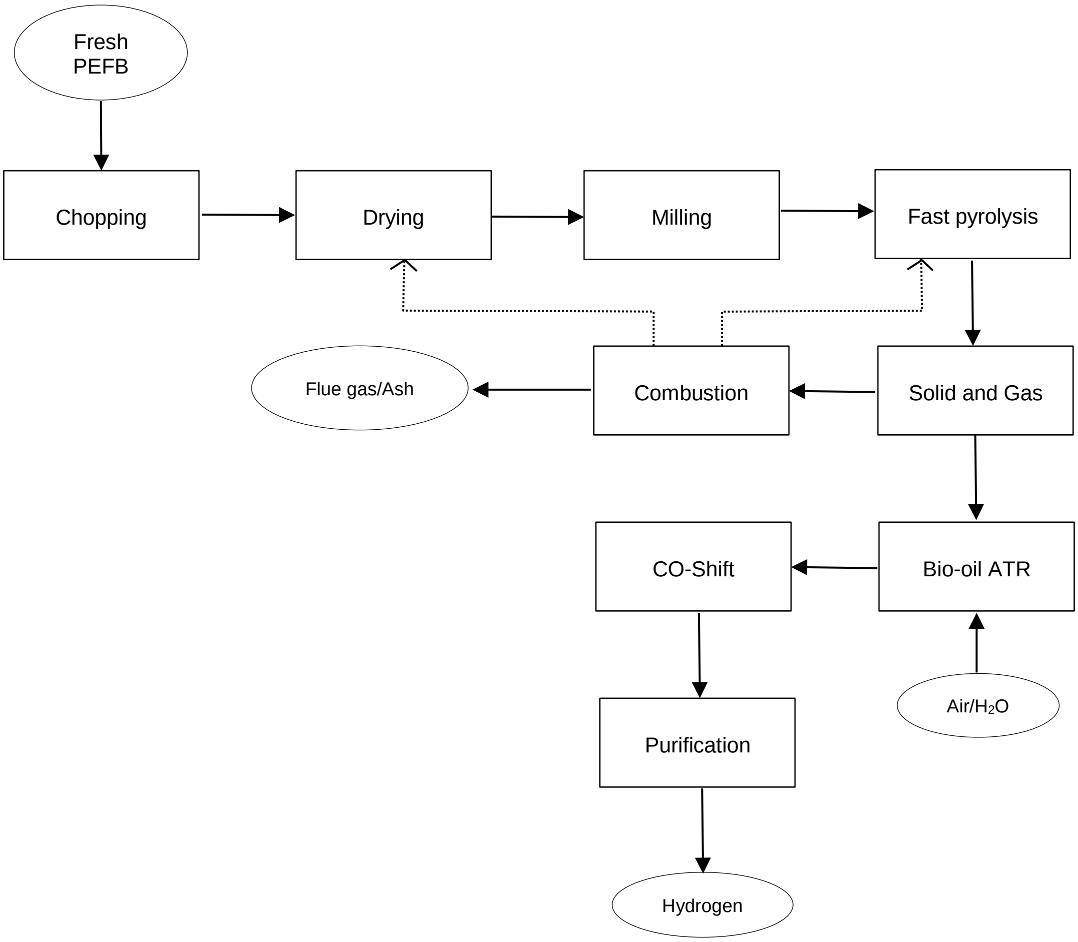

Figure 5.1 Generalised process flow diagram for hydrogen production from PEFB biomass

Fast pyrolysis takes place in a fixed bed reactor at 500 °C and yields a solid char and volatile organics which are further separated using cyclones. Upon cooling, the volatile stream separates into a condensable liquid (bio-oil) and a non-condensable gas (NCG) stream. The bio-oil produced can be stored and transported out of site or reformed on site, here proposed, to obtain syngas or pure hydrogen. The choice of reforming technology greatly influences the profitability and sustainability of the entire process. The process model proposed uses an autothermal reformer operated adiabatically at 3 bar (for the base case) with steam, air and bio-oil as input streams. The main reactions and accompanying side reactions taking place in the reformer are listed in Table 2.4 and Table 4.4. The reformate is cooled to 250 °C and sent to a carbon monoxide (CO) shift reactor where most of the CO reacts with water and converts to CO_2 and H_2 via the WGS reaction. Upon cooling, the resulting stream containing mostly N_2, H_2, CO_2, CO and water vapour moves into a hydrogen purification unit.

For this study, the possibility of using a high pressure water scrubber (HPWS) and a more traditional pressure swing adsorption (PSA) unit for hydrogen purification was investigated. Cozma et al. (2014) proposed an Aspen Plus based HPWS model for the removal of CO_2 from biogas. Their model, which uses a pressurised water scrubber/air stripper system with the possibility of water regeneration and recirculation, initially designed for biogas/CH_4 clean-up is adopted and optimised in this study for hydrogen purification.

5.2.2 Process design in Aspen

Assumptions made for this process design and all ensuing analyses include:

- Steady state process
- No heat losses across pipes, reactors and other related process equipment (unless otherwise stated)
- Negligible pressure drop during solid/fluid transport throughout the process
- Char (biochar) contains only carbon
- Biomass contains only C, H and O.

Aspen Plus® has been used by many researchers to perform simulation of various chemical, petrochemical and energy processes (Visconti et al., 2014, Martin et al., 2016). Aspen Plus uses unit operation blocks to model specific process operations and also supports user-defined Fortran codes which can be used to modify the properties of existing blocks (Doherty et al., 2010, Dufour et al., 2012). One advantage of using this software is that it allows the user to define non-conventional fuels like coal and biomass in terms of their ultimate and proximate analysis and it also has an extensive built in physical properties database that can be used to perform simulation calculations (Mavukwana et al., 2013).

5.2.2.1 Thermodynamic property methods

The Peng-Robinson equation of state with Boston-Mathias modification (PR-BM) was the global thermodynamic property method selected for this simulation. This method is particularly applicable to high temperature and pressure gas-processing, chemical and petrochemical processes (Doherty et al., 2013, Halvorsen et al., 2015) . This property method is comparable to the Soave-Redlich-Kwong equation of state, which other authors have used to simulate biofuel and coal thermochemical conversion processes (Martin et al., 2016, Halvorsen et al., 2015, Preciado et al., 2012). The steam table property method (STEAM-TA) was used to calculate the thermodynamic properties of water when this was used on either the hot side or cold side of shell and tube heat exchangers. The ELECNRTL property method was used to specify the water scrubber while the IDEAL property method was used for the water pump around (WPA) recovery unit and air stripper (both units are used for processes using HPWS). A full description of the equations and merits of these thermodynamic property methods is beyond the scope of this work.

PEFB biomass and ash (obtained after pyrolysis) were defined as non-conventional solids and the HCOALGEN and DCOALIGT models were used to calculate enthalpy, density and other thermodynamic properties based on the ultimate and proximate analyses values. The HCOALGEN is a coal enthalpy model and the correlation method used to determine the heat of combustion, heat of formation and heat capacity are listed in Table 5.1. Several authors have applied these correlation methods, especially the Boie correlation, to biomass and other hydrocarbon fuels (Bates and Ghoniem, 2013, Annamalai et al., 1987).

For this simulation, the Kirov correlation was used to calculate the heat capacity of PEFB biomass. This correlation takes into account the constituent mass fractions as defined by the proximate analysis and treats the heat capacity as a weighted sum of the heat capacities of moisture, ash, fixed carbon, and primary and secondary volatile matter (Aspen Plus V8.8 manual). This is written mathematically as

$$C_{p,i} = \sum_{j=1}^{ncn} w_j C_{p,ij}$$

Where

C_p is the heat capacity,

i is the component index,

j is the constituent index (1 = moisture, 2 = fixed carbon (FC), 3 = primary volatile matter, 4 = secondary volatile matter, 5 = ash),

w_j is the mass fraction of the j^{th} constituent on a dry basis,

ncn is the number of constituents.

Secondary volatile matter is defined as any volatile matter up to 10% on a dry, ash-free basis with the remaining volatile matter being primary (Onarheim et al., 2015).

Table 5.1 HCOALGEN correlations used to calculate thermodynamic properties of PEFB biomass

Property	Calculation method	Component attributes
Heat capacity	Kirov correlation	Proximate analysis
Heat of combustion	Boie correlation	Ultimate and proximate analysis
Heat of formation	Heat-of-combustion-based correlation	Ultimate analysis

The heat capacity, C_p, is temperature dependent and this dependency for each component is calculated using the following equation:

$$C_{p,ij} = a_{i,j1} + a_{i,j2}T + a_{i,j3}T^2 + a_{i,j4}T^3$$

Where a is a parameter or element, i is the component index, and j is the constituent index (Onarheim et al., 2015).

The Boie correlation is given by:

$$\Delta_c h_i^{dm} = \left[a_{1i}w_{C,i} + a_{2i}w_{H,i} + a_{3i}w_{S,i} + a_{4i}w_{O,i} + a_{5i}w_{N,i}\right] \times 10^2 + a_{6i}$$

where a_1- a_6 are parameters and $w_{X,i}$ is the mass fraction of element X in component i (X = C, H, S, O, N). The default Aspen parameters used for the Kirov and Boie correlations are given in Appendix A.

5.2.2.2 Biomass Specification

PEFB biomass has no universal composition since this depends on the actual palm variety, geographical region, and age of plant (Omar et al., 2011).

Table 5.2 Ultimate and proximate analysis of PEFB used for Aspen Plus simulation

Ultimate analysis	
Carbon	51.7
Hydrogen	5.9
Nitrogen	0
Chlorine	0
Sulphur	0
Oxygen	42.4
Proximate analysis	
Moisture	40.0
Fixed Carbon (FC)*	13.3
Volatile Matter (VM)*	83.4
Ash*	3.3

* Value reported on dry basis

The proximate analysis and ultimate analysis of PEFB shown in Table 5.2, and used for this simulation, are assumed based on average values obtained from published data (Chang, 2014, Abdullah and Gerhauser, 2008, Abdullah et al., 2011, Khor et al., 2009a). In Aspen plus, ultimate analysis and proximate analysis values (excluding moisture content) are entered on dry basis only.

5.2.2.3 Bio-oil surrogate

Using the method described in section 3.5.1, six macro-chemical families were identified from the DTG curve presented in Figure 3.7. The experimental DTG results together with the fitted model and constituting families are shown in Figure 5.2 which has been reported in the co-authored work, Dupont et al. (2017).

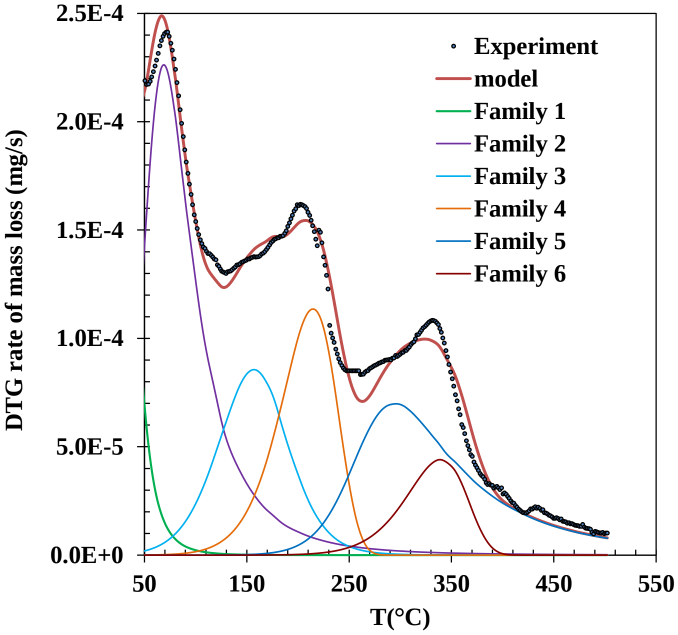

Figure 5.2 PEFB bio-oil DTG and fitted model comprising six macro-chemical families (Dupont et al., 2017)

Table 5.3 presents the boiling temperature range, fitted coefficients, calculated mass fractions and compounds selected to represent the six macro-chemical families identified in the PEFB bio-oil.

Table 5.3 Summary of results obtained from DTG model and representative compounds

Family	BP range, K (peak)	A	E	n	Mass fraction (model)	Representative (model) compound	BP, K	Mass fraction (surrogate)
1	300 – 360 (300)	1×10^{8}	51	2	0.1	Formaldehyde	254	0.083
						Acetaldehyde	293.2	0.008
						2-butanone	353	0.008
2	300 – 500 (340)	3×10^{9}	69.3	3.5	0.3	Water	373	0.238
						Acetic acid	391	0.075
3	340 – 520 (430)	1×10^{5}	52	1.5	0.15	Furfural	434.7	0.136
						Phenol	454.7	0.008
4	380 – 540 (480)	1×10^{6}	68	1	0.15	Creosol	492.5	0.030
						Guaiacol	478	0.121
5	460 – 800 (560)	7×10^{7}	100	4	0.25	Catechol	518.5	0.249
6	500 – 700 (610)	2×10^{7}	101	1	0.05	Palmitic acid	624	0.008
						Levoglucosan	657	0.038

A comparison of some properties of the formulated surrogate bio-oil and that of the actual PEFB bio-oil is given in Table 5.4. It can be seen that the bio-oil surrogate has some similar properties to the actual PEFB bio-oil notably the H/C and O/C ratios.

Table 5.4 Properties of PEFB bio-oil and surrogate

	(Pimenidou and Dupont, 2012)	Bio-oil surrogate
Moisture	24.30	25
Proximate analysis (%)		
Volatile matter	84.3	
Fixed carbon	11.3	
Ash	2.43	
Solids		
Ultimate analysis (%)		
C	45.23	49.2
H	6.53	6.5
O	47.03	44.3
N	8.5×10^{-3}	0
S	0.0611	0
H/C molar ratio	1.7	1.6
O/C molar ratio	0.8	0.7
HHV (MJ kg^{-1})	19.8	17.9
LHV (MJ kg^{-1})	18.4	16.6
Density, kg/m^3		1421
Flash point, °C		72

5.2.2.4 Stream specification and flowsheet development

The Aspen Plus solids template with metric units was used to develop this simulation. In addition to gas and liquid streams, this template supports a wide range of unit operation models for solids processing such as crushers and cyclones. An extensive component list was generated and included hydrogen, CO, CO_2, CH_4, all the bio-oil model compounds listed in Table 5.3, carbon, biomass and ash. Once the thermodynamic property models were selected as described in section 5.2.2.1, the flowsheet was created with the global stream class set to MIXNCPSD (Mixed Stream + Nonconventional Solid with Particle Size Distribution). This stream class includes three sub-stream classes: MIXED, CISOLID, and NCPSD. MIXED components include all liquid and gas components which take part in chemical equilibrium and/or phase equilibrium calculations. The char formed during pyrolysis was defined as a CISOLID (conventional inert solid) stream while PEFB biomass was specified as an NCPSD (non-conventional inert solid) stream. Both char and PEFB biomass do not participate in chemical equilibrium and/or phase equilibrium calculations (Nsaful, 2012).

A flowsheet was then developed in the simulation environment using various default blocks available in Aspen. Figure 5.3 and Figure 5.4 are complete flow diagrams of two process designs carried out in Aspen. The difference between both designs is that Figure 5.3 is the representation of the so called ‘PAWS process’ in which HPWS system is used to separate and recover all the H_2 produced (at about 97 mol% purity). While Figure 5.4 on the other hand, is a representation of the ‘PAPS process’ in which a PSA unit is used to recover a significant amount of pure H_2 (above 75% based on the operating pressure).

The next section provides details of the main Aspen blocks and specifications used in the process design and simulation. The base case scenario presented considers a plant processing 5000 kg/h of fresh PEFB (40% moisture).

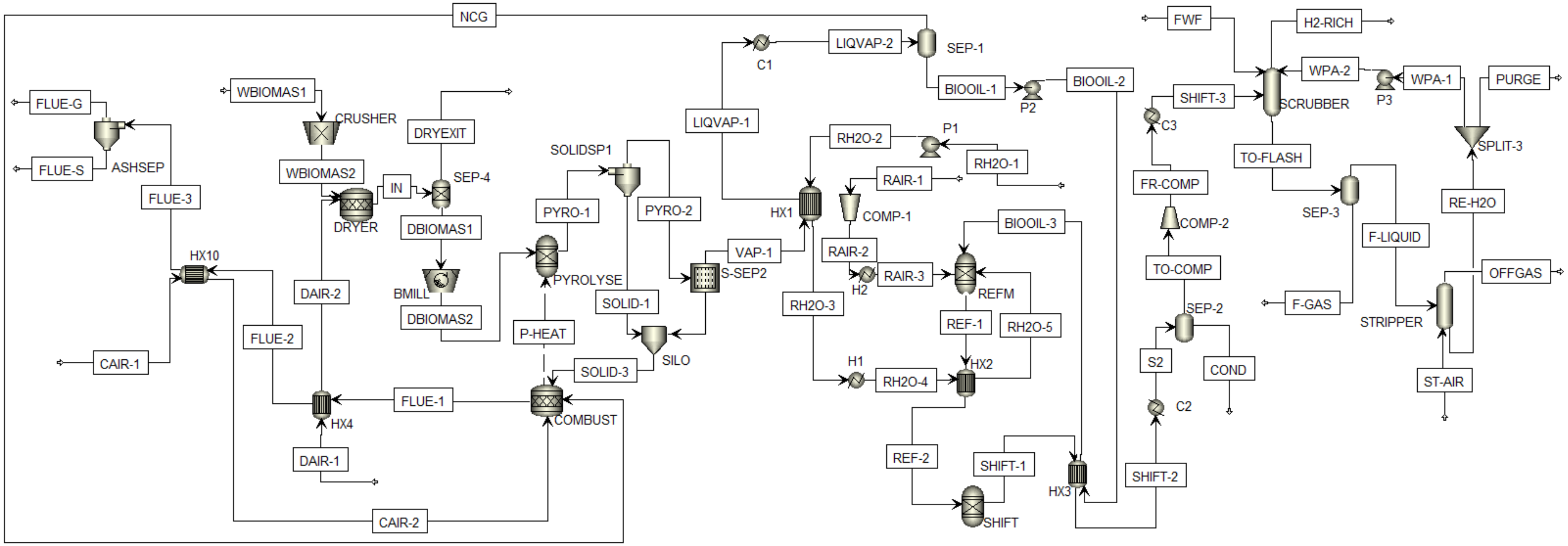

Figure 5.3 Complete Aspen Plus process flow diagram showing pre-processing, pyrolysis, ATR and hydrogen purification by HPWS (PAWS process)

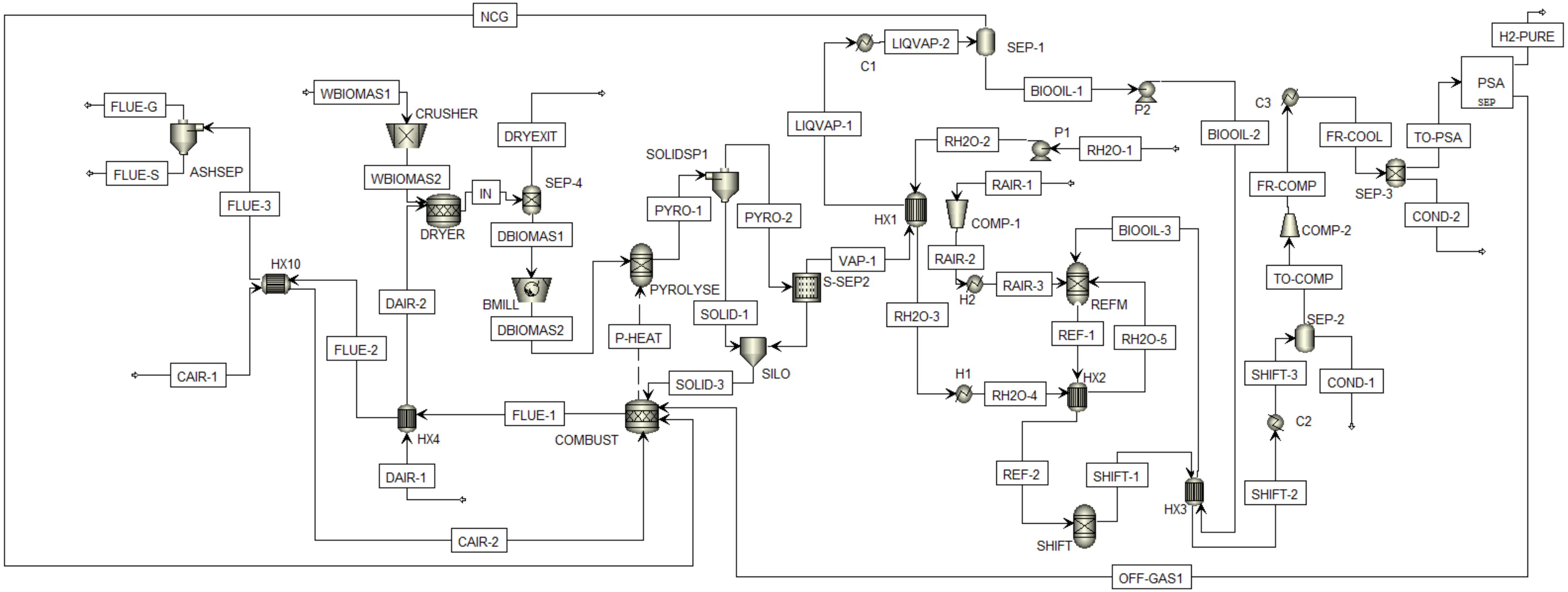

Figure 5.4 Complete Aspen Plus process flow diagram showing pre-processing, pyrolysis, ATR and hydrogen purification by PSA (PAPS process)

5.2.2.5 Unit operations

Crushing and Milling (Block ID – CRUSHER and BMILL)

Size reduction of the fresh PEFB (***WBIOMAS1***) is achieved using two blocks specified by a local particle size distribution (PSD) and a mechanical efficiency of 90%. Table 5.5 and Table 5.6 show the specified lower and upper limits for the PSD for the crusher (***CRUSHER***) and ball mill (***BMILL***). Lack of published data on PEFB grinding characteristics limited the accuracy of the grinding energy required by these operations. However, the Hardgrove Grindability Index (HGI) selected for PEFB was 22 based on available information for other biomass feedstocks (Peryoga et al., 2014, Williams et al., 2015).

Table 5.5 Particle size distribution specified for Crusher (mm)

Interval	Lower limit (mm)	Upper limit (mm)	Weight fraction
1	0.001	0.005	0.1
2	0.005	0.01	0.2
3	0.01	0.015	0.2
4	0.015	0.02	0.2
5	0.02	0.025	0.1
6	0.025	0.03	0.1
7	0.03	0.035	0.1

Table 5.6 Particle size distribution specified for Ball Mill (mm)

Interval	Lower limit (mm)	Upper limit (mm)	Weight fraction
1	0.001	0.002	0.2
2	0.002	0.003	0.2
3	0.003	0.004	0.2
4	0.004	0.005	0.2
5	0.005	0.006	0.2

Drying (Block ID – DRYER and SEP-4)

Drying is achieved using a combination of an adiabatic RStoic reactor (***DRYER***) operating at 1 bar and a two-phase flash separator (***SEP-4***) also operating at 1 bar. Even though biomass drying is not a chemical reaction, the RStoic reactor in Aspen converts a portion the nonconventional biomass feed to water via the following equation (Begum et al., 2013):

$$Biomass(wet) \rightarrow 0.0555084 H_2O \qquad 5.1$$

Aspen Plus treats all nonconventional components as if they have a molecular weight of 1.0. This equation implies that 1 mole of PEFB reacts to form 0.0555084 mole of water. A calculation block controls the extent of water formation and uses the value of the initial moisture content of the PEFB biomass as specified by its proximate analysis and the final moisture content of the dried PEFB, which in this case is set at 10%, to calculate the conversion of the RStoic reactor. The equation used in the calculation block to calculate the feed conversion is given as

$$\mathrm{CONV} = \frac{\mathrm{H2OIN} - \mathrm{H2ODRY}}{100 - \mathrm{H2ODRY}} \qquad 5.2$$

Where $\mathrm{H2OIN}$ is the initial moisture of the fresh PEFB biomass (40%) and $\mathrm{H2ODRY}$ is the final moisture content of the dried product (10%).

The RStoic reactor does not need heat to simulate water removal, nonetheless, a heat source, hot air, is included in this process simulation for completeness and to facilitate energy balance calculations.

The resulting water vapour and warm air are separated from the dried PEFB in a two-phase flash separator, SEP-4, operated adiabatically at 1 bar. After drying, the crushed biomass flow rate reduces to 3333.3 kg/h for the base case.

Pyrolysis (Block ID – PYROLYSE)

PEFB pyrolysis is simulated by an Aspen Plus RYield reactor (***PYROLYSE***). The RYield reactor allows the conversion of the non-conventional stream (PEFB biomass) to conventional products. The yield of conventional products using this reactor was set using a calculator block and the product distribution is given in Table 5.7. The pyrolysis yield of the solid, liquid and gaseous phases are based on average values obtained from existing literature (Onarheim et al., 2015, Abdullah et al., 2010b, Sulaiman and Abdullah, 2011, Zhang et al., 2013)

Table 5.7 Pyrolysis yield at 500 °C and 1 bar for 10% moisture PEFB (3333.3 kg/h)

Phase	**Yield (wt %)**		
Solid (Char and Ash)	15		
Liquid (Bio-oil)	70		
Gas	12		
Ash	3		
Component	**Mass Fraction**	**Component**	**Mass Fraction**
Acetic acid	0.046	Levoglucosan	0.023
Formaldehyde	0.051	Palmitic acid	0.005
Acetaldehyde	0.005	H_2	0.006
2-butanol	0.005	CH_4	0.003
Furfural	0.083	CO	0.061
Phenol	0.005	CO_2	0.051
Creosol	0.018	C (char)	0.12
Guaiacol	0.074	Ash	0.03
Catechol	0.152	H_2O	0.24

Phase Separation (BLOCK ID – SOLIDSP1, S-SEP2 and SEP-1)

Hot pyrolysis vapour/solid mixture passes through two solid separators to recover the solid (char and ash) before condensation and eventual separation into non-condensable gases (NCG) and bio-oil. This two-stage solid separation ensures almost complete removal of char. The first separator (***SOLIDSP1***) is modelled as a cyclone operating with a 90% solid recovery while the second operates as an Electrostatic Solid Separator (ESP), (***S-SEP2***). The vapour leaving the ESP, (***VAP-1***) has a char concentration of less than 1%. In reality, systems attaining such high efficiencies in char recovery are difficult to design leaving some char to collect in the bio-oil produced. NCG and bio-oil separation occurs in a two-step process involving cooling to 30 °C (***HX1*** and ***C1***) followed by two phase flash separation in the ***SEP-1*** block.

Reforming (BLOCK ID – REFORMER)

The recovered bio-oil (***BIOOIL-1***) is pumped to 3 bar, preheated to 120 °C and sent to an adiabatically operated reformer (***REFORMER***) together with superheated steam and compressed air. All heat exchangers are set to operate with a minimum temperature of approach of 20 °C. Autothermal reforming was simulated using the Aspen RGibbs reactor operating at 3 bar for the base case. The RGibbs reactor calculates the equilibrium composition by using the Gibbs minimisation method. This method determines equilibrium product composition without knowing the particular chemical reactions involved by minimising the Gibbs free energy of a fixed reacting system (see Chapter 4). The amount of oxygen (in air) and steam needed for ATR were determined using separate calculator blocks (see Appendix A). The air equivalence ratio (λ) varied from 0.23 to 0.36 (Eq. 6.3) while the molar steam to carbon (S/C) ratio was varied from 1 to 3 (mol steam input/mol carbon in bio-oil). Air used for ATR is preheated to 150 °C (***RAIR-3***) while the steam enters the reformer at 500 °C (***RH2O-5***). The equilibrium temperature attained in the reactor ranged between 600 and 900 °C depending on the S/C ratio and λ.

Water Gas Shift (BLOCK ID – SHIFT)

The reformate is cooled to 250 °C and then sent to a CO-shift reactor (***SHIFT***), modelled as an isothermal RGibbs reactor, operating at 3 bar and 250 °C, where more hydrogen is formed via the WGS reaction. A list of possible products from the shift reactor was created and comprised of CO, CO_2, H_2, H_2O, N_2 and CH_4. CH_4 was set as an inert gas and the temperature approach to equilibrium was set at 0 °C. CO conversion in the shift reactor reached 95%.

H_2 Recovery (BLOCK ID – SCRUBBER, STRIPPER, PSA)

Hydrogen rich syngas from the shift reactor is cooled down and moves to either an HPWS system or a PSA unit where hydrogen recovery occurs. Based on these two hydrogen separation technologies we define two processes; the pyrolysis and autothermal reforming process with hydrogen separation by HPWS (‘PAWS process’) and the pyrolysis and autothermal reforming process with hydrogen separation by PSA (‘PAPS process’). Effective H_2 recovery by both processes depends mostly on the operating pressure. The HPWS hydrogen purification system consists of a scrubber column (***SCRUBBER***) having between 10 to 15 equilibrium stages with pressurised scrubbing water entering above the top stage and feed gas at the bottom stage at the same pressure (10 bar for the base case). Water is condensed out from the cooled product gas leaving the shift reactor and this ‘dry’ gas is compressed to 10 bar (***COMP-2***) and sent to the scrubber. Gas-liquid interactions and Henry’s coefficients were determined using the ELECNRTL property method. Cozma et al. (2013) validated the use of this thermodynamic model in their simulation of biogas upgrading using a HPWS. A design block calculates the amount of scrubbing water needed to achieve a target of 97 mol% hydrogen purity for the output stream. Spent water from the scrubbing column enters a flash separator (***SEP-3***) where its pressure is reduced, inducing desorption of the soluble gases before moving into a stripper column (***STRIPPER***) where the water is regenerated using air and recycled as WPA. To avoid gas and impurity build up in the HPWS system some of the water leaving the stripper is purged while a corresponding amount of make-up fresh water (FWF) is added at the top of the scrubber.

Alternatively, a PSA unit is used to purify the syngas leaving the shift reactor. The hot syngas is cooled down to 40 °C to condense and remove any water before being compressed to 10 bar (for the base case). The compressed gas is cooled down to 30 °C and all moisture removed using a phase separator (***SEP-3***) before it enters the PSA unit. The presence of water is known to negatively affect the functioning of a PSA unit (Martin et al., 2016). Typical PSA hydrogen recovery can range from 50 to about 85% (Martin et al., 2016, Sarkar and Kumar, 2010). For this simulation, the PSA unit is implemented using a splitter block (***PSA***) which separates the incoming syngas into two streams comprising of pure hydrogen (during adsorption) and off-gases (during desorption and purging). Depending on pressure, hydrogen recoveries of 75%, 85% and 90% are achieved for PSA units operating at 10, 20 and 30 bar respectively. To improve the hydrogen yield for the base case simulation, reforming and shift reactions occur at 3 bar but the hydrogen separation is carried out at 10 bar.

Combustion (BLOCK ID – COMBUST)

Char and ash obtained after pyrolysis and solid separation, together with NCG are all burned in a combustor to deliver heat energy across the plant. For this simulation, an isothermal RStoic reactor (***COMBUST***) is used to generate combustion products. Combustion air (***CAIR-1***) is preheated to 250 °C with flue gas before being fed to the combustor. A design block computes the amount of excess air needed for complete and efficient char and NGC combustion. Excess air was varied between 20 to 70% in order to adjust the combustor enthalpy and temperature and provide the energy required for biomass pyrolysis (heat steam P-HEAT). Further energy recovery was achieved by cooling the flue gas produced. The recovered heat was used mainly to preheat air for feedstock drying or generate steam for electricity production in the case where a combined heat power system was used.

***Combined Heat and Power (CHP)* (**not included in basic simulations shown in Figure 5.3 and Figure 5.4**)**

Combined heat and power (or co-generation) is the simultaneous generation of heat and power achieved by using waste heat from steam for process heating and/or for space (district) heating. The generation of heat and power using steam as the working fluid is based on the steam turbine (Rankine) cycle. This cycle consists essentially of four main components: boiler, turbine, condenser and recycle pump. Figure 5.5 shows the basic configuration of an ideal steam turbine CHP plant. Fuel combustion takes place in the boiler where the hot flue gas is used to generated superheated steam. The boiler is designed to raise the pressure of the steam produced to a desired value. The high pressure superheated steam is then expanded through a turbine connected to an electric generator to generate electricity. The exit low pressure steam from the turbine is used for process heating and then cooled in the condenser to obtain water which is pumped back to the boiler.

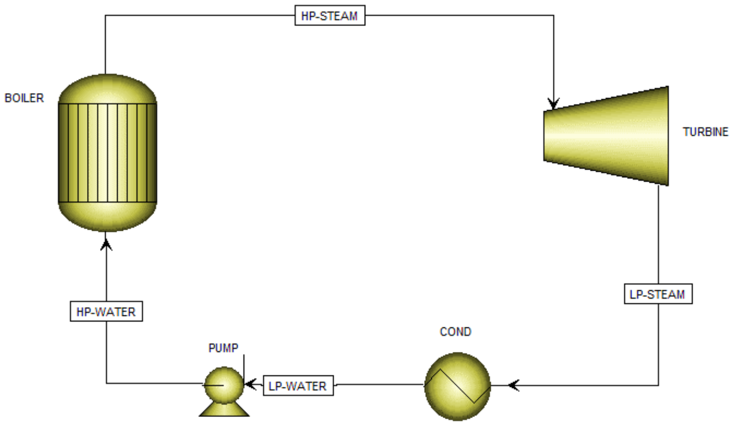

Figure 5.5 Simplified flow diagram of a steam turbine CHP plant (LP-low pressure, HP-high pressure, COND-condenser)

The mechanical work generated by the turbine depends on how much reduction in steam pressure can be attained. Ideal turbine inlet conditions for viable power generation are 42 bar/400°C or 63 bar/480°C (COGEN-Europe and INESTENE, March 2001). Based on the pressure of the outlet steam, steam turbines can be classified as back-pressure turbines (BPT) or condensing extraction turbines (CET).

BPTs are designed for steam to exit as a saturated or superheated vapour at a pressure higher than atmospheric and with enough heat to satisfy process requirements. Such turbines are ideal for plants whose primary aim is to produce heat not electricity. The main advantages of a BPT are that it has a simple configuration, relatively inexpensive and requires less cooling water. Its main disadvantage is that it is not flexible and designed to function properly on a specific thermal load and steam property (temperature and pressure). In a CET, steam expands in a first stage similar to BPT, thereafter, some steam is extracted (passed-out) and used for process heating. The remaining steam is simultaneously expanded and cooled in an integrated condenser and exits at a pressure well below atmospheric. Steam expansion to condensation and below vacuum ensures that a CET delivers more power than the BPT. The condenser temperature, which can be water or air cooled, determines the turbine exit steam pressure. CET are suitable for processes with lower heat-to-power ratio, 2 – 10 (kW/kW), compared to BPT which are suitable for processes with heat-to-power ratios ranging from 4 to 14 (BEE). The main advantage of CET is that they produce more electricity compared to BPT as steam is expanded down to vacuum. Another advantage is their flexibility and ability to regulate their thermal and electricity loads based on the changing needs of the process (EPA-CHPP, 2015). CETs are more complex and expensive to design and install and can have lower efficiencies as most of the waste heat removed during condensation is not at temperatures suitable for process or district use. Depending on the type of turbine used as part of CHP unit, the prefixes BT and CT are used to distinguish processes using a BPT or CET respectively. For example, **PAWS-BT** is short for pyrolysis and autothermal reforming process with hydrogen separation by HPWS using a BPT**;** and **PAPS-CT** is short for pyrolysis and autothermal reforming process with hydrogen separation by PSA using CET.

5.2.2.6 CO_2 emission (environmental impact)

Most of the hydrogen produced industrially is obtained from fossil fuels mainly natural gas, coal and other petroleum liquid products with natural gas (methane) SR alone contributing about 50% (Ewan and Allen, 2005). To estimate the CO_2 savings and environmental impact advantage gained by using PEFB biomass as a source of hydrogen, a complete lifecycle assessment (LCA) needs to be performed and the results compared to that of the more tradition fossil fuel based processes. A full LCA is beyond the scope of this work. Instead a simpler approach is adopted in which the effect on the environment of producing an equivalent amount of hydrogen by SR of natural gas (methane) as fuel is considered. It is also assumed that any net electrical power or heat generated by the PEFB based processes could have been produced by one using methane as energy source and an equivalence is determined based on current energy conversion efficiencies. The CO_2 emission savings therefore corresponds to that eliminated by substituting a fossil fuel, natural gas in this case, with biomass as feedstock for hydrogen production.

The net CO_2 emission for the PEFB biomass based processes is considered to be very low, almost zero. This overly simplified calculation of CO_2 savings assumes that no fossil fuel or input is used for biomass planting, harvesting and storage i.e. all CO_2 released by the plant is reabsorbed during subsequent regrowth of the oil palm plant (Larson et al., 2001). The total greenhouse gas emissions (mostly CO_2) from a process will depend on its size and configuration (extent of heat integration). A complete LCA takes into account the source, storage and transportation facilities needed to make the natural gas available on-site for processing.

Several authors have published data on the CO_2 emissions associated with hydrogen production by steam reforming of natural gas (methane). Spath and Mann (2000) performed a LCA for a 1.5 million Nm^3/day (5600 kg/h) capacity natural gas SR plant. They determined the total greenhouse gas emissions (GHG), expressed in CO_2-equivalent, associated with plant operations and electricity generation to be 9.17 kg CO_2/kg H_2. Ewan and Allen (2005) in their assessment of various routes to hydrogen production based their calculation on a CO_2 emission of 55 kg CO_2/GJ of natural gas fuel energy. This value corresponds to 10.08 kg CO_2/kg H_2; assuming 0.66 MJ of H_2 is produced per MJ of natural gas (Spath and Mann, 2000). Granovskii et al. (2007) evaluated the impact on GHG emissions by replacing fossil fuels with renewable energy for hydrogen and electricity production. Their study was based on a CO_2 emission of 75.7 g CO_2/MJ H_2. This corresponds to 9.15 kg CO_2/kg H_2. In light of the aforementioned studies, a CO_2 emission from a methane SR plant was taken to be 9.5 kg/kg of H_2 for this study. The CO_2 emissions for net electricity generation/consumption by a process is taken as 149.9 g CO_2/ MJ for a thermal plant operating at 40 % efficiency (Granovskii et al., 2007). Heat exported as steam is assumed to be generated by a natural gas fired boiler operating at 75% efficiency. Natural gas LHV is taken as 47.13 MJ/kg and the amount of CO_2 emitted during combustion is obtained from the balanced equation using the stoichiometric ratio 2.74 kg CO_2/ kg CH_4. This corresponds to a CO_2 emission of 58.3 g CO_2/MJ of natural gas. Ewan and Allen (2005) used a reference CO_2 emission of 55 g CO_2/MJ of natural gas in their assessment of various routes of hydrogen production.

5.2.3 Equations

The air equivalence ratio, λ, is calculated as

$$\lambda = \frac{AFR_{actual}}{AFR_{stoic}} \qquad 5.3$$

Where AFR_{actual} is the air to fuel ratio considered and AFR_{stoic} is the stoichiometric air to fuel ratio for complete combustion.

Hydrogen yield, Y_{H_2}

$$Y_{H_2} = \frac{\dot{m}_{H_2}}{\dot{m}_{BM}\ (10\%\ moisture)} \times 100 \qquad 5.4$$

Water Conversion

$$X_{H_2O} = \frac{\dot{m}_{H_2O}(in) - \dot{m}_{H_2O}(out)}{\dot{m}_{H_2O}(in)} \times 100 \qquad 5.5$$

Water efficiency

$$\eta_{H_2O} = \frac{\dot{m}_{H_2}}{\dot{m}_{H_2O}(in)} \times 100 \qquad 5.6$$

Biomass-to-bio-oil conversion efficiency

$$\eta_{BM} = \frac{\dot{m}_{BO}.LHV_{BO}}{\dot{m}_{BM}.LHV_{BM}} \times 100 \qquad 5.7$$

The hydrogen (thermal) efficiency, η_{H_2}, was determined by comparing the LHV of hydrogen produced to the LHV of both biomass (BM) and bio-oil (BO) as feed. The LHV of biomass is assumed to be 11 MJ/kg (Quaak et al., 1999). Meanwhile that for the bio-oil generated by the simulation was similar to the formulated bio-oil surrogate whose LHV was dertermined using bomb calorimetry to be 16.6 MJ/kg (see Table 5.4)

$$\eta_{H_2(BM)} = \frac{\dot{m}_{H_2}.LHV_{H_2}}{\dot{m}_{BM}.LHV_{BM}} \times 100 \qquad 5.8$$

$$\eta_{H_2(BO)} = \frac{\dot{m}_{H_2}.LHV_{H_2}}{\dot{m}_{BO}.LHV_{BO}} \times 100 \qquad 5.9$$

The mechanical work produced by a turbine is calculated as

$$\mathrm{W}_i = \dot{m}_T \times \frac{1}{s_T} \times \eta_T \qquad 5.10$$

Overall process efficiency, η_{pr}, is calculated using the following equation

$$\eta_{pr} = \frac{\dot{m}_{H_2}.LHV_{H_2} + (\dot{P}^+) + (\dot{Q}^+)}{\dot{m}_{PEFB}.LHV_{PEFB} + (\dot{P}^-) + (\dot{Q}^-)} \times 100 \qquad 5.11$$

$$(\dot{P}^+)\ or\ (\dot{P}^-) = \dot{W} - \dot{E} \qquad 5.12$$

$$(\dot{Q}^+)\ or\ (\dot{Q}^-) = \dot{H}_{re} - \dot{H}_{pr} \qquad 5.13$$

Where

$\eta_{H_2(BM)}$ Hydrogen efficiency calculated using biomass (PEFB) as input fuel

$\eta_{H_2(BO)}$ Hydrogen efficiency calculated using bio-oil as input fuel

$\dot{m}_{H_2}$is the mass flow of the hydrogen gas product, kg/h;

$\dot{m}_{PEFB}$ is the mass flow of PEFB, kg/h;

$\dot{m}_{H_2O}$ is the mass flow of water, kg/h;

LHV is the lower heating value (for H_2, bio-oil or biomass), kW-h/kg;

$\dot{m}_T$ is the steam flow into the turbine, kg/h;

W$_i$ is the isentropic work generated by a turbine, kW;

S_T is the specific steam consumption of the turbine, kg/kW-h

η_T is the isentropic efficiency of the turbine;

$(\dot{P}^+)\ or\ (\dot{P}^-)$ correspond to the net power/electricity generated or demanded by the process (MW). This term appears only once in the equation; either as a numerator, $(\dot{P}^+)$, in case of net (positive) work or power generation or as a denominator, $(\dot{P}^-)$, in the case of net (negative) electricity consumption by the process;

$(\dot{Q}^+)\ or\ (\dot{Q}^-)$ correspond to the net heat produced or required by the process (MW). This term appears only once in the equation; either as a numerator, $(\dot{Q}^+)$, in case of net (positive) heat produced or as a denominator, $(\dot{Q}^-)$, in the case of net (negative) heat required by the process;

$\dot{W}$ is the total mechanical work generated by the process, MW;

$\dot{E}$ is the electrical energy needed to power all electrical equipment, MW;

$\dot{H}_{re}$ is the residual heat recovered from cooling the dryer exit stream, MW;

$\dot{H}_{pr}$ is the required process heat obtained by adding heat demand for heater H1 and H1, MW (Figure 5.3 and Figure 5.4);

The thermal efficiency of the process depends greatly on the pyrolysis and reforming steps. The choice of pyrolysis products makes any inference on the thermal efficiency of this process design very subjective. Care was taken to consider the available literature on PEFB pyrolysis in order to develop a model representing a typical fixed bed reactor pyrolysis yield.

5.3 Results and Discussion

5.3.1 Influence of Steam and Air flow

5.3.1.1 Hydrogen yield

Figure 5.6 shows the effect of increasing the S/C ratio on the hydrogen yield (Eq. 5.4) on both the PAWS and PAPS processes for the base case simulation. The equivalence ratio for this plots correspond to the amount of oxygen required for stoichiometric partial oxidation of bio-oil (determined according to the POX equation, Eq. 2.11) and is calculated to be λ = 0.25. Under this condition, there is just enough oxygen present to convert all the carbon (C) in the biofuel to CO without hydrogen (H) oxidation and no side reactions (Krumpelt et al., 2002). As expected, increasing the S/C ratio resulted in an increase in hydrogen yield.

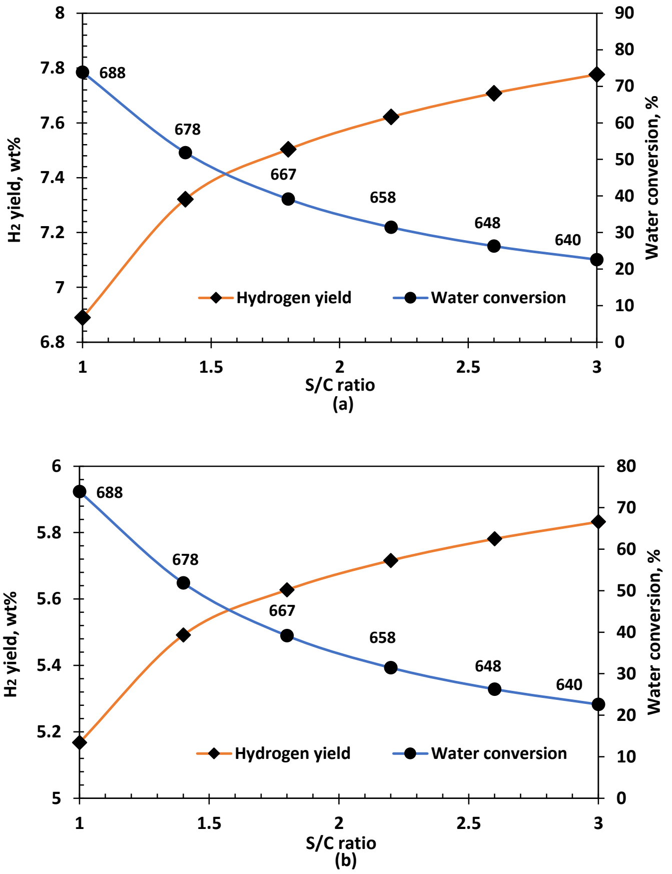

Figure 5.6 Influence of the amount of steam, expressed as S/C ratio, on hydrogen yield for equivalence ratio, λ = 0.25. For the base case, ATR and shifting occur at 1 bar and H_2 recovery is carried out at 10 bar a) PAWS process b) PAPS process. Temperature values are included as data labels in plots.

This increase in hydrogen is due to two factors. Firstly, the presence of more water molecules with increasing S/C ratio compounded with the slight reduction in the equilibrium temperature (from about 690 °C to 640 °C) promotes the WGS reaction in the reformer. The second effect is similar to the first but occurs in the shift reactor where the presence of more water molecules pushes the WGS equilibrium to the right forming more H_2 and CO_2. Figure 5.6 also shows that water conversion reduces form an initial value of 70%, at S/C = 1, to about 20% at S/C =3.

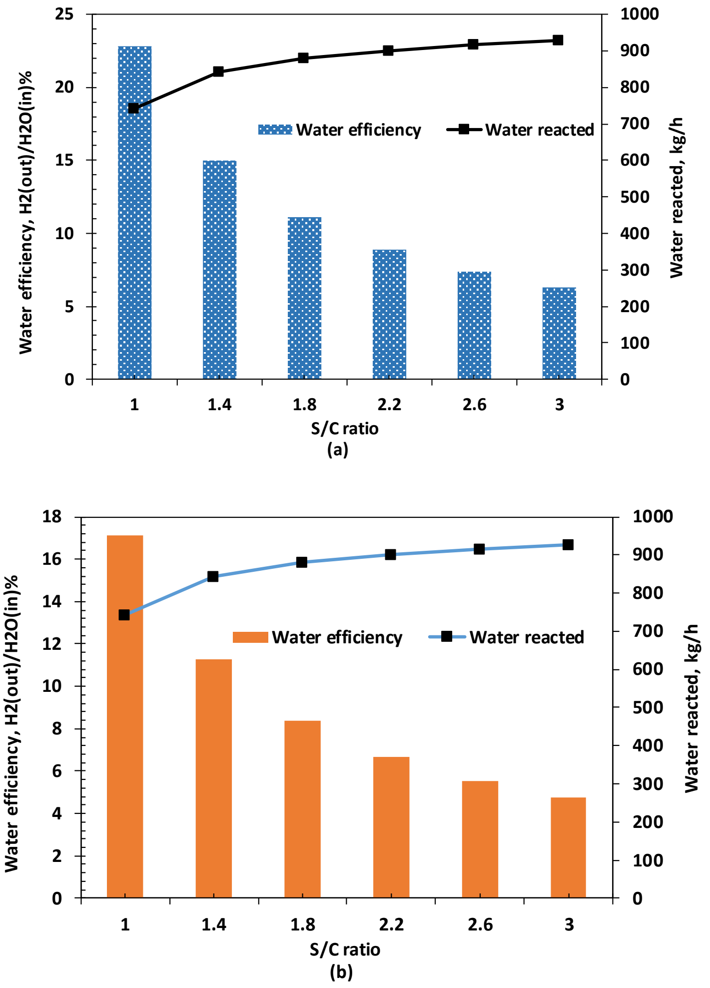

Figure 5.7 Influence of S/C ratio on water conversion efficiency at λ = 0.25. For the base case, ATR and shifting occur at 1 bar and H_2 recovery is carried out at 10 bar a) PAWS process b) PAPS process.

The initial benefit of having more water in the system almost ceases at S/C ratios greater than 2.5. This effect is emphasised further in Figure 5.7 which shows a decrease in water efficiency (Eq. 5.6) and an almost levelling-off of the actual amount of water reacted as S/C ratio increases from 2.2 to 3. In a typical isothermal steam reforming processes, high S/C ratios help prevent the formation of catalytic coke (Martin et al., 2015). This is not necessarily the case for an adiabatic ATR processes as the high steam content lowers the equilibrium temperature and might instead have the undesirable effect of promoting coke formation reaction while deactivating coke gasification reactions. Working at very high

S/C ratios also makes a process more energy intensive and increases the cost of the H_2 or syngas produced. Based on Figure 5.6 and Figure 5.7, the maximum S/C ratio to consider when operating an efficient ATR process should at or below 3. Moreover, above this value, an external fuel source will surely be required to generate the excess steam leading to a more complex heat exchange network and larger downstream separation equipment. The water conversion and water efficiency shown in Figure 5.6 and Figure 5.7 are almost the same; this is because under the equilibrium conditions considered, H_2 gas formation has a very high selectivity compared to other H containing products such as CH_4 and C_2H_6. This might not necessarily be the case for a real life kinetic-driven process.

5.3.1.2 Dry gas composition (reformate)

One advantage of ATR is the variability in product gas composition achieved by changing process variables such as air equivalence ratio λ, S/C ratio and temperature (Holladay et al., 2009). Figure 5.8 shows the nitrogen-free dry gas reformate product obtained by varying the S/C ratio from 1 to 3 for four different λ values. As mentioned in the previous section, increasing the S/C ratio increases the H_2 yield. This also has a concomitant effect on CO_2 while the amounts of CO and CH_4 (when thermodynamically possible) decrease.

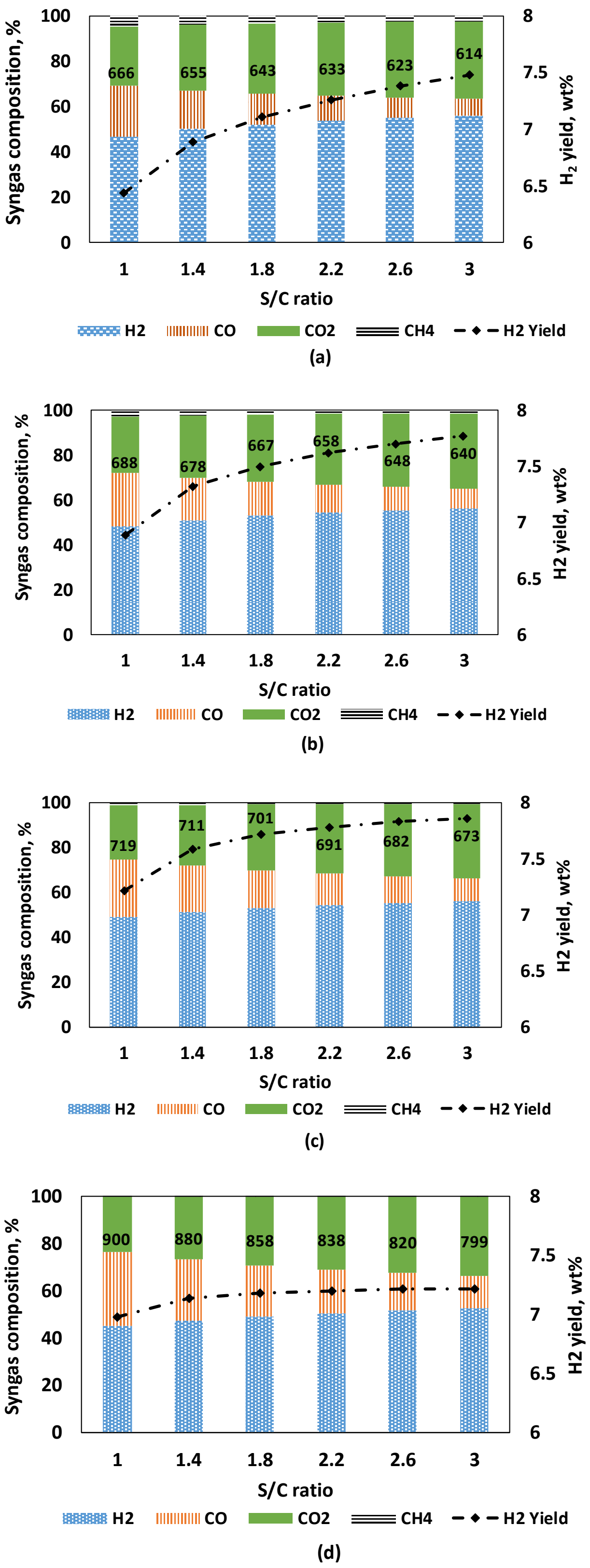

Figure 5.8 Syngas yield on a dry nitrogen-free basis for PAWS and PAPS processes. For the base case, ATR and shifting occur at 1 bar and H_2 recovery is carried out at 10 bar a) λ = 0.23 b) λ = 0.25 c) λ = 0.28 d) λ = 0.36

It is also discernible from Figure 5.8 that for the same S/C ratio, the H_2 yield decreases as the amount of oxygen (ATR air expressed as λ) increases. If the amount of oxygen present in the reactor feed (fuel and air) is lower than that required to convert all C in the fuel to CO ($\lambda < 0.25$ in this case), then H_2 yield will be lower than the possible maximum. The H_2 yield peaks at $\lambda = 0.28$ (7.9 wt%, S/C = 3 for the PAWS process) then starts decreasing as more O_2 (air) is added to the reformer due to increase oxidation of fuel to CO_2 and H_2O.

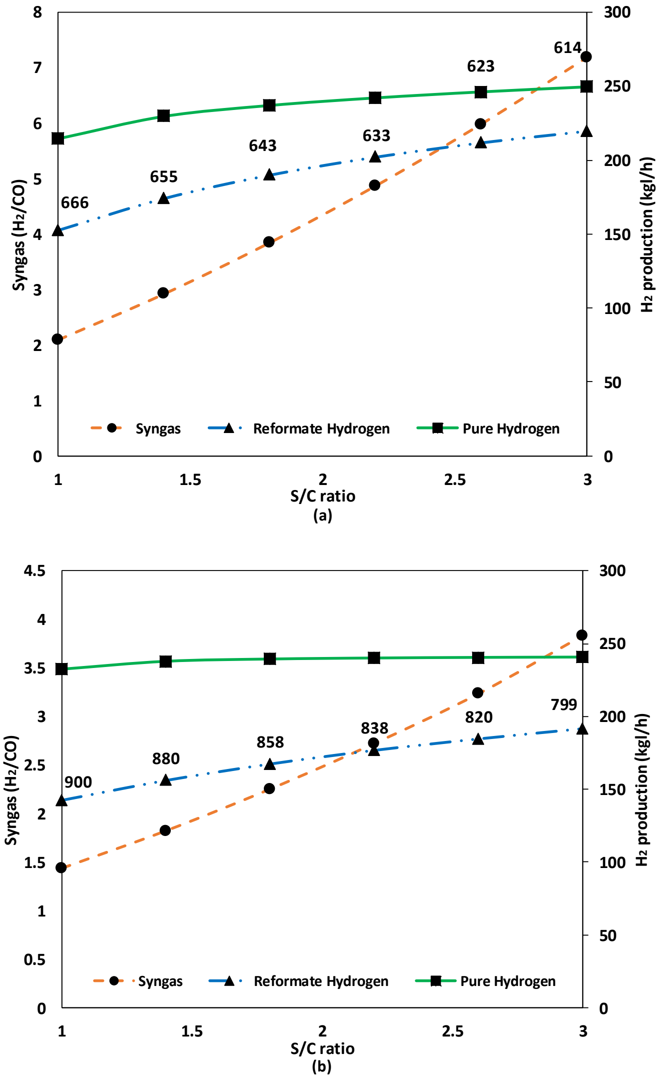

Figure 5.9 Effect of S/C ratio and equivalence ratio on syngas composition expressed as H_2/CO. For the base case, ATR and shifting occur at 1 bar and H_2 recovery is carried out at 10 bar for ATR process using air and HPWS. a) $\lambda = 0.23$. b) $\lambda = 0.36$

As seen on Figure 5.9 different syngas composition (expressed as the H_2/CO ratio) can be obtained depending on the S/C ratio and λ. For the different combinations of air and water considered for this simulation, H_2/CO ratio varied from 2 to 7 (at $\lambda = 0.23$) and from 1.5 to 4 (at $\lambda = 0.36$) after reforming (before shifting). The reformate in this case can be used either directly or after upgrading as feed for synthesising chemicals such as methanol, dimethyl ether (DME), ammonia and other liquid fuels. Such chemical syntheses are achieved either by direct combination or by Fischer Tropsch synthesis. As already discussed in Chapter 4 (section 4.4.3.2), different chemicals have different feed requirements with $H_2/CO = 2$ for Gas-to-Liquid Fischer Tropsch processes and $H_2/CO = 1$ for higher alcohol syntheses (Rostrup-Nielsen et al., 2002c, Aasberg-Petersen et al., 2011, Wilhelm et al., 2001b). The maximum value of M (module) obtained for this simulation was 0.54 for $\lambda = 0.25$ and S/C = 3. The syngas obtained in this simulation will require an addition of pure H_2 to meet the feed requirement for synthesising methanol and dimethyl ether.

5.3.1.3 Hydrogen (thermal) efficiency

One parameter used to evaluate reforming processes is the hydrogen (thermal) efficiency (Eq. 5.8 and 5.9). Figure 5.10 shows the effect of varying steam and oxygen (air) on the hydrogen efficiency using PEFB biomass and bio-oil as starting fuels for the PAWS process. Overall, the hydrogen efficiency increases with increase in S/C ratio. This increase is expected as more hydrogen is produced via the WGS and steam reforming reactions. Varying the equivalence ratio has both a positive and negative effect on the hydrogen efficiency. In all, increasing λ, from say a value of 0.23 leads to an increase hydrogen efficiency up to a maximum value (at λ_{opt}) after which any further increase in λ results in drop a in hydrogen efficiency. λ_{opt} is the optimum equivalence ratio occurring for a given S/C ratio and corresponds to both maximum hydrogen efficiency and hydrogen yield. The value for λ_{opt} reduces as more steam is added; going from 0.31 to 0.27 as the S/C ratio increases from 1 to 3. Being an adiabatic process, a minimum amount of energy is required to get the reforming reactions going. This energy comes from the partial oxidation of bio-oil, which is favoured as more oxygen is added to the reformer. The reformer eventually gets to the point (beyond λ_{opt}) where the addition of oxygen favours the production of CO_2 and H_2O over CO and H_2 (Martin and Wörner, 2011). A maximum hydrogen efficiency of 82 % and 57% is obtained for a process using PEFB bio-oil and biomass respectively as primary feedstock for hydrogen production (Eq. 5.8 and Eq. 5.9 respectively). These hydrogen efficiencies are for the high hydrogen producing PAWS process, consequently the values will be lower for a PAPS process.

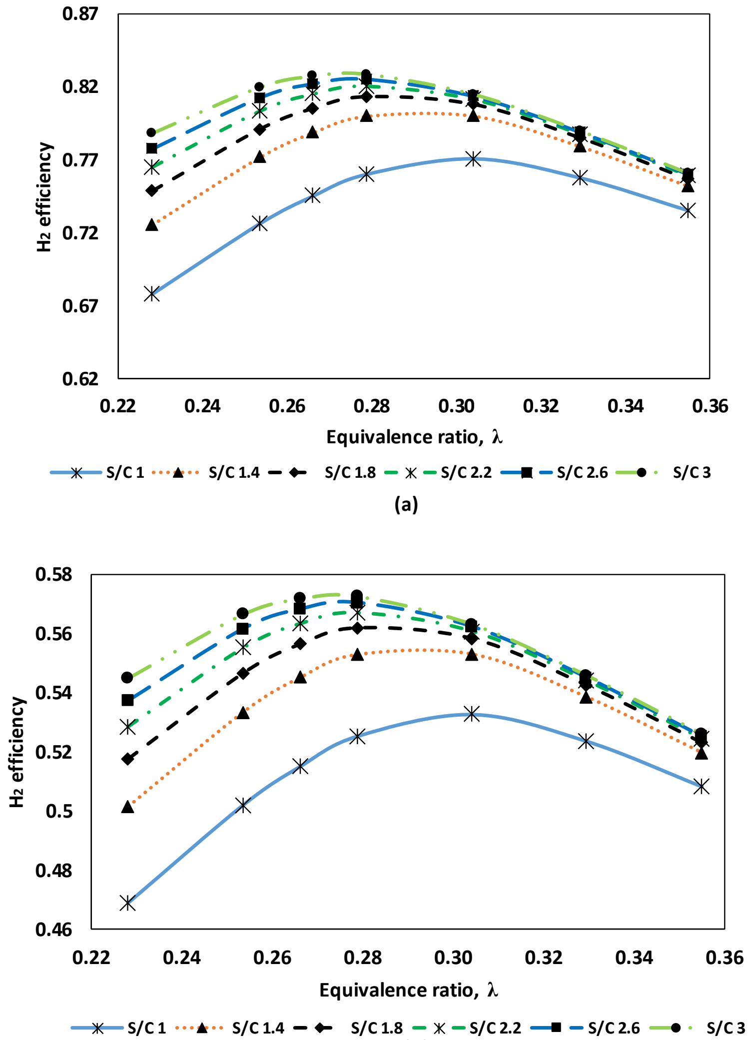

(a)

(b)

Figure 5.10 Hydrogen efficiency for different equivalence ratios and S/C ratios for the PAWS processes. For the base case, ATR and shifting occur at 1 bar and H_2 recovery is carried out at 10 bar (a) Using bio-oil (LHV 16.6 MJ/kg) as starting material (Eq. 5.8) (b) Using Wet PEFB (40% moisture, LHV 11 MJ/kg) as starting material (Eq. 5.9).

Considering the 75% H_2 recovery for bases case PAPS process, the hydrogen efficiency will reduce to 62% (Eq. 5.8) and 43% (Eq. 5.9) with respect to using bio-oil and biomass as input fuel. In both cases, the hydrogen efficiency calculated using PEFB biomass as input fuel is quite low because the LHV of char and NGC obtained during pyrolysis are not included in the calculation since these two products do not directly contribute to the amount of hydrogen produced. Martin and Wörner, 2011 obtained maximum hydrogen efficiencies of 85.6% and 84.6% for their simulation of an ATR process using biodiesel and bioethanol respectively as fuel.

5.3.2 Process efficiency

The overall process efficiency is determined for a process with a heat integrated network designed using pinch analysis. Pinch analysis has been demonstrated to enhance heat integration by reducing the energy requirement (cold and hot utilities) of a process (Bao et al., 2010). The following steps are implemented as outlined in the pinch analysis methodology presented by Kemp (2007):

- Perform mass and energy balance.
- Extract stream data and calculate heat loads and heat capacities.
- Plot hot and cold composite curves and determine the minimum utility requirements.
- Draw network grid diagram to achieve maximum energy recovery.
- Redesign network grid and identify the heat exchanger network that achieves the optimal heat integration from both operational and economic point of view.

Once the pinch analysis was completed, the energy required by other process operations/equipment was determined and the overall process efficiency was then calculated using Eq. 5.11.

5.3.2.1 Mass Balance and Energy balance

The base case examined for this simulation is a 5000 kg/h PEFB biomass capacity plant with 40% initial moisture. The mass balances for PAWS and PAPS process are shown in Figure 5.11 and Figure 5.12 respectively. Pre-treatment and combustion occur at 1 bar while ATR and shifting are carried out at 3 bar and hydrogen separation at 10 bar.

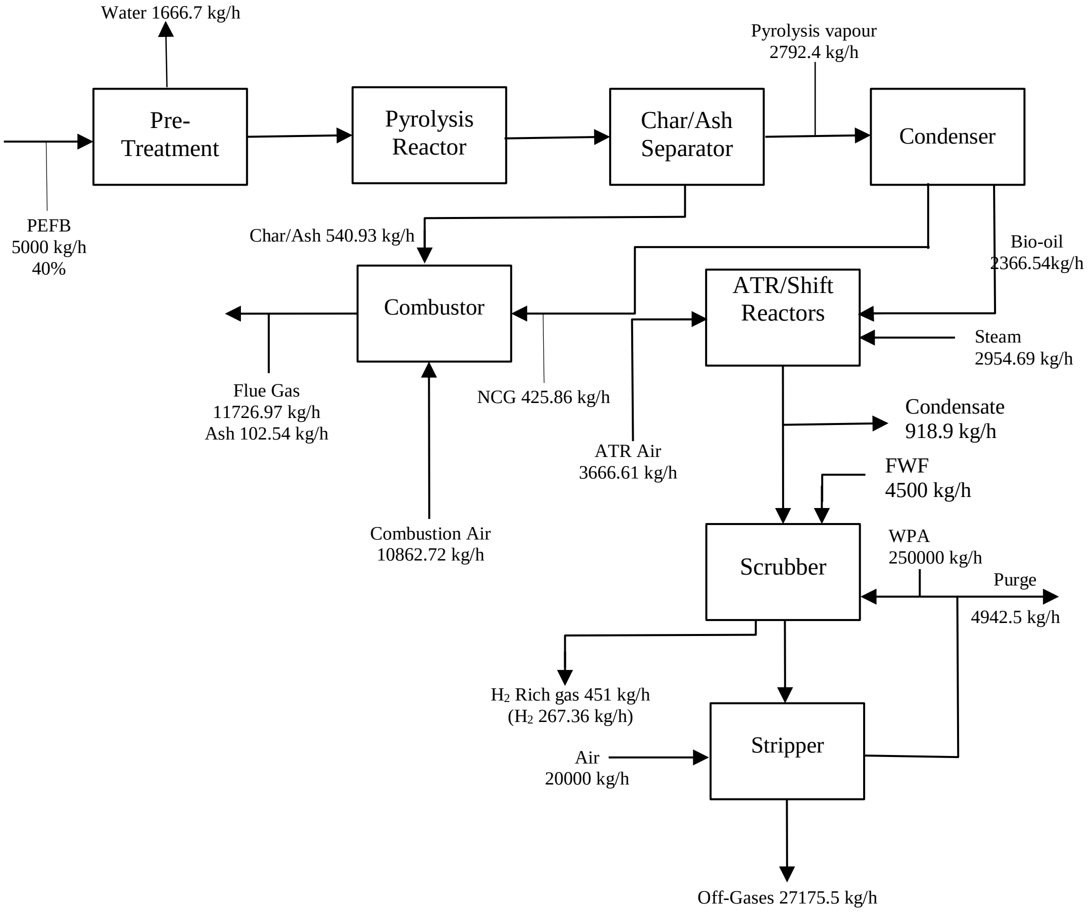

Figure 5.11 Mass balance for a 5000 kg/h biomass PAWS process plant with almost all hydrogen recovered as 97 mol% H_2-rich product gas at 10 bar. S/C = 2.2, λ = 0.28

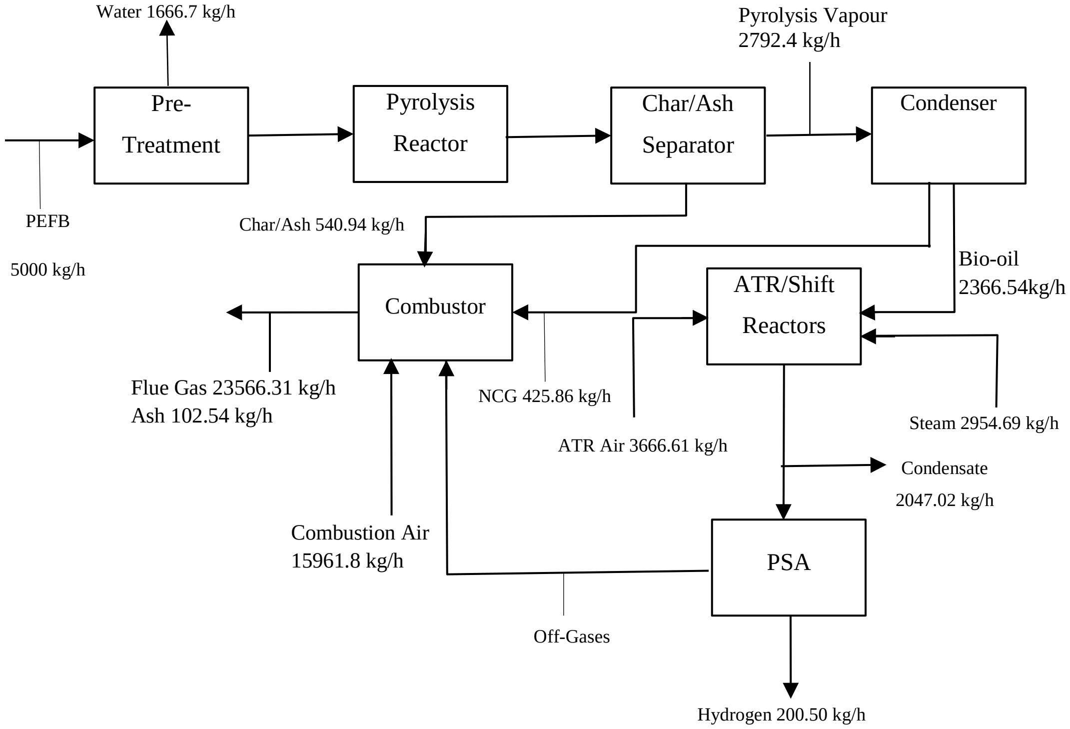

Figure 5.12 Mass balance for 5000 kg/h biomass PAPS process plant with 75 % H_2 recovered as pure gas at 10 bar. S/C = 2.2, λ = 0.28

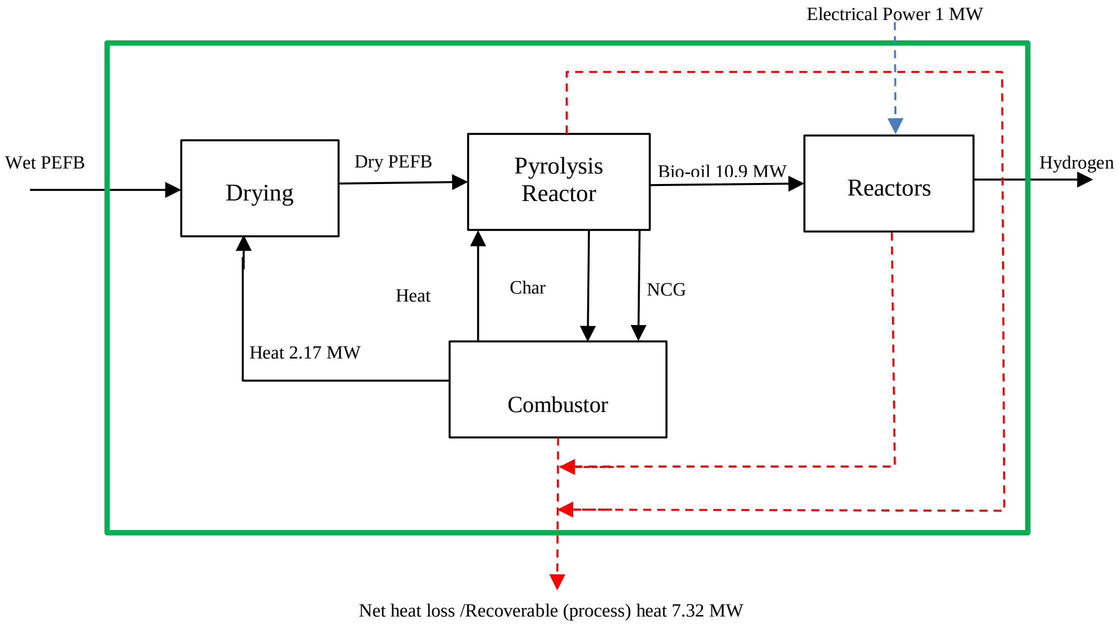

Figure 5.13 Energy balance based on LHV for 5000 kg/h biomass PAWS process plant with almost all hydrogen recovered as 97 mol% H_2-rich product gas at 10 bar. S/C = 2.2, λ = 0.28

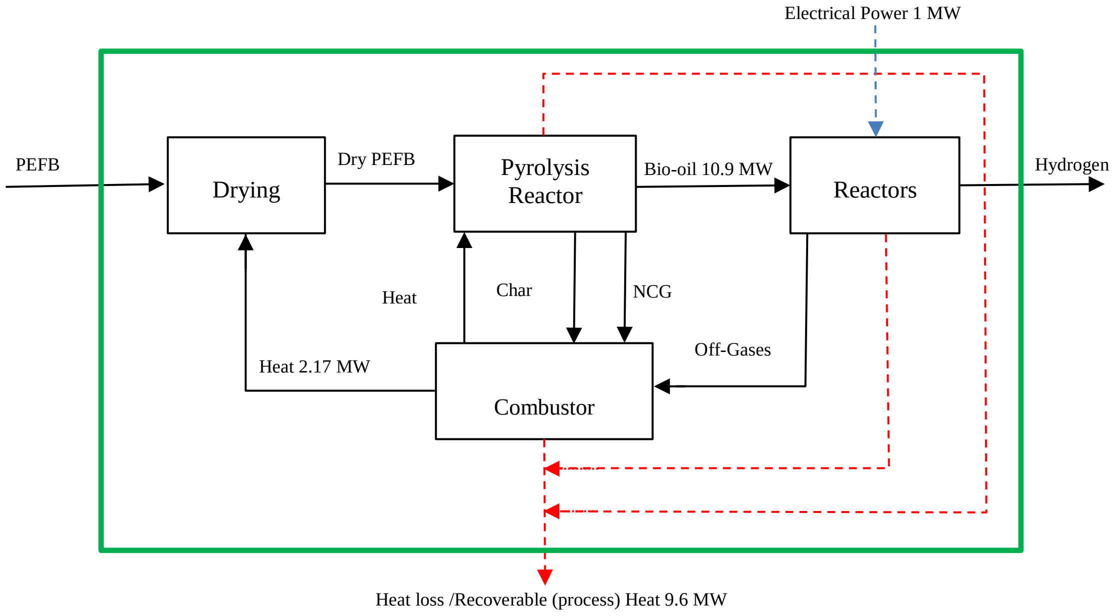

Figure 5.14 Energy balance based on LHV for 5000 kg/h biomass PAPS process plant with 75 % H_2 recovered as pure gas. S/C = 2.2, λ = 0.28

Figure 5.13 and Figure 5.14 summarise the energy balance based on LHV for the base case. The total heat loss and recoverable heat for the PAPS process is significantly larger than that for the PAWS process as 25 % of hydrogen produced in burnt in the combustor.

5.3.2.2 Composite Curves and Grand Composite Curves

Aspen Energy Analyzer software was used to perform the next steps in the pinch analysis process. Table 5.8 shows a list of all streams (hot and cold) used for the pinch analysis. To facilitate heat recovery and generate electricity, the hot air stream used for biomass drying in the non-heat-integrated simulation (Figure 5.3 and Figure 5.4) is replaced with water which becomes superheated as it cools other hot streams. Stream data was extracted directly from Aspen. This was done by the direct heating/cooling of streams from their source temperature (T_s) to the required target temperature (T_t) and noting their change in enthalpy. No other external thermodynamic property library was consulted to determine heat capacities of the process streams considered. Some streams were divided in order to take phase change into account and to facilitate identification of the pinch.

Table 5.8 List of all hot and cold streams considered in Pinch Analysis

Stream	Name	Type	Source (T_s), °C	Target (T_t), °C	Heat Capacity, CP, kW/°C	Heat load, MW	Mass flow, kg/h
1	VAP-1	Hot	500	200	1.517	0.455	2792.4
2	LIQVAP-1	Hot	200	30	4.600	0.782	2792.4
3	REF	Hot	692	250	4.319	1.909	8987.8
4	SHIFT-1	Hot	250	94	4.128	0.644	8987.8
5	SHIFT-2	Hot	94	30	25.359	1.623	8987.8
6	FLUE-1	Hot	1100	115	3.800	3.743	11829.5
7	BIOOIL	Cold	30	120	3.278	0.295	2366.5
8	RH2O-1	Cold	20	133.5	4.150	0.471	2954.7
9	RH2O-2	Cold	133.5	133.6	17750	1.775	2954.7
10	RH2O-3	Cold	133.6	500	1.711	0.627	2954.7
11	RAIR	Cold	139	150	1.038	0.135	3666.6
12	CAIR	Cold	20	250	3.087	0.71	10862.7
13	DH2O-1	Cold	20	250.4	6.506	1.499	5400
14	DH2O-2	Cold	250.4	250.5	25690	2.569	5400
15	DH2O-3	Cold	250.5	400	4.167	0.623	5400
6*	FLUE-1	Hot	1100	115	6.521	6.423	19694.4
13*	DH2O-1	Cold	20	250.4	14.215	2.273	8192
14*	DH2O-2	Cold	250.4	250.5	38970	3.897	8192
15*	DH2O-3	Cold	250.5	400	4.298	0.946	8192
16*	OFF-GAS	Cold	30	150	2.700	0.324	6740.3
17*	FR-COMP	Cold	30	167	3.526	0.483	7070.4

* These streams correspond to values used for the PSA simulation

For this simulation the minimum approach temperature (ΔT_{min}) was set at a global value of 20 °C. The hot and cold composite curves together with values for minimum heating and cooling utilities are shown in Figure 5.15. The hot and cold composite curves are constructed by adding the corresponding enthalpy changes of hot and cold process streams for a given temperature intervals (Kemp, 2005). The pinch, which represents the region of closest approach between both curves, occurs at a hot stream temperature of 94 °C and cold stream temperature of 74 °C for the base case examined. The pinch divides the system into two distinct regions; the region above the pinch act as a heat sink while the region below the pinch acts like a cold sink. For minimum utilities (heating/cooling duties), the only admissible heat transfer above the pinch should be heat flowing in from the hot utility (no cooling). Below the pinch the opposite is true with the only admissible heat transfer is from heat flowing out to the cold utility (no heating) (Kemp, 2005). No heat is allowed to flow across the pinch.

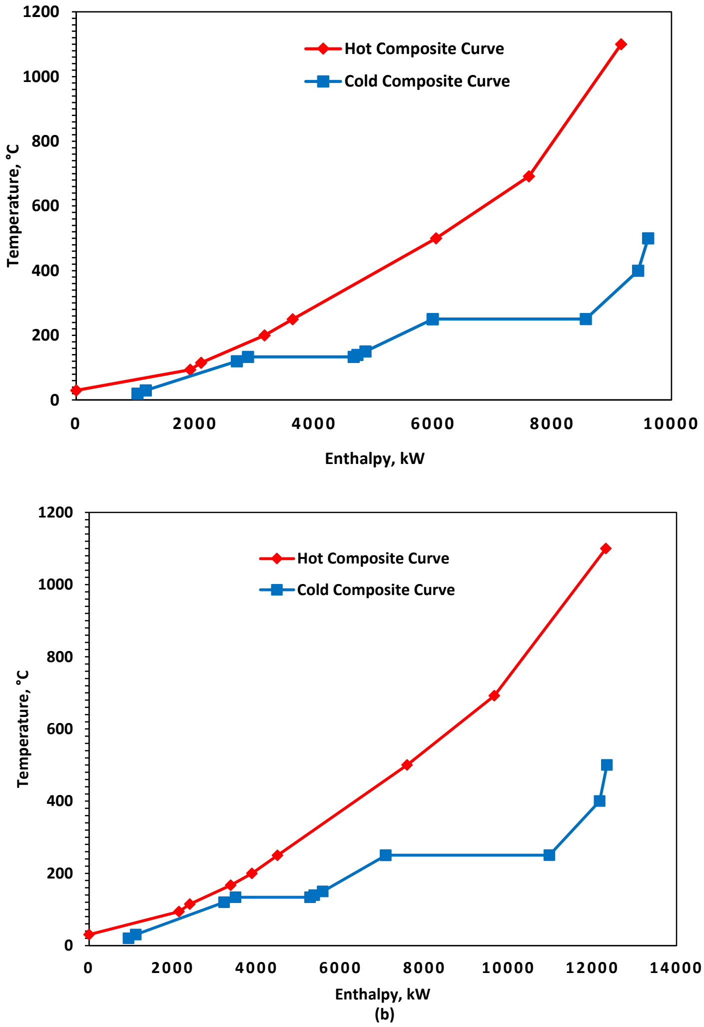

Figure 5.15 Hot and cold composite curves for base case simulation. (a) PAWS process. (b) PAPS process.

Table 5.9 Aspen Energy Analyzer summary

Property	Value (PAWS)	Value (PAPS)
ΔT_{min}	20	20
Hot pinch, °C	94	94
Cold pinch, °C	74	74
Heating, kW	455	23
Cooling, kW	1031	939
Recoverable Heat, kW	8125	11380
Minimum for MER	20	24

Table 5.9 lists a summary of the information generated by Aspen Energy Analyzer. For this simulation, the total recoverable heat is 8124 kW for the PAWS process and 11380 kW for the PAPS process with a total heating duty of 455 kW and 23 kW respectively.

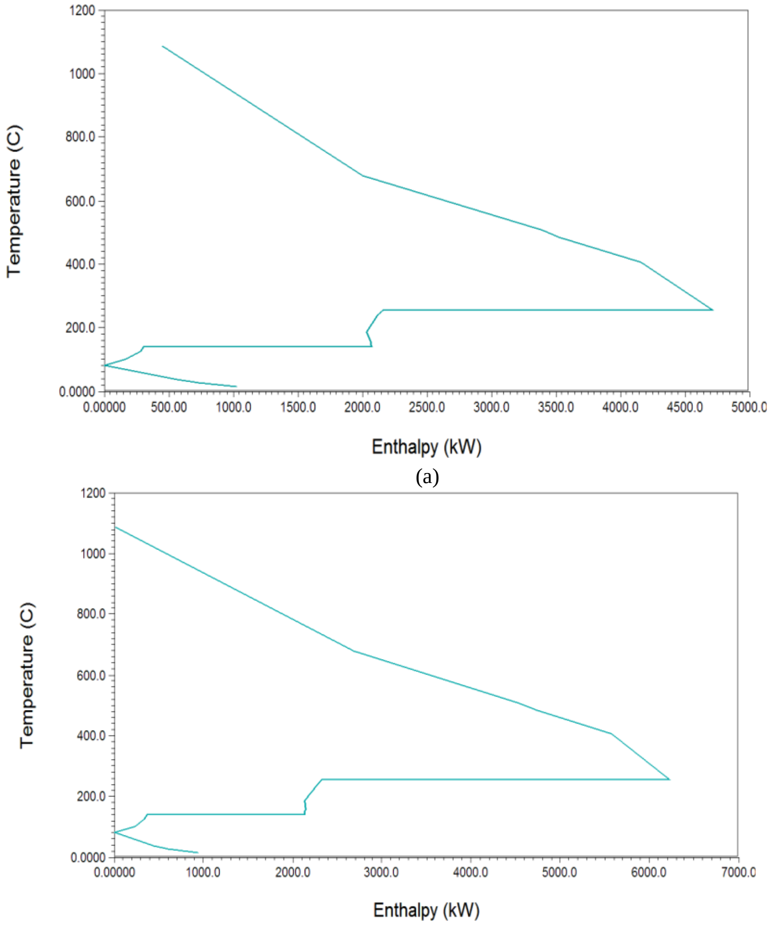

(a)

(b)

Figure 5.16 Grand composite curve. (a) PAWS processes. (b) PAPS processes

The recoverable energy mentioned in Table 5.9 excludes the energy used for pyrolysis obtained directly from combustor cooling. Figure 5.16 shows the grand composite curves for both the PAWS and PAPS processes. The PAPS process presents a case of a ‘quasi’-threshold scenario requiring a negligible amount of hot utility, 23 kW compared to 938 kW of cold utility. The grand composite curves were useful in analysing how to place utilities.

5.3.2.3 Network Grid and Process Flowsheet

According to Linnhoff and Flower (1978), grid diagrams present a convenient and helpful way to represent heat exchanger networks. In drawing a grid diagram, process streams are represented as horizontal lines with hot streams drawn at the top of the grid flowing from left to right while cold streams are drawn at the bottom flowing from right to left. Heat exchange between hot and cold streams is represented by two circles with a vertical line connecting both streams (see Figure 5.17). Kemp (2007) lists the advantages of using a grid diagram in designing a heat exchange network as:

- They are much easier to draw and heat exchangers can be placed in any order without redrawing the stream system
- They represent the countercurrent nature of heat exchangers making it easy to check for stream match feasibility
- The pinch can be shown on a grid diagram

To achieve a design fulfilling the minimum utilities requirement, the heat exchange network is designed by matching streams away from the pinch: above the pinch, hot streams are brought down to the pinch temperature only by exchanging heat with cold streams; below the pinch, cold streams are brought to the pinch temperature by heat exchange with the hot streams. For streams adjacent to the pinch, care was taken to ensure that ΔT_{min} is not violated. To achieve this the following two constrains are respected for any stream matches near the pinch:

Above the pinch

$CP_{hot} \leq CP_{cold}$

Below the pinch

$CP_{hot} \geq CP_{cold}$

Where CP_{hot} is the heat capacity of the hot stream and CP_{cold} the heat capacity of the cold stream.

Figure 5.17 shows a proposed heat exchange network grid diagram that satisfies the minimum heating and cooling requirement (maximum energy recovery) for the PAWS process. For this network the rules ensuring minimal use of utilities are all obeyed i.e.

- No heat transfer across the pinch;
- No cold utilities above the pinch;
- No hot utilities below the pinch.

In designing this network, no forbidden stream matches or layout/safety restrictions where considered. To have a more feasible network design, the entire plant was divided in two ‘zones’. Zone 1 comprised of biomass drying, pyrolysis and combustion. While Zone 2 included bio-oil recovery, ATR and hydrogen recovery. Streams matches were then performed to keep the corresponding streams within their zones. For example, flue gas from the combustor is used principally for drying and pre-heating combustion air while the reformate and shifted streams are used to pre-heat and vaporise steam used for reforming. Figure 5.18 and Figure 5.19 show proposed grid diagrams with feasible stream matches for the PAWS and PAPS respectively.

Table 5.10 Performance of proposed heat exchange network for PAWS and PAPS processes

Property	**PAWS**		**PAPS**	
	Value	**% Target**	**Value**	**% Target**
Heating, kW	714	157	532	2304
Cooling, kW	1290	125	1448	154
Recoverable Heat, kW	8125	100	11380	100
Number of Units	21	105	22	92
HX Area, m^2	1319	105	1602	97

From Table 5.10, it is clear that the hot and cold duties for the both feasible networks are higher than the required minimum targets leaving room for further improvements. However, the stream matches employed for both process present a realistic layout which can be put in place in an actual plant and circumvent the need for a very complex and probably expensive heat exchange network.

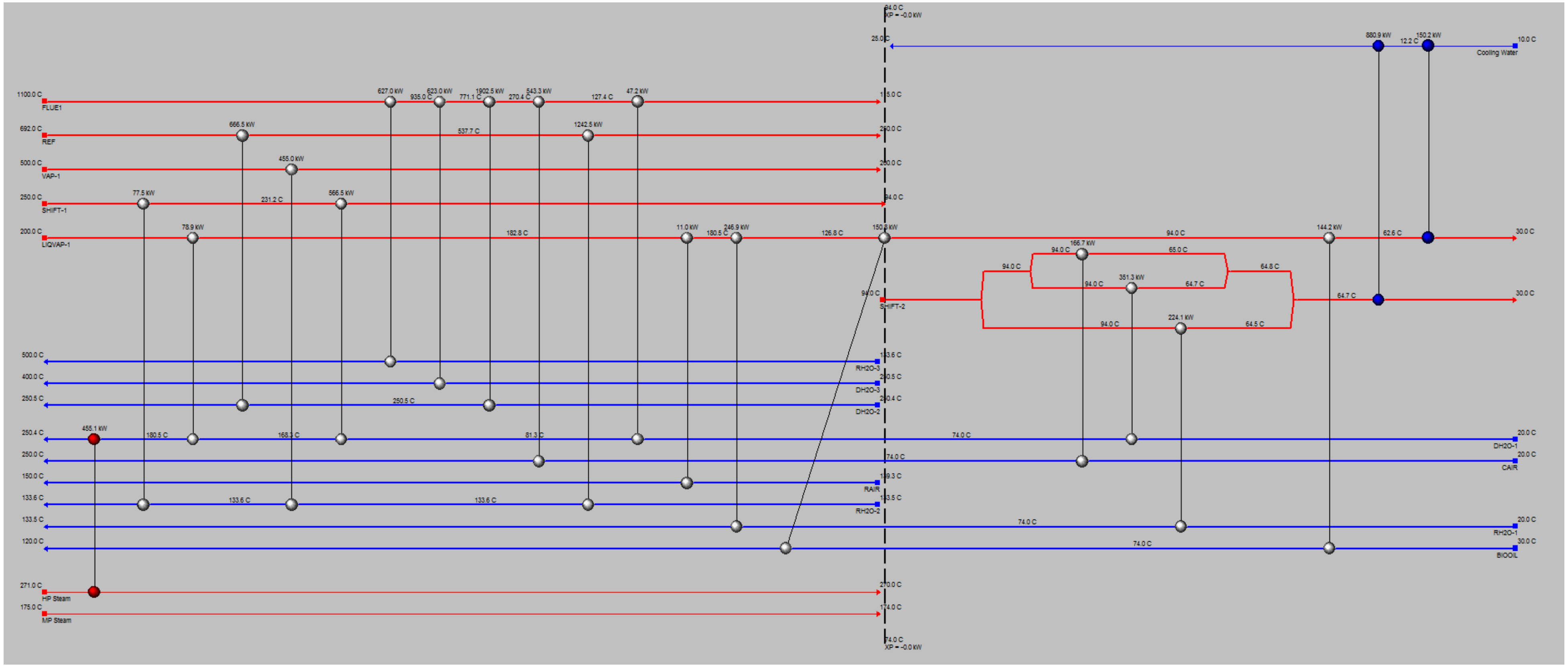

Figure 5.17 Grid diagram for PAWS process satisfying the minimum heating and cooling targets

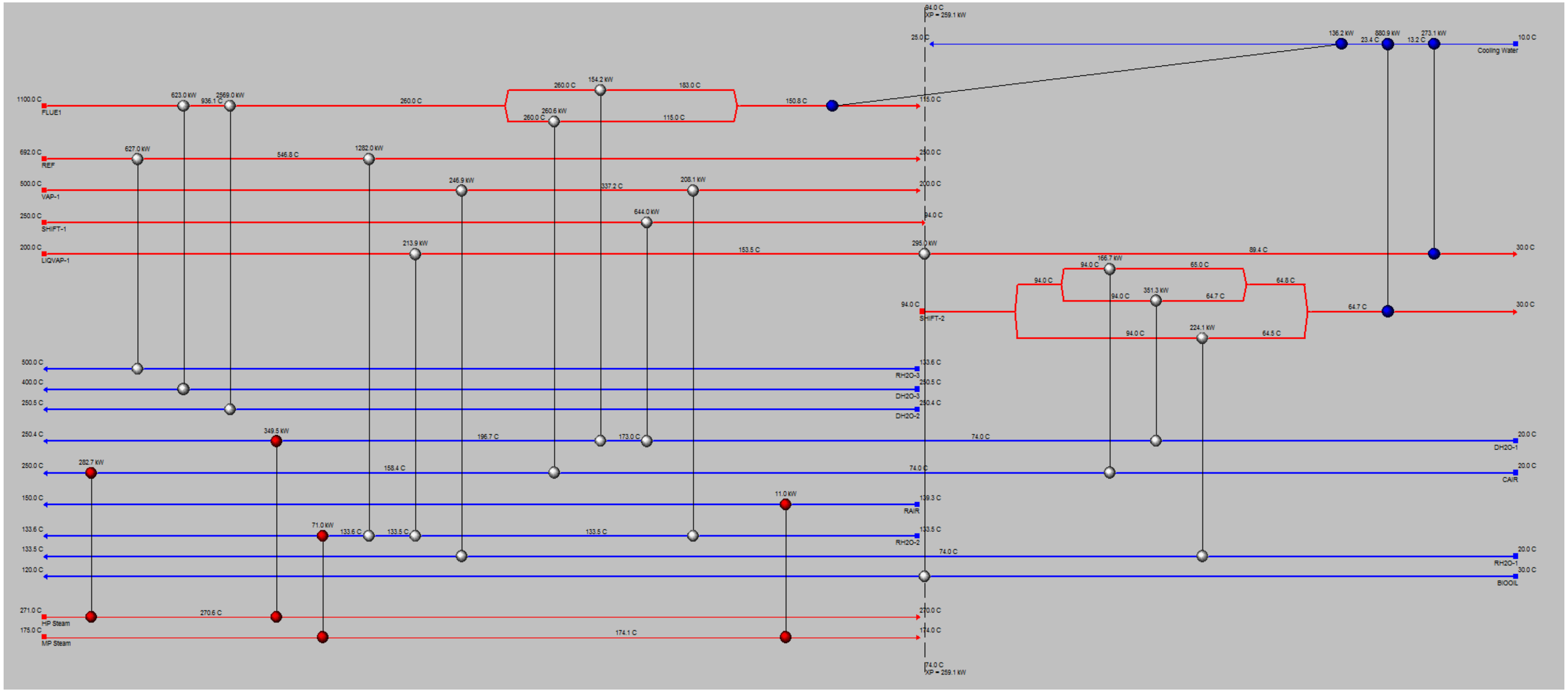

Figure 5.18 Proposed grid diagram representation for a feasible heat integrated PAWS process

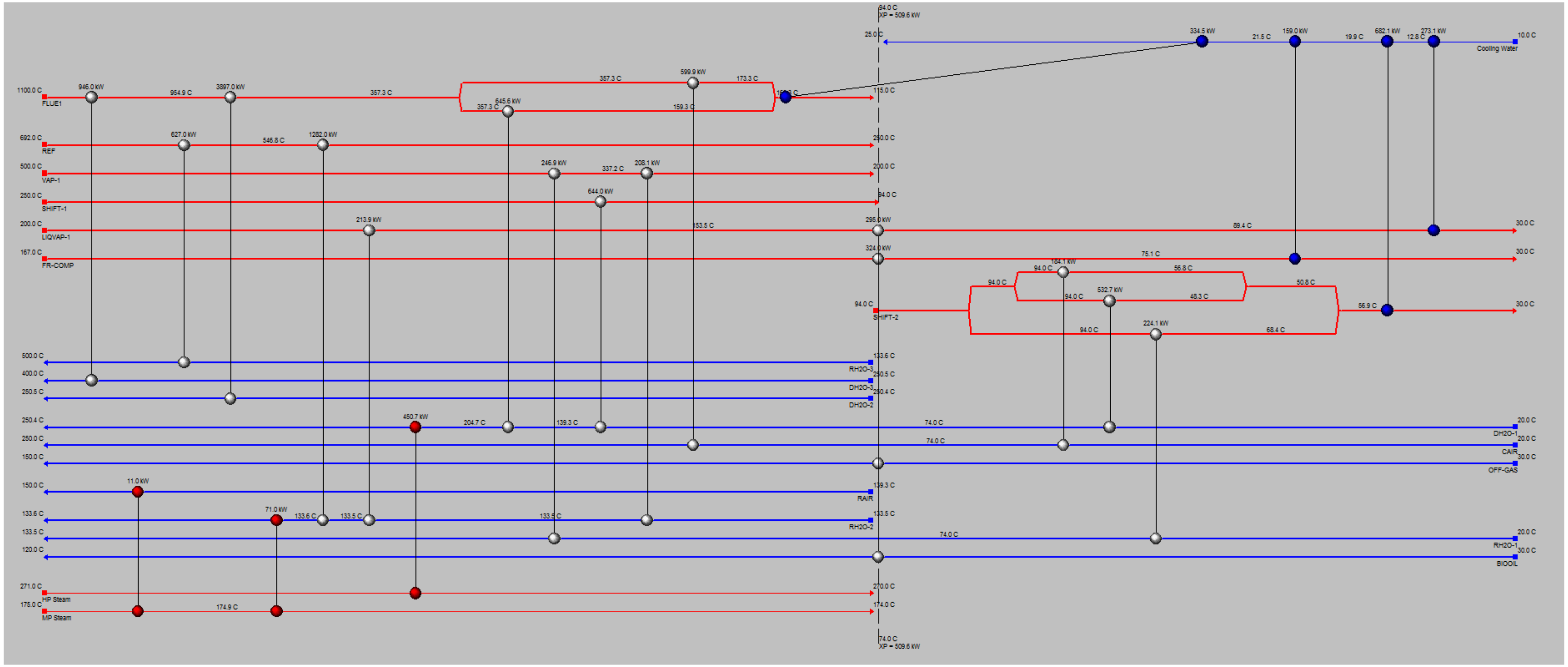

Figure 5.19 Proposed grid diagram representation for feasible heat integrated PAPS process

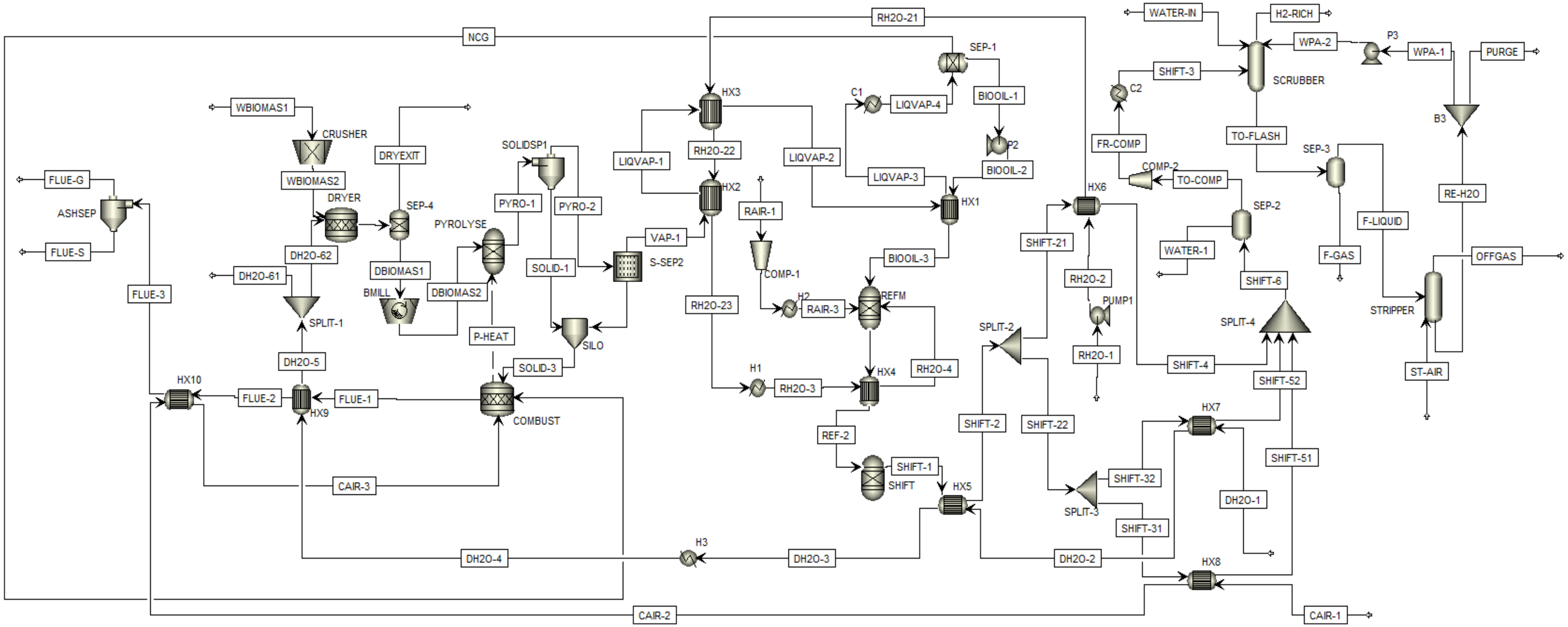

Figure 5.20 Proposed flowsheet for a heat integrated PAWS process

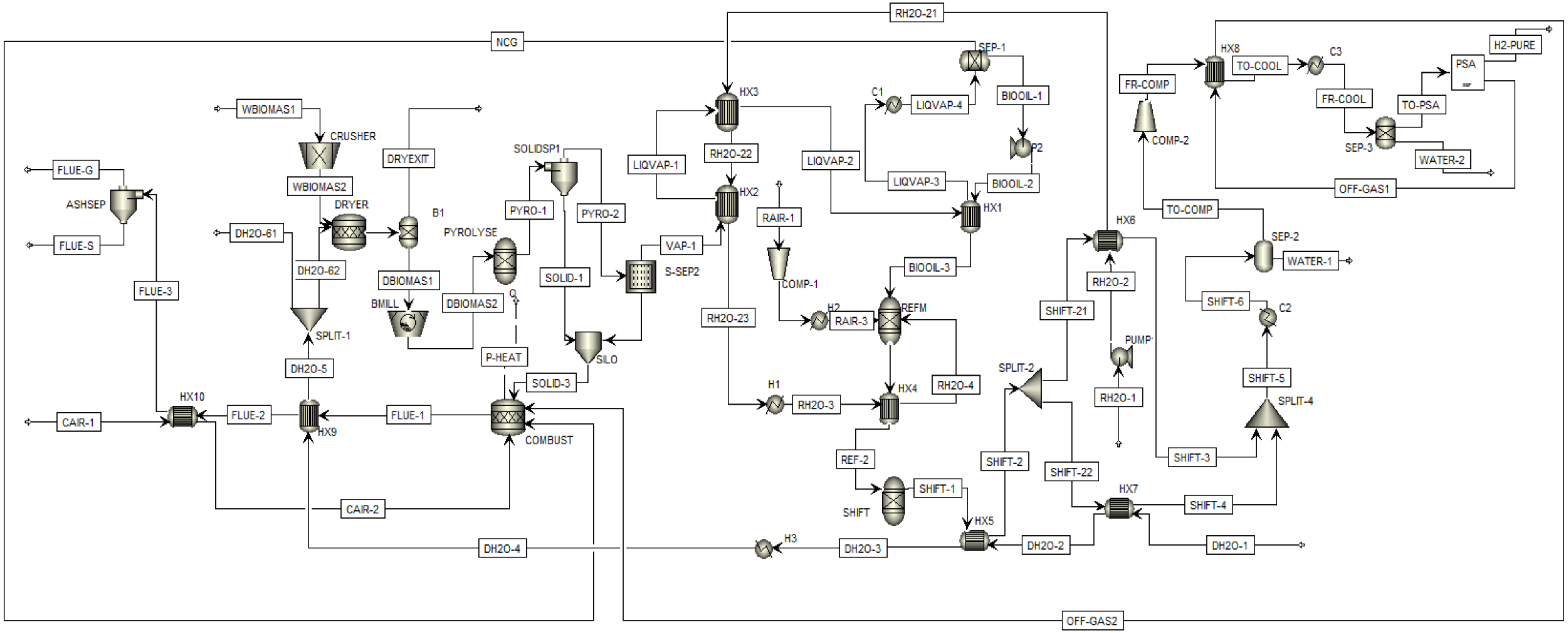

Figure 5.21 Proposed flowsheet for a heat integrated PAPS process

Figure 5.20 and Figure 5.21 show the heat integrated flowsheet for PAWS and PAPS process. It cannot be claimed that these flowsheets represent an optimal heat-integrated design but they provide an excellent basis from which to carry out a plant-wide optimisation. This plant-wide optimisation will primarily depend on the capital and operational costs entailed with adding more heat exchangers to the network and splitting streams to achieve maximum heat recovery. The final plant design will also depend on the cost of utilities, controllability constrains and plant safety.

5.3.2.4 Energy requirement calculations

Grinding energy demand

The electrical energy demand for milling increases with decreasing particle size and also depends on the moisture content of the feedstock and the type of mill (Schell and Harwood, 1994). Several authors have used different methodologies to determine the energy required for biomass comminution. Peryoga et al. (2014) proposed a correlated value of 10kWh/t to estimate the chopping and grinding energy requirement for wet PEFB. This gives a total power consumption of 85 kWh; 50 kWh for chopping and an additional 35 kWh for grinding dried PEFB biomass (for input biomass flowing at 5000 kg/h with initial moisture of 40 %). Spliethoff and Hein (1998) performed milling tests on straw, Miscanthus, and wood using 100 kg/h output cutting and a hammer mills. They were able to establish that the grinding energy requirement to obtained 2 to 6 mm particle size varied between 0.8 and 2% of the biomass calorific value for the cutting mill and below 0.5% for the hammer mill. Assuming a hammer mill is used to grind the 10 % moisture PEFB to 3 mm (LHV=18MJ/kg), the energy required will be 0.09 MJ/kg (25 kWh/t) corresponding to 83.33kWh.

The manufacturer, Azeus Machinery Co Ltd advertises a 3-5 ton per hour (t/h) PEFB shredder with a power rating of 37 kW (7.4kWh/t, using 5 t) and a 2-4 t/h capacity fibre hammer mill with a power rating of 90 kW (22.5 kWh/t, using 4 t). This gives a combined power requirement of 127 kW needed to chop 5000 kg/h incoming PEFB at 40% moisture and mill the 10 % moisture dried residue (Zhengzhou, 2016).

Mindful of these different values, the total power requirement for crushing and milling the 5000 kg/h wet PEFB biomass is taken as 120 kW.

Drying energy requirement

Biomass drying is an important operation in the production of pyrolysis oils as the final water content of the later is determined in part by the initial moisture content of the biomass (Onarheim et al., 2015, Bridgwater et al., 1999). The energy demand for drying is determined directly from the energy required to vaporise a given fraction of water in the fresh PEFB at a set temperature and pressure (101 °C, 1 bar in this case). The moisture remaining in the dried PEFB in kg/h, is given by:

$$PEFB_m = \frac{Xwater(dried\ PEFB)}{1-Xwater(dried\ PEFB)} x\ PEFB_{mf}\ (dry\ matter) \qquad 5.14$$

Where $PEFB_m$ is the moisture left in dried PEFB (kg/h), $Xwater$ is the moisture fraction in the dried PEFB and $PEFB_{mf}$ is the biomass dry matter.

By substituting the following values

$PEFB_{mf} = 3000\ kg/h$ (dry matter, 60% of PEFB biomass feed)

$Xwater = 0.1$

We obtain

$PEFB_m = 333.3\ kg/h$

Dried PEFB = $PEFB_{mf}$+ $PEFB_m$

= 3333.3 kg/h

Evaporated water = 1666.7 kg/h

The minimum energy required for drying is the sum of the evaporation load and the energy required to heat up the solid. For simplicity, heat losses occurring at various stages of the drying process are calculated as a percentage of the evaporation load.

Consider the following properties of PEFB biomass and water:

Specific heat capacity for dried PEFB (10% moisture) = 1.5 kJ/kg.°C (Dupont et al., 2014, Nyakuma et al., 2014).

Specific enthalpy of water at 25 °C and vapour at 101 °C are 104.92 and 2677.84 kJ/kg respectively.

Drying energy = sensible heat (dry PEFB) + Change in enthalpy of evaporated water

$$Drying\ energy = 3333.3\ \frac{kg}{h}\ x\ 1.5\ \frac{kJ}{kg°C}\ (101-25)°C + 1666.7 \frac{kg}{h} x\ (2716.61 - 104.92) \frac{kJ}{kg}$$

$$= 4663200 \frac{kJ}{h}$$

$$= 1.30\ MW$$

For an indirect steam heated dryer working at 70% efficiency (steam energy to moisture evaporation), the total dryer duty will be 1.86 MW. This value corresponds to a specific drying duty demand of 4.0 MJ per kg of evaporated water. Onarheim et al. (2015) used a specific drying duty of 4.9 MJ/kg for a 30 MW LHV bio-oil plant using pine as feedstock with initial moisture of 50% reduced to 8%. The 30% dryer energy losses are distributed as follows: 10% dryer body heat loss, 10% steam distribution heat loss and 10% for all other energy losses for example energy needed to power auxiliary equipment.

Pyrolysis energy requirement

The energy needed to carry out pyrolysis (heat of pyrolysis) for the base case is calculated to be 2219 kJ/kg. This is obtained for a dry biomass fed into the reactor at 101 °C flowing at 3333.33 kg/h and a pyrolysis reactor rate of enthalpy change determined by Aspen Plus to be 2.055 MW. The air flow to the combustor is adjusted so that the combustor rate of enthalpy change is sufficient to satisfy the pyrolysis heating requirement.

Fluid moving energy

Power required to pump an incompressible liquid is given by

$$P_W = \frac{\Delta P \dot{V}}{\eta} \times 100 \qquad 5.15$$

Where

ΔP is the pressure differential across the pump, N/m^2

$\dot{V}$ is the volumetric flow rate, m^3/s

η is the pump efficiency, %.

The isentropic work of compression for a gas is given by

$$C_W = P_1 v_1 \dot{m} \frac{n'}{n'-1}\left[\left(\frac{P_2}{P_1}\right)^{\frac{n'-1}{n'}} - 1\right] \qquad 5.16$$

Where

P_1 and P_2 are the initial (suction) and final (discharge) pressures, N/m^2

v_1 is the initial specific volume of the gas, m^3/kg

$\dot{m}$ is the mass flow rate, kg/s

$\boldsymbol{n'}$ is the polytropic index defined as

$PV^n = constant$

The operating parameters and power rating of pumps and compressors used for this simulation are given on Table 5.11. Some of the pumps and compressors listed in Table 5.11 are not included in Figure 5.20 and Figure 5.21 but their characteristics are calculated based on the known stream flows and pressure differentials.

Table 5.11 Operating parameters for pumps and compressors used in simulation

Pumping	**Flow, m^3/s**	**Pressure change, bar**	**Efficiency, %**	**Power, kW**
PAWS				
P1	8.21E-04	2	90	0.182
P2	5.74E-04	2	90	0.127
P3	6.94E-02	9	90	69.44
P4(FWF)*	1.25E-03	9	90	1.252
P5(DH2O)*	1.31E-03	39	90	5.676
PAPS				
P1	8.21E-04	2	90	0.182
P2	5.74E-04	2	90	0.127
P3(DH2O)*	2.10E-03	39	90	9.113

Compression**	**Flow, m^3/s**	**Pressure change, bar**	**Mechanical Efficiency, %**	
PAWS				
COMP-1	0.860	2	85	130.580
COMP-2	1.048	5	85	531.319
COMP-3(NCG)*	0.150	0.5	85	7.562
COMP-4(ST-AIR)*	2.346	0.5	85	118.627
COMP-5(CAIR)*	2.533	0.5	85	128.082
PAPS				
COMP-1	0.860	2	85	130.580
COMP-2	0.791	5	85	401.422
COMP-3(NCG)*	0.150	0.5	85	7.562
COMP-3(CAIR)*	2.814	0.5	85	142.314

* Pump/compressor not included in flowsheet

** For all compressions, the isentropic work done is calculated using n = 1.4

Electrostatic Precipitator (ESP) power consumption

Several factors have to be considered when calculating the power requirements of an ESP unit. ESPs in general do not have high operating cost but their capital costs are quite high. An easy approximation for ESP power is to take 1 kWh per 1000 m^3 of treated gas. For the base case simulation, the ESP power consumption is taken as 4.8 kW (4842 m^3/h of treated pyrolysis vapour). Peryoga et al. (2014) estimated the ESP power consumption as 9 kW for a process with treated gas flowing at 9878 kg/h.

5.3.2.5 Combined Heat Power unit

A combined heat power (CHP) system using steam turbine as a prime mover was integrated in the process design. The fuel side of the boiler consists of the combustor (block COMBUST on Figure 5.20 and Figure 5.21) while the steam side consists of heat exchanger HX9. In reality HX9 has three separate sections, HX9-E, HX9-V, and EX9-S (not shown). Hot water leaving heat exchanger HX5 (stream DH2O-3) enters the first section, HX9-E called the economiser where it is heated to just below its boiling point. This then flows to the second section, HX9-V called the vaporiser where the hot water is completely vaporised to a saturated vapour. The saturated vapour then moves into the third section, HX9-S called the superheater where it is superheated to the desired temperature, 400 °C in this case. The use of a either a backpressure steam turbine (BST) or a condensing extraction turbine (CET) as a means to generate electricity and the effect on the heat load of the residual steam is analysed in the following sections. This introduces two more variants for the type of processes examined in this work. The traditional PAWS process become either a PAWS process using BPT (**PAWS-BT**) and or a PAWS process using CET (**PAWS-CT**). The PAPS process also becomes either a PAPS process using BPT (**PAPS-BT**) or a PAPS process using CET (**PAPS-CT**).

5.3.2.5.1 Backpressure steam turbine (BST)

Superheated steam produced at 40 bar and 400 °C (stream DH2O-4) is sent into a BST operating at a given specific steam consumption (SSC) and exits as a saturated vapour at 3 bar and 133.5 °C. The turbine exhaust is then used to dry fresh PEFB biomass feed. SSC is defined as the mass flow of steam required to produce a unit power output. For this simulation, the mechanical efficiency of the BPT is set at 0.9 and the SSC is taken to be equal to 6.9 kg/kW-h (corresponding to an isentropic efficiency of 0.9). The value used for SSC is obtained using values generated by the Aspen Plus software. To reduce the heating demand of the process, a design block is used to control the flow rate of the input water (DH2O-1) so that the heat exchanger H3 on Figure 5.20 and Figure 5.21 is no longer required.

PAWS-BT process

For the base case, the work generated by the BPT operated within the PAWS process,W_{HB}, is obtained by substituting the following values into Eq. 5.10:

$\dot{m}_T = 4715\ kg/h$

$S_T = 6.9$

$\eta_T = 0.9$

Whence

$$\mathrm{W}_H = \ 4715\frac{kg}{h} \times \frac{kWh}{6.9\ kg} \times\ 0.9$$

$$= 615.0\ \mathrm{kW}$$

The turbine exhaust has a quality of 0.99 and can provide the 1.85 MW required for drying in an indirect steam heated dryer (e.g. rotary steam tube dryer). Steam exits the dryer as a saturated water-vapour mixture at 133.5 °C and 3 bar with a quality of 0.33. This saturated steam can be cooled further to subcooled water at 120 °C and 3 bar generating an additional 1.02 MW of heat. This additional heat can be used to satisfy other process heat requirements and district heating. The subcooled water is cooled further in a condenser to about 30 °C then pumped to 40 bar and recycled as DH2O-1.

PAPS-BP process

For the base case, the work generated by the BPT operated within the PAPS process, W_{PB}, is obtained by substituting the following values into Eq. 5.10:

$\dot{m}_T = 7571.3\ kg/h$

$S_T = 6.9$

$\eta_T = 0.9$

Whence

$$W_P = 7571.3 \frac{kg}{h} \times \frac{kWh}{6.9\ kg} \times 0.9$$

$$= 987.6\ \text{kW}$$

For this process, the turbine exhaust (133.5 °C, 0.99 quality) is sent to the dryer and leaves as a saturated water-vapour mixture at 133.5 °C and 3 bar with a quality of 0.58. Like for the PAWS-BT, cooling this stream further to subcooled water at 120 °C and 3 bar yields 2.76 MW which can be used for process heating. The steam generated from heat recovery for the PAPS-BP contains almost three times the energy required for biomass drying. This creates the need for an alternative process design to better utilise this excess energy.

5.3.2.5.2 Condensing extraction steam turbine (CET)

One way to better utilise the excess heat load of the BPT exit steam is to increase the electrical output of the plant by using a condensing extraction turbine (CET). This turbine works in two stages. Firstly, the superheated steam, DH2O-4, expands isentropically in the turbine from 40 to 5 bar generating work. This is followed by extraction of some steam for process heating (mostly drying) while the remaining steam is expanded to a saturated liquid/vapour mixture at 20 °C and 0.023 bar. The cold expanded steam is cooled in a condenser and then pumped to 40 bar and recycled as part of stream DH2O-

1 (Figure 5.20 and Figure 5.21). To determine the amount of steam extract needed to satisfy the PEFB biomass drying requirement, the following calculations are performed:

Let

h_{IN}, be the specific enthalpy (kJ/kg) of extracted steam entering the dryer at 164.6 °C and 5 bar.

h_{DO}, be the specific enthalpy (kJ/kg) of hot water exiting the dryer at 120°C and 5 bar.

The calculations below are for a turbine working with an isentropic efficiency of 0.9 and mechanical efficiency of 0.9 corresponding to a SCC equal to 8.2 kg/kWh.

$h_{IN} = 2778.0\ kJ/kg$ (obtained from the steam table)

$h_{DO} = 504\ kJ/kg$ (obtained from the steam table)

Substituting into the equation

$$\dot{m}_D = \frac{H_D}{(h_{IN} - h_{DO})} \times 3600 \frac{s}{h}$$

Where

$\dot{m}_D$ the steam flowing into the dryer, kg/h

H_D the drying enthalpy (1850 kW for the base case)

Gives

$\dot{m}_D = 2945.0\ kg/h$

PAWS-CT

The combined work generated by the CET operated within the PAWS process W_{HC}, is obtained from the sum of W_{s1} and W_{s1}(woke generated from steam expansion in stage 1 and 2 respectively of the CET). Using values obtained from Aspen, the following calculations are performed:

For stage 1

$\dot{m}_T = 4715\ kg/h$

$S_T = 8.2$

$\eta_T = 0.9$

By applying 6.10, the work generated is

$$W_{s1} = 4715.3 \frac{kg}{h} \times \frac{kWh}{8.2\ kg} \times 0.9$$

$$= 517.5\ \mathrm{kW}$$

For stage 2

$\dot{m}_T = 1770.3\ kg/h$ (less steam as some is extracted to used for drying)

$S_T = 5.25$

$\eta_T = 0.9$

Whence

$$W_{s2} = 1770.3 \frac{kg}{h} \times \frac{kWh}{5.25\ kg} \times 0.9$$

$$= 303.5 \text{ kW}$$

Therefore,

$W_{HC} = 821\ kW$

PAPS-CT

Applying the same equations and reasoning to the PAPS-CT, the combined work generated, W_{PC} is obtained as follows:

For stage 1

$\dot{m}_T = 7571.3\ kg/h$

$S_T = 8.2$

$\eta_T = 0.9$

whence

$$W_{s1} = 7571.3 \frac{kg}{h} \times \frac{kWh}{8.2\ kg} \times 0.9$$

$$= 831 \text{ kW}$$

For stage 2

$\dot{m}_T = 4626.3\ kg/h$, $S_T = 5.25$

$\eta_T = 0.9$

whence

$$W_{s2} = 4626.3 \frac{kg}{h} \times \frac{kWh}{5.25\ kg} \times 0.9$$

$$= 793.1 \text{ kW}$$

Therefore

$W_{PC} = 1624.1\ kW$

By using a CET instead of a BPT, the mechanical work generated increases by 33.5% for the PAWS-CT and 64.5% for the PAPS-CT. Another advantage of using a CET is that it reduces the need for an oversized dryer which will otherwise be needed to deal with the excess steam flowing out of the BPT. Figure 5.22 and Figure 5.23 show the complete heat integrated PAWS-BT and PAWS-CT processes. The PAWS-BT process as described uses one turbine (block BPT) while the PAWS-CT process uses two turbines (block CET-1 and CET-2). The corresponding stream results are listed on Table A.3, A.5 and A.6 in Appendix A.

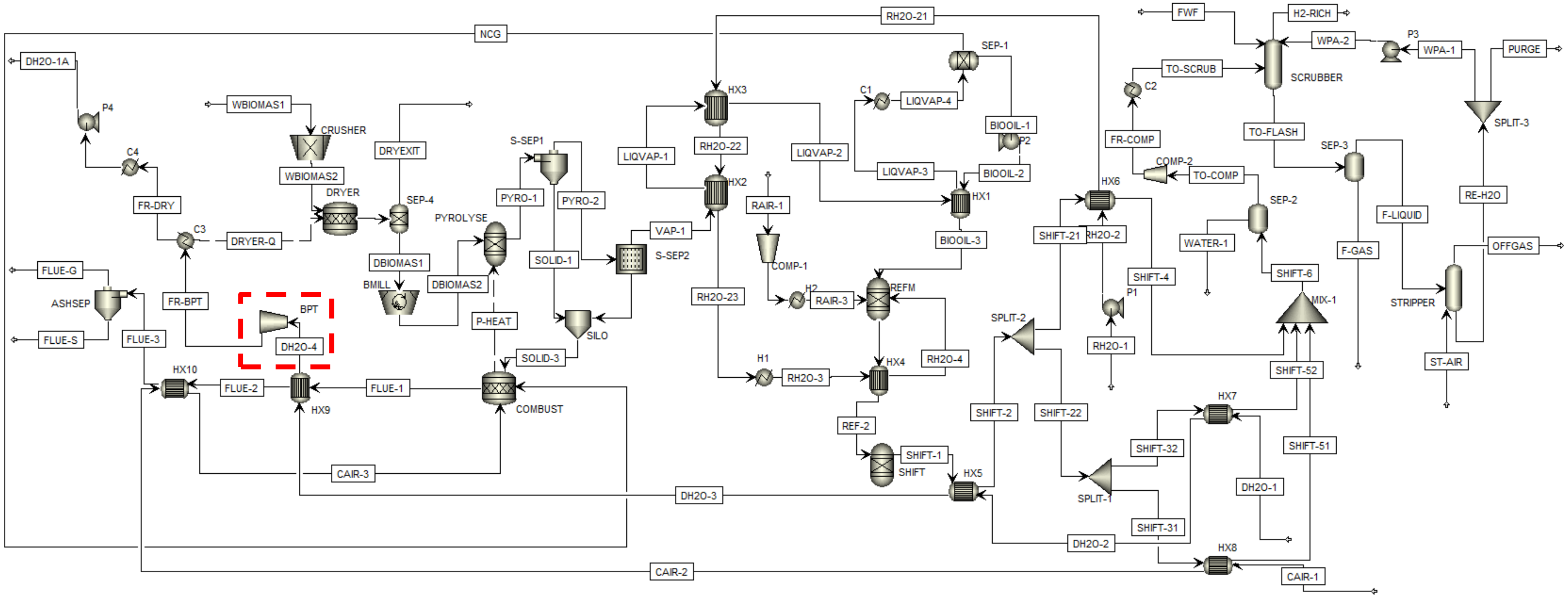

Figure 5.22 Flowsheet for a heat integrated PAWS-BT process

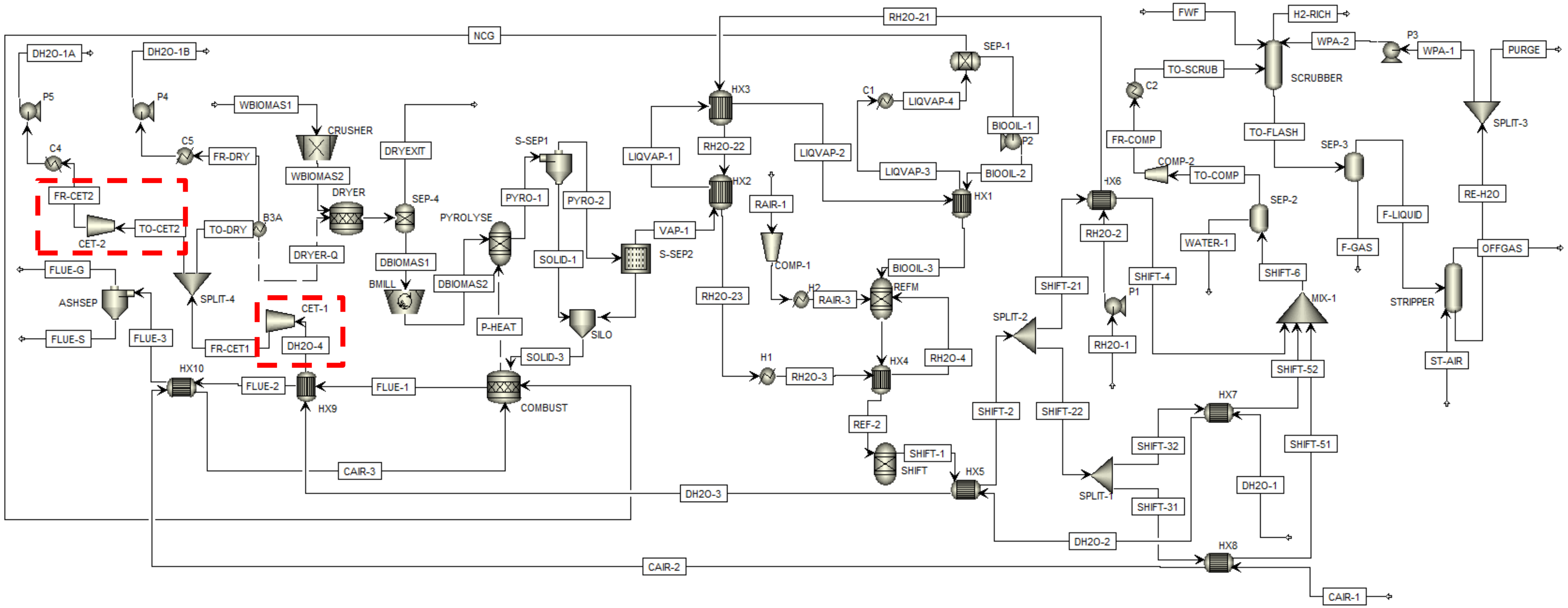

Figure 5.23 Flowsheet for a heat integrated PAWS-CT process

5.3.2.6 Overall process efficiency calculation

The overall process efficiency is calculated using Equation 5.11.

$$\eta_{\mathrm{pr}} = \frac{\dot{m}_{\mathrm{H_2}}.\mathrm{LHV}_{\mathrm{H_2}} + (\dot{P}^{+}) + (\dot{Q}^{+})}{\dot{m}_{\mathrm{PEFB}}.\mathrm{LHV}_{\mathrm{PEFB}} + (\dot{P}^{-}) + (\dot{Q}^{-})} \times 100$$

a) Processes using BPT

PAWS-BT

Considering the following values:

$\dot{m}_{\mathrm{H_2}} = 267.4\ \mathrm{kg/h}$

$\mathrm{LHV}_{\mathrm{H_2}} = 33.58\ \mathrm{kWh/kg}$

$\dot{W} = 0.615\ \mathrm{MW}$

The net heat for the process is obtained by subtracting process heat required from CHP residual heat (Eq. 5.13), i.e.

$(\dot{Q}^{+}) = 1.02 - 0.127$

$\quad = 0.893\ \mathrm{MW}$

Where 0.127 MW is heat needed to satisfy the heating requirement of heaters H1 and H2 (Figure 5.22).

$\dot{m}_{\mathrm{PEFB}} = 5000\ \mathrm{kg/h}$

$\mathrm{LHV}_{\mathrm{PEFB}} = 3.06\ \mathrm{kWh/kg}$

The total electrical energy, $\dot{E}$, is the sum of the crushing, milling, ESP, pumping and compression power.

$\dot{E} = 0.12 + 0.0048 + 0.992$

$\quad = 1.117\ \mathrm{MW}$

The net power, $(\dot{P}^{-})$ in this case is given by (Eq. 5.12)

$(\dot{P}^{-}) = 0.615 - 1.117$

$\quad = -0.502\ MW$

Substituting these values we obtain

$$\eta_{pr} = \frac{8.98 + 0.893}{15.3 + 0.502} \times 100$$

$\quad = 62.5\ \%$

PAPS-BP

Considering the following values:

$\dot{m}_{\mathrm{H_2}} = 200.5\ \mathrm{kg/h}$

$\dot{W} = 0.988$

$\left(\dot{Q}^{+}\right) = 2.76 - 0.127$

$= 2.63\ MW$

$\dot{\mathrm{E}} = 0.12 + 0.0048 + 0.691\ \mathrm{MW}$

$= 0.816\ \mathrm{MW}$

The net power, $\left(\dot{P}^{+}\right)$ in this case is given by

$\left(\dot{P}^{+}\right) = 0.988 - 0.816$

$= 0.172\ MW$

$\eta_{pr} = \frac{6.73+0.172+2.63}{15.3} \times 100$

$= 62.3\ \%$

a) Processes using CET

PAWS-CT

$\left(\dot{Q}^{-}\right) = -0.127\ MW$

$\dot{\mathrm{W}} = 0.821$

$\dot{\mathrm{E}} = 1.117\ \mathrm{MW}$

$\left(\dot{P}^{-}\right) = 0.821 - 1.117$

$= -0.296\ MW$

$\eta_{pr} = \frac{8.98}{15.3+0.296+0.127} \times 100$

$= 57.1\ \%$

PAPS-CT

$\dot{\mathrm{m}}_{\mathrm{H_2}} = 200.5\ \mathrm{kg/h}$

$\left(\dot{Q}^{-}\right) = -0.127\ MW$

$\dot{\mathrm{W}} = 1.624$

$\dot{\mathrm{E}} = 0.816\ \mathrm{MW}$

$\left(\dot{P}^{+}\right) = 1.624 - 0.816$

$= 0.808\ MW$

$\eta_{pr} = \frac{6.73+0.808}{15.3+0.127} \times 100$

$= 48.9\ \%$

The processes using CET (PAWS-CT and PAPS-CT) have lower overall process efficiencies and higher power output ($\dot{\mathrm{W}}$) than BPT based ones. This is mainly due to the fact that the exhaust heat leaving the CET turbine losses most of its thermal energy during condensation as the steam expands to vacuum to produce more power. The choice of using either a BPT or a CET as prime mover for a CHP process depends mostly on the heat-to-power ratio of the plant. Ideally, the turbine should be able to meet the minimum electricity demand of the plant while also providing enough heat to satisfy process heating requirements.

The CHP system put in place for PAWS-BT and PAWS-CT process both fail to match the electrical load of the system. The PAWS-BT process is able to export 0.893 MW of heat for plant-wide use or district use while PAWS-CT process requires 0.127 MW of external heat. The slight increase in electrical output obtained by switching from a BPT to a CET has to be weighed with the extra capital cost of the CET and the need for an additional fuel source for heating. In any case, additional electricity supply from the grid is needed to run both processes and power all auxiliary plant equipment.

The CHP system for PAPS-BP and PAPS-CT process both meet their electrical demand. PAPS-BP process generates an excess of 2.63 MW of thermal energy which can be exported to neighbouring facilities or to a neighbouring process. The relatively high process efficiency of this process relies on the effective use of this energy which in most cases cannot be guaranteed as it depends on locating the hydrogen production plant next to another plant requiring low temperature heating (less than 120 °C) for example an oil palm mill. In case such a scenario is not feasible then the PAPS-CT process presents a better option as the 0.808 MW of extra electricity can be used to power all auxiliary plant equipment with some power possibly leftover to be sold to the grid. A detail economic and environmental analyses is needed in order to select the best option among the different process configurations considered above.

5.4 Sensitivity analyses

5.4.1 Pressure

The effect of pressure on the overall process efficiency of the PAWS-BT/CT and PAPS-BT/CT processes was examined. The pressure change was only applied to the reforming and hydrogen separation sections of the plant. Figure 5.24 shows the influence on overall process efficiency as pressure is changed from the base case, 3 bar, to 10, 20 and 30 bar. In all, process efficiency increased with increase in pressure for both the PAWS-BT and PAPS-BT processes mainly due to increase output of their

CHP system. This increase in heat and power output is achieved as heat is recovered from the cooling of reforming air and steam as they are compressed and pumped respectively to higher pressures.

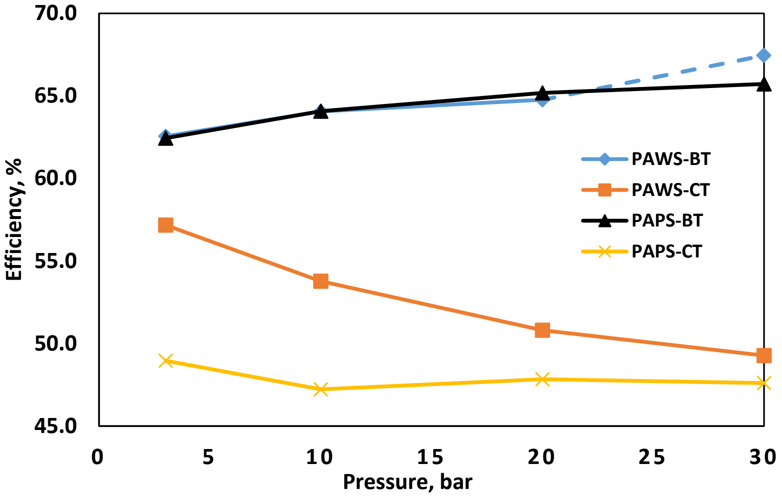

Figure 5.24 Influence of pressure on overall process efficiency for a 5000kg/h PEFB plant operating at 3, 10, 20 and 30 bar.

The trend is somewhat different for PAWS-CT and PAPS-CT processes. The process efficiency reduced for the PAWS-CT process as pressure was increased; while an initial decrease in efficiency was followed by a slight increase as pressure was increased for the PAWA-CT process. The decrease in process efficiency of PAWS-CT processes in mainly due to the reduction in hydrogen production in the reformer and shift reactor as pressure is increased. The initial decrease in efficiency of the PAPS-CT process as pressure increased from 3 to 10 bar is mainly due to the reduction in hydrogen production. This decrease is noticeable because the PSA unit for both cases operates at 10 bar. The concomitant increase in efficiency as pressure is increased to 20 and 30 bar is attributed to the improved performance of the PSA, 85% and 90% hydrogen recovery respectively. An important remark for both PAWS-CT and PAPS-CT processes is that unlike for the base case, at pressures greater than or equal to10 bar, there is no need for any external heating (H1 and H2). This completely eliminates the need for a second fuel burner thereby reducing the complexity of the plant.

5.4.2 Pyrolysis product distribution

For the base case, the biomass-to-bio-oil conversion efficiency based on LHV is 71.2% (for a 70 wt% yield in bio-oil and LHV of 11 and 16.6 MJ/kg for the wet biomass and bio-oil respectively). Demirbas (2001a) suggested that the conversion of biomass to bio-oil can have efficiencies up to 70%. This value for biomass-to-bio-oil conversion affects the hydrogen efficiency of the process (hydrogen yield), the thermal load/output and the electrical load/output. The effect of having different pyrolysis yields on these factors was examined by setting five cases (including the base case). Table 5.12 shows the different scenarios examined for pyrolysis product distribution presented as cases. The cases are labelled from 1 to 5 in increasing bio-oil (pyrolysis liquid) yield. Since the main objective of preforming PEFB biomass pyrolysis is to obtain bio-oil for hydrogen production, Case 1 is considered a poor yield while Case 5 is considered an excellent yield.

Table 5.12 Possible pyrolysis yields listed as cases

Pyrolysis yield	**Case 1**	**Case 2**	**Case 3**	**Case 4***	**Case 5**
Liquid	50	55	60	70	75
Char	25	20	15	15	12
Gas	20	20	22	12	10
Ash	5	5	3	3	3

* Case 4 is the pyrolysis yield used for the base case

Figure 5.25 shows the influence of the various pyrolysis yield studied on the process efficiency. The process efficiency increases as we move from case 1 to 5. This increase in efficiency coincides with the increase in bio-oil fraction in the pyrolysis product.

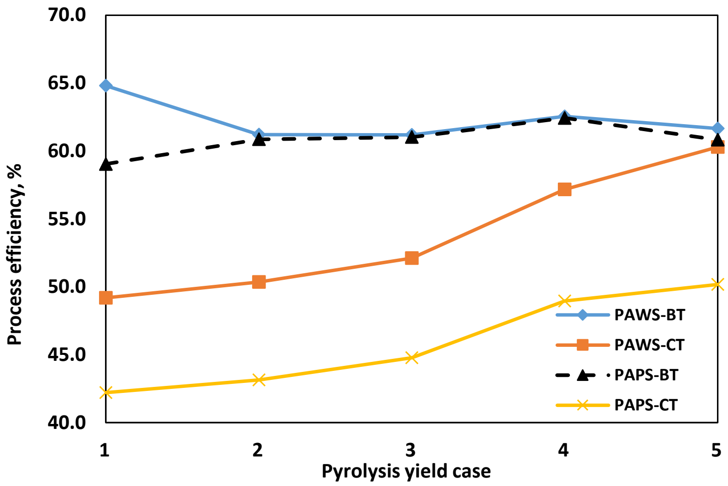

Figure 5.25 Influence of pyrolysis product yield on the overall process efficiency. The five cases examined are labelled from 1 to 5 in increasing bio-oil yield.

PAWS-BT presents a somewhat different picture as case 1 has the highest efficiency. This is mainly due to its very high char yield which present a potential for maximum heat recovery and exportation. This high thermal energy is shown clearly on Figure 5.26 as net heat, Q, for PAWS-BT case 1 and has a value of 3.1 MW with the closest value being that of case 2 with Q equal to 2.1 MW.

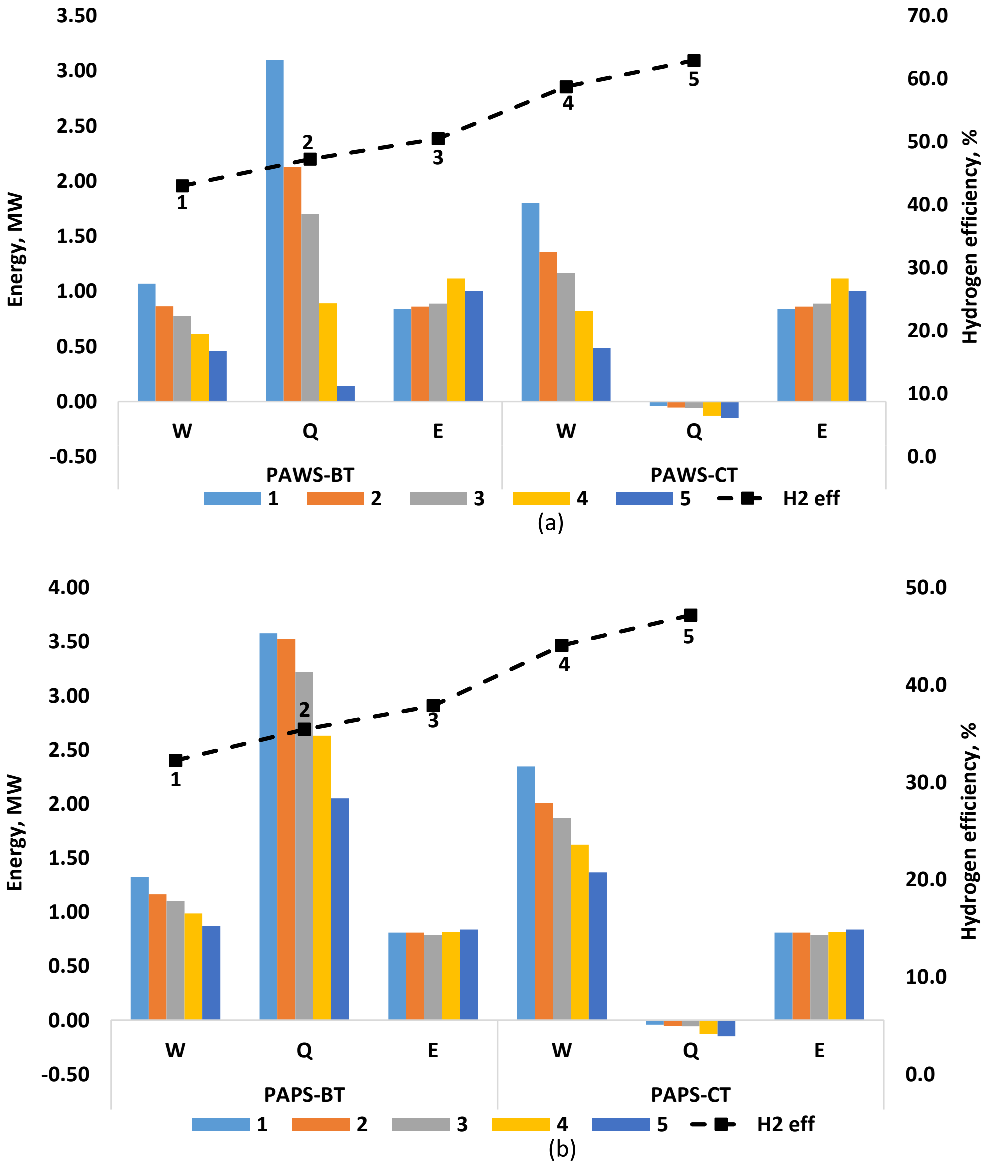

(a)

(b)

Figure 5.26 Turbine work output, W, heat output, H and electrical input, E for the various pyrolysis yield cases examined in this study. a) PAWS processes b) PAPS processes. The numbers 1, 2, 3, 4, and 5 refer to the 5 pyrolysis cases studied.

Put in perspective, this corresponds to a 33% decrease in heat corresponding to a 10 % increase in hydrogen thermal energy (6.5 to 7.1 MW). Figure 5.26 also shows that for the five PAWS-BT cases studied, only case 1 has the potential to satisfy its internal electrical load demand with the remaining cases requiring external power supply. All PAWS-CT, PAPS-BT and PAPS-CT cases studied are able to satisfy their electrical load requirement but the processes using CET (PAWS-CT and PAPS-CT) require external heating, $(\dot{Q}^-)$.

5.4.3 Throughput (plant size)

The influence of biomass throughput on process efficiency was also examined. From Figure 5.27, it is evident that under similar process conditions, the process efficiency is almost independent of the plant size. Only a slight increase is process efficiency is observed (less than 1 %) as the biomass feed is increased from 2500 to 20000 kg/h. This is primarily due to the fact that the dominant terms in the process efficiency equation (hydrogen thermal energy for the numerator and biomass LHV for the denominator) are directly proportional to the feed flow with only a relative slight increase in net heat output, Q and electrical input load, E.

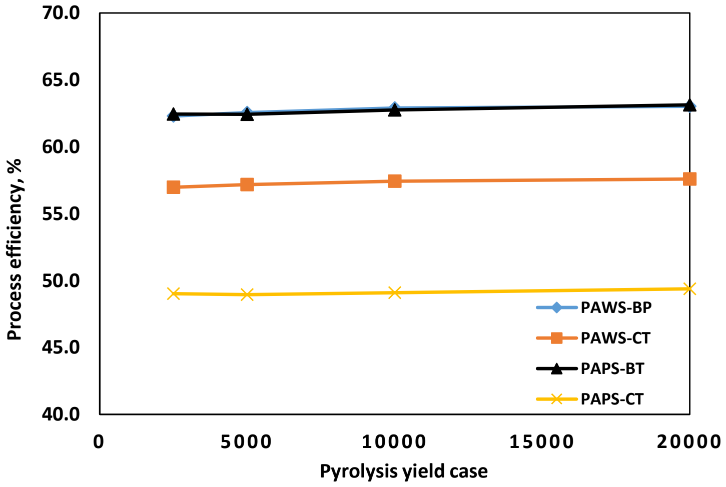

Figure 5.27 Influence of PEFB biomass throughput on process efficiency.

Based on the PEFB biomass input flow (kg/h), the specific turbine work, specific heat output and specific electrical power input are determined respectively to be 0.12, 0.18 and 0.24 kWh/kg of biomass for the PAWS-BT process, 0.17, -0.03, and 0.24 kWh/kg for the PAWS-CT process, 0.2, 0.53, and 0.16 for kWh/kg for the PAPS-BT process and finally 0.33, -0.03 and 0.16 kWh/kg for the PAPS-CT process.

5.4.4 Oxygen from an Air Separation Unit (ASU)

Even though air can be used directly in ATR processes as a source for oxygen, the presence of nitrogen reduces fuel conversion and increases the size and cost of the reactor and other downstream equipment e.g. heat exchangers and separation columns (Lange, 1997). Using pure oxygen or oxygen rich gas, greater than 90 vol%, obtained from an air separation unit (ASU) allows the process to deal with less volume of gas to compress but this comes with an accompanying energy cost resulting in a decrease in overall process efficiency. Air separation processes can be classified as either cryogenic or non-cryogenic. The choice of an air separation process depends on the oxygen flow requirements and the possibility of integration with the rest of the plant/process. Cryogenic air separation is a very mature technology achieving oxygen purities as high as 99.5% and also most energy efficient for high flow oxygen demand process usually greater than 500 tons of per day (TPD). However, non-cryogenic ASU such as PSA or pressure-temperature swing adsorption technology (PTSA) are more competitive for oxygen production of less than 300 TPD (Banaszkiewicz et al., 2014); especially when an oxygen purity of less than 95 % is not detrimental to the process.

The influence of using oxygen produced from an on-site ASU on the process efficiency was investigated for a 10,000 kg/h and 20,000 kg/h biomass throughput process. The ATR oxygen demand for both processes is 1709 kg/h (41.0 ton per day or 'TPD') and 3418 kg/h (82 TPD) respectively. Considering both values correspond to production from a mid-sized ASU (less than 100 TPD), the energy cost of producing oxygen by either a cryogenic or non-cryogenic process will be almost the same with a slight advantage for non-cryogenic process. For further analysis, a stand-alone ASU with a power consumption of 500 kWh/t O_2 was assumed. The extra power consumed by the ASU is calculated for each process and added to the value of $\dot{E}$. Katikaneni et al. (2014) assumed a power consumption of 450 kWh/t O_2 for a 1000 kg/h hydrogen producing plant using a PSA based ASU for the POX of various transportation fuels (heavy naphtha, kerosene, and diesel).

A comparison of the process efficiencies of air based processes with oxygen based ones for the two PEFB biomass flows mentioned is presented in Figure 5.28. There is a clear decrease in overall process efficiency associated with the switch from air to O_2. This is mainly due to the increased power consumption associated with the ASU. There is only a slight decrease in processes efficiency for the PAWS-BT/CT processes as the additional power consumption by the ASU is countered by significant decrease in power needed to compress the reduced gas volume within the process.

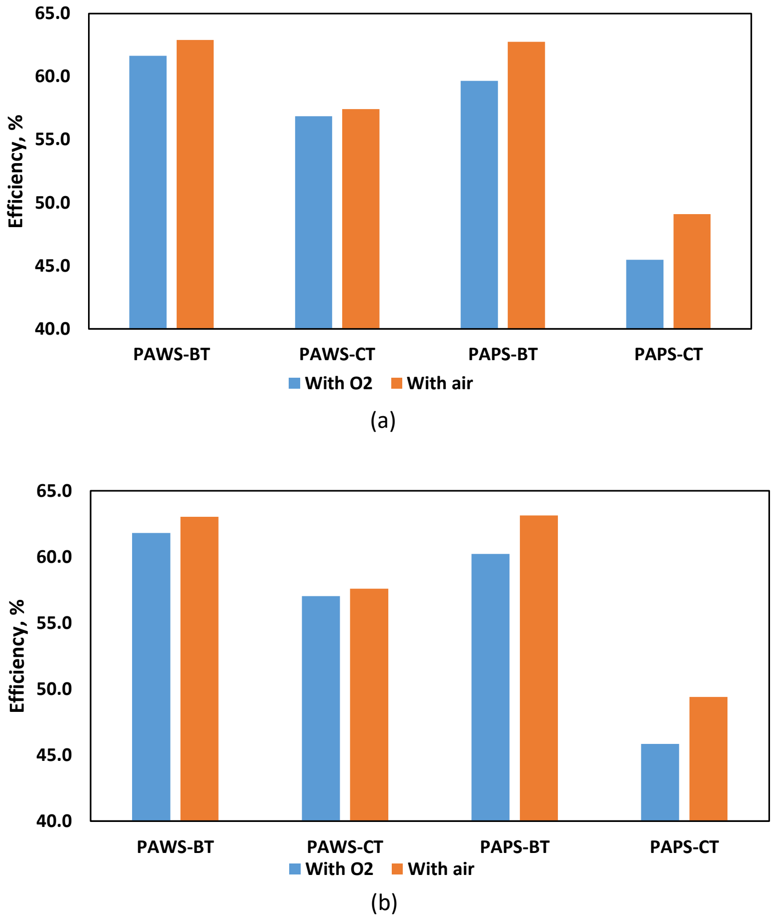

Figure 5.28 Comparing the overall process efficiencies for systems using air with systems using oxygen. a) 10,000 kg/h PEFB plant b) 20,000 kg/h PEFB plant

For example, the process gas compression power demand reduces for the 20,000 kg/h PAWS process from 4.1 MW for air based to 2.9 MW for the PAWS with O_2 (reduces by 1.2 MW). Meanwhile, the additional power consumption from the ASU is determined to be 1.7 MW. The switch from air to O_2 causes a significant drop in the process efficiency of the PAPS-BT/CT processes. As mentioned earlier, the advantage of this switch has to be weight more in terms of capital cost.

5.5 CO_2 emission savings

An estimate for the CO_2 emissions savings associated with the four process configurations examined in this study is shown in Figure 5.29. The figure shows the results for 5,000 kg/h and 20,000 kg/h biomass throughputs. The CO_2 savings for the BPT based processes (PAWS-BT and PAPS-BT) are slightly higher than those for the CET based ones. This difference becomes even more significant as the biomass input is increased from 5000 kg/h to 20,000 kg/h with a corresponding drop of about 8% and 19% respectively.

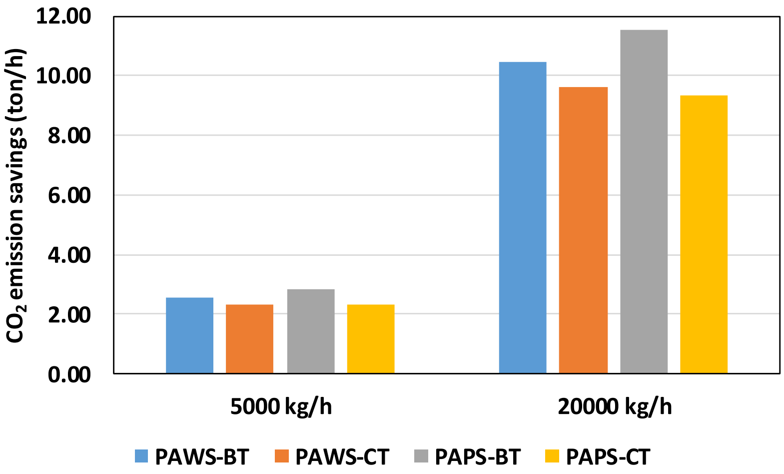

Figure 5.29 CO_2 savings estimate for four plant configurations at throughputs of 5,000kg/h and 20,000 kg/h

The higher CO_2 savings associated with the BPT based process is due to the their net heat export as steam. This assumes the availability of a nearby user for the exported steam and it contributes 10% and 27% to the CO_2 saving for the PAWS-BT process and PAPS-BT process respectively.

5.6 Conclusion

The process design and simulation covered in this chapter has been able to address some of the major challenges associated with the conversion of biomass (from an agricultural waste such as palm empty fruit bunch) to hydrogen or syngas via pyrolysis and reforming. This work was able to demonstrate how to model bio-oil based processes from PEFB by using an appropriate mixture of compounds representing the different macro-chemical families. The final heat integrated processes examined are able to use cogeneration (CHP) to increase their efficiency. With overall efficiencies ranging from 45 to 65%, this makes them quite enticing, probably giving them a competitive edge compared to fossil based processes. To carry this work further a detail study on equipment design and sizing needs to be carried out followed by a thorough economic evaluation and full life cycle assessment of the entire process.

Chapter 6 Autothermal Reforming Experiments in Packed Bed Reactor

6.1 Introduction

Bench scale ATR experiments were performed in a packed bed reactor using a variety of bio-feedstocks and catalysts in particle form (powder/broken down pellets). The aim was to investigate the feasibility and accompanying challenges associated with using different bio-feedstocks for H_2 production in an ATR process. Influence of factors such as feed composition, catalyst metal type (base or noble) and process parameters such S/C molar ratio, air flow and temperature were all examined. The experiments performed are presented in three main sections of this chapter i.e. 6.3, 6.4 and 6.5. Section 6.3 covers ATR of acetic acid using two Ni based catalysts prepared from broken down pellets. The performance of both catalysts was evaluated based on feed conversion, product distribution, H_2 yield, sensitivity to steam and feed flow and resistance to coke formation. The next series of experiments covered in section 6.4 were performed in order to determine the influence of using different chemical compounds (acetic acid, 2-butanone, furfural and m-cresol) and their mixture as feedstock in the ATR process with a prepared noble metal (Rh) catalyst powder. Finally in section 6.5, a more complex bio-oil surrogate was used as feedstock for H_2 production and tested on two prepared Rh based catalysts.

6.2 Output analyses (elemental balances)

Nitrogen flowing into the reactor as part of air was used as an internal standard and also functioned as an inert gas carrier. The actual molar flow, in mol/s, of the dry gases produced during the ATR experiments and measured by the on-line micro GC were determined by applying a N_2 balance. Using the known value of nitrogen flowing into the reactor (as part of air), $\dot{n}_{N_{2(in)}}$, and the measured nitrogen fraction in the dry gas output, $y_{N_{2(out)}}$, the total flowrate of dry product gas, $\dot{n}_{out_D}$, was calculated using the following equation:

$$\dot{n}_{out_D} = \frac{\dot{n}_{N_{2(in)}}}{y_{N_{2(out)}}} \qquad 6.1$$

The value of $\dot{n}_{out_D}$ obtained above was used to determine the molar flow of all the dry product gases, H_2, CO, CO_2, CH_4, and O_2 by substituting into the following equation:

$$\dot{n}_{i_{(out)}} = \dot{n}_{out_D} \times y_{i_{(out)}} \qquad 6.2$$

Where $\dot{n}_{i_{(out)}}$ and $y_{i_{(out)}}$ represent the molar flow and mole fraction (as measured by the micro GC) respectively of the particular dry product gas component.

The bio-feedstock conversion to C_1, C_2 and C_3 gases was determined by applying a carbon balance with the final equation written as:

$$X_{BF} = \left[\frac{\dot{n}_{out_D} \times (y_{CO}+y_{CO_2}+y_{CH_4}+2\times y_{C_2H_6}+2\times y_{C_2H_4}+3\times y_{C_3H_8}+3\times y_{C_3H_6})}{n\times \dot{n}_{BF\,(in)}}\right] \times 100 \qquad 6.3(a)$$

Where X_{BF} is the bio-feedstock conversion, %, n is the carbon coefficient in bio-feedstock (fuel) chemical formula, $C_nH_mO_k$, and $\dot{n}_{BF\,(in)}$ is the bio-feedstock flow rate in mol/s. It will be shown that the C_2 and C_3 gases were never detected in the reactor's product stream, therefore a simplified equation was used as follows:

$$X_{BF} = \left[\frac{\dot{n}_{out_D} \times (y_{CO}+y_{CO_2}+y_{CH_4})}{n\times \dot{n}_{BF\,(in)}}\right] \times 100 \qquad 6.3(b)$$

Water conversion is an important parameter used in gauging the overall extent of water consuming reactions (SR, WGS) during the ATR process. Water conversion was determined by applying a hydrogen balance. The total hydrogen produced as gaseous H_2 and hydrogen contained in organic gases (C_1 to C_3) is attributed to both hydrogen from the bio-feedstock and hydrogen from water. It is determined by calculating the difference between the total hydrogen produced and the hydrogen input from the converted fuel as shown in Eq 6.4. The value of water conversion so calculated was compared and found to be on par with that obtained by closing the balance on atomic O as proposed by other authors (Rennard et al., 2009).

$$\boldsymbol{X_{H_2O}} = \frac{\boldsymbol{(Total\ hydrogen\ molar\ flow\ in\ dry\ product\ gas\ (as\ H_2) - hydrogen\ molar\ flow\ in\ reacted\ feed\ (as\ H_2)}}{\boldsymbol{water\ flow(in)}} \times \mathbf{100} \qquad 6.4$$

Substituting all known variables into Eq. 6.4 we obtain

$$\boldsymbol{X_{H_2O}} = \left[\frac{\boldsymbol{\dot{n}_{out_D} \times \left(y_{H_2}+2\times y_{CH_4}+3\times y_{C_2H_6}+2\times y_{C_2H_4}+4\times y_{C_3H_8}+3\times y_{C_3H_6}\right) - 0.5m \times (\dot{n}_{BF\,(in)} \times X_{BF})}}{\boldsymbol{\dot{n}_{H_2O\,(in)}}}\right] \times \mathbf{100} \qquad 6.5(a)$$

Which in the absence of C_2 and C_3 species in the gas products, simplifies to:

$$X_{H_2O} = \left[\frac{\dot{n}_{out_D} \times (y_{H_2}+2\times y_{CH_4}) - 0.5m \times (\dot{n}_{BF\,(in)} \times X_{BF})}{\dot{n}_{H_2O\,(in)}}\right] \times 100 \qquad 6.5(b)$$

Where *m* is the atomic hydrogen coefficient in bio-feedstock (fuel) chemical formula. Oxygen conversion was calculated directly from known flows using the following equation:

$$X_{O_2} = \frac{\dot{n}_{O_2(in)} - \dot{n}_{O_2(out)}}{\dot{n}_{O_2(in)}} \times 100 \qquad 6.5$$

Where $\dot{n}_{O_2(in)}$ is the O_2 flow into the reactor (as part of air) and $\dot{n}_{O_2(out)}$ is the O_2 flowing out as measured by the GC.

Hydrogen yield was expressed either as a mass fraction of the input fuel (wt%), a mole fraction of input fuel (mol/mol), or mole fraction per input carbon (mol/mol C) according to Eq 6.7, 6.8 and 6.9 respectively.

$$Y_{H_2(wt\%)} = \frac{\dot{n}_{H_2(out)} \times 2.016}{\dot{n}_{BF\,(in)} \times M_{BF}} \times 100 \qquad 6.6$$

$$Y_{H_2(mol)} = \frac{\dot{n}_{H_2(out)}}{\dot{n}_{BF\,(in)}} \qquad 6.7$$

$$Y_{H_2(mol\,C)} = \frac{\dot{n}_{H_2(out)}}{n \times \dot{n}_{BF\,(in)}} \qquad 6.8$$

Where M_{BF} is the molar mass of the bio-feedstock in g mol^{-1}.

H_2 selectivity in the absence of C_2 and C_3 species in the product gases is given by:

$$S_{H_2} = \frac{\dot{n}_{H_2(out)}}{\dot{n}_{H_2(out)} + \dot{n}_{CH_4(out)}} \times 100 \qquad 6.9$$

The selectivity of the C_1 gases CO, CO_2 and CH_4 was calculated using the following equations:

$$S_{CO} = \frac{y_{CO}}{y_{CO} + y_{CO_2} + y_{CH_4}} \times 100 \qquad 6.10$$

$$S_{CO_2} = \frac{y_{CO_2}}{y_{CO} + y_{CO_2} + y_{CH_4}} \times 100 \qquad 6.11$$

$$S_{CH_4} = \frac{y_{CH_4}}{y_{CO} + y_{CO_2} + y_{CH_4}} \times 100 \qquad 6.12$$

For the different bio-feedstocks used, the hourly space velocity was calculated both as weight hourly space velocity (WHSV, h^{-1}) and gas hourly space velocity (GHSV, h^{-1}) using the following equations:

$$WHSV = \frac{Total\ mass\ flow\ of\ all\ feed\ \ (kg/h)}{Mass\ of\ catalyst\ (kg)} \qquad 6.13$$

$$GHSV = \frac{Total\ volumetric\ flow\ of\ all\ feed\ (m^3/h)}{volume\ of\ catalyst\ (m^3)} \qquad 6.14$$

The volumetric flow rates used in calculating the GHSV was determined for all feed (fuel, water and air) at standard conditions of 25 °C and 1 atm.

6.3 Autothermal reforming of acetic acid in a packed bed reactor using Ni-Al ‘18 wt% NiO/Al_2O_3’ and Ni-CaAl ‘15 wt% NiO/CaO/Al_2O_3’ catalysts

Autothermal reforming of acetic acid was performed in a packed bed reactor using Ni-Al and Ni-CaAl catalysts. Both catalysts were supplied by Twigg Scientific & Technical Ltd (UK) as pellets of 11 and 16 mm diameter respectively. The catalysts were crushed to obtain a particle size of 0.355 – 1 mm for this experimental study. The small catalyst size was used in order to minimise any mass transfer related (diffusion) resistance. The possibility of having a pressure drop develop in the reactor during experiments was dispelled as only about 1 g of catalyst was used. Also, a leak/flow test was performed before each experiment to verify this claim. The ATR experiments were design to test the activity of both catalysts and their suitability for hydrogen production by evaluating feed conversion, product distribution, H_2 yield, sensitivity to steam and feed flow and resistance to coke formation.

6.3.1 Experimental procedure

Details of the experimental rig set up and product gas analysis equipment are given in Chapter 3. At the beginning of every experiment, the chiller attached to the rig was switched on and set to -2 °C. All the pipes and connections leading from the vaporisers to the moisture trap were rinsed with acetone to remove any trapped condensates from previous experiments. Crushed catalyst, about 1.0 g, was loaded into a clean 316 stainless steel tube reactor with 10 mm internal diameter. The catalyst was held in place between two 4 μm quartz wool plugs (m.p. 1050 °C) obtained from Fisher Scientific UK Ltd weighing 0.09 g each. Blank experiments were performed using sand (SiO_2) obtained from Sigma-Aldrich, Germany, with a 50 – 70 mesh size. The loaded reactor was then placed in tube furnace (Elite Thermal Systems TSV10/20/85) and connected to the rest of the rig. The whole set up was leak tested under a N_2 flow of 200 cm^3/min using a flowmeter, ADM1000, from Agilent

Technologies. The absence of a leak was confirmed by measuring the same N_2 flow at various points of the rig especially at the reactor exit and at the end of the moisture trap. Once the chiller reached the set temperature of -2 °C, the electric tube furnace was switched on and set to the desired reaction temperature; which in this case ranged between 500 and 650 °C. Due to heat loss occurring between the furnace and the catalyst bed, the actual reaction temperature was controlled based on the readings of the reactor bed thermocouple shown in Figure 3.1. In most cases, the furnace temperature was higher than the reactor bed temperature by at least 10 °C. Depending on the experiment, the catalyst was either used in a fresh (oxidised) or pre-reduced state using hydrogen as the reducing agent. When reduction was required, the reactor bed was heated to 650 °C under continuous N_2 flow after which the N_2 was turned off and a 5 vol% H_2 (in N_2) gas mixture was turned on with its flow set at 200 cm^3/min. Catalyst reduction was monitored using the on-line micro GC and was deemed complete when the recorded H_2 reading increased to 5% up from an initial value of about 3% at the start of the process. Once the catalyst reduction was complete, the H_2 gas mixture was switched off and the system was flushed under high flow of N_2 until no H_2 was detected by the micro GC. While waiting to flush out any remaining H_2 in the process lines, the fuel and water vaporisers were turned on and set to 50 and 120 °C respectively. A heating tape set at 120 °C was also switched on to provide extra heating between the vaporisers and the reactor entrance. With no more H_2 detected by the micro GC and the vaporisers heated to their set temperatures, the N_2 flow was turned off and the ATR experiment was started first by switching on the water syringe pump, followed by the air mass flow controller and finally the bio compound’s syringe pump (acetic acid for this part of the experimental work). The Micro GC used was previously calibrated to detect H_2, N_2, O_2, CO, CH_4, CO_2, C_2H_6 (ethane), C_2H_4 (ethene), C_3H_8 (propane) and C_3H_6 (propene). For most experiments the acetic acid flow was set to 1.000 ml/h on the syringe pump. This value was only changed when the effect of flow rate (hourly space velocity) was investigated. The following equation was used to convert the acetic acid volumetric flow, V_h, in ml/h to the equivalent molar flow, $\dot{n}_{BF\,(in)}$, in mol/s:

$$\dot{n}_{BF\,(in)} = V_h\left(\frac{ml}{h}\right) \times 0.000001\left(\frac{m^3}{ml}\right) \times \frac{1}{3600}\left(\frac{h}{s}\right) \times \rho\left(\frac{kg}{m^3}\right) \times \frac{1}{M_m}\left(\frac{mol}{kg}\right) \qquad 6.15$$

Where

ρ is density (1049 kg/m^3 @ 25 °C) and M_m is the molar mass (0.060 kg/mol) of acetic acid.

Substituting into Eq. 6.12 we obtain

$$\dot{n}_{BF\ (in)} = 4.86 \times 10^{-6}\,\frac{mol}{s}$$

Which corresponds to the following elemental flows (for acetic acid only, $C_2H_4O_2$):

$$C\ =\ 9.72 \times 10^{-6}\,\frac{mol}{s}$$

$$H\ =\ 1.94 \times 10^{-5}\,\frac{mol}{s}$$

$$O\ =\ 9.72 \times 10^{-6}\,\frac{mol}{s}$$

The elemental flow rates were then used to determine and set the flows of the remaining reactants i.e. air and steam based on the molar S/C ratio and the air equivalence ratio.

The different possible reactions taking place during acetic ATR include decomposition, partial oxidation, steam reforming, complete oxidation, water gas shift, methanation and Boudouard reaction and are given in Eq. 6.16 – 6.25.

Decomposition

$$C_2H_4O_2 \rightarrow 2CO + 2H_2 \qquad 6.16$$

$$C_2H_4O_2 \rightarrow CH_4 + CO_2 \qquad 6.17$$

POX

$$C_2H_4O_2 + O_2 \rightarrow 2CO_2 + 2H_2 \qquad 6.18$$

$$C_2H_4O_2 + O_2 \rightarrow 2CO + 2H_2O \qquad 6.19$$

SR

$$C_2H_4O_2 + 2H_2O \rightarrow 2CO_2 + 4H_2 \qquad 6.20$$

COX

$$C_2H_4O_2 + 2O_2 \rightarrow 2CO_2 + 2H_2O \qquad 6.21$$

WGS

$$CO + H_2O \leftrightarrows CO_2 + H_2 \qquad 6.22$$

Methanation

$$CO + 3H_2 \leftrightarrows CH_4 + H_2O \qquad 6.23$$

Boudouard

$2CO \leftrightarrows CO_2 + C$ 6.24

The overall system of reactions taking place during acetic acid ATR is quite complex and may even include gas phase ketonization resulting in the formation of acetone (Eq 6.25)

$2C_2H_4O_2 \rightarrow C_2H_5O + H_2O + CO_2$ 6.25

As mentioned in Chapter 5, the air quivalence ratio is determined as a mole ratio given by

$$\lambda = \frac{Actual\ air-fuel\ mole\ ratio}{Stoichiometric\ air-fuel\ mole\ ratio} \quad 6.26$$

The stoichiometric air required for acetic acid complete oxidation is calculated using Eq. 6.21. This equation gives the stoichiometric O_2 ($\dot{n}_{O_2(stoic)}$) which is converted to stoichiometric air using Eq. 6.28.

$$\dot{n}_{air(stoic)} = 3.76 \times \dot{n}_{O_2(stoic)} + \dot{n}_{O_2(stoic)} \quad 6.27$$

Where air is assumed to be made up of a N_2/O_2 molar ratio of 3.76:1.

At the end of the ATR experiment, the acetic acid syringe pump was turned off and this was immediately followed by switching off the air flowmeter and turning on pure N_2 set at 200 cm^3/min. After which the water syringe pump was also turned off. The exhaust gas leaving the reactor (mostly N_2) was directed to the overhead extractor by turning a 2-way valve (see Figure 3.1) so as to by-pass the moisture trap. The furnace was then switch off and allowed to cool down to room temperature while N_2 flushing was performed overnight to get rid of any trapped vapours in the process line. The chiller was turned off as soon as the reactor bed temperature reached below 50 °C. The condensate trapped in the collector was removed and stored in a 10 ml glass vial for TOC analysis. On the following day, the stainless steel reactor was dismounted from the rig and used catalyst recovered and stored for elemental and electron spectroscopic analyses. A freshly prepared clean reactor was mounted on the rig for the next experiment while the unclean reactor was washed with soap and then rinsed with acetone before it was used again.

6.3.2 Conversion

To determine the reaction conditions needed for optimum hydrogen production, equilibrium calculations where performed using the Aspen Plus® software.

An adiabatic Gibbs reactor (RGibbs) was used with the amount of acetic acid, water and air flowing into the reactor adjusted depending on the particular experiment of interest. The RGibbs reactor calculates the equilibrium composition by using the Gibbs minimisation method as already discussed in Chapter 4 and 5. The Peng-Robinson equation of state with Boston-Mathias modification (PR-BM) was selected as thermodynamic property method due its applicability to high temperature gas-processing, chemical and petrochemical processes (Doherty et al., 2013, Halvorsen et al., 2015).

Table 6.1 is an example of the flow values input to Aspen corresponding to an acetic acid flow of 1.0 ml/h, S/C molar ratio of 2 and equivalence ratio of 0.35. The air flow was varied from 0 ($\lambda = 0$) to a maximum value of 4.62×10^{-5} mol/s corresponding to $\lambda = 1$. The value for maximum air flow was obtained by substituting the value for $\dot{n}_{BF\ (in)}$ into Eq 6.21 then substituting the value for $\dot{n}_{O_2(stoic)}$ into Eq. 6.27. The amount of steam input was determined based on the molar S/C ratio being examined and the carbon flow corresponding to $\dot{n}_{BF\ (in)}$.

Table 6.1 Input values used for equilibrium analysis in Aspen flows used for all reactants

Component	Flow, mol/s	Flow, ml/h
Acetic acid	4.86×10^{-6}	1.000
Water (S/C =2)	1.94×10^{-5}	1.257
O_2 needed for COX*	9.72×10^{-6}	1557.4
Air needed for COX**	4.62×10^{-5}	7412.0

*O_2 needed for COX (complete oxidation to CO_2 and H_2O) is calculated using Eq. 6.21

** Air is assumed to be made up of a N_2/O_2 molar ratio of 3.76:1

Figure 6.1 shows the product gas distribution obtained using the input values listed in Table 6.1. Maximum hydrogen occurs at $\lambda = 0.35$ with an equilibrium temperature of 570 °C; this value is used as the set point for experiments performed to determine the effect of each selected catalyst on conversion, yield, selectivity and carbon formation. The value for λ only varies when the S/C ratio is changed to 1 and 3.

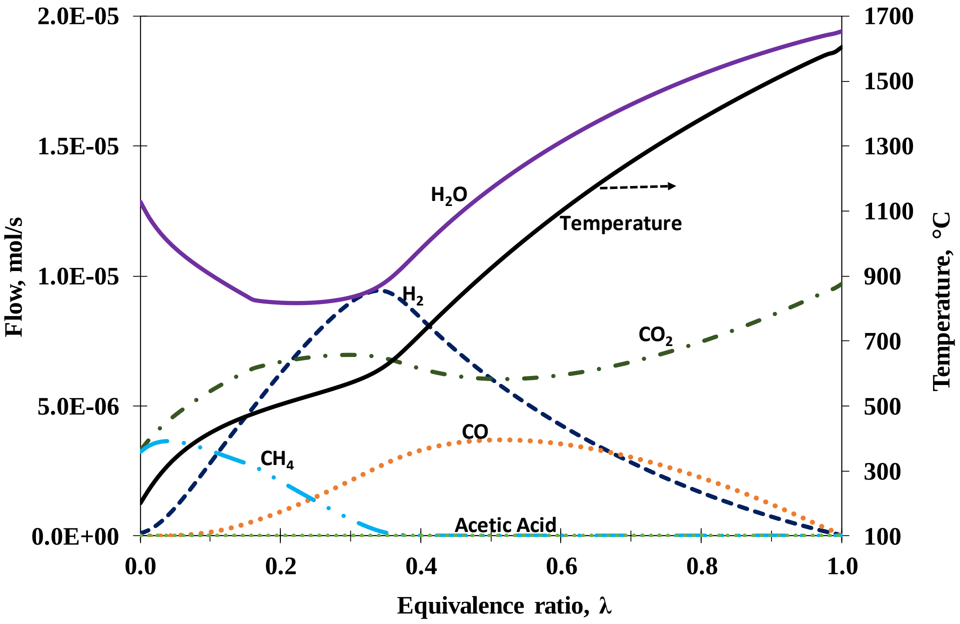

Figure 6.1 Thermodynamic equilibrium plots showing syngas composition and temperature obtained at S/C = 2 while varying λ from 0 to 1 for acetic acid ATR

Surface properties of the Ni-Al and Ni-CaAl catalysts are listed in Table 6.2. The Ni-CaAl catalyst has a slightly larger (moderate) surface area compared to the Ni-Al catalyst whose surface area is very low. The moderate surface area value for the Ni-CaAl catalyst can be attributed to its CaO content which has an initial high surface area of its own and could also be a result of the formation of mix phases formed during the support synthesis (Vagia and Lemonidou, 2008a).

The conversion of acetic acid, water and oxygen obtained using both catalysts and a blank run performed with sand are compared to equilibrium in Figure 6.2. The figure contains average values obtained over two experiments using 1.0 g of either catalyst or sand with acetic acid flow set a 1 ml/h, water flow at 1.257 ml/h (corresponding to a S/C mole ratio of 2) and air flow set at 22 cm^3/min (λ = 0.35).

Table 6.2 Surface properties of Ni-Al and Ni-CaAl catalysts

Catalyst	BET (m^2/g)	BJH surface area (m^2/g)	Pore size (nm)	Pore volume (cm^3/g)
Ni-Al (fresh)	4.251	4.485	1.372	0.012
Ni-Al (reduced)	3.756	4.125	1.255	0.011
Ni-CaAl (fresh)	24.239	19.39	0.738	0.052
Ni-CaAl (reduced)	31.652	32.145	1.215	0.061

The product gas exists the catalyst bed at the pre-set ‘thermoneutral’ temperature of 570°C measured by the reactor bed thermocouple.

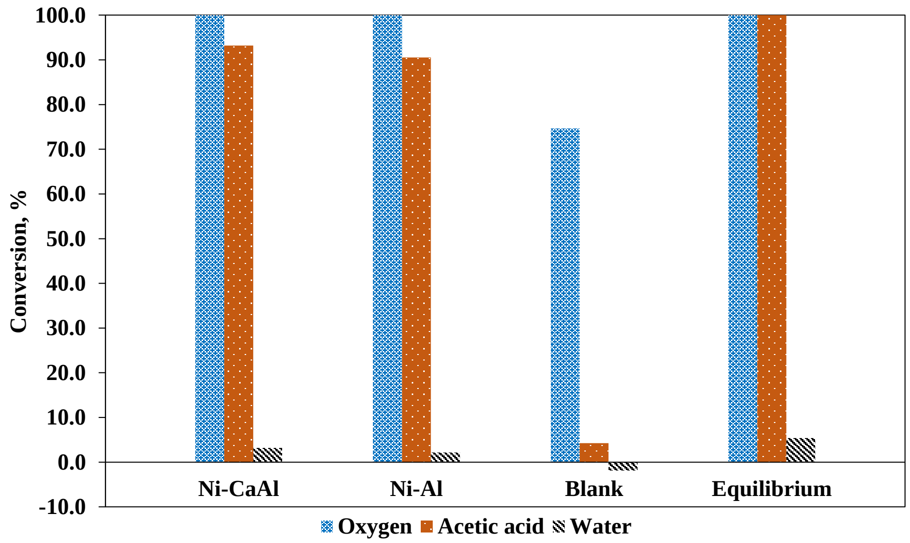

Figure 6.2 Conversion of acetic acid, water and oxygen using Ni-Al and Ni-CaAl catalysts at S/C 2, reactor exit gas temperature of 570 °C and pressure of 1 bar.

The oxygen conversion on both catalysts reached 100% showing their suitability in promoting oxidation reactions in spite of the relatively low reaction temperature used (compared to conventional SR which is usually carried out at 650 °C). Ni-Al catalyst however had a slightly lower acetic acid conversion of 91% compared to 93% obtained for the Ni-CaAl catalyst. A major consequence of this incomplete acetic acid conversion is the corresponding low water conversion due to reduced SR or WGS catalytic activity. The blank experiment (SiO_2 sand) had less than 5% of acetic acid decomposed to C_1 gases (CO, CO_2 and CH_4) at 570 °C. The water conversion for this experiment was negative suggesting that water was formed as a result of the possible ketonization and combustion reactions (Eq 6.21 and 6.25). It was not possible to detect acetone formation with the on-line micro GC used for this study. However, condensate TOC analysis showed 78 % liquid carbon recovery indicating more than 10 % of the initial acetic acid is at least involved in either thermal decomposition or ketonization reaction. Basagiannis and Verykios (2006) investigated the influence of temperature on the homogenous reaction of acetic acid in the presence of steam. They reported the formation of acetone and CO_2 at temperatures greater than 500 °C with H_2, CO and CH_4 formed as a result of thermal decomposition. The high acetic acid conversion obtained goes on to confirm selectivity of Ni-Al and Ni-CaAl catalysts in promoting acetic acid ATR. In terms of stability, the experiments involving Ni-Al catalyst were stopped after about 2 hour due to carbon formation and increased pressure drop in the reactor.

6.3.3 Product distribution and H_2 Yield

The product distribution obtained using Ni-Al and Ni-CaAl catalysts are shown in Figure 6.3. Both catalysts were tested in reduced state and in as-received (fresh, Ni in NiO form) state. It is common practice when performing SR experiments to reduce Ni catalyst with H_2 before their use. This is because it has been established that the Ni metal (not the oxide) provides the active site for reforming reactions (Bengaard et al., 2002, Rostrup-Nielsen, 1973).

The presence of oxygen in the reactor feed creates a strong oxidizing environment leading possibly leading to the oxidation of any previously reduced Ni on the catalyst surface. This raises the question of whether or not to reduce the catalyst before performing ATR experiments.

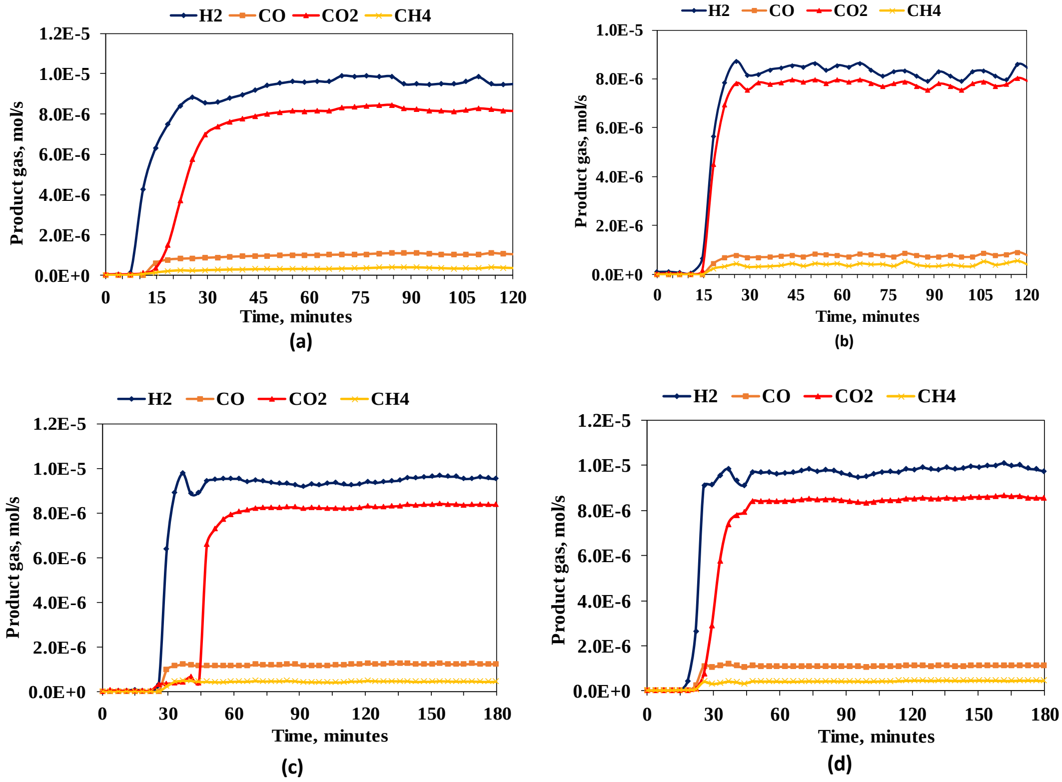

(a) (b) (c) (d)

Figure 6.3 Dry N_2-free product gas obtained during ATR of acetic acid flowing at 1 ml/h, S/C = 2, $\lambda = 0.353$ (Air flow = 22 ml/min), hot product gas at 570 °C and 1 bar. (a) Fresh Ni-Al catalyst. (b) Reduced Ni-Al catalyst. (c) Fresh Ni-CaAl catalyst. (d) Reduced Ni-CaAl catalyst.

The only ATR product gases detected by the micro GC were H_2, CO, CH_4, and CO_2, thus allowing simplified expressions for the carbon conversion, water conversion, hydrogen and carbon product (C_1 gases) selectivity to be used (no C_2 or C_3 species contributions, i.e. Eq. 6.3(b), 6.5(b), 6.10, and 6.11 – 6.13 respectively). This confirms the high selectivity for equilibrium products of both catalysts by promoting reforming reactions (SR and POX) over thermal decomposition. Figure 6.3 (a) and (b) show the results obtained using fresh and reduced Ni-Al catalysts. Both graphs have a different product distribution especially within the first 15 minutes with Figure 6.3 (a) having an 8 minute delay between the on-set on H_2 production and increase in CO, CH_4 and CO_2 production. Meanwhile Figure 6.3 (b) shows an almost concomitant rise in the production of H_2, CO, CH_4 and CO_2 after an initial delay of about 15 minutes into the experiment.

The experiments with Ni-CaAl catalysts showed a somewhat different trend. For Figure 6.3 (c) the spike in H_2 was followed immediately with an increase in CO and CH_4 production followed by a 15 minute delay before an increase in CO_2 was detected. Figure 6.3 (d) presented a case similar to the former with the main difference being a reduce time lap, about 4 minutes, between the increase in H_2, CO and CH_4 production and that of in CO_2. The main drawback observed for the Ni-Al catalyst was its high susceptibility to coking leading to significant pressure drop in the reactor making it difficult to continue the experiment beyond 2 hours before requiring shutdown.

The use of fresh catalyst for SR, POX and ATR of bio-feedstocks have been tested by other authors. SR of acetic acid using fresh 18 wt% $NiO/\alpha\text{-}Al_2O_3$ catalyst (so called 'auto-reduction' process) has been demonstrated previously by Cheng and Dupont (2013). The graphs shown in Figure 6.3 present quite a different picture to that obtained during acetic acid SR confirming that the mechanism for ATR is quite different form that observed during SR of acetic acid. The mechanism proposed by Cheng and Dupont (2013) suggests that acetic acid dissociates and adsorbs on the catalyst surface then undergoes decarboxylation giving rise to an initial spike in CO_2 before subsequent surface reactions produce H_2, CO and CH_4. Initial H_2 and CO produced by surface reactions desorb and react further with surface NiO to produced more reduced metal sites with H_2O and CO_2 formed as products.

$CH_3COOH_{(g)} \rightarrow (CHCOO)_s + H_s$ 6.28

$(CH_3COO)_s \rightarrow (CH_3)_s + CO_2$ 6.29

$(CH_3)_s \rightarrow C_s + 3H_s$ 6.30

$C_s + H_2O \rightarrow CO + H_2$ 6.31

$NiO_{(s)} + H_2 \rightarrow Ni + H_2O$ 6.32

$NiO_{(s)} + CO \rightarrow Ni + CO_2$ 6.33

The presence of oxygen in the feed changes the reaction sequence occurring on the catalyst surface during ATR. No detailed kinetic study has been performed to determine the reaction kinetics/mechanism of ATR (or POX) of oxygenates on nickel supported catalyst. Methane POX and ATR studies have revealed a mechanism in which the initial steps involve the adsorptive dissociation of CH_4 and O_2 on the catalyst surface (Lu et al., 1998b). A similar mechanism can be assumed in which the gaseous acetic acid and O_2 decompose by C – C, C – O and O – O bond cleavages on the top catalyst layer leading to the adsorption of CH_3, CO, OH and O radicals. H_2 is formed by surface reactions and the H_2 gas released moves further down the bed reacting initially with NiO according to Eq. 6.32. Only small concentrations of H_2, CO_2 and CH_4 were detected at the beginning of all the experiments shown in Figure 6.3 with CO only appearing after the spike in H_2 production. This suggests that the decarboxylation reaction is significantly impaired by the presence of adsorbed oxygen. As the reaction proceeds and the concentration of reduced Ni sites increase, gaseous acetic acid and water dissociate and adsorb on these active reforming sites releasing more H_2 and CO. High concentration of adsorbed C and O atoms leads to the formation and desorption of CO_2. Meanwhile some of the adsorbed CH_3 recombines with H and desorbs as CH_4. The appearance of CO, CH_4 and CO_2 therefore coincide with the increase in surface Ni concentration and adsorbed C and O atoms. The late appearance of CO_2 indicates that it is formed from surface and surface/gas phase reactions involving adsorbed C and O with gaseous CO. Diffusion resistance of the gaseous feed and gaseous products through the catalyst bed is not taken into account in the preceding discussion. A detailed characterisation of all reaction products formed 30 minutes into the ATR process and accurate transient studies will help elucidate the actual reaction mechanism taking place.

The average dry product gas composition and hydrogen yield obtained using Ni-Al and Ni-CaAl in both fresh (F) and reduced (R) states are shown in Figure 6.4. The average is taken over several stable results for each gas. Ni-CaAl catalyst appears to be a more active ATR catalyst with average H_2 production reaching 94% and 90% of the expected equilibrium value for the reduced (R) and fresh (F) catalyst respectively; compared to the 86% obtained for the fresh and reduced Ni-Al catalyst. The almost similar results obtained for the fresh and reduced forms of both catalysts confirms that the fresh catalyst is reduced by acetic acid, ‘auto-reduction’, at the start of the experiment to generate active Ni sites.

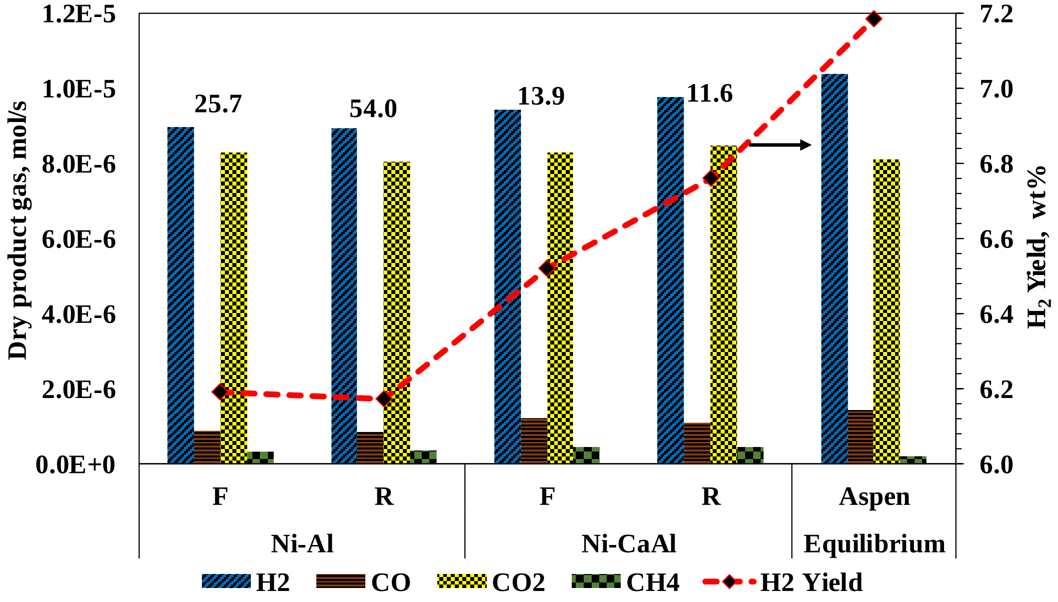

Figure 6.4 Average nitrogen-free dry product gas composition obtained during ATR of acetic acid flowing at 1 ml/h using Ni-Al and Ni-CaAl catalyst in fresh (F) and reduced (R) state. S/C = 2, $\lambda = 0.353$ (Air flow = 22 ml/min), 570 °C and 1 bar. Catalyst coke measured in mg/g(cat).h included as data label for each catalyst tested.

The ‘auto-reduction’ continues until an equilibrium Ni/NiO concentration is reached and steady production of synthesis gas is achieved. This is confirmed by the presence of both Ni and NiO peaks in the XRD patterns of a sample Ni-Al catalyst used in fresh, Ni-Al(F), and reduced, Ni-Al (R) states (see Figure 6.5). The XRD results for Ni-CaAl catalyst are not included due to its large amorphous phase content (Appendix C). The presence of oxygen in the feed, however, does not cause significant oxidation of the reduced catalyst as no NiO is detected in the used Ni-Al(R) catalyst shown in Figure 6.5. This suggests that the oxygen in the feed is completely consumed by reforming reactions and any NiO formed reacts almost immediately with H_2 and CO (Eq 6.32 and 6.33).

The maximum H_2 yield obtained for the results shown in Figure 6.4 was 6.8 wt% for the Ni-CaAl catalyst which is well short 13.4 wt%, the theoretical maximum H_2 yield possible from the SR of acetic acid. Medrano et al. (2008) reported a H_2 yield of 13.1 wt% for the steam reforming of acetic acid using a co-precipitated Ni/Al/Ca catalyst in a fluidized bed reactor operated at 650 °C and a S/C molar ratio of 5.58.

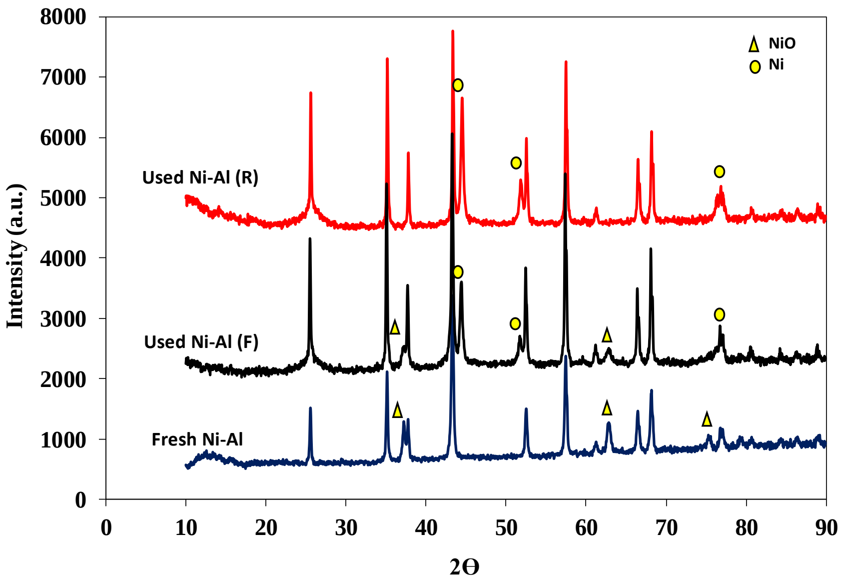

Figure 6.5 XRD patterns of Ni-Al catalyst showing the fresh catalyst (Fresh Ni-Al), used fresh catalyst (used Ni-Al (F)) and used reduced catalyst, (used Ni-Al (R)). All unlabelled peaks belong to the α-Al_2O_3 support

The better performance of the Ni-CaAl catalyst was expected as the addition of CaO to the Al_2O_3 support hinders the formation of the spinel compound, $NiAl_2O_4$, which is known to impair the reducibility of NiO; while at the same time improving the same property by forming $CaAl_2O_4$ (Cabello et al., 2014, Lu et al., 1998a). Another reason for the better performance of Ni-CaAl catalysts was its superior resistance to coke formation; with only 13.9 and 11.6 mg/g(cat).h coke deposit detected compared to 25.7 and 54.0 mg/g(cat).h deposited for the Ni-Al catalyst in used fresh and reduced states respectively (see data labels on Figure 6.4). The fresh Ni-Al catalyst experienced far less coking compared to the reduced from. This suggests that the 'less' active fresh catalyst had a better resistance to coke formation than the more active reduced catalyst and this can be attributed to the presence of less active NiO sites on the surface of the used fresh catalyst (see Figure 6.5). Based on these observations, all further reforming experiments were performed using only fresh 'unreduced' catalyst. The eventual success of an ideal ATR depends on the ability of the catalyst to promote the exothermic oxidation reaction(s) needed to support the endothermic steam reforming reaction. This ability was tested for the fresh Ni-Al and Ni-CaAl catalysts by performing POX experiments (no steam) while maintaining the same reactor temperature, acetic acid flow and air flow as discussed above. The dry N_2-free product gas obtained for both catalysts after 3 hours is shown in Figure 6.6. A similar trend in product gas composition variation is witnessed for both catalysts with the only significant difference being the extra 7 minutes required by the Ni-CaAl catalyst to record an increase in H_2 gas production.

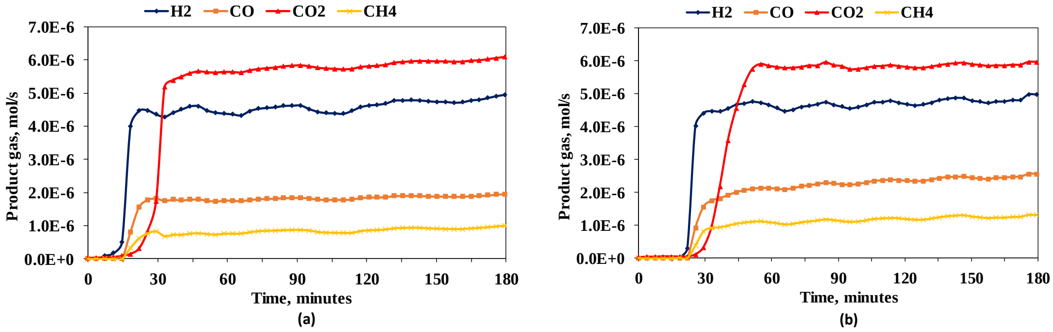

Figure 6.6 Dry N_2-free product gas obtained for POX of acetic acid flowing at 1 ml/h, $\lambda = 0.353$ (Air flow = 22 ml/min), 570 °C and 1 bar. (a) Fresh Ni-Al catalyst (b) Fresh Ni-CaAl catalyst.

Table 6.3 provides a summary of the POX experiment results reported in Figure 6.6. The Ni-Al catalyst had a poor acetic acid conversion of just 78% compared to 91% obtained for the Ni-CaAl catalyst.

Table 6.3 Result summary of the POX of acetic acid on fresh Ni-Al and Ni-CaAl catalysts. Acetic acid flow, 1 ml/h, $\lambda = 0.353$ (Air flow = 22 ml/min), hot product gas at 570 °C

Catalyst	Conversion, %		H_2O formation efficiency**, %	Product distribution, mol%				H_2/CO	Carbon, mg/g(cat).h	
	HAc*	O_2		H_2	CO	CO_2	CH_4		POX	ATR
Equilibrium	100	100	100	38	19	39	4	2.05	0	0
Ni-Al	78	97	61	35	14	44	7	2.50	50.1	25.7
Ni-CaAl	91	99	53	33	17	41	8	2.01	34.9	13.9

* Acetic acid

** Calculated by dividing the actual amount of water formed during the experiment by the amount of water predicted by thermodynamic equilibrium

The low acetic acid conversion for the Ni-Al resulted in significant coking measured at 50.1 mg/g(cat).h (17 wt% on catalyst) compared to 34.9 mg/g(cat).h (10 wt%) for Ni-CaAL. However the Ni-Al catalyst had a better H_2 selectivity with higher H_2/CO ratio of 2.50 (see Table 6.3). This implies that the Ni-Al catalyst is more active in promoting the WGS reaction. This catalyst is also more selective for the complete oxidation reaction as confirmed by the slightly higher concentration in H_2O and CO_2. Meanwhile the Ni-CaAl catalyst is more active in promoting SR reaction and so performs better under ATR condition resulting in its higher hydrogen yield. Both catalysts perform better in ATR compared to POX as evidenced by the reduced coking for the former (see Table 6.3). The presence of steam during ATR helps to create a stronger oxidizing/reforming environment which proves beneficial for both catalysts.

6.3.4 S/C mole ratio

The influence of varying the S/C ratio on the ATR of acetic acid using fresh Ni-Al and Ni-CaAl catalyst was investigated and the results shown in Figure 6.7.

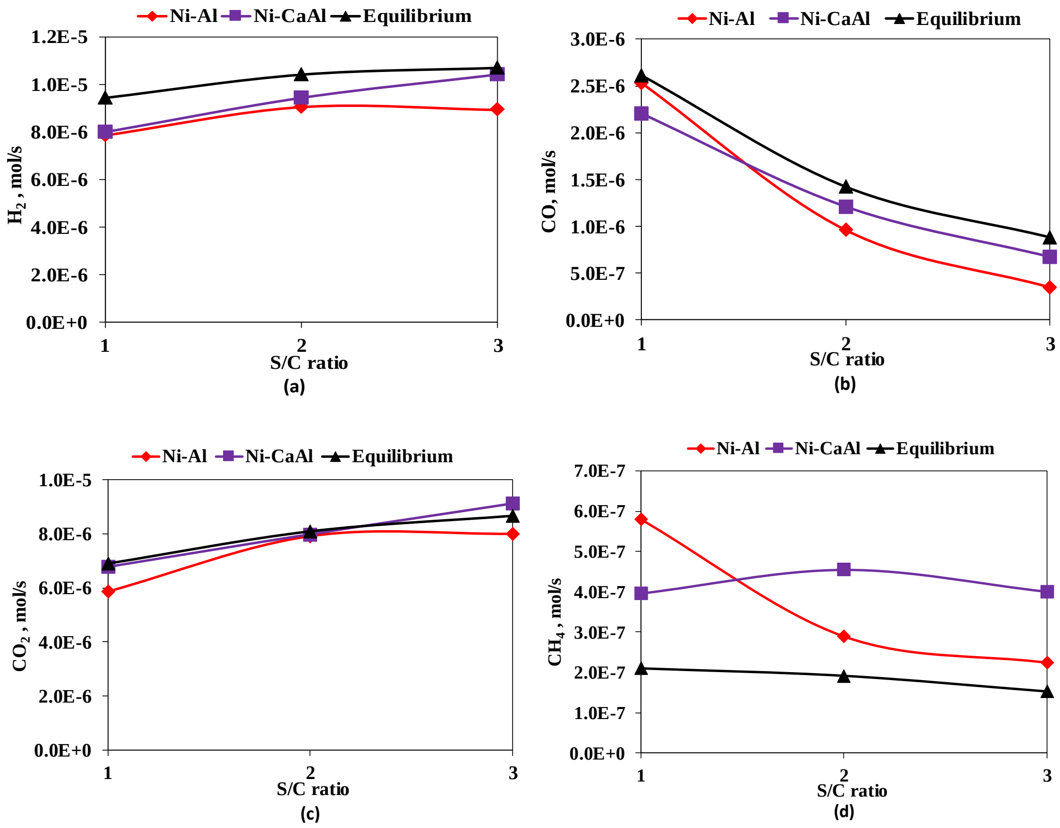

Figure 6.7 Effect of S/C ratio on average syngas composition compared to thermodynamic equilibrium values. Acetic acid flow, 1 ml/h with corresponding λ and temperature values of (0.340, 610 °C), (0.353, 570 °C) and (0.374, 545 °C) for S/C ratio of 1, 2 and 3 respectively.

Based on previous equilibrium studies it is expected that as S/C ratio increases, the amount of H_2 and CO_2 produced should increase while the amount of CO produced reduces simultaneously. This is mainly due to the shift of the WGS reaction towards H_2 and CO_2 production as explained by Le Chatelier's principle. The trend obtained for H_2, CO and CO_2 was as expected for both catalysts. CH_4 production however showed quite a different trend. For the Ni-Al catalyst, the CH_4 concentration was almost three time more than the equilibrium value expected for S/C = 1 and this reduced significantly as the S/C ratio was increased to 2 and 3. The Ni-CaAl catalyst on the other hand showed an increase in CH_4 production as the S/C ratio was increased from 1 to 2. This was followed by a slight decrease at S/C = 3. Methanation is therefore more severe with the Ni-CaAl catalyst than with Ni-Al. This confirms that the Ni-Al is more suitable to steam reform to H_2 than Ni-CaAl in the conditions tested here. Increasing the S/C ratio from 1 to 3 apparently has no significant effect on the crystalline phases present on the used catalyst as shown in Figure 6.8. Ni is the principal Ni-containing phase detected with only a minute NiO peak detected for the experiment carried out at S/C = 2. This confirms the earlier conclusion that most of the NiO in the fresh catalyst is reduced to Ni during ATR.

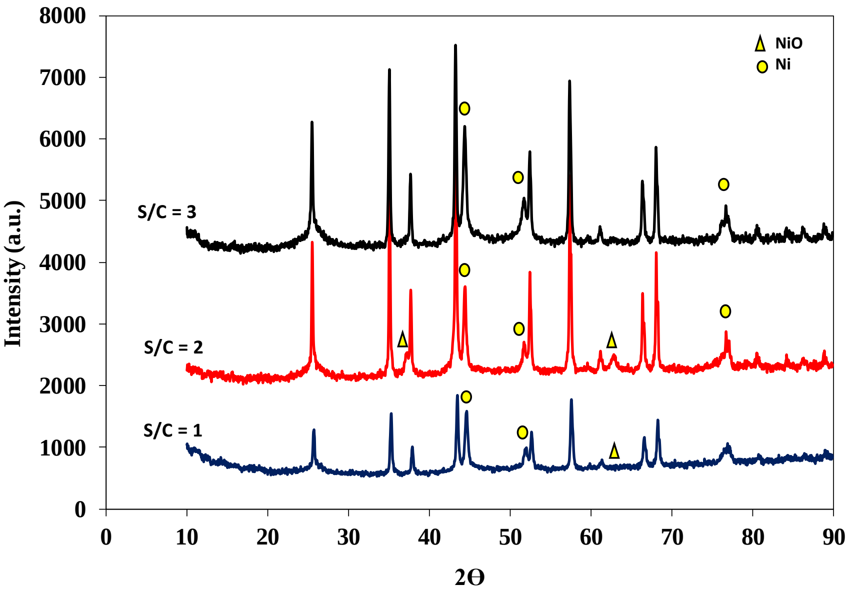

Figure 6.8 XRD patterns of Ni-Al catalyst for experiments performed using fresh catalyst at S/C 1, 2 and 3 and 1 bar. Acetic acid flow, 1 ml/h, with corresponding λ and temperature values of (0.340, 610 °C), (0.353, 570 °C) and (0.374, 545 °C). All unlabelled peaks belong to the α-Al_2O_3 support.

However, it should be expected that if for some reason higher air flows (higher λ) are used, then the concentration of surface NiO phase in the used catalyst will increase as seen in the work published by Medrano et al. (2008).

6.3.5 Space Velocity

The effect of varying the space velocity on the performance of the ATR process using fresh Ni-Al and Ni-CaAl catalyst was investigated. The space velocity (expressed as WHSV and GHSV) was investigated by varying acetic acid flow while keeping all other parameters constant at 1g of catalyst, S/C = 2, λ = 0.353, 570 °C and 1 bar. WHSV was defined as the total mass of feed flowing into the reactor at 20 °C divided by the mass of catalyst used (Eq. 6.13). The GHSV was calculated by diving the total volumetric flow rate of all feed entering the reactor by the volume of catalyst (Eq. 6.14). Volumetric flows for acetic acid, water and air were determined by substituting the known molar flow rates into the ideal gas equation at NTP (20 °C and 1 atm). Figure 6.9 shows the influence of space velocity on H_2 purity, H_2 yield and conversion of acetic acid, water and oxygen.

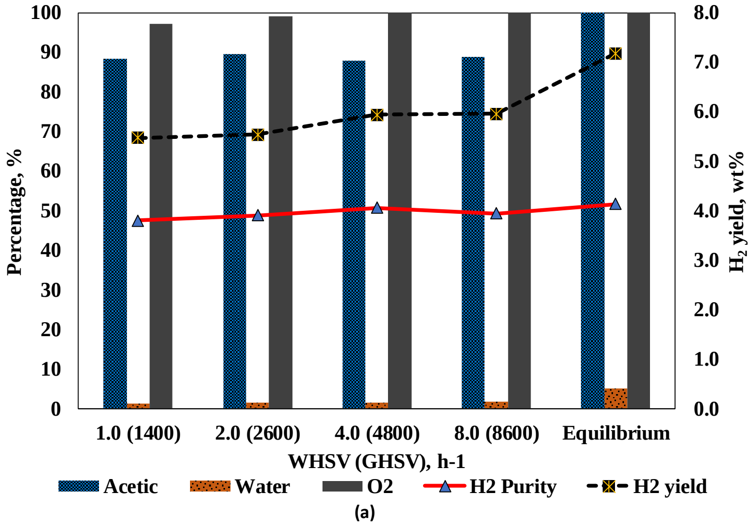

(a)

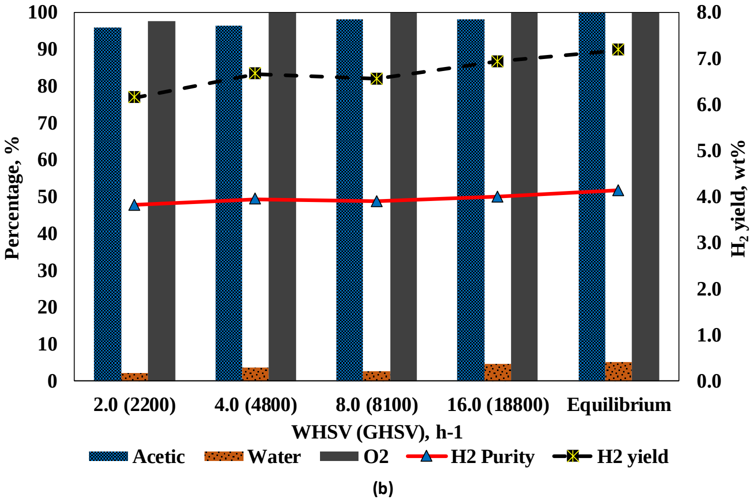

(b)

Figure 6.9 Influence space velocity on H_2 purity, H_2 yield, and conversion of acetic acid, water and oxygen. All flows at S/C = 2 and $\lambda = 0.353$ corresponding to a reactor exit temperature of 570 °C. (a) Ni-Al (b) Ni-CaAl

The Ni-CaAl catalyst performed better than the Ni-Al for all space velocities examined with a hydrogen yield average of 6.6 wt% compared to 5.7 wt% for the latter. Both catalysts have a similar and almost constant value for H_2 purity with Ni-CaAl having a higher acetic acid and water conversion. The lower water conversion for the Ni-Al catalyst is an indication of its affinity to promote acetic acid oxidation leading to lower H_2 yield and slightly higher CO_2 selectivity as shown in Figure 6.10. Figure 6.10 also shows the increase in catalyst coking, expressed in mg/g(cat).h, as the space velocity is increased. The coking rate increased in tandem with acetic acid flow rate into the reactor for both catalysts. The Ni-CaAl showed better resistance to coke formation with only about 1/3 of the value compared to Ni-Al catalyst for the same space velocity.

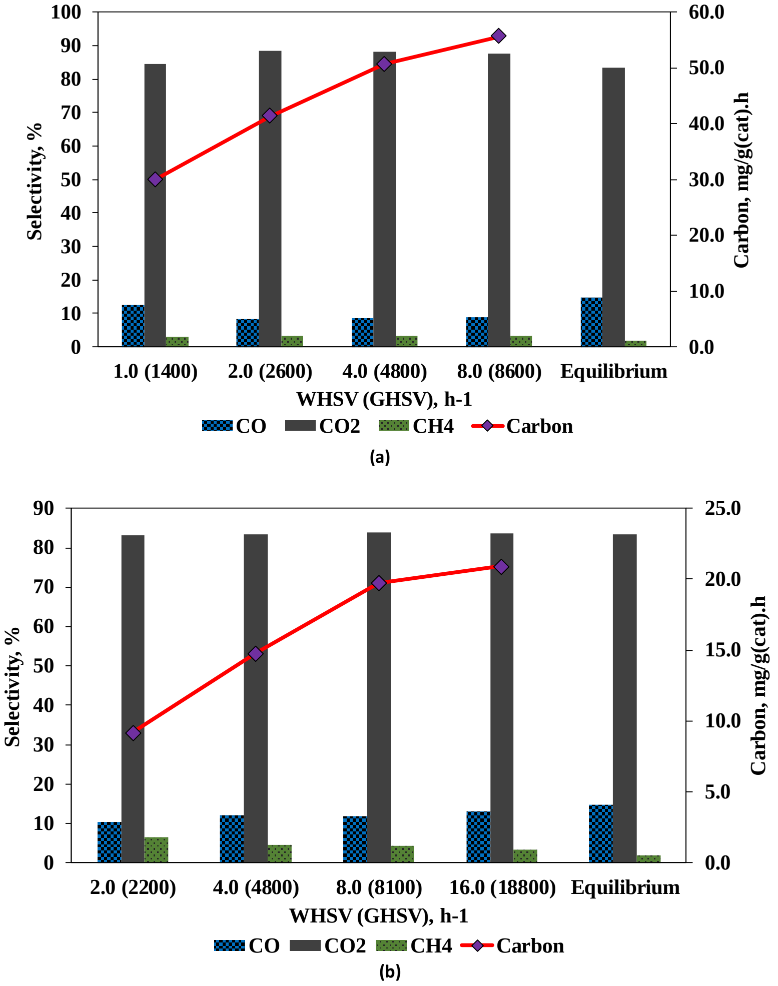

Figure 6.10 Effect of increasing WHSV (and GHSV), on CO, CO_2 and CH_4 selectivity and carbon formation. All flows at S/C = 2 and λ = 0.353 corresponding to a reactor exit temperature of 570 °C. (a) Ni-Al (b) Ni-CaAl

High flows caused rapid formation of coke on the Ni-Al catalyst and the experiment had to be stopped after 30 minutes due to pressure increase in the reactor. Gutierrez et al. (2011) reported a similar problem when Ni/Al_2O_3 catalyst was used for the ATR of ethanol. Both Ni-Al and Ni-CaAl catalysts however showed a steady decrease in the fraction of fuel carbon deposit formed with increase in space velocity implying the possible existence of maximum or saturation value.

This could also imply that the Ni-CaAl catalyst in particular performs better at higher feed flow. This can be due to the formation of hotspots in the catalyst bed which promote coke gasification. Formation of hotpots can however have a negative effect on the catalyst stability as it might lead to sintering and catalyst deactivation. Liguras et al. (2004) obtained similar results for their work on the autothermal reforming (which they referred to as ‘catalytic partial oxidation’) of ethanol using Ni/La_2O_3 supported over cordierite monoliths as catalyst. They reported a decrease in CO_2 selectivity accompanied by an increase CO selectivity as the space velocity was increased from 3620 – 9055 h^{-1} at 600 °C, S/C ratio of 1.5 and O_2/C ratio of 0.305. They attributed this to the increase in catalyst bed temperature caused by the increase in feed flow as more ethanol is combusted within the same catalyst volume. The higher bed temperatures drive reforming reactions to completion and at the same time favour the reverse WGS reaction.

6.3.6 Coke formation

Catalyst coking and deactivation pose a major problem during ATR of bio-feedstocks. The overall low temperatures required for optimal H_2 production (less than 600 °C) hinder coke gasification reactions thereby promoting carbon deposition on catalyst. The influence of process parameters on the rate of coke formation have been discussed individually in the preceding sections. Figure 6.11 and Figure 6.12 show respectively pictures of the used Ni-Al and Ni-CaAl catalysts and their morphology as seen using SEM. Both catalysts were used in their fresh (oxidised) state for ATR experiments performed with a S/C molar ratio of 2 and $\lambda = 0.353$.

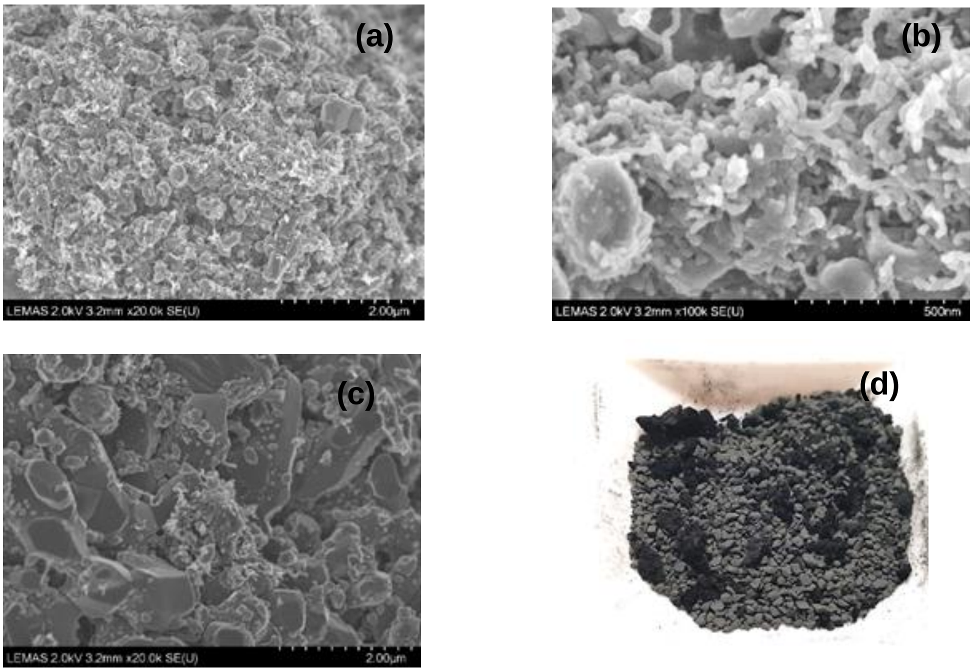

Figure 6.11 SEM images showing coking on Ni-Al catalyst. Acetic acid flow, 1 ml/h, 1 g of catalyst, S/C = 2, $\lambda = 0.353$ (Air flow = 22 ml/min), 570 °C and 1 bar.

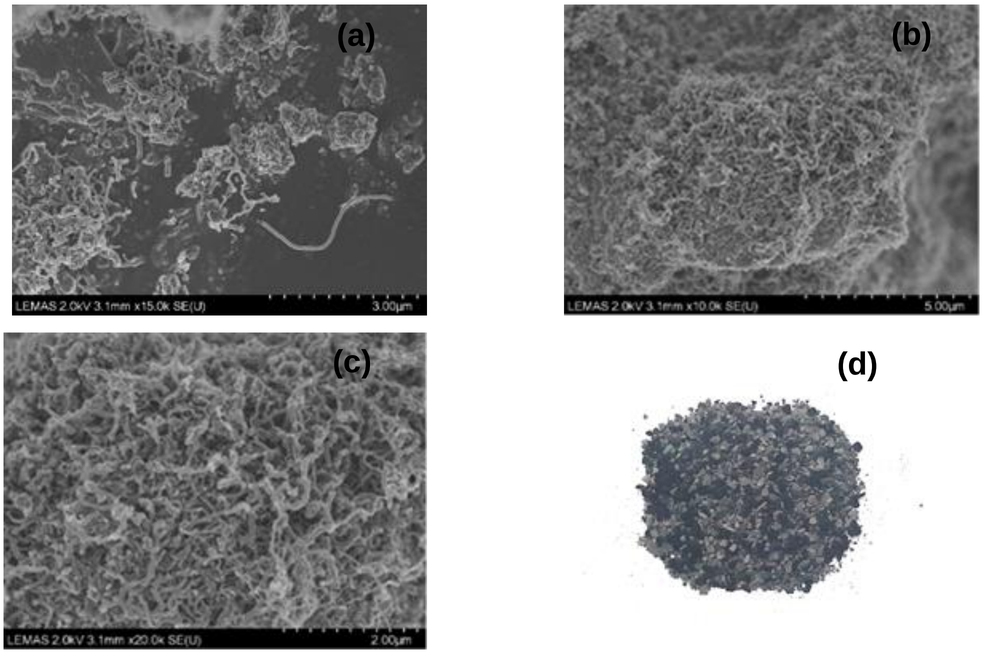

Figure 6.12 SEM images of showing coking on Ni-CaAl catalyst. Acetic acid flow, 1 ml/h, 1 g of catalyst, S/C = 2, $\lambda = 0.353$ (Air flow = 22 ml/min), 570 °C and 1 bar.

For both catalysts, coking resulted in the formation of a carbonaceous mass surrounding individual (or group of) catalyst particles. This carbon deposits consisted of a dense filamentous network as revealed by the SEM images. Coking is a major problem when Ni based catalysts are used for reforming, especially at low temperatures. Marquevich et al. (1999) reported rapid coking when commercial Ni catalysts was used in the SR of acetic acid at temperatures lower than 650 °C. One possible explanation is that the Boudouard reaction (Eq. 6.24) and the direct formation of carbon from hydrocarbon decomposition (cracking) are favoured below 700 °C (Gutierrez et al., 2011). Figure 6.11(d) is a picture of used Ni-Al catalyst in which a lumps of agglomerated coke particles measuring up to 5 mm can be identified. Coking was largely observed to have occurred only at the top of the catalyst bed exposed to the input feed. This led, in most cases, to clogging and massive pressure drop in the reactor reducing the experimental duration in most cases to less than 2 hours for the Ni-Al catalyst. In such cases, most of the catalyst particles found lower in the bed were almost without any coke as seen on Figure 6.11(d). Figure 6.11(c) is an SEM image of a used Ni-Al catalyst surface void of any carbon filaments. Cheng and Dupont (2013) reported a similar result for the integrated catalyst reduction and acetic acid SR process for which a similar 18 wt% NiO/α-Al_2O_3 catalyst was used. The Ni-CaAl catalyst on the other hand showed less coking and a better distribution of carbon deposit in the catalyst bed (see Figure 6.12(d)). The carbon deposits formed in most cases were about the same size as the individual catalyst particles. No bed clogging was witnessed when using this catalyst for all experiments performed, lasting up to three hours.

6.3.7 Summary

Ni-Al and Ni-CaAl catalyst both showed excellent selectivity for reforming products during acetic acid ATR experiments. The main drawback with the Ni-Al catalyst was its susceptibility for coking unlike the Ni-CaAl catalyst which showed a higher resistance to coke formation. This led to lower acetic acid conversion and hydrogen yield for the Ni-Al catalyst. Experiments performed using fresh and reduced forms of both catalyst resulted in a similar product gas composition for both catalyst. However, the fresh Ni-Al catalyst formed less coke compared to the reduced form.

6.4 Autothermal reforming of acetic acid, 2-butanone, m-cresol, furfural and their mixture in a packed bed reactor using Rh-Al ‘1% Rh/Al_2O_3’ catalyst

Autothermal reforming of acetic acid, 2-butanone (methyl ethyl ketone), furfural, m-cresol and their mixture was examined in a packed bed reactor using Rh-Al catalyst. The aim was to test the performance of a noble metal catalyst in ATR experiments using compounds with different chemical structures as bio-feedstock. These compounds were selected as representative compounds found in bio-oils obtained from biomass pyrolysis. Acetic acid and 2-butanone can be derived from cellulose decomposition, furfural from hemicellulose (pentosane) decomposition and m-cresol from the decomposition of lignin (phenolics). To render results comparable amongst the different bio-feedstocks, a constant carbon molar flow was maintained for all experiments. Acetic acid flowing at 1 ml/h was selected as the reference. This corresponds to a carbon molar flow of 9.71×10^{-6} mol/s. The other bio-feedstocks had their flows adjusted using the Excel solver function to obtain the same carbon flow value. Table 6.4 shows the flow values used for the different bio-feedstocks tested in this study.

Table 6.4 Experimental flows for bio-feedstocks

Component	Density*, g/ml	Carbon flow, mol/s	Flow, ml/h	Error, %
Acetic (HAc)	1.049	9.71×10^{-6}	1.000	-
2-butanone	0.805	9.71×10^{-6}	0.781	0
Furfural	1.16	9.69×10^{-6}	0.578	0.25
M-cresol	1.03	9.69×10^{-6}	0.523	0.25
Mixture	1.01	9.69×10^{-6}	0.702	0

* Density measured at 25 °C

6.4.1 Catalyst characterisation

6.4.1.1 Surface area and pore size determination by N_2 sorption

As mentioned in (Chapter 3), the two catalysts prepared by wet impregnation for this research work were Rh-Al and RhCe-Al. Even though the RhCe-Al catalyst was used only for experiments described in section 6.5, characterisation results for both catalysts will be presented here as a means to facilitate result discussions. Some physical properties of both catalysts in fresh and reduced state and the γ-Al_2O_3 support are listed in Table 6.5.

Table 6.5 Physical properties of prepared catalysts

Catalyst	BET (m^2/g)	BJH surface area (m^2/g)	Pore size (nm)	Pore volume (cm^3/g)
Rh-Al (fresh)	228.8	245.4	6.001	0.4386
Rh-Al (reduced)	229.3	244.4	6.056	0.7930
RhCe-Al (fresh)	203.2	232.7	5.995	0.7576
RhCe-Al (reduced)	215.3	258.1	6.008	0.7688
γ-Al_2O_3	303.9	322.6	6.175	1.051

The large specific surface area exhibited by both catalysts is due to their high γ-Al_2O_3 content. The 25 to 35% drop in surface area of the prepared catalysts compared to the alumina support can be attributed mostly to attrition occurring during catalyst preparation. This might not have been the case if a different method such as incipient wetness was used. Specchia et al. (2010) prepared a 1 wt% Rh/Al_2O_3 catalyst by incipient wetness using 1 mm γ-Al_2O_3 spheres with surface area of 157 m^2/g. Their prepared catalyst showed minimal variation in properties with a surface area of 152 m^2/g and pore volume of 0.45 cm^3/g. The RhCe-Al catalyst showed more loss in surface area compared to the alumina support. Srivastava and Pant (2012) prepared a $1\%Rh/5\%CeO_2Al_2O_3$ catalyst to use for the oxidative steam reforming of bioethanol. They reported a BET surface area, pore volume and pore diameter of 203.7 m^2/g, 0.6 cm^3/g and 10.85 nm respectively. They attributed the lower surface area to the higher metal loading (Rh and Ce) and possible interactions between CeO_2 and the support which can lead to the blockage of smaller pores. Figure 6.13 (a) and (c) show the N_2-adsorption/desorption isotherm of the prepared Rh-Al and RhCe-Al catalysts respectively. According to the IUPAC classification, the isotherms obtained can be characterised as type IV with both exhibiting H_1 type hysteresis.

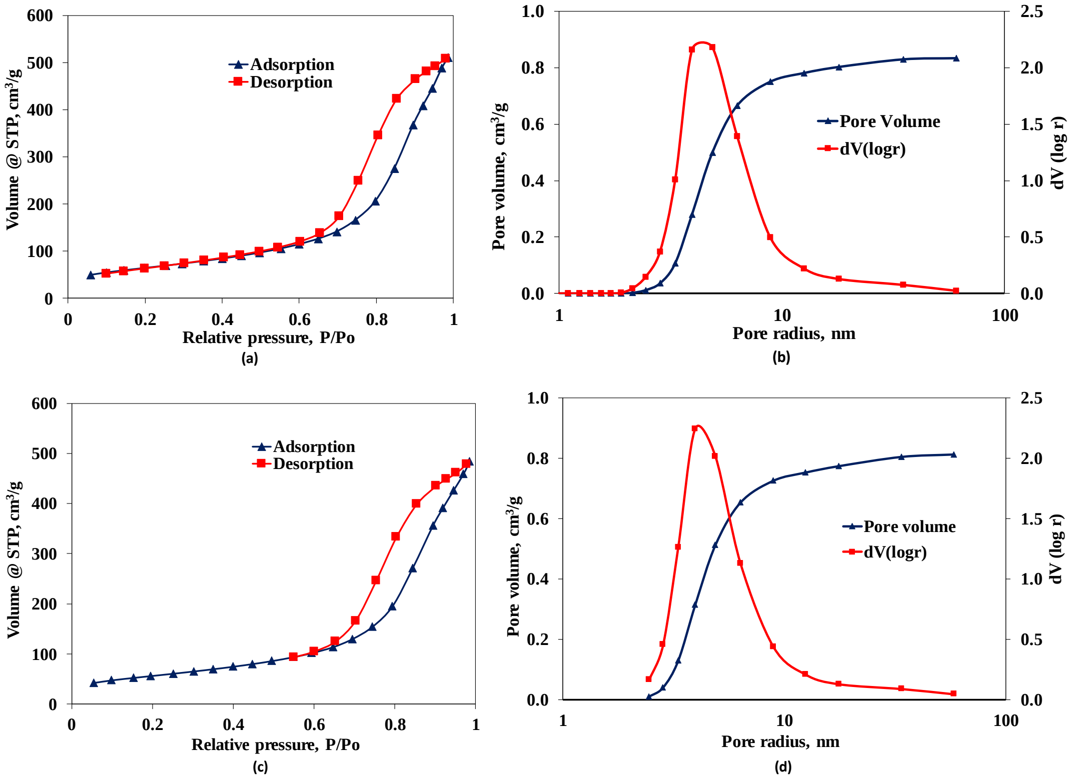

Figure 6.13 Surface property plots. (a) Nitrogen adsorption/desorption isotherm for Rh-Al. (b) Pore-size distribution for Rh-Al. (c) Nitrogen adsorption/desorption isotherm for RhCe-Al. (b) Pore-size distribution for RhCe-Al

The Type IV isotherms show multilayer covering and the hysteresis loops attest to the presence of mesoporosity in both catalysts. The hysteresis is a result of capillary condensation in mesopores which typically range from 2 – 50 nm (Groen et al., 2003). Pore size distribution, obtained using the BJH model is shown in Figure 6.13 b and d for Rh-Al and RhCe-Al catalysts respectively. It indicates a narrow distribution of mostly mesopores ranging from 2 to 14 nm and could either be ink bottle, trough shaped or cylindrical pores judging from the hysteresis (Alothman, 2012).

6.4.1.2 CFE-SEM

Figure 6.14 shows SEM images of the Rh-Al and RhCe-Al catalysts. Both surfaces show quite a uniform spongy morphology as expected of the γ-alumina support. Elemental dispersion, as determined EDX, for the Rh-Al and RhCe-Al catalysts is shown in Figure 6.15 and Figure 6.16 respectively. It can be seen from Figure 6.15 that Rh is not quite uniformly distributed on the catalyst surface examined.

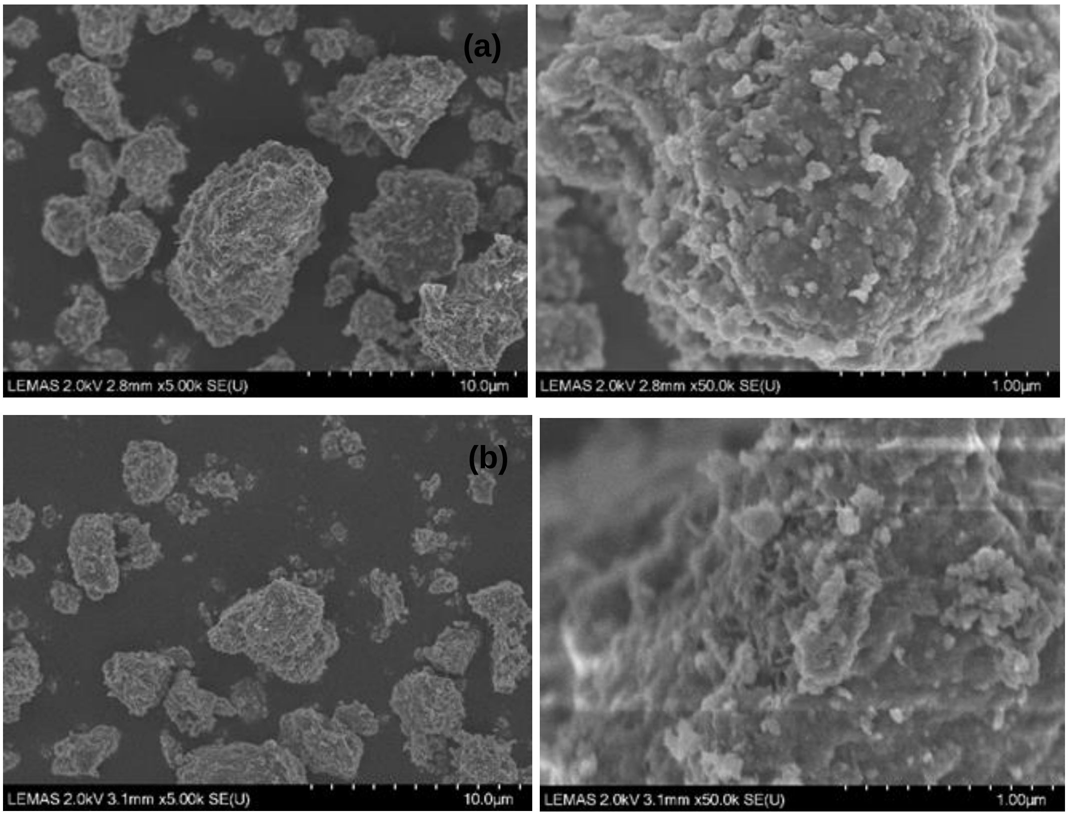

Figure 6.14 CFE-SEM images showing 5k and 50k magnification of catalysts prepared by wet impregnation and calcined at 650 °C. (a) Rh-Al catalyst. (b) RhCe-Al catalyst.

This might be attributed to the low metal loading used (1%) and the very gentle stirring maintained during the catalyst preparation. Roh et al. (2008) calculated a 32% dispersion for a 1% Rh/γ-Al_2O_3 catalyst using H_2 chemisorption studies. Rh dispersion was however slightly enhanced in the bimetallic RhCe-Al catalysts as seen on Figure 6.16.

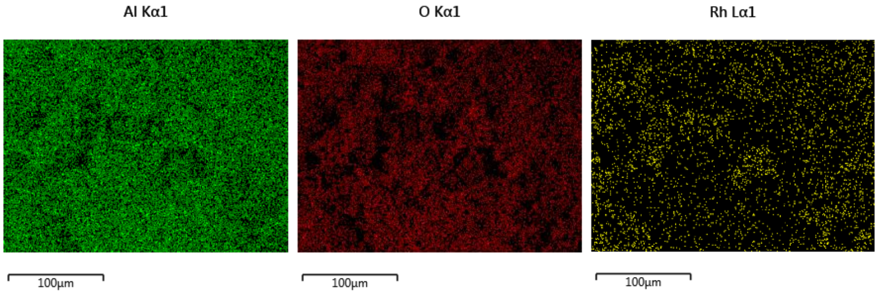

Figure 6.15 Elemental dispersion of the Rh-Al catalyst prepared by wet impregnation and calcined at 650 °C.

The presence of Ce in the RhCe-Al catalyst therefore increased the distribution of Rh on the alumina support. The increase in Rh dispersion in the presence of Ce has been reported by other authors (Li et al., 2009, De Rogatis et al., 2008).This observation is also in agreement with that made by Wang and Lu (1998) and Ocsachoque et al. (2011) in which Ce promoted Ni/Al_2O_3 catalyst showed increased metal dispersion and smaller particle (metal) size compared to the un-promoted catalyst.

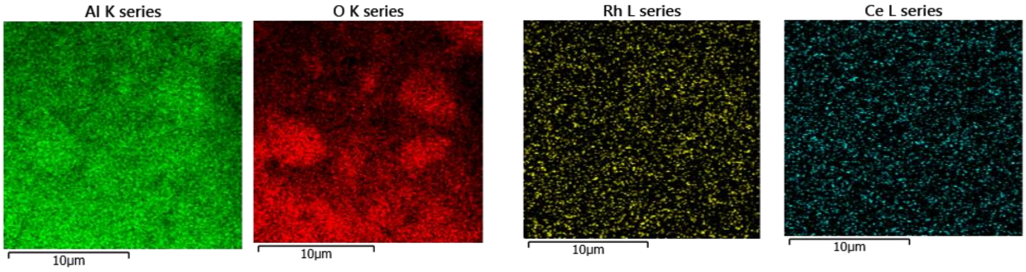

Figure 6.16 Elemental dispersion of the RhCe-Al catalyst prepared by wet impregnation and calcined at 650 °C.

6.4.1.3 FEG-S/TEM

The size of the Rh particles deposited on the support for the prepared catalysts were observed under TEM and shown in Figure 6.17.

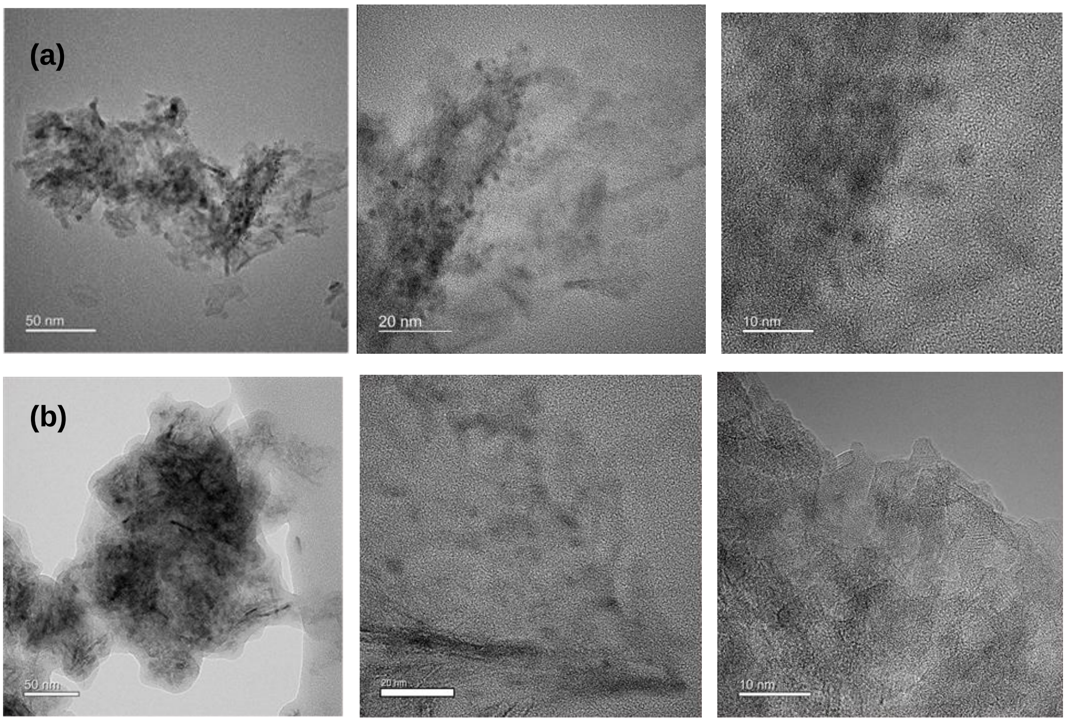

Figure 6.17 TEM images of prepared catalysts. a) Rh-Al catalyst b) RhCe-Al catalyst. Both catalyst prepared by wet impregnation followed by overnight oven drying at 100 °C then calcination at 550 °C for 4 hours.

The three different magnifications for the Rh-Al catalyst show dark spots indicative of the denser Rh particles with an approximate size ranging from 1 to 3 nm (see Figure 6.17a). It was more difficult to distinguish between Ce and Rh particles in the RhCe-Al catalyst. However, the metal particles detected by TEM had approximately the same size as those obtained for the Rh-Al catalyst (see Figure 6.17b). This suggests that the presence of the Cerium metal does not significantly affect the Rh deposition mechanism on the alumina support.

6.4.1.4 XRD

XRD plots for the prepared Rh-Al and RhCe-Al catalysts in fresh and reduced form are shown in Figure 6.18. The γ-Al_2O_3 support is responsible for most of the observed peaks with its characteristic peaks occurring at 2θ = 33.6°, 37.5°, 39.4°, 45.6°, and 67.4°. The low metal loading therefore made it difficult, for either the active metal or its oxide, to be significantly detected by XRD on the reduced and fresh forms of the prepared catalysts respectively. Oliveira et al. (2013) and Duarte et al. (2012) obtained similar XRD results for their prepared 1.5%Rh/Al_2O_3 and 0.5%Rh/Al_2O_3 catalysts respectively. They attributed the lack of Rh_2O_3 peak detection to the low metal loading and high dispersion on the γ-Al_2O_3. For catalysts using γ-Al_2O_3 support, Duarte et al. (2012) also reported that CeO_2 peaks were only detectable when their loading exceeded 6 wt%. The presence of CeO_2 on the fresh RhCe-Al catalyst can however be confirmed by the disappearance of the γ-Al_2O_3 (220) peak in favour of the CeO_2 (111) and (200) peaks.

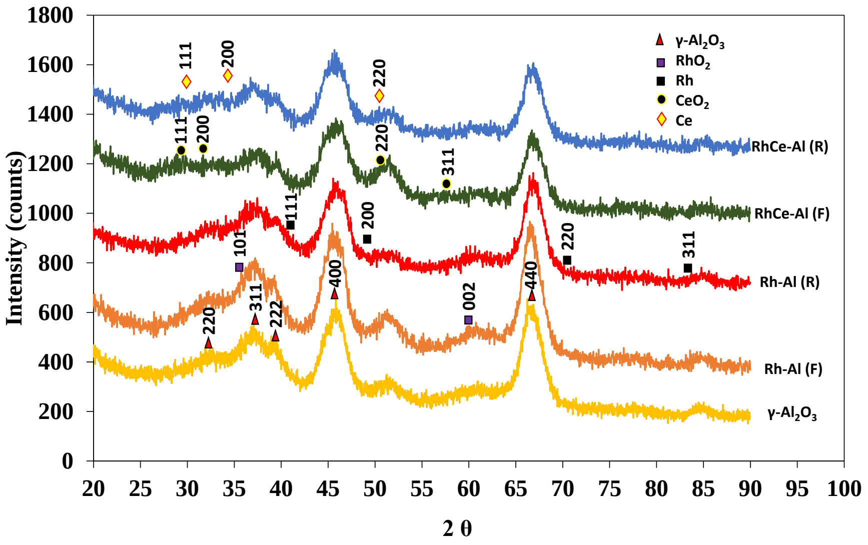

Figure 6.18 XRD patterns of the γ-Al_2O_3 support and prepared catalysts in fresh (F) and reduced (R) form

6.4.2 Experimental procedure

The overall procedure used for the ATR experiments for the different bio-feedstock is similar to that described in section 6.3.1. The Rh-Al catalyst was not reduced with H_2 prior to the ATR experiment and only 0.2g of catalyst was used. Each experiment was performed for 3 hours. The elemental flow rates listed in Table 6.4 were used to set the flows for the remaining reactants i.e. air and steam based on the molar S/C ratio and the equivalence ratio.

As with the case for acetic acid, different possible reactions also take place during 2-butanone, furfural and m-cresol ATR. The main reactions occurring are decomposition, partial oxidation, steam reforming, complete oxidation, water gas shift, methanation and Boudouard reaction.

6.4.3 Conversion

Aspen plus software was used to perform thermodynamic equilibrium analysis leading to the eventual selection of optimal conditions needed to perform the ATR experiments for each bio-compound used as feed. An Aspen adiabatic Gibbs reactor (RGibbs) was used with the amount of bio-feedstock set to the values listed in Table 6.4. The air flow was varied from $\lambda = 0$ to $\lambda = 1$ while the amount of steam input was determined based on the S/C molar ratio being examined. Figure 6.19 shows the equilibrium plots obtained for 2-butanone, furfural, m-cresol and the mixture (see Figure 6.1 for the corresponding acetic acid plot).

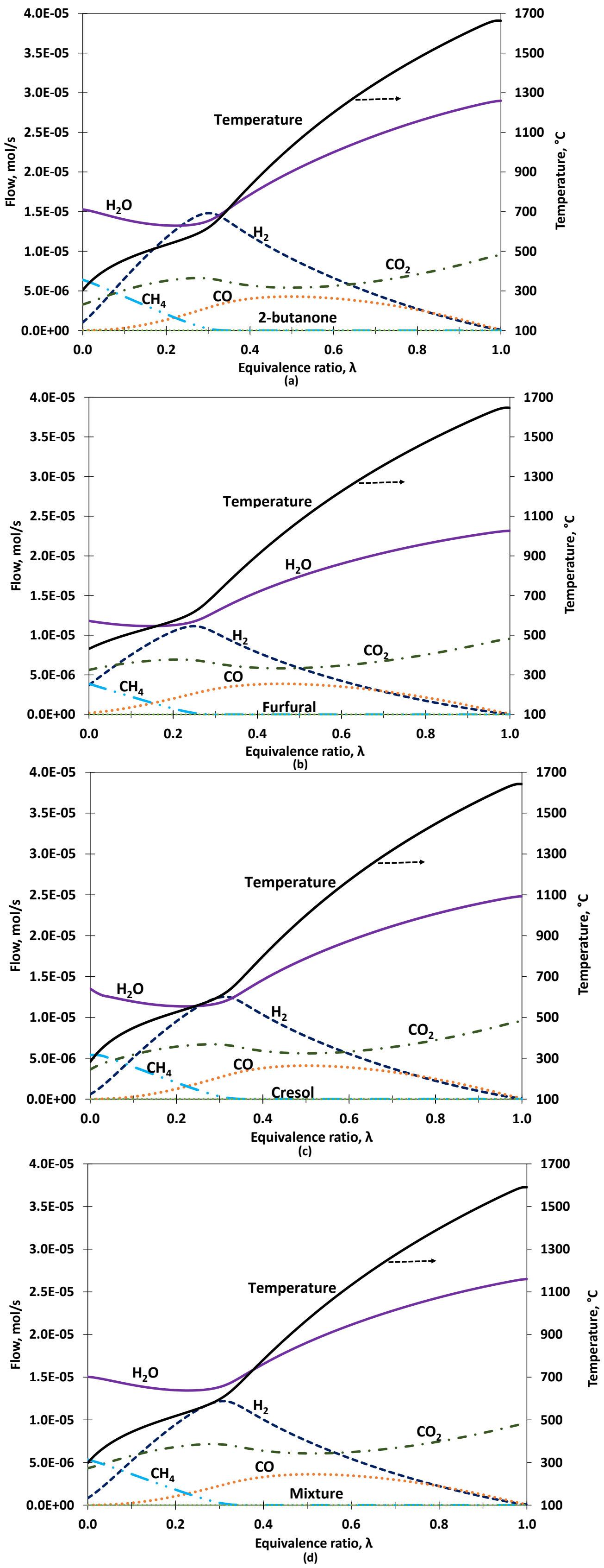

Figure 6.19 Thermodynamic equilibrium plots for showing syngas composition and temperature obtained at S/C = 2 while varying λ from 0 to 1. (a) 2-butanone (b) Furfural (c) m-cresol (d) Mixture

The overall variation in equilibrium composition is quite similar for the four bio-compounds and their mixture. Complete conversion of feedstock occurs for all values of λ examined. The optimal λ selected for each bio-compound is that corresponding to maximum H_2 yield.

Table 6.6 Summary of optimal parameters used for the different bio-compounds used as feedstock in the ATR experiments

Bio-feedstock	Water (ml/h)	Air (ml/min)	Equivalence ratio, λ	Temperature, °C
Acetic acid	1.257	21.9	0.35	570
2-butanone	1.257	24.6	0.29	604
Furfural	1.257	15.6	0.25	620
m-cresol	1.257	23.7	0.31	622
Mixture	1.257	22.0	0.31	609

Table 6.6 lists the feed flow values used to obtain optimal H_2 production. The oxygen, fuel and water conversions obtained using the Rh-Al catalyst for the different bio-compounds are shown in Figure 6.20. The figure also contains equilibrium water conversion values for comparison.

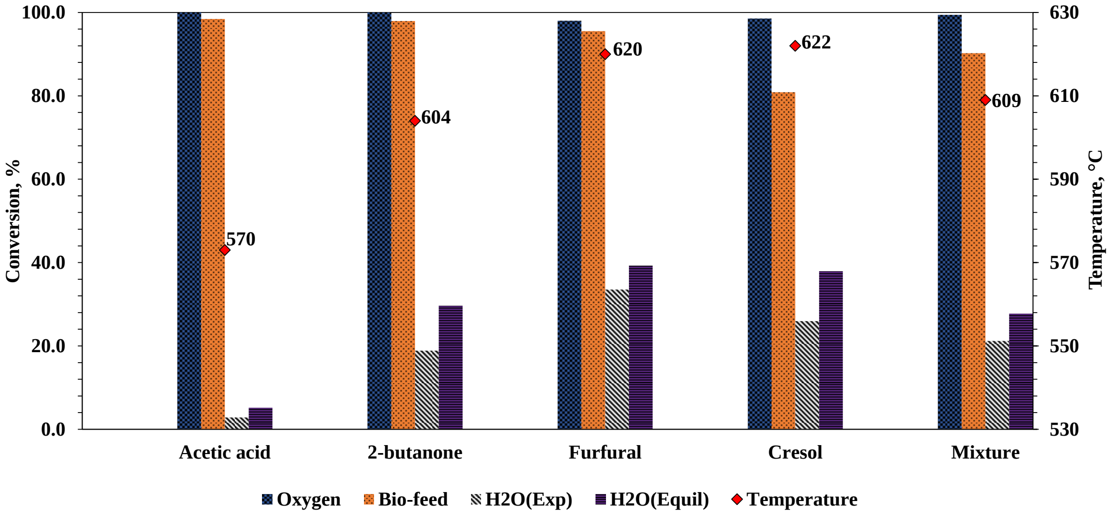

Figure 6.20 Conversion of oxygen, bio-feedstock (bio-feed) and water (experiment and equilibrium) using Rh-Al catalyst at S/C 2 and 1 bar. Reactor exit gas temperatures are included as labels for each bio-feed. Equilibrium water conversion (H2O(Equil)) is also included for comparison. λ values used are given in Table 6.6.

The results in Figure 6.20 represent average values calculated for readings spanning 2 hours without any noticeable deactivation (total experiment duration was 3 hours). Very high acetic acid and 2-butanone conversions, 98%, were achieved accompanied by complete oxygen consumption in both cases. Furfural conversion was 95% while m-cresol conversion was down to 81% with oxygen conversions of 98 and 99 %

respectively. The mixture had an average carbon conversion of 90% with O_2 conversion reaching over 99%. Water conversion was positive in all cases. This confirms the catalyst's ability to promote water consuming reactions such as SR, WGS and coke gasification. Compared to equilibrium values, the highest water conversion of 34% was achieved by furfural, which represents 86% of the equilibrium value; while the lowest value of 3% was achieved during acetic acid ATR (55% of the equilibrium value). Positive water conversions obtained for all fuels can be correlated to suitability of the Rh-Al catalyst to promote the endothermic SR reaction. This ability increases with reaction temperature as seen on Figure 6.20 (Gutierrez et al., 2011). The low conversion of m-cresol led to the formation of a coloured polluted condensate containing mostly the unreacted compound. This raises the issue of condensate disposal and/or possible recycling; which could lead to the overall increase in complexity and cost for processes using heavy bio-compounds as sources for hydrogen (Wu and Liu, 2010b).

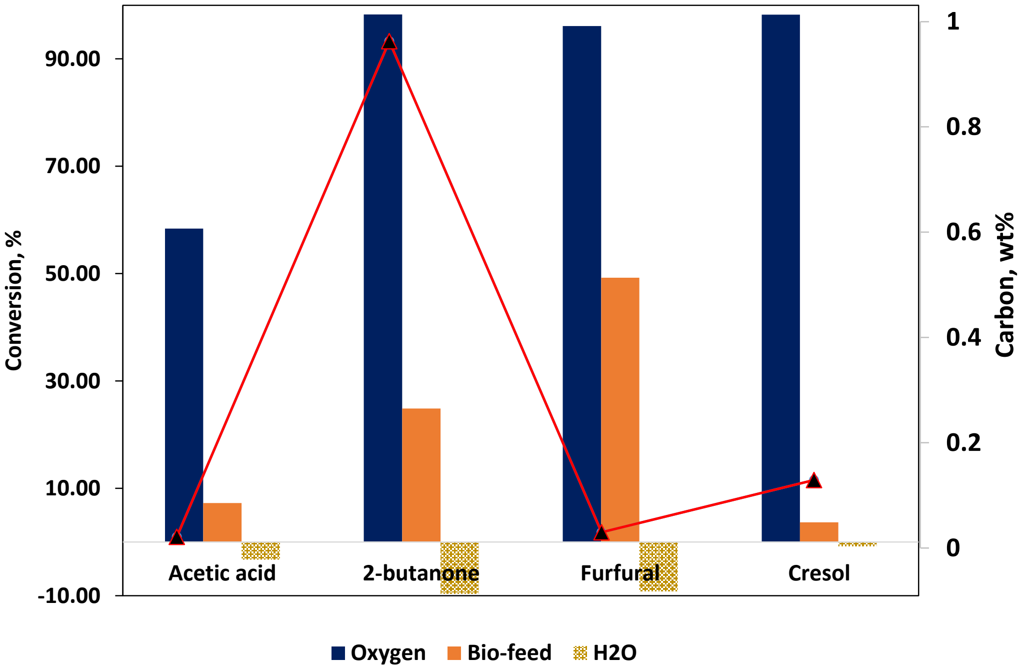

Figure 6.21 Conversion of oxygen, bio-compound (bio-feed) and water; and carbon formed during blank ATR experiments using sand bed at S/C = 2, 1 bar and 570 °C. λ values used are given in Table 6.6

To determine if the conversions obtained for the bio-feeds was entirely due to the Rh-Al catalyst, blank experiments were performed using sand and the results are shown in Figure 6.21. The overall high O_2 conversion for all four bio-feedstocks was an indicator of the formation of non-equilibrium products which could not be detected by the on-line micro GC. However, thermal cracking and oxidation was more evident for furfural and 2-butanone and this was accompanied with significant water production (water conversion of -10%). The Rh-Al catalyst is therefore quite effective in converting bio-compounds to H_2 and C_1 gases.

6.4.4 Product distribution and H_2 yield

The product distribution and hydrogen yield for the different feedstocks are shown in Figure 6.22. Each bio-feed was reacted under pre-determined conditions for maximum hydrogen yield (see section 6.4.3). As expected, each feedstock resulted in a slightly different dry gas composition and hydrogen yield. This difference is down to their unique molar elemental composition (i.e. C:H:O) yielding different coefficients (c, d, e, and f) in the general ATR equation (Eq. 2.13).

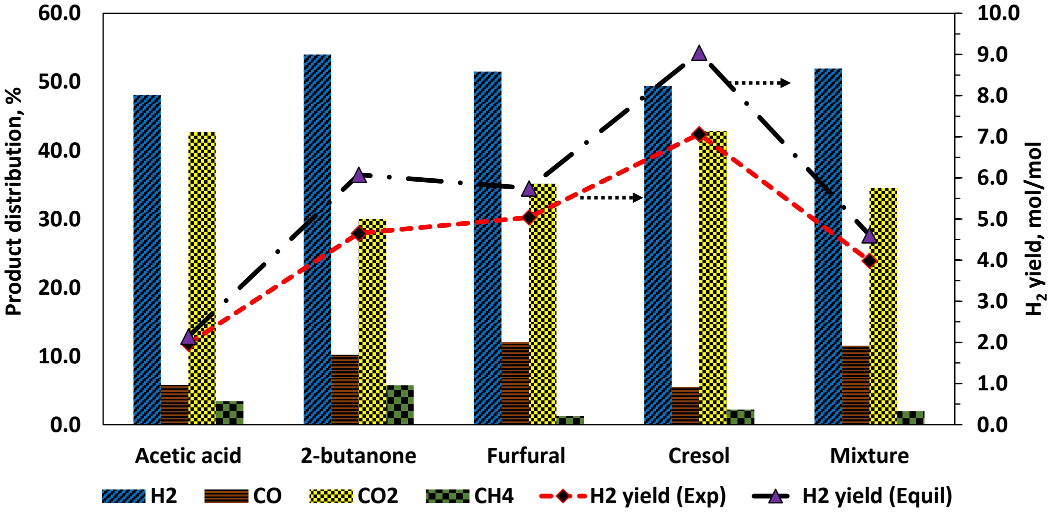

Figure 6.22 Product distribution obtained for ATR of acetic acid, 2-butanone, furfural, m-cresol and their mixture at 570, 604, 620, 622, and 609 °C respectively. S/C = 2 and 1 bar. H_2 yield in mol / mol of bio-feed (Eq. 6.7).

The only ATR product gases detected by the micro GC were H_2, CO, CH_4, and CO_2 confirming the high selectivity the Rh-Al catalyst for reforming reactions (SR and POX) over thermal cracking (Kaila et al., 2007).

Acetic acid ATR produced a dry gas composition and H_2 yield close to equilibrium values. The low conversion of m-cresol (81%) resulted in poor H_2 yield and a gas composition different from equilibrium. The bio-compounds' mixture however showed good results with H_2 yield close to the equilibrium value. This suggests a possible synergistic mechanism in which the different compounds in the mixture facilitate the decomposition and reforming of each other possibly via the release and absorption of heats of reactions.

To account for possible heat loss occurring during an actual ATR process, ATR experiments were performed at 570 °C and S/C = 2 for all four compounds with a constant air flow of 22 cm^3/min corresponding to λ values of 0.35, 0.26, 0.35, and 0.29 for acetic acid, 2-butanone, furfural and m-cresol respectively. This process condition (570 °C) corresponds to that required for optimal acetic acid ATR and has the lowest equilibrium temperature amongst the other compounds examined as listed on Table 6.6. The assumption made here is that this will correspond to the minimal temperature in a properly insulated ATR reactor with acceptable heat loss. Amongst the three other bio-compounds only 2-butanone showed a lower conversion and H_2 yield when ATR was performed at a lower temperature and air flow (see Table 6.7). Furfural and m-cresol converted better to C_1 gases at the lower temperature but achieved lower H_2 yield.

Table 6.7 Comparison between the product distribution and conversion achieved during ATR bio-feedstocks at their respective optimal conditions to acetic acid conditions of 22 ml/min air and 570 °C. λ values of 0.35, 0.26, 0.35, and 0.29 for acetic acid, 2-butanone, furfural and m-cresol respectively for experiments at 570 C. See Table 6.6 for the other λ values used

Bio-feed	**T, °C**	**Conversion, %**		**Product distribution, N_2 free mol%**				**H_2 yield, wt%**	**Carbon, mg/g(cat).h**
		Bio-feed to C_1	H_2O	H_2	CO	CO_2	CH_4		
Acetic	570	98	3	48	6	43	3	6.6	5.5
2-butanone	605	98	19	54	10	30	6	13.0	6.3
	570	94	18	51	8	33	9	11.0	5.9
Furfural	620	96	34	52	12	35	1	10.6	17.1
	570	98	29	48	14	34	5	9.0	9.1
M-cresol	622	81	26	49	6	43	2	13.2	24.9
	570	93	25	48	14	34	5	11.4	15.0
Mixture	608	86	21	52	12	35	2	10.6	15.3

The CH_4 selectivity increased during the lower temperature ATR for 2-butanone, furfural and m-cresol. For 2-butanone and furfural, increase in CH_4 selectivity corresponded to a simultaneous decrease in CO selectivity (see Figure 6.23). This can be attributed to the methanation reaction; where CO is used as a co-reactant with H_2 to produce methane and water (Eq. 6.23). The increase in net water production results in a lower water conversion value as given in Table 6.7. The low temperature ATR of m-cresol produced a dry gas mixture with higher CO and lower CO_2 selectivity when compared to optimal conditions. This probably indicates the preference of thermal decomposition reactions over reforming reactions. Table 6.7 also shows that coke formation reduced for 2-butanone, furfural and m-cresol with the lower temperature ATR. The decrease in coke formation during the low temperature ATR of 2-butanone and m-cresol occurs regardless of the lower λ of the process.

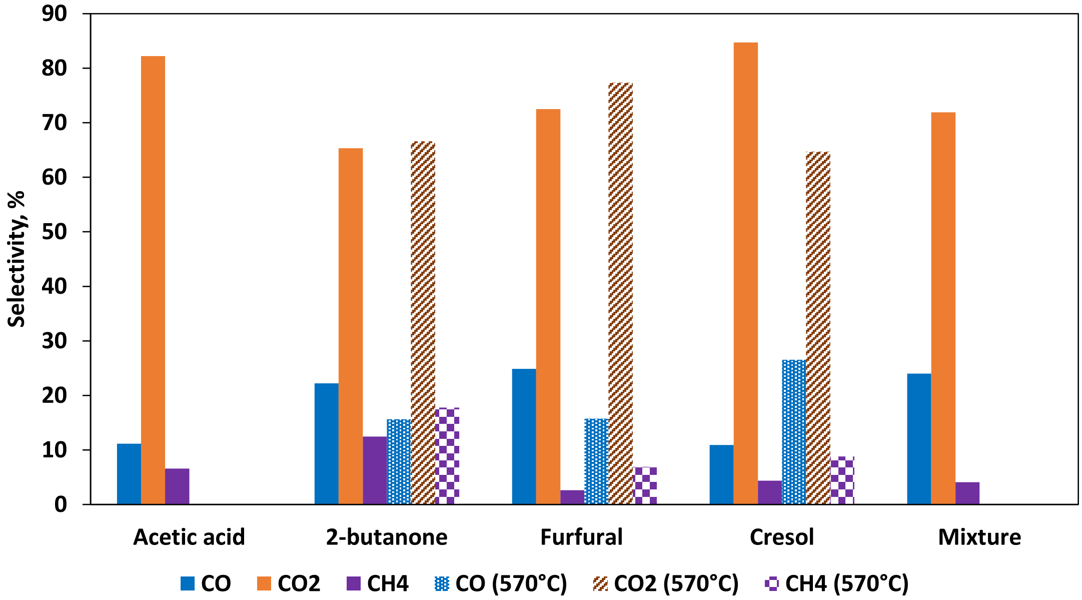

Figure 6.23 Selectivity to carbon gases obtained for ATR of acetic acid, 2-butanone, furfural, m-cresol and their mixture at their optimal temperatures and λ values used are given in Table 6.6 for S/C = 2, 1 bar . The selectivity obtained for the low temperature (570 °C) ATR of 2-butanone, furfural, and m-cresol is also included (see Table 6.7 for the corresponding λ values).

This suggests that the Rh-Al catalyst is more active in promoting reforming and coke gasification reactions at the lower temperature (570 °C) than the respective optimal temperature of 605 °C and 622 °C for 2-butanone and m-cresol. These results confirm that optimal thermodynamic conditions might not correspond to optimal catalytic conditions due to coke formation and deactivation reactions. In some cases, a higher air flow might be required to maintain a steady process over long durations with minimal coking. The downside of this will be a decrease in H_2 yield as in the case of furfural, 2-butanone and m-cresol in Table 6.7.

6.4.5 S/C ratio and space velocity

The influence of S/C molar ratio on the ATR of acetic acid using Rh-Al was investigated and the results shown in Figure 6.24. It is assumed that similar results will be obtained for the other three bio-compounds. S/C = 0 corresponds to POX conditions with the reactor exit gas having a temperature of 570 °C and is included only for comparison with S/C = 2 process. H_2 production increased with increase in S/C up to 2 and then decreased at S/C = 3. As mentioned in section 6.3.4, adding steam favours the equilibrium shift of the WGS reaction towards H_2 and CO_2 production. Rh/Al_2O_3 catalysts have been demonstrated to have increased WGS activity at temperatures ranging from 500 to 600 °C (Roh et al., 2008).

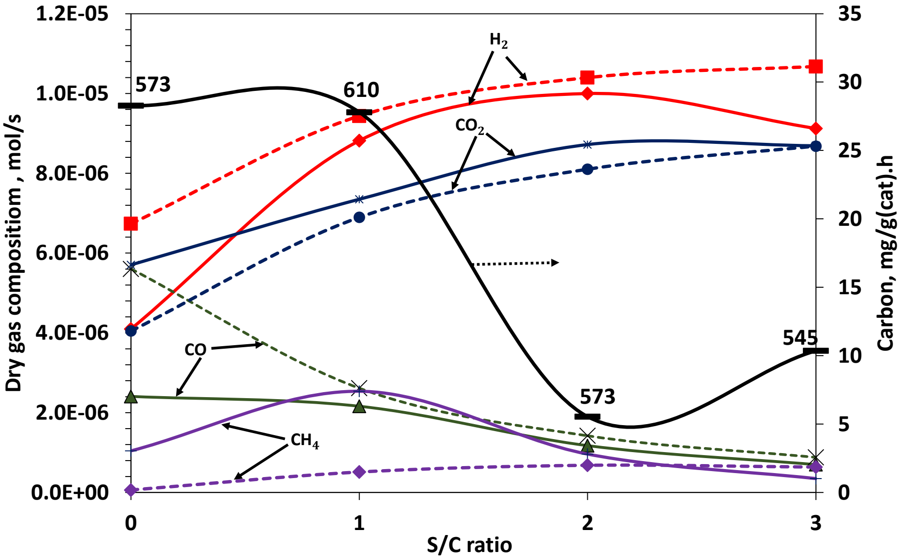

Figure 6.24 Effect of S/C ratio on average production of H_2, CO, CO_2 and CH_4 (solid lines) compared to thermodynamic equilibrium values (dashed lines) for acetic acid ATR. Acetic acid flow of 1 ml/h with corresponding λ and temperature values of (0.353, 570°C), (0.340, 610 °C), (0.353, 570 °C) and (0.374, 545 °C) for S/C ratio of 0, 1, 2 and 3 respectively.

The effect of adding steam during ATR is highlighted by the difference in output values obtained for S/C = 0 and S/C = 2. The H_2 yield more than doubles meanwhile carbon formation reduces from about 30 to 5 mg/g(cat).h. Adding more water into the reformer reduces the reaction and reformate temperature making it increasingly difficult for the catalyst to completely convert the acetic feed to H_2 and CO/CO_2. This leads to increase coking and decrease in H_2 production at S/C = 3.

The suitability of the Rh-Al catalyst to handle high bio-feed flow was examined using acetic acid and the result depicted in Figure 6.25. H_2 production increased very slightly as the space velocity (WHSV) increased from 10 to 40 h^{-1}. This was accompanied by a decrease in CO and CH_4 and an increase in CO_2 production. This change in dry gas composition can be attributed to a slight promotion of WGS reaction due to better feed mixing as feed flow rate is increased into the reactor. Further increase of the WHSV to 80 h^{-1} however leads to a slight reduction in H_2 production with a concomitant decrease in CO_2 and CO production. A very high WHSV slightly diminishes the extent of the WGS reaction probably due to the formation of hot spots on the catalyst as a result of the exothermic oxidation and coke gasification reactions.

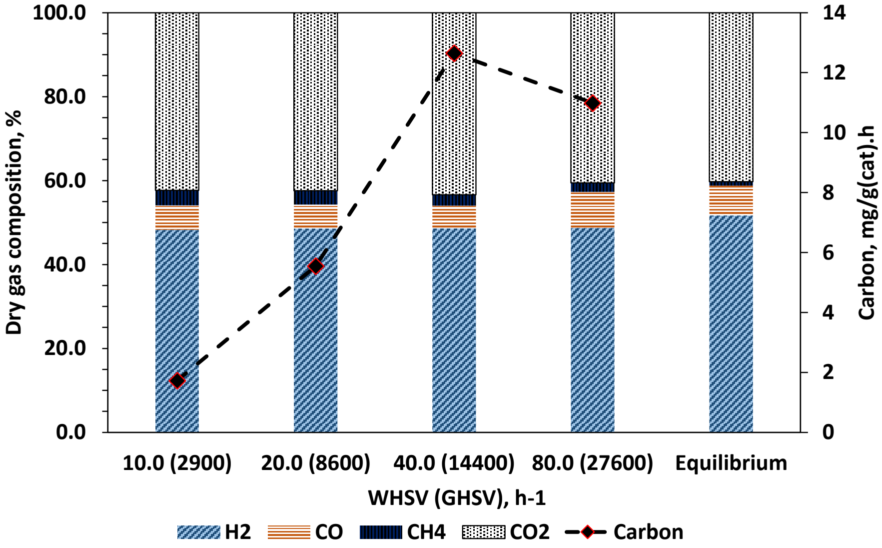

Figure 6.25 Influence WHSV (and GHSV), on dry gas composition and coke formation during acetic acid ATR at S/C = 2 and λ = 0.353 corresponding to a reactor exit temperature of 570 °C ,1 bar and 0.2 g of catalyst.

This is further confirmed by measuring the extent of coke formation with increase in WHSV (see Figure 6.25). Solid carbon deposited on the catalyst first increases as WHSV is increased from 10 to 40 h^{-1} and then reduces with further increase of WHSV. The lower catalytic coke at WHSV 80 h^{-1} confirms the possible existence of hot spots and increased coke gasification reactions (see section 6.3.5 for the results reported by Liguras et al. (2004)).

6.4.6 Coking and catalyst deactivation

Process factors influencing coke formation on the Rh-Al catalyst during ATR of the different feed bio-compounds have been discussed in the preceding sections. The Rh-Al catalyst performed better than the Ni catalysts examined in section 6.3.

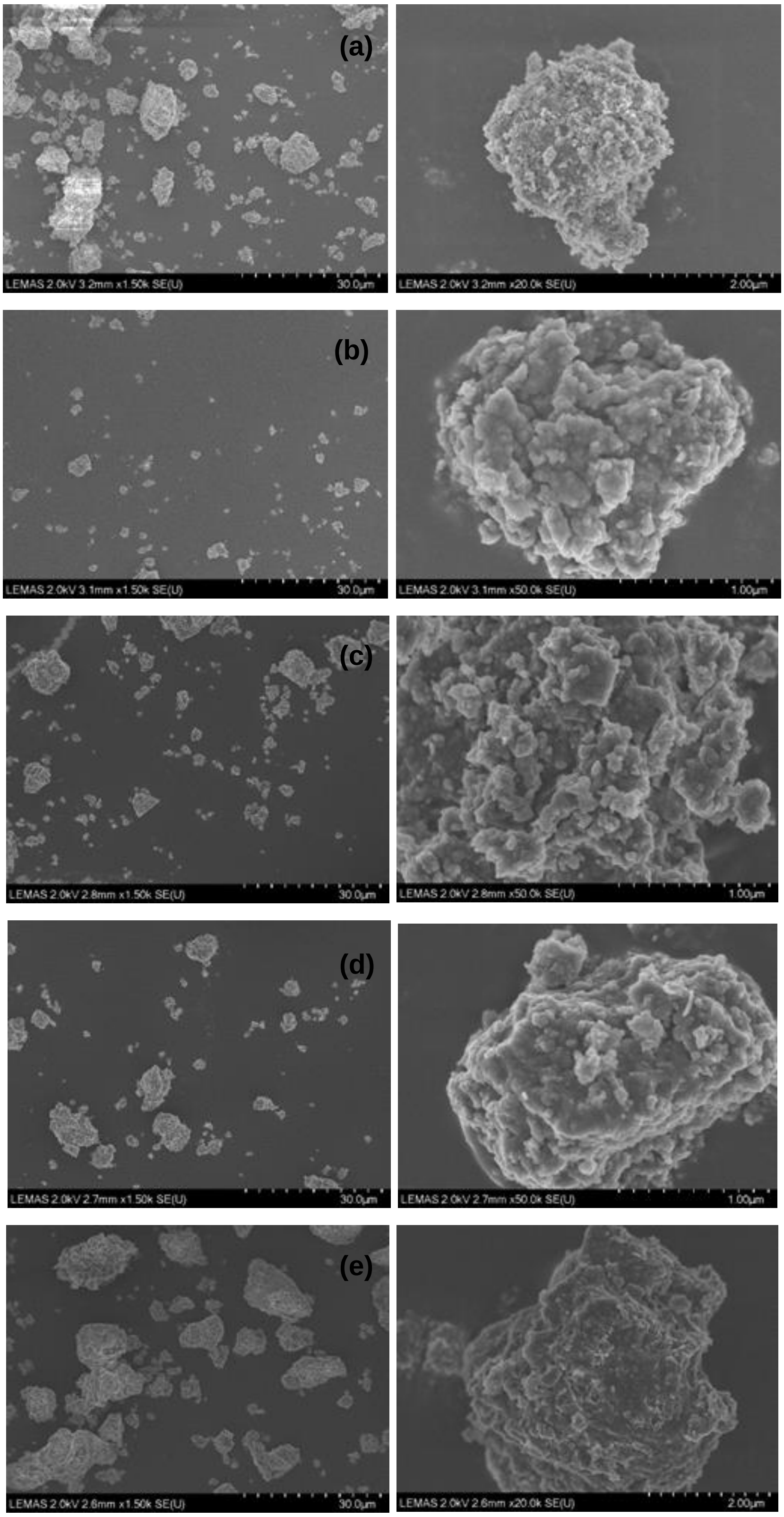

Figure 6.26 SEM images of showing used Rh-Al catalyst at S/C = 2 and 1 bar. (a) Acetic acid (b) 2-butanone (c) Furfural (d) m-cresol (e) mixture

For the same reaction conditions (acetic acid flowing at 1ml/h, water at 1.257 ml/h and air set at 22 cm^3/min), the total carbon deposited on the catalyst on a mass basis (mass of carbon/mass of catalyst) was 0.8 wt%, 3.8 wt% and 14.7wt% for experiments performed using Rh-Al, Ni-CaAl and Ni-Al catalysts respectively. The amount of coke deposited on the Ni-Al catalyst increases if the reaction is allowed to proceed for 3 hours. Amongst the five bio-feeds tested on the Rh-Al catalyst, acetic acid formed the least carbon deposits (0.6 wt%) while m-cresol formed the most (8.2 wt%). The SEM images for the five bio-feedstocks (including the mixture) are shown in Figure 6.26. Unlike the Ni based catalyst, no significant carbon filament structures could be identified on the catalyst surface.

XRD analysis were performed on the used catalyst to verify if any significant change occurred in catalyst structure during ATR (see Figure 6.27).

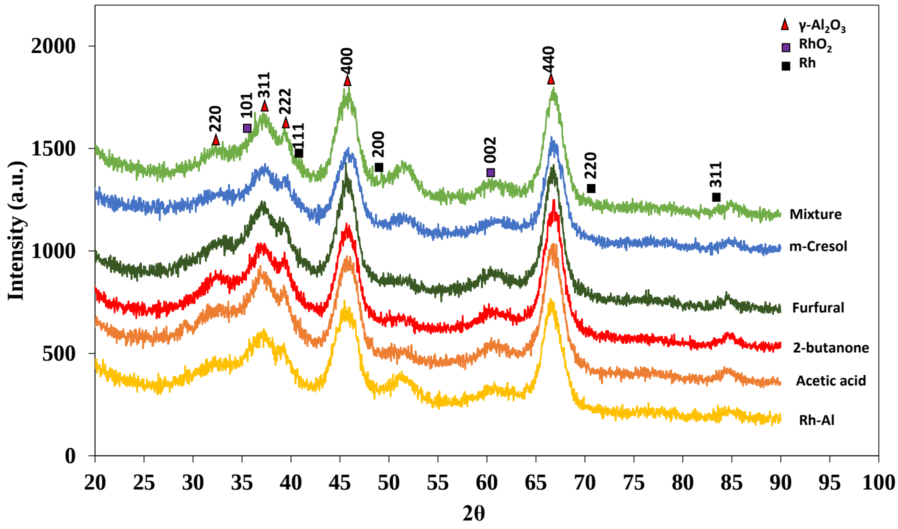

Figure 6.27 XRD patterns of the fresh Rh-Al catalyst and the used catalyst from the ATR of acetic acid, 2-butanone, furfural, m-cresol and their mixture at 570, 604, 620, 622, and 609 °C respectively. S/C = 2 and 1 bar.

The XRD patterns for the used catalysts are quite similar to that of the fresh catalyst. However a slight increase in the crystallinity of the γ-Al_2O_3 could be noticed especially for the catalysts used for the 2-butanone and furfural experiments. This could be due to onset of phase transformation taking place in the support. (Duarte et al., 2012) reported similar results for Rh/Al_2O_3 catalysed used for steam methane reforming.

6.4.7 Summary

High conversions of the bio-feed to C_1 gases, greater than 90%, were obtained for most of the bio-feedstock tested except m-cresol and the mixture. Only C_1 carbon gases were detected confirming that the excellent performance of the Rh-Al catalyst in forming equilibrium products. ATR experiments performed at temperatures lower than the value predicted by thermodynamic equilibrium for optimal H_2 production gave mixed results. For some compounds, the lower temperature experiments gave a higher H_2 yield than at the higher equilibrium predicted temperature. This suggests that the Rh-Al catalyst could be more active in promoting reforming at the lower temperatures and that actual optimal reaction conditions could be different from those predicted by equilibrium. The Rh-Al catalyst also showed excellent resistance to coke formation. Compared to standard Ni/Al_2O_3 catalyst, only 0.8 wt% coke deposit was formed on the Rh-Al catalyst compared to 15 wt% for the former.

6.5 Autothermal reforming of bio-oil surrogate mixture using Rh-Al ‘1wt%Rh/Al_2O_3’ and RhCe-Al ‘1wt%Rh-3wt%Ce/Al_2O_3’ catalyst in a packed bed reactor

Autothermal reforming experiments were extended to include the use of a bio-oil surrogate as feedstock for H_2 production. The aim was to investigate how this complex mixture of compounds will behave as feed to an autothermal reformer by comparing it to results obtained for single and simple mixture bio-feeds as discussed in sections 6.3 and 6.4. The Rh-Al and RhCe-Al catalysts were used for this study. Their preparation and characterisation have been discussed in Chapter 3 and section 6.4.1 respectively.

6.5.1 Bio-oil surrogate mixture

The preparation of the bio-oil surrogate mixture is described in section 3.5.2. The bio-oil composition and properties are presented in Chapter 5 where it is produced and used as part of the process simulation.

6.5.2 Experimental procedure

The bio-oil surrogate flow was set by choosing a constant carbon flow of 1.5×10^{-5} mol/s. This value was then used to determine the air and water flow based on the desired S/C molar ratio and equivalence ratio respectively. The experimental set up was similar to that described and used in sections 6.3 and 6.4. For all experiments, 0.2 g of catalyst was weighed and placed in the reactor and heated in the tube furnace under constant N_2 flow of 200 cm^3/min until the reaction temperature was achieved.

6.5.3 Conversion

As with the other bio-feedstocks used in the previous sections of this chapter, Aspen plus software was used to perform equilibrium analysis so as the determine optimal conditions for ATR. The individual bio-oil component flow values listed in Table 6.8 were entered as input into the Aspen software for S/C molar ratios of 2.2 and 3, while λ was varied from 0 to 1 for each case. The value, $\lambda = 1$, corresponds to the stoichiometric complete oxidation of the bio-oil. Due its high water content, the amount of oxygen input (air flow) required for bio-oil ATR is determined on a moisture free basis

Table 6.8 Bio-oil surrogate component flow values used in Aspen plus simulation

Component	Flow, mol/s	C flow, mol/s
Formaldehyde	1.07×10^{-6}	1.18×10^{-6}
Acetaldehyde	6.97×10^{-8}	1.54×10^{-7}
2-butanone	4.36×10^{-8}	1.92×10^{-7}
Acetic acid	4.88×10^{-7}	1.08×10^{-6}
Water	5.14×10^{-6}	0.00
Furfural	5.49×10^{-7}	3.02×10^{-6}
Phenol	3.49×10^{-8}	2.30×10^{-7}
creosol	8.71×10^{-8}	7.68×10^{-7}
Guaiacol	2.53×10^{-7}	1.95×10^{-6}
Catechol	8.80×10^{-7}	5.82×10^{-6}
Palmitic acid	8.71×10^{-9}	1.54×10^{-7}
Levoglucosan	8.71×10^{-8}	5.76×10^{-7}
Total	$\mathbf{8.71\times10^{-6}}$	$\mathbf{1.51\times10^{-5}}$

According to Eq. 2.12, the moles of O_2 required for stoichiometric combustion, $O_{2(COX)}$, is given by

$$\boldsymbol{O_{2(COX)} = F_{mf} \times \left(n + \frac{m}{4} - \frac{k}{2}\right)} \qquad 6.34$$

Where F_{mf} is the flow rate of the moisture free (m.f.) bio-oil in mol/s.

n, m and k are the coefficients for carbon, hydrogen, and oxygen in the molecular formula of the bio-oil.

The moisture free bio-oil composition is $C_{0.38}H_{0.45}O_{0.17}$. Using the constant carbon flow of 1.5×10^{-5} mol/s, the value of F_{mf} is determined to be 3.95×10^{-5} mol/s corresponding to an actual bio-oil flow rate 1.291 ml/h. Substituting known values into Eq 6.34 gives an O_2 flow of 1.60×10^{-5} mol/s which in turn corresponds to an air flow of 7.63×10^{-5} mol/s (32.6 cm^3/min).

The equilibrium plot for S/C = 2.2 is shown in Figure 6.28. The amount of water flowing into the reactor was adjusted to account for the bio-oil moisture in order to achieve the desired S/C molar ratio.

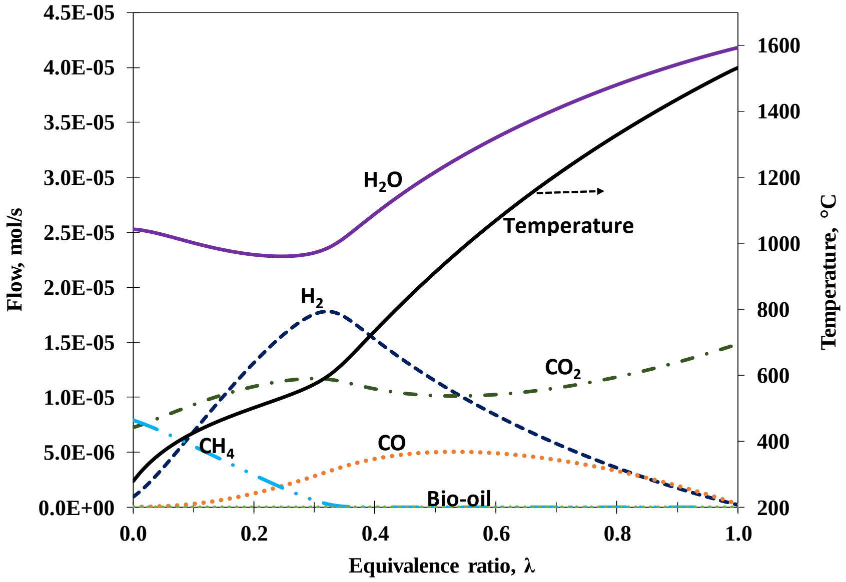

Figure 6.28 Thermodynamic equilibrium plots for showing syngas composition and temperature obtained at S/C = 2.2 and 1 bar while varying λ from 0 to 1 for bio-oil surrogate (m.f.) ATR.

Maximum H_2 yield is obtained at λ = 0.318 on mf basis (or 0.233 on whole bio-oil basis) at an equilibrium temperature of 593 °C (see Figure 6.28). The graph shows a similar trend to that obtained for single component and multicomponent mixtures (Figure 6.1 and Figure 6.19 respectively). For S/C = 3, maximum hydrogen production occurred at λ = 0.391.

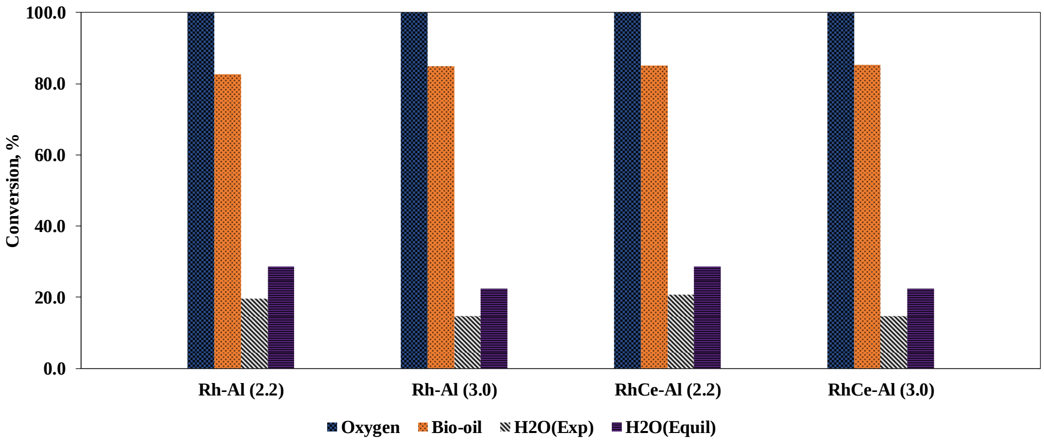

Figure 6.29 Conversion of oxygen, bio-oil and water (experiment and equilibrium) using Rh-Al and RhCe-Al catalysts at 1 bar with reactor bed temperatures of 593 °C (λ = 0.318) and 572 °C (λ = 0.391) for S/C ratio of 2.2 and 3 respectively (S/C ratio in brackets next to catalyst name).

Figure 6.29 depicts the bio-oil, oxygen and water conversion for the Rh-Al and RhCe-Al catalysts. The Rh-Al catalysts performed slightly better with a bio-oil conversion of 84 and 87 % at S/C ratio 2.2 and 3 compared to 83 and 85% for the RhCe-Al catalyst. Water conversion was almost similar for both catalysts reaching an average value of about 70 and 65 % of the equilibrium value for S/C ratio of 2.2 and 3 respectively. One major reason accounting for the overall low bio-oil conversion was the formation of carbon deposits on the reactor wall. This is mainly because the bio-oil fractions decompose and polymerise even under mild heating conditions and most components have different vaporisation temperatures (Rioche et al., 2005).

The slim improvement in performance of the Rh-Al catalyst over RhCe-Al could be due to the difference in the Rh active sites on the catalyst surface. Cerium (in the form of ceria) has been reported to influence the form and state of the Rh particles in promoted Rh catalysts by favouring the formation of stable Rh–O coordination (Eriksson et al., 2007, Oliveira et al., 2013, Duarte et al., 2012). The Rh/Ce (or ceria) interaction could somehow be limiting the ability for Rh to cleave C–C and C–H bonds and transfer surface O in the oxidizing ATR environment. Kurungot and Yamaguchi (2004) reported a drop in methane SR activity as the amount of ceria doping on Rh/Al_2O_3 catalyst was increased from 0 to 2%. The increase in feed conversion associated with some ceria doped Rh catalyst as reported by other authors can be explained by the simultaneous increase in metal dispersion that usually ensues. When there is no significant difference in metal dispersion between the doped and un-doped catalyst, the un-doped Rh catalyst tends to have a higher activity. Eriksson et al. (2007) associated the higher methane conversion and increased syngas selectivity of $Rh/CeO_2–ZrO_2$ catalyst over Rh/ZrO_2 to the higher metal dispersion of 59% on the former compared to 28% for the latter.

6.5.4 Product distribution and selectivity

The product distribution and hydrogen yield obtained during bio-oil ATR using Rh-Al and RhCe-Al catalysts are shown in Figure 6.30. H_2 production was slightly higher on the RhCe-Al catalyst compared to Rh-Al. Hydrogen yield (expressed as mol H_2/mol C in feed) was about 80% of the equilibrium value for the different conditions shown in the figure. This value is consistent with the bio-oil conversion shown in Figure 6.29. No C_2 or C_3 gases were obtained confirming the high activity and selectivity of both catalysts in forming equilibrium products. Other researchers have reported a similar behaviour for Rh based catalysts in SR, POX and ATR experiments. Aupretre et al. (2002) obtained only C_1 gases (CO, CO_2 and CH_4) during the SR of ethanol using 1%Rh/Al_2O_3 catalyst at the stoichiometric S/C ratio of 1.5, 700 °C and 1 atm . They obtained 0.5% ethane (dry gas mixture) when the reaction temperature was reduced to 600 °C.

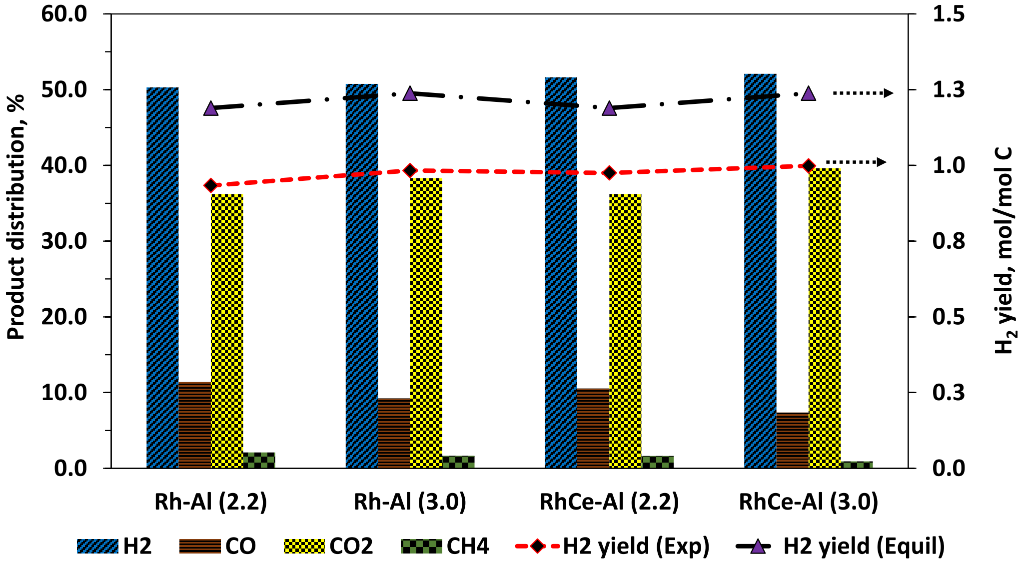

Figure 6.30 Product distribution for bio-oil surrogate ATR using Rh-Al and RhCe-Al catalysts at 1 bar and S/C molar ratio of 2.2 and 3 (S/C is written in brackets next to catalyst name corresponding to a reaction temperature of 593 and 572 °C respectively). $\lambda = 0.318$ and 0.391 for S/C ratio of 2.2 and 3 respectively.

Cavallaro et al. (2003) detected acetaldehyde together with C_1 gases in the ATR of ethanol at 650 °C only for O/C < 0.62 mol/mol with a 5% Rh/Al_2O_3 catalyst. The higher H_2 selectivity of the RhCe-Al catalyst is highlighted further in Table 6.9.

Table 6.9 Products selectivity and carbon formation for bio-oil surrogate ATR at 1 bar and S/C molar ratio of 2.2 and 3 (corresponding to a reaction temperature of 593 and 572 °C respectively). $\lambda = 0.318$ and 0.391 for S/C ratio of 2.2 and 3 respectively.

		Selectivity						**Carbon**
Catalyst	**S/C**	**H_2**	**CO**	**CO_2**	**CH_4**	**H_2/CO**	**CO_2/CO**	**(mg/g(cat).h)**
Rh-Al	2.2	96.0	22.9	72.9	4.2	4.4	3.2	65.4
RhCe-Al	2.2	96.9	21.8	74.8	3.4	4.9	3.4	54.2
Equilibrium	2.2	98.2	20.8	77.1	2.2	5.7	3.7	0.0
Rh-Al	3	96.8	18.8	77.8	3.4	5.5	4.1	71.6
RhCe-Al	3	98.3	15.4	82.7	1.9	7.1	5.4	51.1
Equilibrium	3	98.6	14.0	84.2	1.8	8.8	6.0	0.0

This increase in H_2 selectivity is accompanied by a simultaneous decrease in CO and CH_4 and increase in CO_2 selectivity. This all suggests that the presence of Ce (or ceria) on the catalyst surface decreases its methanation activity while concurrently increasing its WGS activity (Eq 6.24 and 6.23 respectively). A similar result was reported by Salge et al. (2005) for their ATR experiments performed with ethanol using Rh and Rh-Ce catalysts supported on ceramic foams. This increase activity obtained from ceria addition is significant as metallic Rh has been demonstrated to have a low WGS activity (Aupretre et al., 2004).

6.5.5 Air flow

To increase the bio-oil conversion and possibly the H_2 yield, the amount of air used during the ATR experiment was increased to a value higher than that required for maximum H_2 production as predicted by thermodynamic equilibrium calculations. For both catalysts, the increase in air flow was done by a factor of 1.1 (10%) and 1.15 (15%) of the optimal equilibrium value. The bio-oil and water conversions together with product distribution are presented in Table 6.10. The bio-oil surrogate conversion increased with increase in air flow.

Table 6.10 Conversion and product distribution for ATR of bio-oil at S/C ratio of 2.2 and 3 for different air flows at 1 bar.

S/C	Catalyst	λ*	Temp, °C	Conversion, %		Dry gas composition, %				H_2/CO	H_2 yield, mol/mol C
				Bio-oil	Water	H_2	CO	CO_2	CH4		
2.2	Rh-Al	0.318[1]	593	83.7	20.4	50.3	11.4	36.2	2.1	4.42	0.93
		0.35[2]	641	91.7	16.3	48.8	16.1	34.5	0.6	3.04	0.89
		0.366[3]	670	95.2	16.5	48.7	14.6	36.4	0.3	3.34	0.91
	RhCe-Al	0.318	593	82.5	20.1	51.6	10.5	36.2	1.6	4.90	0.98
		0.35	641	91.8	20.0	50.9	11.7	36.5	0.8	4.34	0.98
		0.366	670	94.5	20.5	51.6	11.7	36.6	0.1	4.43	1.03
3	Rh-Al	0.335[1]	572	87.1	14.8	50.8	9.2	38.3	1.7	5.49	0.98
		0.368[2]	620	93.7	17.0	52.7	6.7	40.1	0.4	7.82	1.02
		0.385[3]	647	95.3	11.7	50.6	9.4	39.8	0.2	5.36	0.89
	RhCe-Al	0.335	572	84.9	14.6	52.1	7.4	39.6	0.9	7.07	1.00
		0.368	620	93.4	15.5	51.4	6.5	41.2	0.9	7.89	1.00
		0.385	647	89.4	16.3	53.3	7.7	38.8	0.2	6.94	1.00

* Equivalence ratio values calculated on moisture free basis

[1] optimal equivalence ratio

[2] 10% increase of optimal equivalence ratio [3] 15% increase of optimal equivalence ratio

This increase in fuel conversion did not however always have the desirable effect of increasing H_2 yield. Except for a RhCe-Al catalyst, the H_2 yield reduced as the air flow was increased by 10 and 15%. The additional oxygen in both cases reacted with H_2 and CO to produce water and CO_2. The higher CO_2 composition and H_2/CO ratio of experiments performed using RhCe-Al confirm its slightly better water gas shift activity at the temperatures examined. One clear advantage of using a high air flow is that the increase bio-oil conversion means both less carbon deposition and lower concentration of unconverted feed ends up in the condensate (less polluted condensate).

6.5.6 Catalyst deactivation

Though the long term stability of Rh based catalysts has been confirmed by several authors, the performance of regenerated Rh-Al and RhCe-Al catalysts was tested in this study. After an initial experiment lasting for 3 hours, catalyst regeneration (coke oxidation) was carried out with an air flow of 250 cm^3/min at 700 °C. The combustion product gas (containing CO_2, O_2 and N_2 from air) was monitored with the on-line micro GC and regeneration was complete when the CO_2 concentration reduced to zero. The results presented in Figure 6.31 (a) and (b) clearly show that the Rh-Al catalyst drops in activity after undergoing two regeneration cycles (i.e. used for the third time).

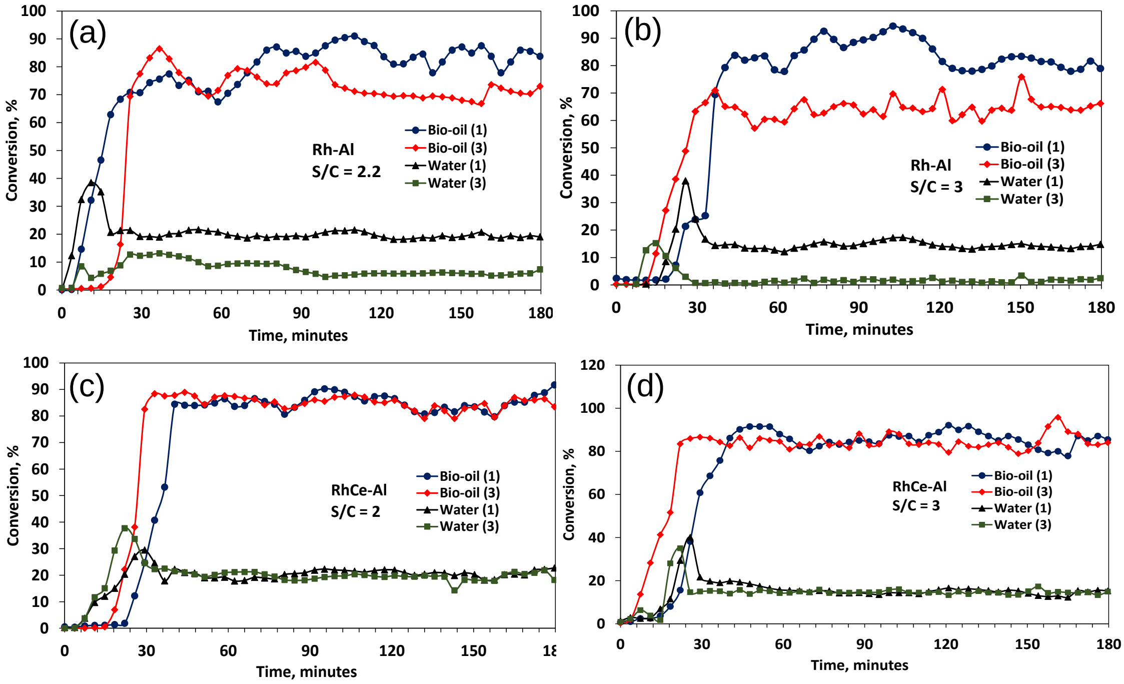

Figure 6.31 Bio-oil and water conversion obtained for fresh catalysts and twice regenerated catalyst. The numbers 1 and 3 indicate the number of times (cycles) the catalyst is used. a) Rh-Al catalyst at S/C = 2.2. b) Rh-Al catalyst S/C = 3. c) RhCe-Al catalyst at S/C = 2.2. d) RhCe-Al at S/C = 3. Reactions conditions were maintained for optimal H_2 yield at 592 °C ($\lambda = 0.318$) and 572 °C ($\lambda = 0.391$) for S/C molar ratio of 2.2 and 3 respectively for S/C ratio of 2.2 and 3 respectively.

Rh-Al catalyst deactivation was even more severe for experiments carried out at S/C molar ratio of 3. This was probably due to the increase coking occurring at the higher S/C ratio. The increase in coking implied more time was needed for regeneration probably leading to more pronounced loss of catalytic activity, as char oxidation would have resulted in local exotherms and sintering. The RhCe-Al catalyst on the other hand showed no significant deactivation. The observed stability of the RhCe-Al can be associated to the ability of Ce^{3+} ions to occupy octahedral sites on the alumina support thus obstructing the loss of surface area which occurs during thermal treatment as Al^{3+} cations transition from tetrahedral to octahedral sites (Damyanova et al., 2002).

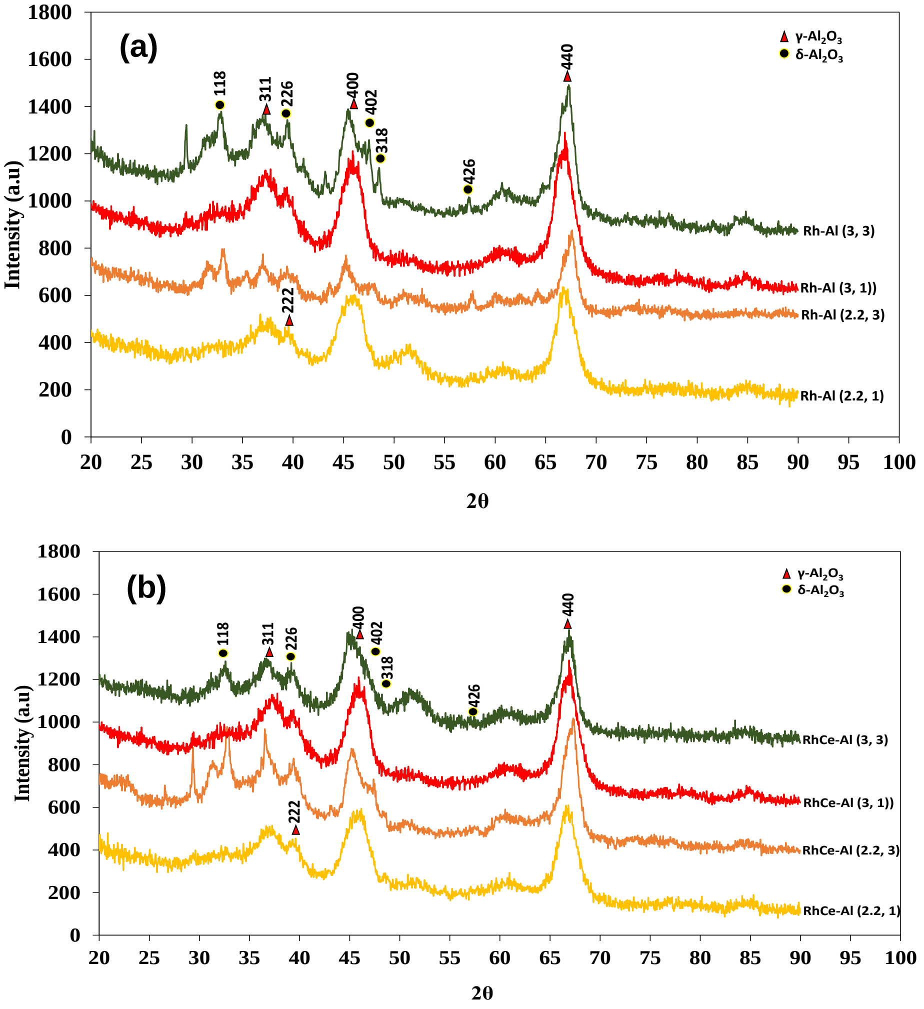

Figure 6.32 XRD patterns of single used (fresh) and twice regenerated Rh-Al and RhCe-Al catalyst. Reactions conditions were maintained for optimal H_2 yield at 592 ($\lambda = 0.318$) and 572 °C ($\lambda = 0.391$) for S/C molar ratio of 2.2 and 3 respectively. The numbers written next to the catalyst name indicate the S/C molar ratio and number of times the catalyst sample has been used.

This obstructive behaviour of Ce^{3+} ions therefore stabilizes the γ-alumina support and the effect is even more pronounced at low Ce (or ceria) loadings (Srivastava and Pant, 2012, Damyanova et al., 2002). Ozawa and Kimura (1990) showed that the presence of CeO_2 particles improve γ-Al_2O_3 thermal stability by also preventing sintering as well as phase transformation. However, some phase transition and loss of surface area still occurs even with the doped ceria catalyst, as shown by the XRD patterns depicted in Figure 6.32. The appearance of the δ-Al_2O_3 phase is only seen with regenerated catalyst and even more so on the Rh-Al catalyst. Apart from blocking phase transition, Rh–O–Ce bonds formed in the presence of O_2 contribute in inhibiting sintering of rhodium particles also accounting for the stability observed for the RhCe-Al catalyst (Cao et al., 2017).

6.5.7 Coke formation

As with the other feed bio-compounds examined in section 6.3 and 6.4, coke was formed on the catalyst bed during the ATR experiments with the bio-oil surrogate. Table 6.9 list the amount of coke deposited on Rh-Al and RhCe-Al catalyst. The RhCe-Al catalyst was more resistant to coke formation than the Rh-Al catalyst.

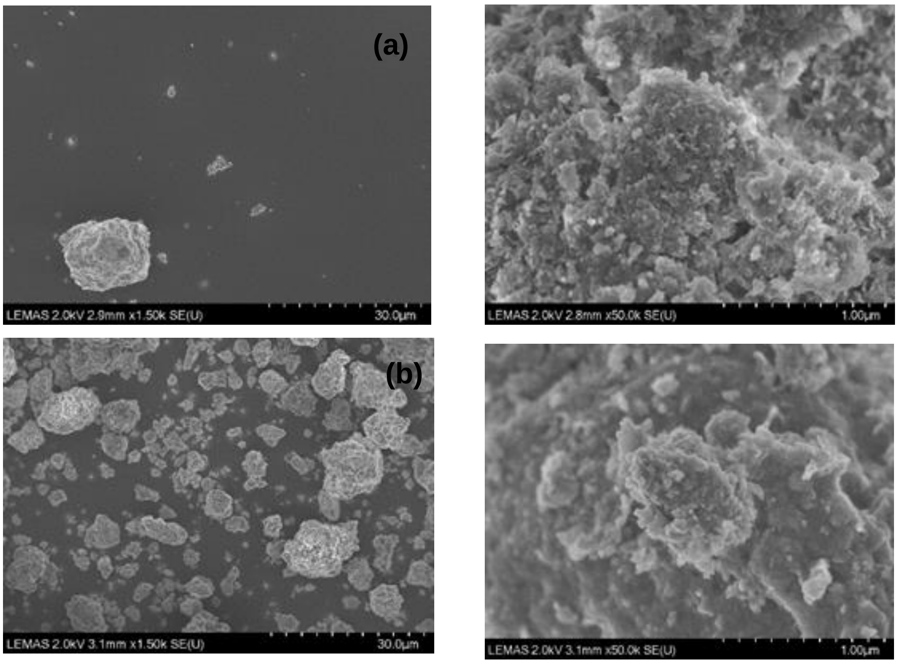

Figure 6.33 SEM images of showing used Rh-Al and RhCe-Al catalyst after bio-oil ATR experiments. Bio-oil flow, 1.291 ml/h, 0.2 g of catalyst, S/C = 2.2, λ = 0.318, 593 °C and 1 bar. a) Rh-Al catalyst. B)RhCe-Al catalyst

This resistance to coking can be attributed to the slightly better Rh dispersion and greater stability of RhCe-Al. SEM images of the used Rh-Al and RhCe-Al are shown in Figure 6.33. Apart from the different coke forming reactions mentioned in section 2.3, dehydration and decomposition reactions of some bio-oil components can lead to the formation of ethylene, a known coke precursor. Such reactions are favoured by the acid alumina support (De Rogatis et al., 2008). Unlike for the Ni based catalyst, no filamentous carbon structures or whiskers could be seen on the catalyst surface. Formation of carbonaceous deposits on the reactor walls and in fittings was a major a problem encountered during the ATR of the bio-oil surrogate (see Appendix C for picture). This was due to poor vaporisation of some of the bio-oil components and their ability to polymerise on contact with the hot reactor wall, pipes and fittings. One way to improve the contact between such bio-oil components and catalyst is the use of fluidized bed reactors or by using a more performant injection system, such as a nebulizer.

6.5.8 Mechanism

The method presented in Chapter 4 was used to determine the dominant reactions taking place during the ATR of the bio-oil surrogate. By determining the individual contributions of the dominant reactions, an attempt was made to explain the difference in catalyst performance as reflected by the product distributions obtained. As in Chapter 4, two mechanism routes were proposed. One was the ‘POX’ or direct mechanism with the dominant reactions consisting of POX, SR, WGS, Boudouard reaction (BO-RX), methanation of carbon (MEN), carbon gasification (C-GS1 and C-GS2), methane steam reforming (ME-SR), hydrogen oxidation (H-OX) and carbon monoxide oxidation (CO-OX). The other mechanism tested was the ‘COX’ or indirect mechanism consisting of thermal decomposition (DEC), COX, SR, WGS, reverse water gas shift (R-WGS), methane steam reforming (ME-SR), methanation of carbon (MEN), carbon gasification (C-GS1 and C-GS2), and hydrogen oxidation (H-OX). The reaction nomenclature presented in Chapter 4 (Table 4.4) is maintained. Figure 6.34 shows the main contributing reactions to H_2 production for ATR experiments carried out using the Rh-Al and RhCe-Al catalysts at S/C ratios of 2.2 and 3 with equivalent ratios of 0.318 and 0.391 respectively. As predicted by the equilibrium results in Chapter 4, under the experimental conditions examined, bio-oil SR had no contribution to H_2 production for experiments performed with either the Rh-Al or

RhCe-Al catalyst. The direct mechanism for both catalysts show a reliance on POX, C-GS1 and ME-SR for H_2 production. In addition, the results obtained for the RhCe-Al catalyst show that almost 20% of H_2 is produced from the WGS. This confirms the possible increase in WGS activity achieved by the addition of Ce to the Rh catalyst.

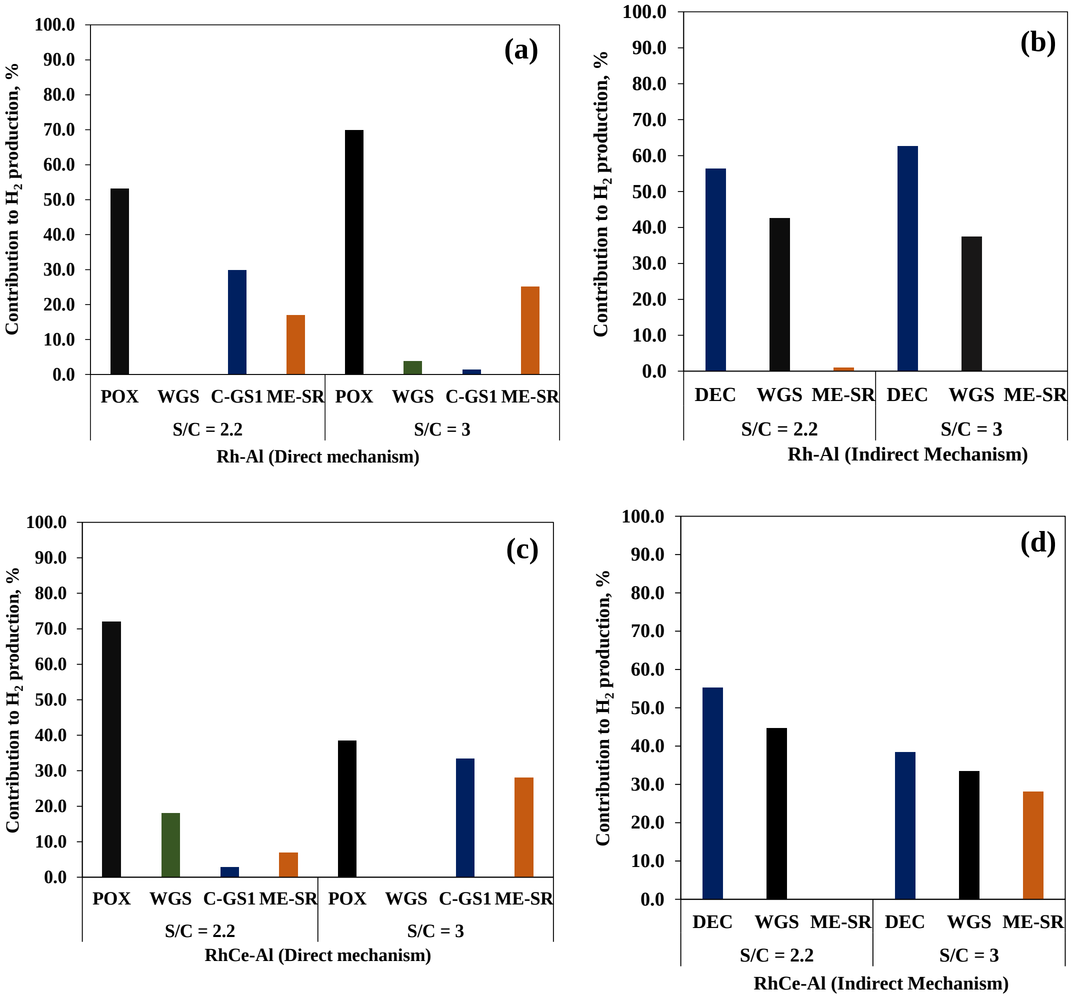

Figure 6.34 Contribution of different reactions to H_2 production for bio-oil surrogate ATR carried at S/C = 2.2, and 3 a) Rh-Al direct mechanism. b) Rh-Al indirect mechanism. c) RhCe-Al direct mechanism. d) RhCe-Al indirect mechanism. Reactions conditions correspond to values presented in Table 6.10 for $\lambda = 0.318$ and 0.335 for S/C ratio of 2.2 and 3 respectively.

The indirect or 'COX' mechanism for both catalysts show similar results with H_2 formation mainly from the DEC and WGS reactions. However, the RhCe-Al catalyst shows significant methanation (from the ME-DC reaction) and subsequent SR of most of the methane formed (ME-SR) as seen in Figure 6.34d. The methane is formed as a result of gasification of the carbon formed as a product of the Boudouard reaction. The contribution to bio-oil consumption shows that both catalysts rely only on POX reaction for initial gasification of bio-oil components to syngas. The initial syngas components produced by this route react further, possibly by WGS, BO-RX, MEN and C-GS1 to produce notably H_2 and achieve the final gas composition.

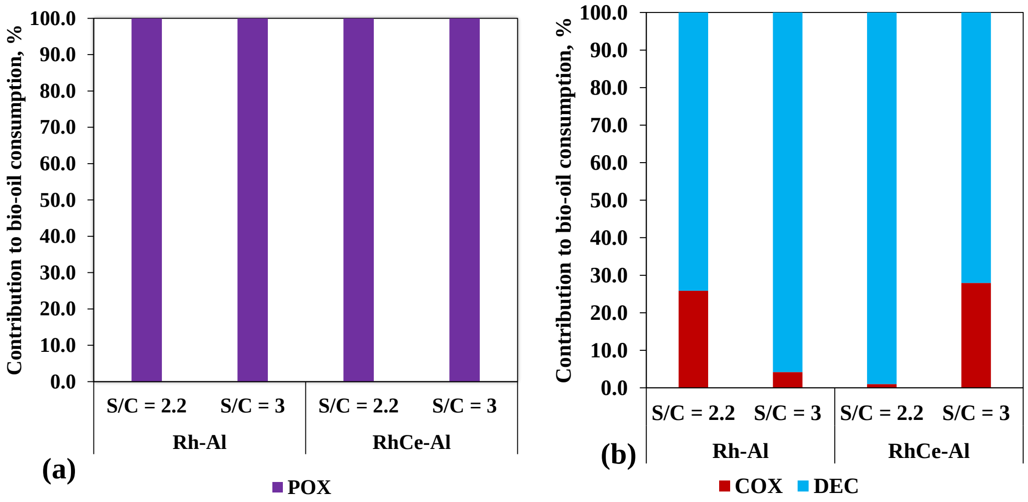

Figure 6.35 Contribution to bio-oil consumption for ATR carried at S/C = 2.2 and 3 a) Direct mechanism. b) Indirect mechanism. Reactions conditions correspond to values presented in Table 6.10 for $\lambda = 0.318$ and 0.335 for S/C ratio of 2.2 and 3 respectively.

The indirect mechanism on the other hand showed significant contribution to bio-oil consumption by COX and decomposition reactions depending on the catalyst and amount of steam present (see Figure 6.35b). For the Rh-Al catalyst, the COX reaction accounted for about 25% of the bio-oil consumption at the S/C ratio of 2.2 (593 °C) compared to only 4% contribution at S/C ratio of 3 (572 °C). This difference in COX activity can be used to explain the difference in catalyst coking (see Table 6.9); with less coke formed during the ATR experiment with S/C 2.2 (65.4 mg/g(cat).h) compared to that at S/C 3 (71.6 mg/g(cat).h). The RhCe-Al catalyst on the other hand showed a reversed trend with the COX reaction contributing 28% to bio-oil consumption at a S/C ratio of 3 and only 1% at S/C ratio of 2.2. Table 6.9 also show that for this catalyst, less coke was deposited during ATR experiments carried out at a S/C ratio of 3 corresponding to the higher COX activity.

6.5.9 Summary

Bio-oil carbon conversion to C_1 gases for the bio-oil surrogate mixture was slightly better with the Rh-Al catalyst but less than 90% for both catalysts due to the formation of carbon deposits on the front end of the reactor wall and pipe fittings before the catalyst bed. The discrepancy in performance of both catalysts was attributed to the difference in the Rh active sites on the ceria doped catalyst. The absence of any C_2 or C_3 compounds in the product gas confirmed the selectivity of both catalyst to equilibrium products. Using higher air flow of 10 and 15% of optimum value increased the bio-oil conversion but had the undesirable effect of reducing the H_2 production for the Rh-Al catalyst as more H_2O and CO_2 was formed. Experiments performed with regenerated catalyst after oxidation revealed that the Rh-Al catalyst suffered more from deactivation when compared to the RhCe-Al catalyst. The stability of the RhCe-Al catalyst was attributed to the formation of stable Rh-ceria interactions which prevent metal sintering. Overall, the slight loss in activity by the addition of Ce to a Rh supported catalyst is outweighed by the gain in stability and increase resistance to coke formation and increase in WGS activity.

6.6 Conclusion

Different catalysts and feedstocks were tested in packed bed ATR experiments for the production of hydrogen/syngas. Ni based catalysts proved to be active for ATR of acetic acid but the performance was tainted by the formation of coke. Rh-Al was demonstrated to be an excellent ATR catalyst with a high selectivity for equilibrium products irrespective of the chemical nature of the bio-feedstock used. The suitability of the Rh-Al and catalyst and its ceria doped form, RhCe-Al, for use in the ATR of bio-oil was tested using a surrogate bio-oil. The un-doped Rh catalyst gave an overall better fuel conversion with a slightly lower H_2 selectivity compared to the cerium (ceria) doped Rh catalyst. The ceria doped Rh catalyst showed excellent stability maintaining the same product gas composition after undergoing two regeneration cycles.

Chapter 7 Autothermal Reforming of Acetic Acid in a Monolithic Reactor

7.1 Introduction

Bench scale ATR experiments were extended to test the performance of two honeycomb monoliths R-M (1 wt% Rh/γ-Al_2O_3 washcoat on cordierite) and RC-M (1wt%Rh-3wt%Ce/ γ -Al_2O_3 washcoat on cordierite), provided by Twigg Scientific & Technical Ltd (UK). Due to the size of the monoliths (19 mm o.d.), a larger 316 stainless steel reactor had to be fitted in place of the one used for the packed bed experiments described in Chapter 6. A 22 mm (o.d) stainless steel tube supplied by Swagelok UK had its internal diameter extended by drilling from an initial value of 18 mm to the desired 19 mm able to contain the monoliths. A new furnace, TSV12/38/120 supplied by Elite Thermal Systems Ltd, was used to accommodate for the larger reactor. No other modifications were performed on the existing rig except using appropriate tube fittings where necessary to connect the new reactor. Acetic acid ATR was performed in order to determine the influence of the amount of steam on the feed conversion, product distribution and gas selectivity. All terms used for process analyses match the definitions and equations given in Chapter 6.

7.2 Experimental procedure

The experimental procedure used to investigate the monolithic reactors was similar to that given in Chapter 6 (section 6.4.2). The monolith was lowered into the stainless steel reactor and held in the middle by the protruding wall marking the end of the initial tube drilling carried out to increase the tube's internal diameter (from 18 to 19 mm). A thermocouple was fitted at the bottom to measure the bulk gas temperature in the reactor. This temperature reading actually corresponded to that of the hot product gases flowing out of the monolith and was used to control the electric furnace. Like with the packed bed experiments, the set-up was leak tested at several points under a N_2 flow of 200 cm^3/min using a portable flowmeter. The furnace was heated to the desired reaction temperature while the fuel and water vaporisers were heated to 50 and 120 °C respectively. All this was done under continuous flow of N_2 and the syringe pumps and flow meters turned on once the set temperatures were achieved as no catalyst reduction was required.

7.3 Conversion

The method used to determine conditions for optimal hydrogen production via thermodynamic equilibrium analysis in Aspen is presented in Chapter 6, section 6.3.2. For experiments with the monoliths, an acetic acid flow of 2 ml/h was selected and all other flows determined based on the desired S/C molar ratio and λ. Three different ATR conditions were examined and the flow setting are listed on Table 7.1.

Table 7.1 Flow settings for ATR experiments using R-M and RC-M monoliths

ATR condition	Water, ml/h	Air, ml/min	S/C	λ	Temperature, °C
1	1.257	42.3	1	0.341	613
2	2.514	43.3	2	0.353	570
3	3.771	46.4	3	0.375	546

The conversion of acetic acid, water and oxygen obtained using both monoliths for the three conditions listed in Table 7.1 are shown in Figure 6.2. Acetic acid conversion varied only slightly from 91 to 92% as the S/C ratio was increased from 1 to 3 for the R-M monolith.

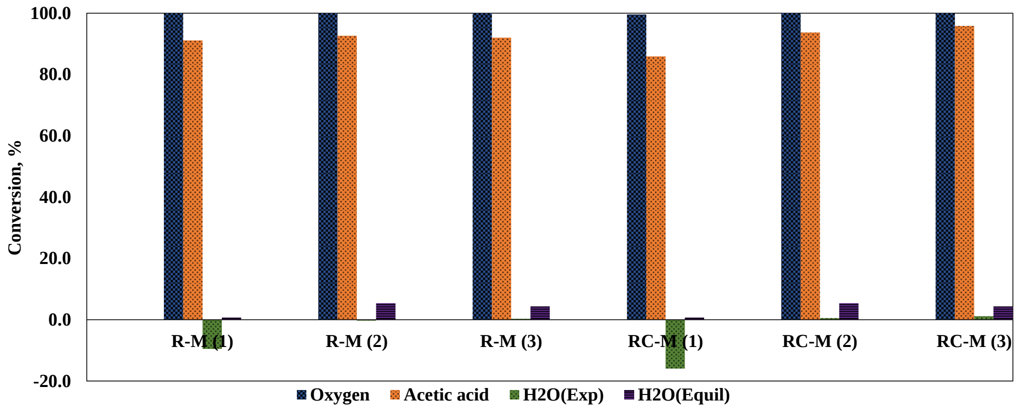

Figure 7.1 Conversion of acetic acid, water and oxygen using R-M and RC-M monoliths for ATR with water flow set at S/C molar ratio of 1, 2, 3 (corresponding to reactor temperatures of 613, 570 and 546 °C respectively) and pressure of 1 bar. The S/C ratio is written in parentheses next to catalyst name.

This seemingly constant values suggests that the activity of this monolith is not intrinsically modified by the presence of steam during the ATR process and that the catalysts maintains almost constant activity within the examined temperature range of 546 to 613 °C.

The marginal increase in acetic acid conversion can be attributed to the slight increase in air flow as the ATR condition is varied from 1 to 3. The RC-M monolith on the other hand showed improved acetic acid conversion (86, 94 and 96 %) as the S/C molar ratio was varied from 1 to 2 and 3 respectively. This suggests that the ceria doped catalyst is sensitive to the amount of steam present in the reacting mixture. The ability of this catalyst to facilitate acetic acid conversion reactions is enhanced by the presence of water as a consequence of increased promotion of water consuming reactions (SR and WGS) and fuel decomposition. This was confirmed by the slightly better water conversion obtained for this monolith compared to R-M. The oxygen conversion on both catalysts reached 100% confirming the ability of Rh based catalyst to promote oxidation reactions (Kaila et al., 2008).

7.4 Product distribution and H_2 Yield

The product distribution obtained using the R-M and RC-M monoliths are shown in Figure 7.2. Both monoliths show a similar product distribution over time with the R-M monolith having more stable results that RC-M. An initial induction time was required to stabilise active sites on the monoliths before the appearance of syngas. This induction time was less than 5 minutes for the R-M monolith indicating that Rh_2O_3 was the active form of the metal during ATR. This result is in agreement with that obtained by Kaila et al. who showed that Rh_2O_3 was the active form of Rh in Zirconia supported RhPt bimetallic catalyst used for the ATR of simulated gasoline (Kaila et al., 2008). For both monoliths, H_2 was the first gas component to spike followed almost immediately by a simultaneous increase in CO_2 and CO concentration. This suggests that very little gaseous phase homogenous decomposition occurs, rather, acetic acid, O_2 and H_2O all dissociatively adsorb on active sites on the catalyst surface with the ensuing surface reactions leading ultimately to the desorption of H_2, CO_2, CO and CH_4. Only small concentrations of H_2 and CO_2 were detected at the beginning of the experiment with the RC-M monolith (Figure 6.3b) with CO only appearing after the spike in H_2 production. Like with the Ni based catalysts discussed in Chapter 6, the delayed detection of CO_2 suggests that acetic acid decarboxylation (Eq 6.26) is inhibited by adsorbed oxygen.

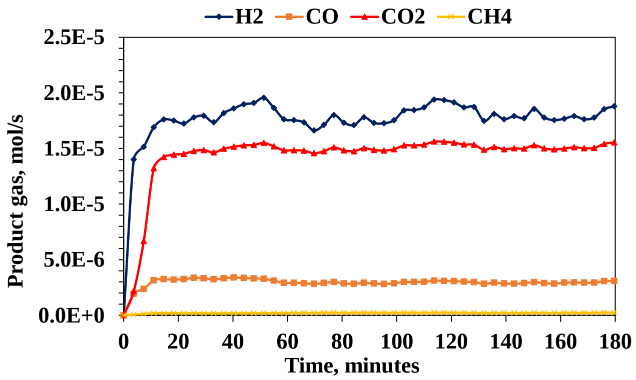

(a)

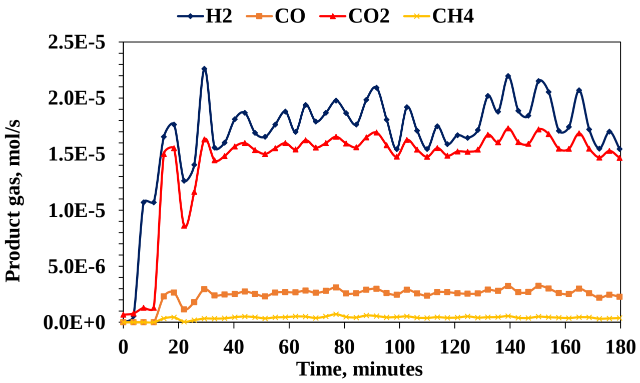

(b)

Figure 7.2 Dry N_2-free product gas obtained during ATR of acetic acid flowing at 2 ml/h, S/C = 2, $\lambda = 0.353$ (Air flow = 43.6 ml/min), hot product gas at 570 °C and 1 bar. (a)R-M monolith. (b) RC-M monolith.

The H_2 and C_1 product gas selectivities obtained during acetic acid ATR at S/C molar ratio of 2 are given in Table 7.2. The R-M catalyst showed a better H_2 and CO selectivity compared to the RC-M monolith and equilibrium.

Table 7.2 Selectivities and hydrogen yield obtained for ATR of acetic acid flowing at 2 ml/h, S/C = 2, $\lambda = 0.353$ (Air flow = 43.6 ml/min), hot product gas at 570 °C and 1 bar

Monolith / Catalyst	**Selectivity**						**H_2 yield**
	H_2	**CO**	**CO_2**	**CH_4**	**H_2/CO**	**CO_2/CO**	**wt%**
Equilibrium	98.2	14.6	83.4	2.0	7.3	5.7	7.2
R-M	98.8	16.3	82.5	1.2	6.1	5.1	6.2
RC-M	97.5	14.2	83.4	2.4	6.7	5.9	6.3
Rh-Al	95.2	13.8	81.6	4.7	7.0	6.2	6.2
Ni-Al*	96.2	9.1	87.1	3.8	10.7	9.6	6.2
Ni-CaAl*	95.7	10.9	84.7	4.4	8.9	7.8	6.8

* Acetic acid ATR results obtained with nickel based catalysts (see chapter 6) are included for comparison

The RC-M monolith however had a slightly higher hydrogen yield and this can be attributed to its better WGS activity as confirmed by the higher H_2/CO and CO_2/CO ratios. This monolith is more active in promoting the WGS reaction leading to the higher H_2 yield despite is lower H_2 selectivity caused by its methanation activity. In both cases, the H_2 yield is well short of the equilibrium value. Table 7.2 also includes results obtained using the powder Rh-Al catalyst (1wt%Rh/Al_2O_3) discussed in chapter 6. The products gas in this case had a slightly lower hydrogen selectivity owing to a higher methanation activity. This methanation activity can be attributed to the lower Rh loading of the powder catalyst compared to the monoliths (Cavallaro, 2000, Aupretre et al., 2004). However, the better acetic acid conversion (98%) obtained using this powder catalyst resulted in a hydrogen yield value similar to that obtained with the monoliths (see section 6.4.3).

The results obtained using the Ni based catalyst presented in chapter 6 showed quite a different selectivity suggesting the involvement of different reaction mechanisms (see Table 7.2). The Ni based catalysts had lower H_2 selectivity (higher methanation) but this was compensated by their lower CO and higher CO_2 selectivity. The dry gas composition for the powdered Ni catalysts confirms their better WGS activity compared to the Rh monoliths and that the system is probably kinetic driven since it is far from equilibrium, judging by the product gas composition. The higher H_2 yield obtained for the Ni-CaAl catalyst can be attributed to its higher conversion, 93%, compared to the 90% for the Ni-Al catalyst.

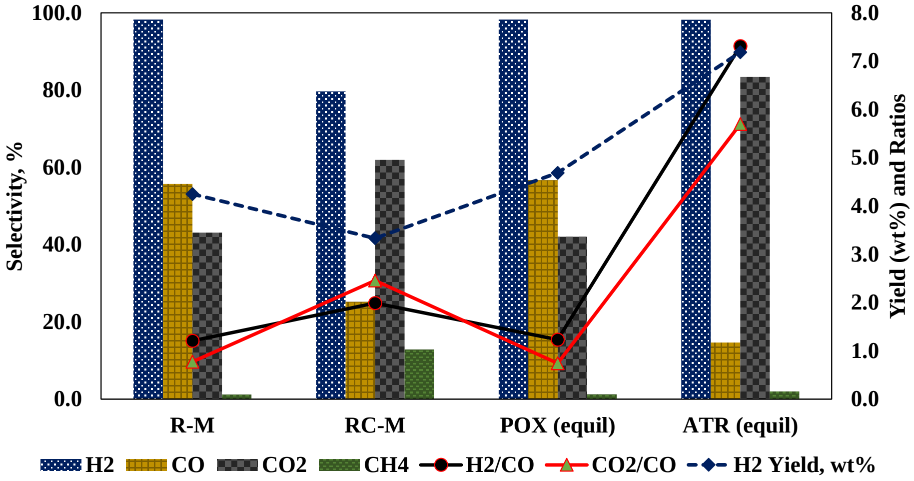

Figure 7.3 Carbon gases and hydrogen gas selectivity, hydrogen yield and product gas ratios obtained during acetic acid POX using R-M and RC-M monoliths (with fuel conversions of 93 and 78 % respectively). Acetic acid flow 2 ml/h, 670 °C and 1 bar. POX and ATR (at S/C = 2) equilibrium results are included for comparison.

POX experiments were performed to test the activity of both monoliths in promoting oxidation reactions. The selectivity and H_2 yield obtained together with product gas ratios are depicted in Figure 7.3. The R-M monolith gave very good results with an acetic acid conversion of 93% and product gas composition similar to equilibrium POX results. This good performance by the R-M monolith confirms its excellent activity as a POX catalyst. The RC-M monolith could only manage 78% acetic acid conversion resulting in a lower H_2 yield. The higher H_2/CO and CO_2/CO ratios for this monolith confirms it ability to shift the gas mixture towards H_2 production via the WGS reaction. This explains why this monolith performs better for high steam flow ATR experiments as given in Table 7.2.

7.5 Effect of the amount of steam during ATR

The influence of S/C molar ratio on the ATR of acetic acid using R-M and RC-M honeycomb monoliths was investigated and the results shown in Figure 6.7. At S/C molar ratio of 1, the R-M monolith showed better results than RC-M. This was probably due to its better POX activity as explained the preceding section. Increasing the S/C molar ratio to 2 and 3 leads to a reverse in order of activity as the RC-M monolith gave a higher H_2 yield.

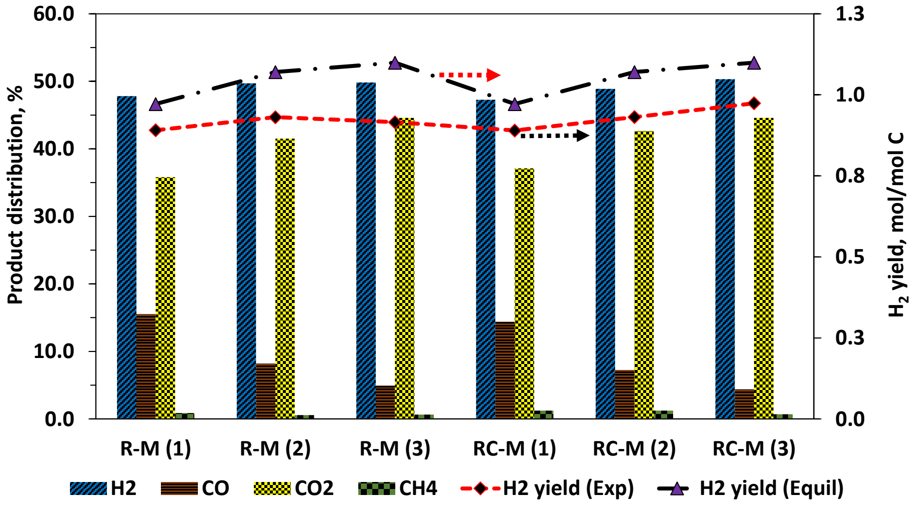

Figure 7.4 Effect of S/C ratio on average syngas composition compared to thermodynamic equilibrium values. Acetic acid flow, 1 ml/h with corresponding λ and temperature values of (0.340, 610 °C), (0.353, 570 °C) and (0.374, 545 °C) for S/C ratio of 1, 2 and 3 respectively.

For both monoliths, the increase in CO_2 and corresponding decrease in CO production indicates an increase in WGS activity as with the case with all other catalysts presented so far in this work. Increasing the S/C molar ratio up to 3 did not have a ‘quenching’ effect mainly because the reacting system was supported by external heating. This might not be the case in an actual ATR process making it necessary to operate at the lower S/C ratio of 1 and 2. Rennard et al. (2009) reported a decrease in WGS activity and hydrogen production during ATR of glycerol using Rh-Ce foam as the S/C ratio was increased above 1. From the balanced SR reaction (Eq. 6.21) it is evident that only 2 moles of water are required per mole of acetic acid (S/C = 1) for a stoichiometric reaction with maximum H_2 yield. For both monoliths, a choice of S/C = 2 might prove to be a good compromise leading to good process outputs and energy savings.

7.6 Space Velocity

The influence of doubling the GHSV on feed conversion and gas selectivity was investigated and the results for the R-M and RC-M monoliths are shown in Figure 7.5. There was no substantial change in the acetic acid conversion and dry gas composition as the GHSV was increased from 5.7×10^2 to 1.14×10^3 h^{-1}. H_2 and C_1 gas selectivity remained constant suggesting no significant increase in diffusion resistance for the GHSV examined.

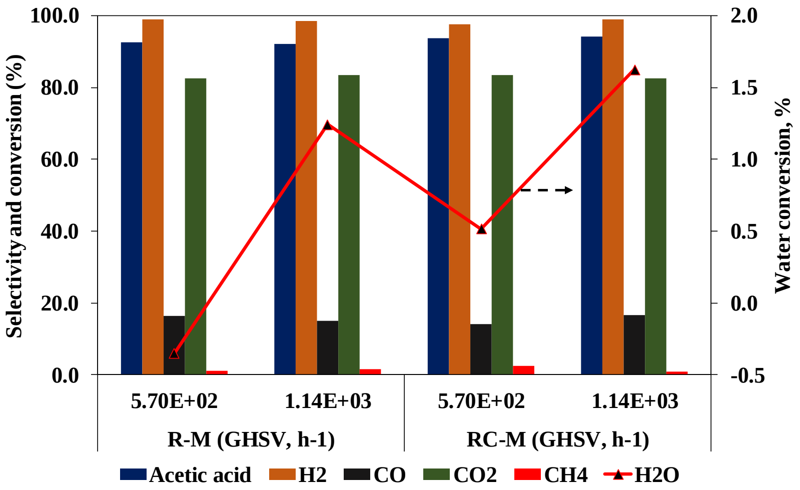

Figure 7.5 Influence of GHSV on feed conversion and dry product gas selectivity. S/C = 2, λ = 0.353 and hot product gas at 570.

Monoliths have been demonstrated to able to maintain good catalytic activity even at very high feed flows. Unfortunately the rig setup used for these experiments did not permit higher space velocities to be tested. Hohn and Schmidt (2001) studied the effect of high space velocities on product yield during the partial oxidation of methane using different Rh coated foam monoliths. They showed that the Rh monoliths were able to maintain high conversion and H_2 yield at GHSV up to 10^5 h^{-1} with further increase leading eventually to a drop in the catalyst performance. The drop in activity was more pronounced for monoliths with lower Rh loadings. They suggested that the low front temperatures due to blow out resulting from convective heat transfer was responsible for the poor convention and product yield at very high GHSV. Higher flows will need to be tested to determine the value for which such conditions exist during acetic acid ATR.

7.7 Reaction Mechanism

No definitive studies have been carried out to determine the actual reaction mechanism occurring during the ATR of oxygenates (bio-feedstocks) on Rh based catalysts. While some published results seem to suggest the direct mechanism in which the oxygen in the feed is only involved in the POX reaction (Eq. 6.19 and 6.20) followed by WGS reaction, other authors tend to favour the indirect mechanism in which oxygen is involved in complete oxidation (Eq. 6.22) followed by steam reforming and WGS reactions. Using the methodology described in Chapter 4, the contribution to hydrogen production and fuel conversion of the different reactions taking place during acetic acid ATR were investigated (see Figure 7.6 and Figure 7.7 respectively). Two reaction schemes were tested. In the first instance, a direct mechanism (also referred to as 'POX' mechanism) was proposed for which the only reactions taking place were DEC (Eq. 6.17), POX (Eq. 6.20), SR (Eq. 6.21), WGS (Eq. 6.23), MEN (Eq 7.1), C-GS1 (Eq. 7.2) and BO-RX (Eq. 6.25).

Carbon methanation (MEN)

$$C + 2H_2 \leftrightarrows CH_4 \qquad 7.1$$

C-GS1 (Carbon gasification)

$$C + H_2O \leftrightarrows CO + H_2 \qquad 7.2$$

The second reaction scheme proposed was the indirect mechanism (also referred to here as the 'COX' mechanism) consisting of the DEC, COX (Eq. 6.22), SR, WGS, ME-SR (reverse of 6.24), MEN, C-GS2 (Eq. 7.3) and H-OX (Eq. 7.4).

C-GS2 (Carbon gasification)

$$C + 2H_2 \leftrightarrows CH_4 \qquad 7.3$$

H-OX (Hydrogen oxidation)

$$H_2 + \tfrac{1}{2} O_2 \rightarrow H_2O \qquad 7.4$$

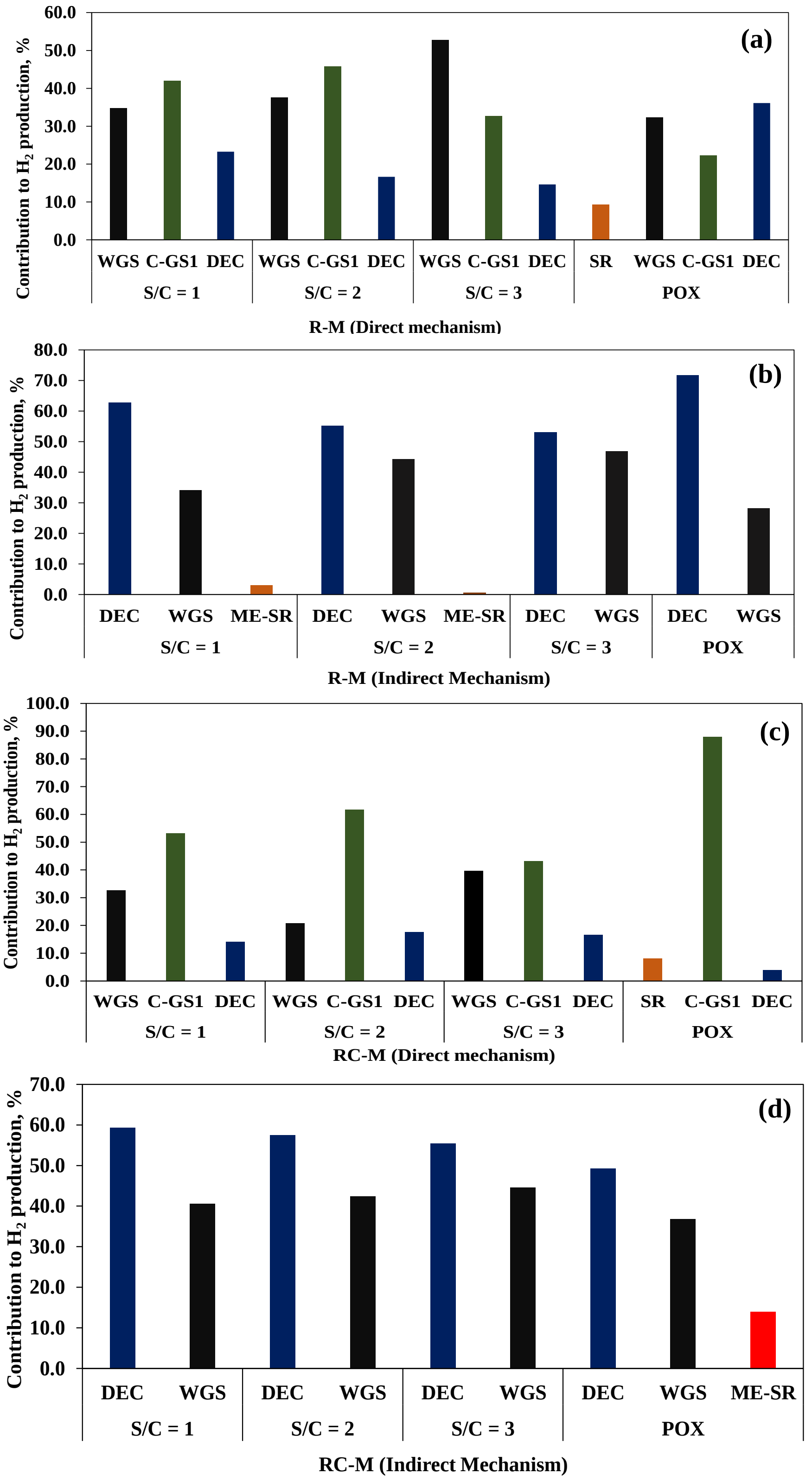

Figure 7.6 Contribution of different reactions to H_2 production for acetic acid ATR carried at S/C = 1, 2, and 3 and POX conditions a) R-M direct mechanism. b) R-M indirect mechanism. c) RC-M direct mechanism. d) RC-M indirect mechanism. Reactions conditions correspond to values presented in sections 7.4 and 7.5.

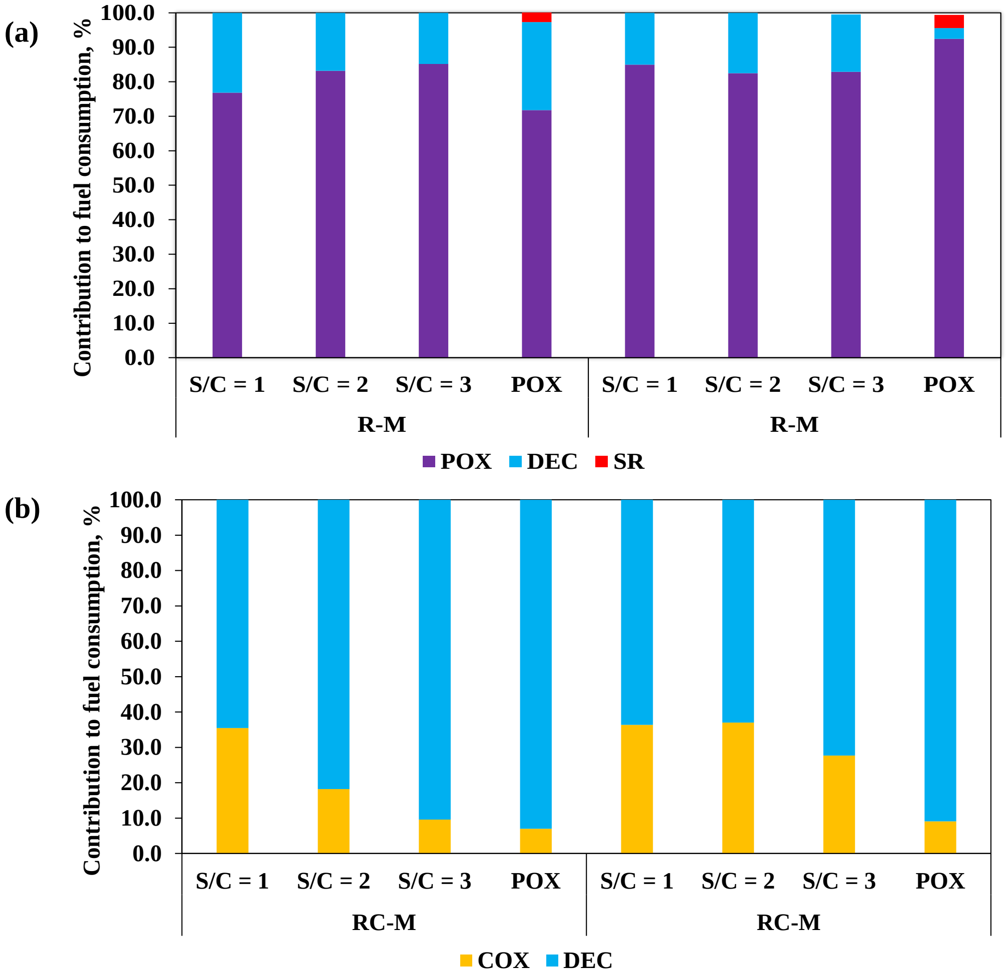

Figure 7.7 Contribution to acetic acid (fuel) consumption for ATR carried at S/C = 1, 2, and 3 and POX conditions a) Direct mechanism. b) Indirect mechanism. Reactions conditions correspond to values presented in sections 7.4 and 7.5.

Under the conditions examined, the direct ‘POX’ mechanism for both monoliths rely almost entirely on POX and decomposition (DEC) reactions for acetic acid consumption. This leads to a massive rise in CO concentration which provide suitable conditions for the Boudouard reaction to take place. H_2 production is assured by WGS, decomposition and gasification of the carbon formed during the Boudouard reaction. As depicted on Figure 7.6 and Figure 7.7, the overall contribution of these reactions depend on the amount of steam present and the type of monolith. The R-M monolith shows more reliance on WGS than RC-M while the latter relies more on carbon gasification (C-GS1). This suggests that the Boudouard reaction plays a more active role on the ceria promoted monolith. This is further confirmed by the direct mechanism results for the POX experiment with more than 85 % of hydrogen formed with the RC-M monolith resulting from C-GS1.

For the indirect ‘COX’ mechanism, acetic acid consumption is assured mainly by COX and DEC reactions while H_2 is produced principally by DEC and WGS reactions. This mechanism is far simpler and relies on a fewer number of equations compared to the direct mechanism. The R-M monolith had a more significant increase in WGS activity with increase in S/C ratio compare to the RC-M monolith which showed less variation in the contribution of this reaction. The non-reliance on carbon gasification for the indirect mechanism makes it more favourable from a kinetic standpoint.

Even though both mechanisms could fit the product gas concentrations obtained using the honeycomb monoliths, a good ATR catalyst should preferentially promote POX and WGS reactions as this avoids the formation of hot spots due to the high temperatures associated with complete combustion therefore making it more durable. Further work should be performed in which the temperature profile existing in the monolith can be investigated and the actual mechanism taking place revealed.

7.8 A note on bio-oil surrogate ATR in a monolithic reactor

Attempts were made to perform bio-oil ATR using both R-M and RC-M monoliths. The experiments could not last for more than one hour due to the formation of carbonaceous material on the frontend of the monolith obstructing feed flow and causing pressure drop as can be seen in the images shown in Figure 7.8.

Figure 7.8 Images of a monolith after bio-oil ATR experiment for S/C molar ratio of 2.2 carried out at 1 bar and 593°C.

No reliable results were obtained. This raises the question on suitability of using monoliths for the reforming of complex bio-feedstocks like bio-oil. Such systems will require modifications to ensure complete low temperature vaporisation of the feed and direct carbon deposition into the monolithic channels.

7.9 Conclusion

The use of monolithic reactors in the ATR of a simple bio-feedstock (acetic acid) was demonstrated. The two Rh based honeycomb monoliths tested showed great performance in feed conversion and product selectivity. The R-M monolith performed better for the low S/C molar ratio of 1 while the RC-M monolith gave better results as this value was increased to 2 and 3. The possible risk of quenching at high steam flow was discussed but further experiments will need to be performed to investigate the variation in the monolith’s temperature profile as more steam is feed into the reactor. The monolith reactors showed very high stability as they could be regenerated and reused without any noticeable change in activity.

An attempt to explain product yield by simultaneously solving the possible reactions taking place gave rise to two possible mechanistic schemes. Firstly, a direct ‘POX’ mechanism with acetic acid consumption completely accounted by POX and decomposition (DEC) reactions and H_2 production assured by WGS, decomposition and gasification. Secondly, a somewhat simpler indirect ‘COX’ mechanism for which acetic acid consumption is assured mainly by COX and DEC reactions while H_2 is produced principally by DEC and WGS reactions.

Chapter 8 Conclusion and Future Work

8.1 Conclusion

Autothermal reforming of bio-oil for hydrogen and syngas production was investigated by means of thermodynamic equilibrium, process modelling and experimental studies. Model compounds typically found in bio-oil, specifically oil obtained from the fast pyrolysis of palm empty fruit bunch (PEFB), were used for the different investigations carried out in this project.

Initial thermodynamic equilibrium analysis was performed on a moisture free (mf) PEFB bio-oil, whose average composition was determined using data from published literature to be $C_{0.3724}H_{0.5304}O_{0.0886}$ and modelled as a mixture of acetic acid, phenol, levoglucosan, palmitic acid and furfural. Five mf bio-oil mixtures were proposed by mixing these five model compounds to match the average mf PEFB bio-oil composition. By varying S/C ratio from 1 to 4 and considering four values of the oxygen equivalence ratio, $\Phi = 0.15$, 0.31 (Φ_{POX}), 0.46, and 0.61, it was realised that similar equilibrium results were obtained for all five bio-oil mixtures considered. This led to the conclusion that hydrogen yield and concentration of other equilibrium products were insensitive to actual bio-oil chemical composition for a given mixture elemental composition. The molar elemental composition proved to be the determining factor for equilibrium hydrogen and syngas yield. The maximum hydrogen yield obtained was about 12 wt% at S/C = 1 and increased to about 18 wt% at S/C = 4. This increase in hydrogen yield is attributed to the equilibrium shift to the right of the WGS reaction (towards forming more products) as more steam is introduced in the system. Equilibrium studies also revealed that carbon (in the form of graphite) can only exist in equilibrium at a $S/C = 1$ and $\Phi < 0.30$; implying that higher values of S/C and Φ should be used in order to avoid the formation of carbon (theoretically). A close examination of the syngas obtained from the ATR of mf bio-oil mixture indicates that S/C ratios between 1 and 2 and $\Phi < \Phi_{POX}$ are required to obtain a $H_2/CO = 2$ necessary for Gas-to-liquid (GTL) Fischer-Tropsch synthesis. On the other hand, syngas for the synthesis of higher alcohols with a $H_2/CO = 1$ can only be achieved with low S/C ratio (S/C ≤ 1) and equivalence ratios slightly larger than the value required for stoichiometric partial oxidation, that is, $\Phi > \Phi_{POX}$.

Mechanisms consisting of global reactions were proposed to account for equilibrium product yields by determining the contribution of each participating reaction to product gas composition. A direct or ‘POX’ mechanism was proposed in which H_2 was produced from partial oxidation (POX), steam reforming (SR) and water gas shift (WGS) reactions. For this POX mechanism, ATR can be viewed as partial oxidation combined with WGS instead of the more traditional notion of exothermic oxidation coupled with endothermic SR. Another mechanism validated was the indirect or ‘COX’ mechanism in which thermal decomposition accounted for about 30% of bio-oil consumption with hydrogen production assured by feed decomposition to carbon, steam reforming, water gas shift and carbon gasification reactions.

A process design and simulation was done using the Aspen Plus software. The main objective of the design was to establish the feasibility of producing H_2 from an agricultural residue/waste such as wet PEFB. The process design included PEFB biomass pyrolysis to produce bio-oil, followed by ATR of this bio-oil to obtain syngas which was then shifted and seperated to give pure H_2. Two designs were proposed based on the H_2 separation method used; a 100 % H_2 recovery process using high pressure water scrubbing (PAWS process) and a 75 % H_2 recovery process using pressure swing adsorption (PAPS process). Key to both designs was the bio-oil composition and yield. PEFB bio-oil was simulated using a surrogate formulated from a mixture of 12 compounds (formaldehyde, acetaldehyde, 2-butanone, water, acetic acid, furfural, phenol, creosol, guaiacol, catechol, palmitic acid and levoglucosan). The compounds were selected to represent the macro-chemical families found in PEFB bio-oil and matched their respective mass fractions. Initial sensitivity analysis on process factors indicate that the maximum S/C ratio to use is 3 for any optimal design using ATR for hydrogen production. Above this value, the effectiveness in converting more steam to H_2 reduces and moreover, an external heating source will be required to generate any extra steam used in the reformer. For a process with PEFB as input fuel, maximum hydrogen efficiencies of 57% and 43% were obtained for the PAWS and PAPS process respectively. These values increased significantly to 82 % and 62% for both processes when bio-oil was considered as the input fuel for the hydrogen efficiency calculation. Complete heat integration was achieved using Pinch Analysis. Different types of turbines were also used as part of a combined heat and power (CHP) unit in a bid to increase energy recovery and process efficiency. Overall process efficiencies were determined to range from 45 to 65%, making the proposed designs quite enticing and presenting a real possibility of producing H_2 from an otherwise discarded agricultural waste, thereby presenting a case for value addition and competition with fossil based processes.

Packed bed ATR experiments were performed using several model compounds and different catalysts. ATR of acetic acid experiments were carried out using two nickel based catalysts, Ni-Al and NiCa-Al. Acetic acid conversions of 91% and 93% were obtained for Ni-Al and NiCa-Al catalyst respectively for ATR carried out at S/C = 2, $\lambda = 0.35$ (air equivalence ratio) and reactor exit gas temperature of 570 °C (backend temperature). Both catalysts showed excellent selectivity for reforming products during acetic acid ATR experiments. The Ni-CaAl catalyst appeared to be a more active with average H_2 production reaching 94% and 90% of the expected equilibrium value for the reduced and fresh catalyst respectively; compared to the 86% obtained for the fresh and reduced Ni-Al catalyst. The maximum H_2 yield obtained was 6.8 wt% for the Ni-CaAl catalyst, which falls well below the 13.1 wt% reported by some authors for acetic acid SR performed under similar conditions without air. XRD results confirmed that the presence of oxygen in the feed did not cause significant oxidation of pre-reduced Ni-Al catalyst as no significant NiO peaks could be detected; at the same time, fresh Ni-Al catalyst (oxidised catalyst) was almost completely reduced during acetic acid ATR with only diminished peaks of NiO detected. Catalyst activity was therefore not significantly hindered when used in the fresh (oxidised) state and so most ATR experiments in this study where carried out using the fresh catalyst. The main drawback with the Ni-Al catalyst was its susceptibility for coking unlike the NiCa-Al catalyst which showed a higher resistance to coke formation. Under the same experimental conditions, coke deposition on the NiCa-Al catalyst was determined to be 13.9 and 11.6 mg/g(cat).h for the fresh and reduced catalyst respectively, while the Ni-Al catalyst had coke formations calculated to be 25.7 and 54.0 mg/g(cat).h for its fresh and reduced forms respectively. It was also demonstrated that the Ni-Al catalyst performed better in ‘POX’ conditions while the NiCa-Al catalyst performed better under ‘ATR’ conditions. This better performance of the NiCa-Al catalyst under ATR conditions was attributed to it higher SR and WGS activities. However, it should be noted that the Ni-Al catalyst is in fact a more active reforming catalyst than the NiCa-Al catalyst but its very high affinity for coke formation and resulting poor fuel conversion make it to appear less active. This was confirmed by the higher methanation observed for the NiCa-Al catalyst as S/C ratio was increased from 1 to 3. At high acetic acid flow rates, a steady decrease in the fraction of fuel carbon deposited on both Ni-Al and Ni-CaAl catalysts was observed. This was attributed to the formation of hotspots in the catalyst bed which promote coke gasification reactions. Formation of hotpots can however have a negative effect on the catalyst stability as it might lead to sintering and catalyst deactivation.

The ATR of acetic acid, 2-butanone, furfural, m-cresol and their mixture was also examined in a packed bed reactor using prepared Rh-Al catalyst. High fuel conversions were obtained with values of 98, 98, 95, 81 and 90 % for acetic acid, 2-butanone, furfural, m-cresol and their mixture respectively. Only C_1 carbon gases were detected confirming the excellent performance of the Rh-Al catalyst in forming only equilibrium products irrespective of the chemical nature of the bio-feedstock used. Acetic acid ATR gave a dry gas composition and H_2 yield close to equilibrium values. The low conversion of m-cresol (81%) resulted in poor H_2 yield and a gas composition different from equilibrium. The mixture of all four model compounds however showed good results with H_2 yield close to the equilibrium value. This suggests the possible existence of an overall ‘synergistic’ mechanism in which the different compounds in the mixture facilitate the decomposition and reforming of each other via the release and absorption of heats of reactions on the catalyst’s surface. ATR experiments performed at temperatures slightly lower than the value predicted by equilibrium for optimal H_2 production gave quite interesting results for 2-butanone, furfural and m-cresol. As expected, a lower H_2 selectivity was obtained for all three fuels (due to increase methanation) but this was however accompanied by lower coke formation on the catalyst surface. This suggests that the Rh-Al catalyst could be more active in promoting reforming at the lower temperatures examined and that actual optimal operating conditions could be different from that predicted by equilibrium. Compared to standard Ni-Al catalyst, the Rh-Al catalyst showed excellent resistance to coke formation with only 0.8 wt% coke deposit formed compared to 14.7 wt% for Ni-Al catalyst for acetic acid ATR experiments performed under similar conditions. Coke formation on the Rh-Al catalyst was shown to be dependent on the chemical structure of the feed used with 5.5, 6.3, 17.5, 24.9 and 15.3 mg/g(cat).h deposited during acetic acid, 2-butanone, furfural, m-cresol and their mixture respectively.

A last set of packed bed ATR experiments were carried out using a formulated PEFB bio-oil surrogate and prepared Rh-Al and RhCe-Al catalysts. The Rh-Al catalysts performed slightly better with a bio-oil conversion of 84 and 87 % at S/C ratio 2.2 and 3 compared to 83 and 85% for the RhCe-Al catalyst. One reason for the overall low bio-oil conversions obtained was the formation of carbon deposits on the reactor walls and pipes caused by the decomposition of some of the ‘heavier’ components found in the bio-oil surrogate. The lower conversion of the ceria doped RhCe-Al catalyst was attributed to interaction between Rh and Ce and the formation of more stable Rh–O coordination which reduces the availability of Rh for reforming. However, H_2 production was slightly higher on the RhCe-Al catalyst with a H_2 yield of about 83% of the equilibrium value compared to 80% obtained for the Rh-Al catalyst. The higher H_2 selectivity of the RhCe-Al catalyst was accompanied by a simultaneous decrease in CO and CH_4 and increase in CO_2 selectivities. This all suggests that the presence of Ce (or ceria) on the catalyst surface decreases its methanation activity while concurrently increasing its WGS activity. Using higher air flows, 10 and 15% of the equilibrium value need for maximum H_2 yield, increased the bio-oil conversion but had the undesirable effect of reducing the H_2 production for the Rh-Al catalyst as more H_2O and CO_2 was formed. H_2 yield stayed the same or improved slightly for the RhCe-Al catalyst Experiments performed with regenerated catalyst revealed that the Rh-Al catalyst suffered more from deactivation when compared to the RhCe-Al catalyst. The stability of the RhCe-Al catalyst was attributed to the the formation of stable Rh-ceria interactions which prevent metal sintering. Overall, the slight loss is activity by the addition of Ce to a Rh supported catalyst is outweighed by the gain in stability and resistance to coke formation. Mechanism fitting was attempted with the results obtained using both the Rh-Al and RhCe-Al catalysts. This was used to predict the main reaction contributing the H_2 production and bio-oil consumption. As predicted by mechanism fitting of equilibrium results, bio-oil SR had no contribution to H_2 production for experiments performed with either the Rh-Al or RhCe-Al catalyst. The direct (or POX) mechanism for both catalysts showed a reliance on POX, C-GS1 and ME-SR reactions for H_2 production. In addition, the results obtained for the RhCe-Al catalyst showed that almost 20% of H_2 is produced from the WGS reaction. This confirms the possible increase in WGS activity achieved by the addition of Ce to the Rh catalyst. The indirect (or COX) mechanism for both catalysts showed similar results with H_2 formation mainly from the DEC and WGS reactions. However, the RhCe-Al catalyst had significant methanation (from the ME-DC reaction) and subsequent SR of most of the methane formed (ME-SR). For the direct mechanism, contribution to bio-oil consumption was solely from POX reaction for both catalysts. Meanwhile for the indirect mechanism, bio-oil consumption was by COX and DEC reactions depending on the catalyst and amount of steam present; for the Rh-Al catalyst, the COX reaction accounted for about 25% of the bio-oil consumption at the S/C ratio of 2.2 (593 °C) compared to only 4% contribution at S/C ratio of 3 (572 °C). The RhCe-Al catalyst on the other hand showed a reversed trend with the COX reaction contributing 28% to bio-oil consumption at a S/C ratio of 3 and only 1% at S/C ratio of 2.2.

Bench scale acetic acid ATR experiments were carried out with two honeycomb monoliths, R-M and RC-M. The two Rh based honeycomb monoliths showed great performance in feed conversion and product selectivity. The R-M monolith performed better for the low S/C molar ratio of 1 while the RC-M monolith gave better results as the S/C ratio was increased to 2 and 3. Acetic acid conversion varied only slightly from 91 to 92% as the S/C ratio was increased from 1 to 3 for the R-M monolith. This seemingly constant value for acetic acid conversion confirms that the SR reaction might not play a significant role in acetic acid consumption during the ATR process within the examined temperature range of 546 to 613 °C. The RC-M monolith on the other hand showed improved acetic acid conversion (from 85% to 95%) as the S/C molar ratio was varied from 1 to 3. This proved that the performance of the ceria doped catalyst was sensitive to the amount of steam present in the feed and this increase in activity facilitated acetic acid conversion reactions. Both monoliths gave a similar product distribution over time consisting of only H_2 and C_1 gases with the R-M monolith having more stable results that RC-M. The R-M catalyst showed a better H_2 and CO selectivity compared to the RC-M monolith and equilibrium. However, RC-M monolith had a slightly higher hydrogen yield and this can be attributed to its better WGS activity as confirmed by the higher H_2/CO and CO_2/CO ratios. The hydrogen yield obtained for both monoliths of 6.2 and 6.3 wt% for R-M and RC-M respectively was well short of the equilibrium value of 7.2 wt%. Mechanism fitting was also attempted in order to determine the main reactions contributing to H_2 production and bio-oil consumption. Similar results were obtained for the direct and indirect mechanism as with equilibrium results for the mf bio-oil mixture. For the a direct (POX) mechanism, acetic acid consumption was completely accounted for by POX and DEC reactions and H_2 production assured by WGS, DEC and gasification reactions. A somewhat simpler indirect (COX) mechanism was established for which acetic acid consumption is assured mainly by COX and DEC reactions while H_2 is produced principally by DEC and WGS reactions. These proposed ‘mechanisms’, like with those from the thermodynamic equilibrium studies and bio-oil surrogate ATR, do not take into consideration the kinetic aspects of the reactions involved and can only be used to fit results of systems at or close to equilibrium and therefore suited for processes operating at relatively low space velocities and high catalytic activity.

8.2 Future work

The work carried out in this project is far from completing the knowledge gap existing on bio-oil ATR. A lot more research needs to be done before bio-oil ATR can compete with fossil fuels as a source of both cheap and renewable syngas and hydrogen. Some avenues for future work are proposed below.

1. To complete the thermodynamic analysis carried out in this project, a detailed kinetic study should be performed in order to firmly establish the actual reaction mechanisms taking place on some select catalysts.
2. The proposed Aspen Plus process design can be refined further to include detailed equipment design and sizing. Specifically, a kinetic reactor block (such as a plug flow reactor) should be used to simulate ATR as this will facilitate eventual scale-up calculations.
3. A complete life cycle assessment (LCA) and economic assessment should be performed in order to accurately determine the eventual cost, both environmental and economical, of H_2 and syngas produced from agricultural wastes such as PEFB biomass.
4. The ATR experiments performed in this study should be extended to include stability tests with experiments running for more than 24 hours. This will aid

in final catalyst screening and selection based on parameters such as size, metal loading and support.

5. ATR reforming experiments should be performed using actual bio-oils and the experimental rig modified to eliminate or minimise the problems faced with bio-oil vaporisation and coke formation.
6. More research should be focused on finding cheap and alternative means to stabilise bio-oil in order to improve their fuel properties such as volatility and resistance to aging reactions.
7. Finally, it will be interesting to design and operate a pilot scale ATR reactor setup and investigate the possibility of running thermoneutral ATR experiments requiring little or no external heating.

References

AASBERG-PETERSEN, K., BAK HANSEN, J. H., CHRISTENSEN, T. S., DYBKJAER, I., CHRISTENSEN, P. S., STUB NIELSEN, C., WINTER MADSEN, S. E. L. & ROSTRUP-NIELSEN, J. R. 2001a. Technologies for large-scale gas conversion. *Applied Catalysis A: General,* 221**,** 379-387.

AASBERG-PETERSEN, K., DYBKJÆR, I., OVESEN, C. V., SCHJØDT, N. C., SEHESTED, J. & THOMSEN, S. G. 2011. Natural gas to synthesis gas – Catalysts and catalytic processes. *Journal of Natural Gas Science and Engineering,* 3**,** 423-459.

AASBERG-PETERSEN, K., HANSEN, J. H. B., CHRISTENSEN, T. S., DYBKJAER, I., CHRISTENSEN, P. S., NIELSEN, C. S., MADSEN, S. E. L. W. & ROSTRUP-NIELSEN, J. R. 2001b. Technologies for large-scale gas conversion. *Applied Catalysis a-General,* 221**,** 379-387.

ABDULLAH, N. & GERHAUSER, H. 2008. Bio-oil derived from empty fruit bunches. *Fuel,* 87**,** 2606-2613.

ABDULLAH, N., GERHAUSER, H. & SULAIMAN, F. 2010a. Fast pyrolysis of empty fruit bunches. *Fuel 89 (2010) 2166–2169,* 2166-2169**,** 89.

ABDULLAH, N., GERHAUSER, H. & SULAIMAN, F. 2010b. Fast pyrolysis of empty fruit bunches. *Fuel,* 89**,** 2166-2169.

ABDULLAH, N., SULAIMAN, F. & GERHAUSER, H. 2011. Characterisation of Oil Palm Empty Fruit Bunches for Fuel Application. *Journal of Physical Science,* 22**,** 1-24.

ABNISA, F., ARAMI-NIYA, A., DAUD, W. W. M. A., SAHU, J. N. & NOOR, I. M. 2013. Utilization of oil palm tree residues to produce bio-oil and bio-char via pyrolysis. *Energy Conversion and Management,* 76**,** 1073-1082.

AGHAMOHAMMADI, N., REGINALD, S., SHAMIRI, A., ZINATIZADEH, A., WONG, L. & NIK SULAIMAN, N. 2016. An Investigation of Sustainable Power Generation from Oil Palm Biomass: A Case Study in Sarawak. *Sustainability,* 8**,** 416.

AGRELL, J., BIRGERSSON, H., BOUTONNET, M., MELIAN-CABRERA, I., NAVARRO, R. M. & FIERRO, J. L. G. 2003. Production of hydrogen from methanol over Cu/ZnO catalysts promoted by ZrO2 and Al2O3. *Journal of Catalysis,* 219**,** 389-403.

AKHTAR, J. & AMIN, N. A. S. 2011. A review on process conditions for optimum bio-oil yield in hydrothermal liquefaction of biomass. *Renewable and Sustainable Energy Reviews,* 15**,** 1615-1624.

AKHTAR, J., KUANG, S. K. & AMIN, N. S. 2010. Liquefaction of empty palm fruit bunch (EPFB) in alkaline hot compressed water. 35**,** 1220-1227.

ALI, K. A., ABDULLAH, A. Z. & MOHAMED, A. R. 2015. Recent development in catalytic technologies for methanol synthesis from renewable sources: A critical review. *Renewable and Sustainable Energy Reviews,* 44**,** 508-518.

ALOTHMAN, Z. 2012. A Review: Fundamental Aspects of Silicate Mesoporous Materials. *Materials,* 5**,** 2874-2902.

ALSTRUP, I., CLAUSEN, B. S., OLSEN, C., SMITS, R. H. H. & R, R.-N. J. 1998a. Promotion of Steam Reforming Catalysts. *In:* PARMALIANA,

A., SANFILIPPO, D., FRUSTERI, F., VACCARI, A. & ARENA, F. (eds.) *Natural Gas Conversion V, Proceedings ofthe 5th International Natural Gas Conversion Symposium.* Giardini Naxos - Taormina: Elsevier B.V.

ALSTRUP, I., TAVARES, M. T., BERNARDO, C. A., SÙRENSEN, O. & ROSTRUP-NIELSEN, J. R. 1998b. Carbon formation on nickel and nickel-copper alloy catalysts. *Materials and Corrosion,* 49**,** 367-372.

ANNAMALAI, K., SWEETEN, J. M. & RAMALINGAM, S. C. 1987. Estimation of gross heating value of biomass fuels. *Transactions of the ASAE,* 30**,** 1205-1208.

ARREGI, A., LOPEZ, G., AMUTIO, M., BARBARIAS, I., BILBAO, J. & OLAZAR, M. 2016. Hydrogen production from biomass by continuous fast pyrolysis and in-line steam reforming. *RSC Advances,* 6**,** 25975-25985.

ASENCIOS, Y. J. O., NASCENTE, P. A. P. & ASSAF, E. M. 2012. Partial oxidation of methane on NiO–MgO–ZrO2 catalysts. *Fuel 97 (2012) 630–637,* 97**,** 630-637.

AUPRETRE, F., DESCORME, C. & DUPREZ, D. 2002. Bio-ethanol catalytic steam reforming over supported metal catalysts. *Catalysis Communications,* 3**,** 263-267.

AUPRETRE, F., DESCORME, C. & DUPREZ, D. 2004. Hydrogen production for fuel cells from the catalytic ethanol steam reforming. *Topics in Catalysis,* 30-1**,** 487-491.

AUTA, M., ERN, L. M. & HAMEED, B. H. 2014. Fixed-bed catalytic and non-catalytic empty fruit bunch biomass pyrolysis. *Journal of Analytical and Applied Pyrolysis,* 107**,** 67-72.

AYABE, S., OMOTO, H., UTAKA, T., KIKUCHI, R., SASAKI, K., TERAOKA, Y. & EGUCHI, K. 2003. Catalytic autothermal reforming of methane and propane over supported metal catalysts. *Applied Catalysis a-General,* 241**,** 261-269.

BA, T. Y., CHAALA, A., GARCIA-PEREZ, M. & ROY, C. 2004. Colloidal properties of bio-oils obtained by vacuum pyrolysis of softwood bark. Storage stability. *Energy & Fuels,* 18**,** 188-201.

BABU, B. V. 2008. Biomass pyrolysis: a state-of-the-art review. *Biofuels, Bioproducts and Biorefining,* 2**,** 393-414.

BALAT, M. 2008. Potential importance of hydrogen as a future solution to environmental and transportation problems. *International Journal of Hydrogen Energy,* 33**,** 4013-4029.

BALAT, M. 2009. Gasification of Biomass to Produce Gaseous Products. *Energy Sources, Part A: Recovery, Utilization, and Environmental Effects,* 31**,** 516-526.

BALAT, M. 2010. Thermochemical Routes for Biomass-based Hydrogen Production. *Energy Sources, Part A: Recovery, Utilization, and Environmental Effects,* 32**,** 1388-1398.

BANASZKIEWICZ, T., CHOROWSKI, M. & GIZICKI, W. 2014. Comparative analysis of cryogenic and PTSA technologies for systems of oxygen production. 1373-1378.

BAO, B., EL-HALWAGI, M. M. & ELBASHIR, N. O. 2010. Simulation, integration, and economic analysis of gas-to-liquid processes. *Fuel Processing Technology,* 91**,** 703-713.

BART, J. C., PALMERI, N. & CAVALLARO, S. 2010. *Biodiesel science and technology: from soil to oil*, Elsevier.

BASAGIANNIS, A. C. & VERYKIOS, X. E. 2006. Reforming reactions of acetic acid on nickel catalysts over a wide temperature range. *Applied Catalysis A: General,* 308**,** 182-193.

BASAGIANNIS, A. C. & VERYKIOS, X. E. 2007a. Catalytic steam reforming of acetic acid for hydrogen production. *International Journal of Hydrogen Energy,* 32**,** 3343-3355.

BASAGIANNIS, A. C. & VERYKIOS, X. E. 2007b. Steam reforming of the aqueous fraction of bio-oil over structured Ru/MgO/Al2O3 catalysts. *Catalysis Today,* 127**,** 256-264.

BATES, R. B. & GHONIEM, A. F. 2013. Biomass torrefaction: modeling of reaction thermochemistry. *Bioresour Technol,* 134**,** 331-40.

BEE. *Chapter 7 Cogeneration by Bureau of Energy Efficiency* [Online]. India. Available: http://www.em-ea.org/guide%20books/book-2/2.7%20cogeneration%20.pdf [Accessed 14/07/2017 2017].

BEGUM, S., RASUL, M., AKBAR, D. & RAMZAN, N. 2013. Performance Analysis of an Integrated Fixed Bed Gasifier Model for Different Biomass Feedstocks. *Energies,* 6**,** 6508-6524.

BEHERA, S. N., SHARMA, M., ANEJA, V. P. & BALASUBRAMANIAN, R. 2013. Ammonia in the atmosphere: a review on emission sources, atmospheric chemistry and deposition on terrestrial bodies. *Environ Sci Pollut Res Int,* 20**,** 8092-131.

BEIS, S. H., ONAY, O. & KOCKAR, O. M. 2002. Fixed-bed pyrolysis of safflower seed: influence of pyrolysis parameters on product yields and compositions. *Renewable Energy,* 26**,** 21-32.

BENGAARD, H. S., NØRSKOV, J. K., SEHESTED, J., CLAUSEN, B. S., NIELSEN, L. P., MOLENBROEK, A. M. & ROSTRUP-NIELSEN, J. R. 2002. Steam Reforming and Graphite Formation on Ni Catalysts. *Journal of Catalysis,* 209**,** 365-384.

BHARADWAJ, S. S. & SCHMIDT, L. D. 1995. Catalytic Partial Oxidation of Natural-Gas to Syngas. *Fuel Processing Technology,* 42**,** 109-127.

BPP.L.C 2016. BP Statistical review of world energy June 2016. 65 ed. London: BP.

BRANCA, C., GIUDICIANNI, P. & DI BLASI, C. 2003. GC/MS characterization of liquids generated from low-temperature pyrolysis of wood. *Industrial & Engineering Chemistry Research,* 42**,** 3190-3202.

BRIDGWATER, A. V. 1999. Principles and practice of biomass fast pyrolysis processes for liquids. *Journal of Analytical and Applied Pyrolysis,* 51**,** 3-22.

BRIDGWATER, A. V. 2003. Renewable fuels and chemicals by thermal processing of biomass. *Chemical Engineering Journal,* 91**,** 87-102.

BRIDGWATER, A. V. 2012. Review of fast pyrolysis of biomass and product upgrading. *Biomass and Bioenergy,* 38**,** 68-94.

BRIDGWATER, A. V., MEIER, D. & RADLEIN, D. 1999. An overview of fast pyrolysis of biomass. *Organic Geochemistry,* Volume 30**,** 1479-1493.

BRIDGWATER, A. V. & PEACOCKE, G. V. C. 2000. Fast pyrolysis processes for biomass. *Renewable & Sustainable Energy Reviews,* 4**,** 1-73.

CABELLO, A., GAYÁN, P., GARCÍA-LABIANO, F., DE DIEGO, L. F., ABAD, A., IZQUIERDO, M. T. & ADÁNEZ, J. 2014. Relevance of the catalytic activity on the performance of a NiO/CaAl2O4 oxygen carrier in a CLC process. *Applied Catalysis B: Environmental,* 147**,** 980-987.

CAO, Y., RAN, R., WU, X., WU, X., WAN, J. & WENG, D. 2017. Ageing resistance of rhodium supported on CeO2–ZrO2 and ZrO2: Rhodium nanoparticle structure and Rh–support interaction under diverse ageing atmosphere. *Catalysis Today,* 281**,** 490-499.

CAVALLARO, S. 2000. Ethanol Steam Reforming on Rh/Al2O3Catalysts. *Energy & Fuels,* 14**,** 1195-1199.

CAVALLARO, S., CHIODO, V., VITA, A. & FRENI, S. 2003. Hydrogen production by auto-thermal reforming of ethanol on Rh/Al2O3 catalyst. *Journal of Power Sources,* 123**,** 10-16.

CHANG, A. C. C., CHANG, H.-F., LIN, F.-J., LIN, K.-H. & CHEN, C.-H. 2011. Biomass gasification for hydrogen production. *International Journal of Hydrogen Energy,* 36**,** 14252-14260.

CHANG, C.-C., CHANG, C.-T., CHIANG, S.-J., LIAW, B.-J. & CHEN, Y.-Z. 2010. Oxidative steam reforming of methanol over CuO/ZnO/CeO2/ZrO2/Al2O3 catalysts. *International Journal of Hydrogen Energy,* 35**,** 7675-7683.

CHANG, S. H. 2014. An overview of empty fruit bunch from oil palm as feedstock for bio-oil production. *Biomass and Bioenergy,* 62**,** 174-181.

CHATTANATHAN, S. A., ADHIKARI, S. & ABDOULMOUMINE, N. 2012. A review on current status of hydrogen production from bio-oil. *Renewable & Sustainable Energy Reviews,* 16**,** 2366-2372.

CHEN, X., TADD, A. R. & SCHWANK, J. W. 2007. Carbon deposited on Ni/Ce–Zr–O isooctane autothermal reforming catalysts. *Journal of Catalysis,* 251**,** 374-387.

CHENG, F. & DUPONT, V. 2013. Nickel catalyst auto-reduction during steam reforming of bio-oil model compound acetic acid. *International Journal of Hydrogen Energy,* 38**,** 15160-15172.

CHOI, Y. & STENGER, H. G. 2003. Water gas shift reaction kinetics and reactor modeling for fuel cell grade hydrogen. *Journal of Power Sources,* 124**,** 432-439.

COGEN-EUROPE & INESTENE March 2001. A guide to cogeneration. The European Association for the Promotion of Cogeneration.

COLLARD, F.-X. & BLIN, J. 2014. A review on pyrolysis of biomass constituents: Mechanisms and composition of the products obtained from the conversion of cellulose, hemicelluloses and lignin. *Renewable and Sustainable Energy Reviews,* 38**,** 594-608.

COLLARD, F.-X., BLIN, J., BENSAKHRIA, A. & VALETTE, J. 2012. Influence of impregnated metal on the pyrolysis conversion of biomass constituents. *Journal of Analytical and Applied Pyrolysis,* 95**,** 213-226.

COMAS, J., MARIÑO, F., LABORDE, M. & AMADEO, N. 2004. Bio-ethanol steam reforming on Ni/Al2O3 catalyst. *Chemical Engineering Journal,* 98**,** 61-68.

COZMA, P., GHINEA, C., MĂMĂLIGĂ, I., WUKOVITS, W., FRIEDL, A. & GAVRILESCU, M. 2013. Environmental Impact Assessment of High Pressure Water Scrubbing Biogas Upgrading Technology. *CLEAN - Soil, Air, Water,* 41**,** 917-927.

COZMA, P., WUKOVITS, W., MĂMĂLIGĂ, I., FRIEDL, A. & GAVRILESCU, M. 2014. Modeling and simulation of high pressure water scrubbing technology applied for biogas upgrading. *Clean Technologies and Environmental Policy,* 17**,** 373-391.

CZERNIK, S. & BRIDGWATER, A. V. 2004a. Overview of Applications of Biomass Fast Pyrolysis Oil. *Energy Fuels,* 18**,** 590-598.

CZERNIK, S. & BRIDGWATER, A. V. 2004b. Overview of Applications of Biomass Fast Pyrolysis Oil. *Energy & Fuels,* 18**,** 590-598.

CZERNIK, S., EVANS, R. & FRENCH, R. 2007. Hydrogen from biomass-production by steam reforming of biomass pyrolysis oil☆. *Catalysis Today,* 129**,** 265-268.

CZERNIK, S. & FRENCH, R. 2014. Distributed production of hydrogen by auto-thermal reforming of fast pyrolysis bio-oil. *International Journal of Hydrogen Energy,* 39**,** 744-750.

DAMYANOVA, S., PEREZ, C. A., SCHMAL, M. & BUENO, J. M. C. 2002. Characterization of ceria-coated alumina carrier. *Applied Catalysis a-General,* 234**,** 271-282.

DE JONG, M., REINDERS, A. H. M. E., KOK, J. B. W. & WESTENDORP, G. 2009. Optimizing a steam-methane reformer for hydrogen production. *International Journal of Hydrogen Energy,* 34**,** 285-292.

DE ROGATIS, L., MONTINI, T., CASULA, M. F. & FORNASIERO, P. 2008. Design of Rh@Ce0.2Zr0.8O2–Al2O3 nanocomposite for ethanol steam reforming. *Journal of Alloys and Compounds,* 451**,** 516-520.

DEDOV, A. G., LOKTEV, A. S., KOMISSARENKO, D. A., MAZO, G. N., SHLYAKHTIN, O. A., PARKHOMENKO, K. V., KIENNEMANN, A. A., ROGER, A. C., ISHMURZIN, A. V. & MOISEEV, I. I. 2015. Partial oxidation of methane to produce syngas over a neodymium–calcium cobaltate-based catalyst. *Applied Catalysis A: General,* 489**,** 140-146.

DEJONG, M., REINDERS, A., KOK, J. & WESTENDORP, G. 2009. Optimizing a steam-methane reformer for hydrogen production. *International Journal of Hydrogen Energy,* 34**,** 285-292.

DELUGA, G. A., SALGE, J. R., SCHMIDT, L. D. & VERYKIOS, X. E. 2004. Renewable hydrogen from ethanol by autothermal reforming. *Science,* 303**,** 993-7.

DEMIRBAS, A. 2001a. Biomass resource facilities and biomass conversion processing for fuels and chemicals. *Energy Conversion and Management,* 42**,** 1357-1378.

DEMIRBAS, A. 2001b. Yields of hydrogen-rich gaseous products via pyrolysis from selected biomass samples. *Fuel,* 80**,** 1885-1891.

DEMIRBAŞ, A. 2002. Hydrogen Production from Biomass by the Gasification Process. *Energy Sources,* 24**,** 59-68.

DEMIRBAS, M. F. 2006. Technological Options for Producing Hydrogen from Renewable Resources. *Energy Sources, Part A: Recovery, Utilization, and Environmental Effects,* 28**,** 1215-1223.

DEMIRBAS, M. F. 2011. Biofuels from algae for sustainable development. *Applied Energy,* 88**,** 3473-3480.

DI LUCIA, L. & KRONSELL, A. 2010. The willing, the unwilling and the unable – explaining implementation of the EU Biofuels Directive. *Journal of European Public Policy,* 17**,** 545-563.

DOHERTY, W., REYNOLDS, A. & KENNEDY, D. 2010. Computer simulation of a biomass gasification-solid oxide fuel cell power system using Aspen Plus. *Energy,* 35**,** 4545-4555.

DOHERTY, W., REYNOLDS, A. & KENNEDY, D. 2013. Aspen Plus Simulation of Biomass Gasification in a Steam Blown Dual Fluidised Bed. *Materials and processes for energy: communicating current research and technological developments.* Formatex Research Centre.

DUARTE, R. B., NACHTEGAAL, M., BUENO, J. M. C. & VAN BOKHOVEN, J. A. 2012. Understanding the effect of Sm2O3 and CeO2 promoters on the structure and activity of Rh/Al2O3 catalysts in methane steam reforming. *Journal of Catalysis,* 296**,** 86-98.

DUFOUR, A., AUTHIER, O., MAUVIEL, G., CORRIOU, J. P., VERDIER, G. & ABDELOUAHED, L. 2012. Detailed Modeling of Biomass Gasification in Dual Fluidized Bed Reactors under Aspen Plus. *Energy & Fuels,* 26**,** 3840-3855.

DUPONT, C., CHIRIAC, R., GAUTHIER, G. & TOCHE, F. 2014. Heat capacity measurements of various biomass types and pyrolysis residues. *Fuel,* 115**,** 644-651.

DUPONT, V., YUN, H. A. H., WHITE, R. & TANDE, L. N. High methane conversion efficiency by low temperature steam reforming of bio-feedstock. REGATEC 2017, 4th International Conference on renewable Energy gas Technology, 22-23 May 2017 2017 Pacengo (Verona), Italy. 25-28.

DYBKJAER, I. 1995a. Tubular Reforming and Autothermal Reforming of Natural-Gas - an Overview of Available Processes. *Fuel Processing Technology,* 42**,** 85-107.

DYBKJAER, I. 1995b. Tubular reforming and autothermal reforming of natural gas - an overview of available processes. *Fuel Processing Technology,* 42**,** 85-107.

EG&G TECHNICAL SERVICES INC 2004. *Fuel Cell Handbook,* Morgantown, West Virginia, U.S. Department of Energy.

ELLIS, M. W., VON SPAKOVSKY, M. R. & NELSON, D. J. Fuel Cell Systems: Efficient, Flexible Energy, Conversion for the 21st Century. Proceedings of the IEEE, 2001.

ENGER, B. C., LØDENG, R. & A, H. 2008a. A review of catalytic partial oxidation of methane to synthesis gas with emphasis on reaction mechanisms over transition metal catalysts. *Applied Catalysis A: General,* 346**,** 1-27.

ENGER, B. C., LØDENG, R. & HOLMEN, A. 2008b. A review of catalytic partial oxidation of methane to synthesis gas with emphasis on reaction mechanisms over transition metal catalysts. *Applied Catalysis A: General,* 346**,** 1-27.

ENGER, B. C., LØDENG, R. & HOLMEN, A. 2009a. Evaluation of reactor and catalyst performance in methane partial oxidation over modified nickel catalysts. *Applied Catalysis A: General,* 364**,** 15-26.

ENGER, B. C., LØDENG, R. & HOLMEN, A. 2009b. Modified cobalt catalysts in the partial oxidation of methane at moderate temperatures. *Journal of Catalysis,* 262**,** 188-198.

EPA-CHPP 2015. Catalog of CHP Technologies USA.

ERIKSSON, S., ROJAS, S., BOUTONNET, M. & FIERRO, J. L. G. 2007. Effect of Ce-doping on Rh/ZrO2 catalysts for partial oxidation of methane. *Applied Catalysis A: General,* 326**,** 8-16.

EWAN, B. & ALLEN, R. 2005. A figure of merit assessment of the routes to hydrogen. *International Journal of Hydrogen Energy,* 30**,** 809-819.

FATSIKOSTAS, A. 2004. Reaction network of steam reforming of ethanol over Ni-based catalysts. *Journal of Catalysis,* 225**,** 439-452.

FIERRO, V., AKDIM, O. & MIRODATOS, C. 2003. On-board hydrogen production in a hybrid electric vehicle by bio-ethanol oxidative steam reforming over Ni and noble metal based catalysts. *Green Chemistry,* 5**,** 20-24.

FIXMAN, E. M., ABELLO, M. C., GORRIZ, O. F. & ARRÚA, L. A. 2007. Preparation of Cu/SiO2 catalysts with and without tartaric acid as template via a sol–gel process. *Applied Catalysis A: General,* 319**,** 111-118.

GARCÍA-GARCÍA, I., ACHA, E., BIZKARRA, K., MARTÍNEZ DE ILARDUYA, J., REQUIES, J. & CAMBRA, J. F. 2015a. Hydrogen production by steam reforming of m-cresol, a bio-oil model compound, using catalysts supported on conventional and unconventional supports. *International Journal of Hydrogen Energy,* 40**,** 14445-14455.

GARCÍA-GARCÍA, I., ACHA, E., BIZKARRA, K., MARTÍNEZ DE ILARDUYA, J., REQUIES, J. & CAMBRA, J. F. 2015b. Hydrogen production by steam reforming of m-cresol, a bio-oil model compound, using catalysts supported on conventional and unconventional supports. *International Journal of Hydrogen Energy*.

GARCIA-PEREZ, M., CHAALA, A., PAKDEL, H., KRETSCHMER, D. & ROY, C. 2007. Characterization of bio-oils in chemical families. *Biomass and Bioenergy,* 31**,** 222-242.

GARCIA, L., FRENCH, R., CZERNIK, S. & CHORNET, E. 2000. Catalytic steam reforming of bio-oils for the production of hydrogen: effects of catalyst composition. *Applied Catalysis a-General,* 201**,** 225-239.

GELLINGS, C. W. & PARMENTER, K. E. 2016. Energy efficiency in fertilizer production and use.

GORDON, S. & MCBRIDE, B. J. 1994. *Computer program for calculation of complex chemical equilibrium compositions and applications*, National Aeronautics and Space Administration.

GOYAL, H. B., SEAL, D. & SAXENA, R. C. 2008. Bio-fuels from thermochemical conversion of renewable resources: A review. *Renewable and Sustainable Energy Reviews,* 12**,** 504-517.

GRANOVSKII, M., DINCER, I. & ROSEN, M. 2007. Greenhouse gas emissions reduction by use of wind and solar energies for hydrogen and electricity production: Economic factors. *International Journal of Hydrogen Energy,* 32**,** 927-931.

GROEN, J. C., PEFFER, L. A. A. & PÉREZ-RAMíREZ, J. 2003. Pore size determination in modified micro- and mesoporous materials. Pitfalls and limitations in gas adsorption data analysis. *Microporous and Mesoporous Materials,* 60**,** 1-17.

GRUIA, A. 2008. Hydrotreating. *In:* JONES, D. S. J. S. & PUJADÓ, P. R. (eds.) *Handbook of Petroleum Processing.* Springer, Dordrecht.

GUPTA, R. B. & PANT, K. K. 2008. Fundamentals and Use of Hydrogen as a Fuel. *In:* GUPTA, R. B. (ed.) *Hydrogen Fuel Production, Transport, and Storage.* CRC Press.

GUTIERREZ, A., KARINEN, R., AIRAKSINEN, S., KAILA, R. & KRAUSE, A. O. I. 2011. Autothermal reforming of ethanol on noble metal catalysts. *International Journal of Hydrogen Energy,* 36**,** 8967-8977.

HALVORSEN, B. M., ADHIKARI, U. & EIKELAND, M. S. Gasification of Biomass for Production of Syngas for Biofuel. 56th Conference on Simulation and Modelling 2015 Linköping, Sweden. 255-260.

HANIKA, J., LEDERER, J., TUKAC, V., VESELY, V. & KOVÁC, D. 2011. Hydrogen production via synthetic gas by biomass/oil partial oxidation. *Chemical Engineering Journal,* 176-177**,** 286-290.

HAYES, R. E. & KOLACZKOWSKI, S. T. 1997. *Introduction to Catalytic Combustion,* Amsterdam, Netherlands, Gordon and Breach Science Publishers.

HAYNES, D. J. & SHEKHAWAT, D. 2011. Oxidative Steam Reforming. 129-190.

HEITNES, K., LINDBERG, S., ROKSTAD, O. A. & HOLMEN, A. 1995. Catalytic Partial Oxidation of Methane to Synthesis Gas. *Catalysis Today,* 24**,** 211-216.

HOHN, K. L. & SCHMIDT, L. D. 2001. Partial oxidation of methane to syngas at high space velocities over Rh-coated spheres. *Applied Catalysis a-General,* 211**,** 53-68.

HOLLADAY, J. D., HU, J., KING, D. L. & WANG, Y. 2009. An overview of hydrogen production technologies. *Catalysis Today,* 139**,** 244-260.

HOSOYA, T., KAWAMOTO, H. & SAKA, S. 2007. Pyrolysis behaviors of wood and its constituent polymers at gasification temperature. *Journal of Analytical and Applied Pyrolysis,* 78**,** 328-336.

HOU, T., YUAN, L., YE, T., GONG, L., TU, J., YAMAMOTO, M., TORIMOTO, Y. & LI, Q. 2009a. Hydrogen production by low-temperature reforming of organic compounds in bio-oil over a CNT-promoting Ni catalyst. *International Journal of Hydrogen Energy,* 34**,** 9095-9107.

HOU, T., YUAN, L., YE, T., GONG, L., TU, J., YAMAMOTO, M., TORIMOTO, Y. & LI, Q. 2009b. Hydrogen production by low-temperature reforming of organic compounds in bio-oil over a CNT-promoting Ni catalyst. *International Journal of Hydrogen Energy,* 34**,** 9095-9107.

ISAHAK, W. N. R. W., HISHAM, M. W. M., YARMO, M. A. & YUN HIN, T.-Y. 2012. A review on bio-oil production from biomass by using pyrolysis method. *Renewable and Sustainable Energy Reviews,* 16**,** 5910-5923.

JACOBSON, K., MAHERIA, K. C. & DALAI, A. K. 2013. Bio-oil valorization: A review. *Renewable and Sustainable Energy Reviews,* 23**,** 91-106.

JAHIRUL, M., RASUL, M., CHOWDHURY, A. & ASHWATH, N. 2012. Biofuels Production through Biomass Pyrolysis —A Technological Review. *Energies,* 5**,** 4952-5001.

JONES, G., JAKOBSEN, J., SHIM, S., KLEIS, J., ANDERSSON, M., ROSSMEISL, J., ABILDPEDERSEN, F., BLIGAARD, T., HELVEG, S. & HINNEMANN, B. 2008. First principles calculations and experimental insight into methane steam reforming over transition metal catalysts. *Journal of Catalysis,* 259**,** 147-160.

JONGA, M. D., REINDERSA, A. H. M. E., KOK, J. B. W. & WESTENDORP, G. 2009. Optimizing a steam-methane reformer for hydrogen production. *International Journal of Hydrogen Energy,* 34**,** 285-292.

KAILA, R. K., GUTIÉRREZ, A., KORHONEN, S. T. & KRAUSE, A. O. I. 2007. Autothermal reforming of n-dodecane, toluene, and their mixture on mono- and bimetallic noble metal zirconia catalysts. *Catalysis Letters,* 115**,** 70-78.

KAILA, R. K., GUTIÉRREZ, A., SLIOOR, R., KEMELL, M., LESKELÄ, M. & KRAUSE, A. O. I. 2008. Zirconia-supported bimetallic RhPt catalysts: Characterization and testing in autothermal reforming of simulated gasoline. *Applied Catalysis B: Environmental,* 84**,** 223-232.

KALINCI, V., HEPBASLI, A. & DINCER, I. 2009. Biomass-based hydrogen production: A review and analysis. *International Journal of Hydrogen Energy,* 34**,** 8799-8817.

KAMM, B., KAMM, M., GRUBER, P. R. & KROMUS, S. 2005. Biorefinery Systems – An Overview. *In:* KAMM, B., R, G. P. & KAMM, M. (eds.) *Biorefineries-Industrial Processes and Products: Status Quo and Future Directions.* Weinheim: Wiley-VCH Verlag GmbH, . .

KAMM, B., KAMM, M., GRUBER, P. R. & KROMUS, S. 2006. Biorefinery systems–an overview. *Biorefineries-industrial processes and products: status quo and future directions***,** 1-40.

KAN, T., STREZOV, V. & EVANS, T. J. 2016. Lignocellulosic biomass pyrolysis: A review of product properties and effects of pyrolysis parameters. *Renewable and Sustainable Energy Reviews,* 57**,** 1126-1140.

KATIKANENI, S. P., AL-MUHAISH, F., HARALE, A. & PHAM, T. V. 2014. On-site hydrogen production from transportation fuels: An overview and techno-economic assessment. *International Journal of Hydrogen Energy,* 39**,** 4331-4350.

KEMP, I. C. 2005. Reducing Dryer Energy Use by Process Integration and Pinch Analysis. *Drying Technology,* 23**,** 2089-2104.

KEMP, I. C. 2007. *Pinch Analysis and Process Integration: A User Guide on Process Integration for the Efficient Use of Energy*, Butterworth-Heinemann.

KHOR, K., LIM, K. & ZAINAL, Z. 2009a. Characterization of bio-oil: a by-product from slow pyrolysis of oil palm empty fruit bunches. *American Journal of Applied Sciences,* 6**,** 1647-1652.

KHOR, K. H., LIM, K. O. & ZAINAL, Z. A. 2009b. Characterization of bio-oil: a by-product from slow pyrolysis of oil palm empty fruit bunches. *American Journal of Applied Sciences 6 (9): 1647-1652, 2009,* 6**,** 1647-1652.

KIM, S. W., KOO, B., RYU, J., LEE, J., KIM, C. & LEE, D. 2013. Bio-oil from the pyrolysis of palm and Jatropha wastes in a fluidized bed. *Fuel Processing Technology,* 108**,** 118-124.

KING, J. W., HOLLIDAY, R. L., LIST, G. R. & SNYDER, J. M. 2001. Hydrogenation of vegetable oils using mixtures of supercritical carbon dioxide and hydrogen. *Journal of the American Oil Chemists' Society,* 78**,** 107-113.

KIRUBAKARAN, V., SIVARAMAKRISHNAN, V., NALINI, R., SEKAR, T., PREMALATHA, M. & SUBRAMANIAN, P. 2009. A review on gasification of biomass. *Renewable and Sustainable Energy Reviews,* 13**,** 179-186.

KOLIOS, G., FRAUHAMMER, J. & EIGENBERGER, G. 2000. Autothermal fxed-bed reactor concepts. *Chemical Engineering Science,* 55**,** 5945-5967.

KRUMPELT, M., KRAUSE, T. R., CARTER, J. D., KOPASZ, J. P. & AHMED, S. 2002. Fuel processing for fuel cell systems in transportation and portable power applications. *Catalysis Today,* 77**,** 3-16.

KUMAR, R., AHMED, S. & KRUMPELT, M. 1996. The low-temperature partial oxidation reforming of fuels for transportation fuel cell systems. *Fuel cell seminar.* Kissimmee, FL (United States), 17-20 Nov 1996: Argonne National Laboratory, Argonne, IL.

KURUNGOT, S. & YAMAGUCHI, T. 2004. Stability improvement of Rh/gamma-Al2O3 catalyst layer by ceria doping for steam reforming in an integrated catalytic membrane reactor system. *Catalysis Letters,* 92**,** 181-187.

LANGE, J. P. 1997. Perspectives for Manufacturing Methanol at Fuel Value. *Industrial and Engineering Chemistry Research,* 36**,** 4282-4290.

LARIMI, A. S. & ALAVI, S. M. 2012. Ceria-Zirconia supported Ni catalysts for partial oxidation of methane to synthesis gas. *Fuel,* 102**,** 366-371.

LARMINIE, J. & DICKS, A. 2003. *Fuel Cell Systems Explained,* Southern Gate, Chichester, John Wiley & Sons Ltd.

LARSON, E. D., WILLIAMS, R. H. & LEAL, M. R. L. V. 2001. A review of biomass integrated-gasifier/gas turbine combined cycle technology and its application in sugarcane industries, with an analysis for Cuba. *Energy for Sustainable Development,* 5**,** 54-76.

LATIFI, M., BERRUTI, F. & BRIENS, C. 2014. Non-catalytic and catalytic steam reforming of a bio-oil model compound in a novel “Jiggle Bed” Reactor. *Fuel,* 129**,** 278-291.

LAURI, P., HAVLÍK, P., KINDERMANN, G., FORSELL, N., BÖTTCHER, H. & OBERSTEINER, M. 2014. Woody biomass energy potential in 2050. *Energy Policy,* 66**,** 19-31.

LEVIN, D. B. & CHAHINE, R. 2010. Challenges for renewable hydrogen production from biomass. *International Journal of Hydrogen Energy,* 35**,** 4962-4969.

LI, Y., FU, Q. & FLYTZANI-STEPHANOPOULOS, M. 2000. Low-temperature water-gas shift reaction over Cu- and Ni-loaded cerium oxide catalysts. *Applied Catalysis B-Environmental,* 27**,** 179-191.

LI, Y., WANG, X., XIE, C. & SONG, C. 2009. Influence of ceria and nickel addition to alumina-supported Rh catalyst for propane steam reforming at low temperatures. *Applied Catalysis A: General,* 357**,** 213-222.

LIBRA, J. A., RO, K. S., KAMMANN, C., FUNKE, A., BERGE, N. D., NEUBAUER, Y., TITIRICI, M.-M., FÜHNER, C., BENS, O., KERN, J. & EMMERICH, K.-H. 2014. Hydrothermal carbonization of biomass residuals: a comparative review of the chemistry, processes and applications of wet and dry pyrolysis. *Biofuels,* 2**,** 71-106.

LIGURAS, D. K., GOUNDANI, K. & VERYKIOS, X. E. 2004. Production of hydrogen for fuel cells by catalytic partial oxidation of ethanol over structured Ni catalysts. *Journal of Power Sources,* 130**,** 30-37.

LIGURAS, D. K., KONDARIDES, D. I. & VERYKIOS, X. E. 2003. Production of hydrogen for fuel cells by steam reforming of ethanol over supported noble metal catalysts. *Applied Catalysis B: Environmental,* 43**,** 345-354.

LIMA DA SILVA, A., MALFATTI, C. D. F. & MÜLLER, I. L. 2009. Thermodynamic analysis of ethanol steam reforming using Gibbs energy minimization method: A detailed study of the conditions of carbon deposition. *International Journal of Hydrogen Energy,* 34**,** 4321-4330.

LIN, Y. C., CHO, J., TOMPSETT, G. A., WESTMORELAND, P. R. & HUBER, G. W. 2009. Kinetics and Mechanism of Cellulose Pyrolysis. *Journal of Physical Chemistry C,* 113**,** 20097-20107.

LINNHOFF, B. & FLOWER, J. R. 1978. Synthesis of heat exchanger networks: I. Systematic generation of energy optimal networks. *AIChE Journal,* 24**,** 633-642.

LIU, D., QUEK, X. Y., CHEO, W. N. E., LAU, R., BORGNA, A. & YANG, Y. 2009. MCM-41 supported nickel-based bimetallic catalysts with superior stability during carbon dioxide reforming of methane: Effect of strong metal–support interaction. *Journal of Catalysis,* 266**,** 380-390.

LIU, Q., WANG, S., ZHENG, Y., LUO, Z. & CEN, K. 2008. Mechanism study of wood lignin pyrolysis by using TG–FTIR analysis. *Journal of Analytical and Applied Pyrolysis,* 82**,** 170-177.

LIU, S.-K. & LIN, Y.-C. 2012. Autothermal Partial Oxidation of Glycerol to Syngas over Pt-, LaMnO3-, and Pt/LaMnO3-Coated Monoliths. *Industrial & Engineering Chemistry Research,* 51**,** 16278-16287.

LONG, R., PICIOCCIO, K. & ZAGORIA, A. 2011. Optimising H2 Production and Use. *In:* UOP LLC, A. H. C. (ed.) *Petroleum Technology Quarterly.* Hopesay, Craven Arms, U.K.: Crambeth Allen Publishing Ltd.

LU, Y., LIU, Y. & SHEN, S. K. 1998a. Design of stable Ni catalysts for partial oxidation of methane to synthesis gas. *Journal of Catalysis,* 177**,** 386-388.

LU, Y., XUE, J. Z., YU, C. C., LIU, Y. & SHEN, S. K. 1998b. Mechanistic investigations on the partial oxidation of methane to synthesis gas over a nickel-on-alumina catalyst. *Applied Catalysis a-General,* 174**,** 121-128.

LUTZ, A., BRADSHAW, R., KELLER, J. & WITMER, D. 2003. Thermodynamic analysis of hydrogen production by steam reforming. *International Journal of Hydrogen Energy,* 28**,** 159-167.

LWIN, Y. 2000. Chemical Equilibrium by Gibbs Energy Minimization on Spreadsheets. *International journal of engineering education,* 16**,** 335-339.

MANTILLA, S. V., GAUTHIER-MARADEI, P., GIL, P. Á. & CÁRDENAS, S. T. 2014. Comparative study of bio-oil production from sugarcane bagasse and and palm empty fruit bunch: Yield optimization and bio-oil characterization. *Journal of Analytical and Applied Pyrolysis 108 (2014) 284–294,* 108**,** 284-294.

MARDA, J. R., DIBENEDETTO, J., MCKIBBEN, S., EVANS, R. J., CZERNIK, S., FRENCH, R. J. & DEAN, A. M. 2009. Non-catalytic partial oxidation of bio-oil to synthesis gas for distributed hydrogen production. *International Journal of Hydrogen Energy,* 34**,** 8519-8534.

MARQUEVICH, M., CZERNIK, S., CHORNET, E. & MONTANE, D. 1999. Hydrogen from biomass: Steam reforming of model compounds of fast-pyrolysis oil. *Energy & Fuels,* 13**,** 1160-1166.

MARTIN, S., ALBRECHT, F. G., VAN DER VEER, P., LIEFTINK, D. & DIETRICH, R.-U. 2016. Evaluation of on-site hydrogen generation via steam reforming of biodiesel: Process optimization and heat integration. *International Journal of Hydrogen Energy,* 41**,** 6640-6652.

MARTIN, S., KRAAIJ, G., ASCHER, T., WAILS, D. & WÖRNER, A. 2015. An experimental investigation of biodiesel steam reforming. *International Journal of Hydrogen Energy,* 40**,** 95-105.

MARTIN, S. & WÖRNER, A. 2011. On-board reforming of biodiesel and bioethanol for high temperature PEM fuel cells: Comparison of autothermal reforming and steam reforming. *Journal of Power Sources,* 196**,** 3163-3171.

MAVUKWANA, A., JALAMA, K., NTULI, F. & HARDING, K. 2013. Simulation of sugarcane bagasse gasification using Aspen Plus. *International Conference on Chemical and Environmental Engineering.* Johannesburg (South Africa).

MCGRATH, T. E., CHAN, W. G. & HAJALIGOL, M. R. 2003. Low temperature mechanism for the formation of polycyclic aromatic hydrocarbons from the pyrolysis of cellulose. *Journal of Analytical and Applied Pyrolysis,* 66**,** 51-70.

MEDRANO, J., OLIVA, M., RUIZ, J., GARCIA, L. & ARAUZO, J. 2008. Catalytic steam reforming of acetic acid in a fluidized bed reactor with oxygen addition. *International Journal of Hydrogen Energy,* 33**,** 4387-4396.

MELCHIORI, T., DI FELICE, L., MOTA, N., NAVARRO, R. M., FIERRO, J. L. G., ANNALAND, M. V. S. & GALLUCCI, F. 2014. Methane partial oxidation over a LaCr0.85Ru0.15O3 catalyst: Characterization, activity tests and kinetic modeling. *Applied Catalysis A: General,* 486**,** 239-249.

MING, Q., HEALEY, T., ALLEN, L. & IRVING, P. 2002. Steam reforming of hydrocarbon fuels. *Catalysis Today 77 (2002) 51–64,* 77**,** 51-64.

MOHAN, D., PITTMAN, C. U. & STEELE, P. H. 2006. Pyrolysis of Wood/Biomass for Bio-oil: A Critical Review. *Energy & Fuels,* 20**,** 848-889.

MURCIA-MASCARÓS, S., NAVARRO, R. M., GÓMEZ-SAINERO, L., COSTANTINO, U., NOCCHETTI, M. & FIERRO, J. L. G. 2001. Oxidative Methanol Reforming Reactions on CuZnAl Catalysts Derived from Hydrotalcite-like Precursors. *Journal of Catalysis,* 198**,** 338-347.

NAHAR, G. & DUPONT, V. 2013. Recent advances in hydrogen production via autothermal reforming process (ATR): A review of patents and research articles. *Recent Patents on Chemical Engineering,* 6**,** 8-42.

NAHAR, G. & DUPONT, V. 2014. Hydrogen via steam reforming of liquid biofeedstock. *Biofuels,* 3**,** 167-191.

NAHAR, G. A. 2010. Hydrogen rich gas production by the autothermal reforming of biodiesel (FAME) for utilization in the solid-oxide fuel cells: A thermodynamic analysis. *International Journal of Hydrogen Energy,* 35**,** 8891-8911.

NAIK, S. N., GOUD, V. V., ROUT, P. K. & DALAI, A. K. 2010. Production of first and second generation biofuels: A comprehensive review. *Renewable and Sustainable Energy Reviews,* 14**,** 578-597.

NI, M., LEUNG, D. Y. C. & LEUNG, M. K. H. 2007. A review on reforming bio-ethanol for hydrogen production. *International Journal of Hydrogen Energy,* 32**,** 3238-3247.

NI, M., LEUNG, D. Y. C., LEUNG, M. K. H. & SUMATHY, K. 2006. An overview of hydrogen production from biomass. *Fuel Processing Technology,* 87**,** 461-472.

NSAFUL, F. 2012. *Process modelling of sugar mill biomass to energy conversion processes and energy integration of pyrolysis.* MSc, Stellenbosch University.

NYAKUMA, B. B., JOHARI, A., AHMAD, A. & ABDULLAH, T. A. T. 2014. Comparative Analysis of the Calorific Fuel Properties of Empty Fruit Bunch Fiber and Briquette. *Energy Procedia,* 52**,** 466-473.

OCSACHOQUE, M., POMPEO, F. & GONZALEZ, G. 2011. Rh–Ni/CeO2–Al2O3 catalysts for methane dry reforming. *Catalysis Today,* 172**,** 226-231.

OLIVEIRA, R. L., BITENCOURT, I. G. & PASSOS, F. B. 2013. Partial Oxidation of Methane to Syngas on Rh/Al2O3 and Rh/Ce-ZrO2 Catalysts. *Journal of the Brazilian Chemical Society,* 24**,** 68-75.

OMAR, R., IDRIS, A., YUNUS, R., KHALID, K. & AIDA ISMA, M. I. 2011. Characterization of empty fruit bunch for microwave-assisted pyrolysis. *Fuel,* 90**,** 1536-1544.

ONARHEIM, K., SOLANTAUSTA, Y. & LEHTO, J. 2015. Process Simulation Development of Fast Pyrolysis of Wood Using Aspen Plus. *Energy & Fuels,* 29**,** 205-217.

OOI, Z. X., TEOH, Y. P., KUNASUNDARI, B. & SHUIT, S. H. 2017. Oil palm frond as a sustainable and promising biomass source in Malaysia: A review. *Environmental Progress & Sustainable Energy,* 36**,** 1864-1874.

OU, T.-C., CHANG, F.-W. & ROSELIN, L. S. 2008. Production of hydrogen via partial oxidation of methanol over bimetallic Au–Cu/TiO2 catalysts. *Journal of Molecular Catalysis A: Chemical,* 293**,** 8-16.

OZAWA, M. & KIMURA, M. 1990. Effect of Cerium Addition on the Thermal-Stability of Gamma-Alumina Support. *Journal of Materials Science Letters,* 9**,** 291-293.

PACESILA, M., BURCEA, S. G. & COLESCA, S. E. 2016. Analysis of renewable energies in European Union. *Renewable and Sustainable Energy Reviews,* 56**,** 156-170.

PANT, K. & GUPTA, R. B. 2008. Fundamentals and Use of Hydrogen as a Fuel. *In:* GUPTA, R. B. (ed.) *Hydrogen Fuel Production, Transport, and Storage.* CRC Press.

PAPAVASILIOU, J. 2004. Production of hydrogen via combined steam reforming of methanol over CuO–CeO2 catalysts. *Catalysis Communications,* 5**,** 231-235.

PARTHASARATHY, P. & NARAYANAN, K. S. 2014. Hydrogen production from steam gasification of biomass: Influence of process parameters on hydrogen yield – A review. *Renewable Energy,* 66**,** 570-579.

PASTOROVA, I., BOTTO, R. E., ARISZ, P. W. & BOON, J. J. 1994. Cellulose Char Structure - a Combined Analytical Py-Gc-Ms, Ftir, and Nmr-Study. *Carbohydrate Research,* 262**,** 27-47.

PATEL, S. & PANT, K. K. 2007. Hydrogen production by oxidative steam reforming of methanol using ceria promoted copper–alumina catalysts. *Fuel Processing Technology,* 88**,** 825-832.

PÉREZ-FORTES, M., SCHÖNEBERGER, J. C., BOULAMANTI, A. & TZIMAS, E. 2016. Methanol synthesis using captured CO 2 as raw material: Techno-economic and environmental assessment. *Applied Energy,* 161**,** 718-732.

PERYOGA, Y., DEWI SOLIKHAH, M. & AGUS RAKSODEWANTO, A. 2014. Production Cost Assessment of Palm Empty Fruit Bunch Conversion to Bio-oil via Fast Pyrolysis. *International Journal on Advanced Science, Engineering, InformationTechnology* 4**,** 6-12.

PIMENIDOU, P. & DUPONT, V. 2012. Characterisation of palm empty fruit bunch (PEFB) and pinewood bio-oils and kinetics of their thermal degradation. *Bioresource Technology,* 109**,** 198-205.

PIRKER, J., MOSNIER, A., KRAXNER, F., HAVLÍK, P. & OBERSTEINER, M. 2016. What are the limits to oil palm expansion? *Global Environmental Change,* 40**,** 73-81.

PRECIADO, J., ORTIZ-MARTINEZ, J., GONZALEZ-RIVERA, J., SIERRA-RAMIREZ, R. & GORDILLO, G. 2012. Simulation of Synthesis Gas Production from Steam Oxygen Gasification of Colombian Coal Using Aspen Plus�. *Energies,* 5**,** 4924-4940.

QU, T., GUO, W., SHEN, L., XIAO, J. & ZHAO, K. 2011. Experimental Study of Biomass Pyrolysis Based on Three Major Components: Hemicellulose, Cellulose, and Lignin. *Industrial & Engineering Chemistry Research,* 50**,** 10424-10433.

QUAAK, P., KNOEF, H. & STASSEN, H. 1999. Energy from biomass : a review of combustion and gasification technologies. *In:* PAPER, W. B. T. (ed.) *Energy Series.* Washington, D.C: World Bank.

RABIEI, Z. 2012. Hydrogen management in refineries. *Petroleum & Coal,* 54**,** 357-368.

RADLEIN, D., PISKORZ, J. & SCOTT, D. S. 1991. Fast Pyrolysis of Natural Polysaccharides as a Potential Industrial-Process. *Journal of Analytical and Applied Pyrolysis,* 19**,** 41-63.

RAMACHANDRAN, R. 1998. An overview of industrial uses of hydrogen. *International Journal of Hydrogen Energy,* 23**,** 593-598.

REMÓN, J., BROUST, F., VALETTE, J., CHHITI, Y., ALAVA, I., FERNANDEZ-AKARREGI, A. R., ARAUZO, J. & GARCIA, L. 2014. Production of a hydrogen-rich gas from fast pyrolysis bio-oils: Comparison between homogeneous and catalytic steam reforming routes. *International Journal of Hydrogen Energy,* 39**,** 171-182.

REN21 2015. REN12 Renewables 2015 Global Status Report. Paris: REN21 Secretariat.

RENNARD, D., FRENCH, R., CZERNIK, S., JOSEPHSON, T. & SCHMIDT, L. 2010. Production of synthesis gas by partial oxidation and steam reforming of biomass pyrolysis oils. *International Journal of Hydrogen Energy,* 35**,** 4048-4059.

RENNARD, D. C., KRUGER, J. S. & SCHMIDT, L. D. 2009. Autothermal catalytic partial oxidation of glycerol to syngas and to non-equilibrium products. *ChemSusChem,* 2**,** 89-98.

RESENDE, K. A., ÁVILA-NETO, C. N., RABELO-NETO, R. C., NORONHA, F. B. & HORI, C. E. 2015. Thermodynamic analysis and reaction routes of steam reforming of bio-oil aqueous fraction. *Renewable Energy,* 80**,** 166-176.

RINGER, M., PUTSCHE, V. & SCAHILL, J. 2006. Large-Scale pyrolysis oil production: A technology assessment and economic analysis. National Renewable Energy Laboratory ,Technical report, NREL/TP-510-37779, November 2006.

RIOCHE, C., KULKARNI, S., MEUNIER, F. C., BREEN, J. P. & BURCH, R. 2005. Steam reforming of model compounds and fast pyrolysis bio-oil on supported noble metal catalysts. *Applied Catalysis B: Environmental,* 61**,** 130-139.

RODRIGUES, C. P., SILVA, V. T. D. & SCHMAL, M. 2009. Partial oxidation of ethanol on Cu/Alumina/cordierite monolith. *Catalysis Communications,* 10**,** 1697-1701.

ROH, H.-S., WANG, Y. & KING, D. L. 2008. Selective Production of H2 from Ethanol at Low Temperatures over Rh/ZrO2–CeO2 Catalysts. *Topics in Catalysis,* 49**,** 32-37.

ROSTRUP-NIELSEN, J. R. 1973. Activity of Nickel Catalysts for Steam Reforming of Hydrocarbons. *Journal of Catalysis,* 31**,** 173-199.

ROSTRUP-NIELSEN, J. R. 1993. Production of synthesis gas. *Catalysis Today,* 18**,** 305-324.

ROSTRUP-NIELSEN, J. R. 2000. New aspects of syngas production and use. *Catalysis Today,* 63**,** 159-164.

ROSTRUP-NIELSEN, J. R., SEHESTED, J. & NØRSKOV, J. K. 2002a. Hydrogen and synthesis gas by steam- and C02 reforming. *Advance Catalysis,* 47**,** 65-139.

ROSTRUP-NIELSEN, J. R., SEHESTED, J. & NØRSKOV, J. K. 2002b. Hydrogen and Synthesis Gas by Steam- and CO2 Reforming. *Advances in Catalysis,* 47**,** 65-139.

ROSTRUP-NIELSEN, J. R., SEHESTED, J. & NØRSKOV, J. K. 2002c. Hydrogen and Synthesis Gas by steam and CO2 reforming. *Advances in Catalysis,* 47**,** 65 - 139.

RUENGVILAIRAT, P., TANATAVIKORN, H. & VITIDSANT, T. 2012. Bio-Oil Production by Pyrolysis of Oil Palm Empty Fruit Bunch in Nitrogen and Steam Atmospheres. *Journal of Sustainable Bioenergy Systems,* 02**,** 75-85.

SALGE, J., DELUGA, G. & SCHMIDT, L. 2005. Catalytic partial oxidation of ethanol over noble metal catalysts. *Journal of Catalysis,* 235**,** 69-78.

SALHI, N., BOULAHOUACHE, A., PETIT, C., KIENNEMANNC, A. & RABIA, C. 2011. Steam reforming of methane to syngas over NiAl2O4 spinel catalyst. *International Journal of Hydrogen Energy,* 36**,** 11433-11439.

SARKAR, S. & KUMAR, A. 2010. Large-scale biohydrogen production from bio-oil. *Bioresour Technol,* 101**,** 7350-61.

SCAHILL, J., DIEBOLD, J. P. & FEIK, C. 1997. Removal of residual char fines from pyrolysis vapors by hot gas filtration. *In:* A.V., B. & D.G.B., B. (eds.) *Developments in Thermochemical Biomass Conversion.* Dordrecht: Springer.

SCHELL, D. J. & HARWOOD, C. 1994. Milling of Lignocellulosic Biomass - Results of Pilot-Scale Testing. *Applied Biochemistry and Biotechnology,* 45-6**,** 159-168.

SCHUYTEN, S., GUERRERO, S., MILLER, J. T., SHIBATA, T. & WOLF, E. E. 2009. Characterization and oxidation states of Cu and Pd in Pd–CuO/ZnO/ZrO2 catalysts for hydrogen production by methanol partial oxidation. *Applied Catalysis A: General,* 352**,** 133-144.

SCOTT, D. S. & PISKORZ, J. 1984. The continuous flash pyrolysis of biomass. *The Canadian Journal of Chemical Engineering,* 62**,** 404-412.

SEHESTED, J. 2006. Four challenges for nickel steam-reforming catalysts. *Catalysis Today,* 111**,** 103-110.

SEMBIRING, K. C., RINALDI, N. & SIMANUNGKALIT, S. P. 2015. Bio-oil from Fast Pyrolysis of Empty Fruit Bunch at Various Temperature. *Energy Procedia,* 65**,** 162-169.

SEMELSBERGER, T., BROWN, F., BORUP, R. L. & INBODY, M. A. 2004. Equilibrium products from autothermal processes for generating hydrogen-rich fuel-cell feeds. *International Journal of Hydrogen Energy,* 29**,** 1047-1064.

SHEN, D. K., GU, S. & BRIDGWATER, A. V. 2010. Study on the pyrolytic behaviour of xylan-based hemicellulose using TG–FTIR and Py–GC–FTIR. *Journal of Analytical and Applied Pyrolysis,* 87**,** 199-206.

SHEN, J. 2002. Influence of preparation method on performance of Cu/Zn-based catalysts for low-temperature steam reforming and oxidative steam reforming of methanol for H2 production for fuel cells. *Catalysis Today,* 77**,** 89-98.

SILVA, F. D. A., RUIZ, J. A. C., DE SOUZA, K. R., BUENO, J. M. C., MATTOS, L. V., NORONHA, F. B. & HORI, C. E. 2009. Partial oxidation of methane on Pt catalysts: Effect of the presence of ceria–zirconia mixed oxide and of metal content. *Applied Catalysis A: General,* 364**,** 122-129.

SKOGSTAD, G. 2016. Policy feedback and self-reinforcing and self-undermining processes in EU biofuels policy. *Journal of European Public Policy,* 24**,** 21-41.

SMITH, M. W. & SHEKHAWAT, D. 2011a. Catalytic Partial Oxidation. 73-128.

SMITH, M. W. & SHEKHAWAT, D. 2011b. Chapter 5 Catalytic Partial Oxidation. *In:* SHEKHAWAT, D., BERRY, D. A. & SPIVEY, J. J. (eds.) *Fuel Cells: Technologies for Fuel Processing.* Amsterdam: Elsevier.

SPATH, P. L. & MANN, M. K. 2000. Life cycle assessment of hydrogen production via natural gas steam reforming. *In:* LABORATORY, N. R. E. (ed.) *National Technical Information Service.* Golden, Colorado: US Department of Energy.

SPECCHIA, S., VELLA, L. D., DE ROGATIS, L., MONTINI, T., SPECCHIA, V. & FORNASIERO, P. 2010. Rh-based catalysts for syngas production via SCT-CPO reactors. *Catalysis Today,* 155**,** 101-107.

SPLIETHOFF, H. & HEIN, K. R. G. 1998. Effect of co-combustion of biomass on emissions in pulverized fuel furnaces. *Fuel Processing Technology,* 54**,** 189-205.

SRIVASTAVA, A. & PANT, K. K. 2012. Oxidative Steam Reforming of Bioethanol over Rh/CeO2-Al2O3 Catalyst for Hydrogen Production. *Journal of Thermodynamics & Catalysis,* 04.

SUKIRAN, M. A., CHIN, C. M. & BAKAR, N. 2009. Bio-oils from Pyrolysis of Oil Palm Empty Fruit Bunches. *American Journal of Applied Sciences,* 6**,** 869-875.

SULAIMAN, F. & ABDULLAH, N. 2011. Optimum conditions for maximising pyrolysis liquids of oil palm empty fruit bunches. *Energy,* 36**,** 2352-2359.

TAKEZAWA, N. & IWASA, N. 1997. Steam reforming and dehydrogenation of methanol: Difference in the catalytic functions of copper and group VIII metals. *Catalysis Today,* 36**,** 45-56.

TANABE, Y. & NISHIBAYASHI, Y. 2013. Developing more sustainable processes for ammonia synthesis. *Coordination Chemistry Reviews,* 257**,** 2551-2564.

TANDE, L. N. & DUPONT, V. 2016. Autothermal reforming of palm empty fruit bunch bio-oil: thermodynamic modelling. *AIMS Energy,* 4**,** 68-92.

TARRAGO-TRANI, M. T., PHILLIPS, K. M., LEMAR, L. E. & HOLDEN, J. M. 2006. New and existing oils and fats used in products with reduced trans-fatty acid content. *J Am Diet Assoc,* 106**,** 867-80.

TAVAZZI, I., BERETTA, A., GROPPI, G., DONAZZI, A., MAESTRI, M., TRONCONI, E. & FORZATTI, P. 2007. Catalytic partial oxidation of CH4 and C3H8: experimental and modeling study of the dynamic and steady state behavior of a pilot-scale reformer. 167**,** 319-324.

TRANE, R., DAHL, S., SKJØTH-RASMUSSEN, M. S. & JENSEN, A. D. 2012. Catalytic steam reforming of bio-oil. *International Journal of Hydrogen Energy,* 37**,** 6447-6472.

TRIMM, D. L. 1997. Coke formation and minimisation during steam reforming reactions. *Catalysis Today,* 37**,** 233-238.

TRIMM, D. L. 1999. Catalysts for the control of coking during steam reforming. *Catalysis Today,* 49**,** 3-10.

VAGIA, E. & LEMONIDOU, A. 2007. Thermodynamic analysis of hydrogen production via steam reforming of selected components of aqueous bio-oil fraction. *International Journal of Hydrogen Energy,* 32**,** 212-223.

VAGIA, E. C. & LEMONIDOU, A. A. 2008a. Hydrogen production via steam reforming of bio-oil components over calcium aluminate supported nickel and noble metal catalysts. *Applied Catalysis A: General,* 351**,** 111-121.

VAGIA, E. C. & LEMONIDOU, A. A. 2008b. Thermodynamic analysis of hydrogen production via autothermal steam reforming of selected components of aqueous bio-oil fraction. *International Journal of Hydrogen Energy,* 33**,** 2489-2500.

VASILIOU, A. K., KIM, J. H., ORMOND, T. K., PIECH, K. M., URNESS, K. N., SCHEER, A. M., ROBICHAUD, D. J., MUKARAKATE, C., NIMLOS, M. R., DAILY, J. W., GUAN, Q., CARSTENSEN, H. H. & ELLISON, G. B. 2013. Biomass pyrolysis: thermal decomposition mechanisms of furfural and benzaldehyde. *J Chem Phys,* 139**,** 104310.

VISCONTI, A., MICCIO, M. & JUCHELKOVÁ, D. Equilibrium-based simulation of lignocellulosic biomass pyrolysis via Aspen plus. *In:* MASTORAKIS, N. E., DEMIRALP, M., MUKHOPADHYAY, N. & MAINARDI, F., eds. Proceedings of the 8th International Conference on Applied Mathematics,

Simulation, Modelling, 2014 Florence. WSEAS Press.

VOLDSUND, M., JORDAL, K. & ANANTHARAMAN, R. 2016. Hydrogen production with CO2 capture. *International Journal of Hydrogen Energy,* 41**,** 4969-4992.

WANG, D. N., CZERNIK, S. & CHORNET, E. 1998. Production of hydrogen from biomass by catalytic steam reforming of fast pyrolysis oils. *Energy & Fuels,* 12**,** 19-24.

WANG, S., CAI, Q., ZHANG, F., LI, X., ZHANG, L. & LUO, Z. 2014. Hydrogen production via catalytic reforming of the bio-oil model compounds: Acetic acid, phenol and hydroxyacetone. *International Journal of Hydrogen Energy,* 39**,** 18675-18687.

WANG, S. B. & LU, G. Q. 1998. Role of CeO2 in Ni/CeO2-Al2O3 catalysts for carbon dioxide reforming of methane. *Applied Catalysis B-Environmental,* 19**,** 267-277.

WANG, X. & GORTE, R. J. 2002. A study of steam reforming of hydrocarbon fuels on Pd/ceria. *Applied Catalysis A: General,* 224**,** 209-218.

WARD, J., RASUL, M. G. & BHUIYA, M. M. K. 2014. Energy Recovery from Biomass by Fast Pyrolysis. *Procedia Engineering,* 90**,** 669-674.

WBA. 2016. *World Bioenergy Association: Global Bioenergy Statistics* [Online]. Available: http://worldbioenergy.org/content/wba-gbs [Accessed 2017].

WEI, J. 1975. Catalysis for Motor Vehicle Emissions. 24**,** 57-129.

WILHELM, D. J., SIMBECK, D. R., KARP, A. D. & DICKENSON, R. L. 2001a. Syngas production for gas-to-liquids applications technologies, issues and outlook. *Fuel Processing Technology,* 71**,** 139-148.

WILHELM, D. J., SIMBECK, D. R., KARP, A. D. & DICKENSON, R. L. 2001b. Syngas production for gas-to-liquids applications: technologies, issues and outlook. *Fuel Processing Technology,* 71**,** 139-148.

WILLIAMS, M. C. 2011. Fuel Cells. 11-27.

WILLIAMS, O., EASTWICK, C., KINGMAN, S., GIDDINGS, D., LORMOR, S. & LESTER, E. 2015. Investigation into the applicability of Bond Work Index (BWI) and Hardgrove Grindability Index (HGI) tests for several biomasses compared to Colombian La Loma coal. *Fuel,* 158**,** 379-387.

WU, C., HUANG, Q., SUI, M., YAN, Y. & WANG, F. 2008. Hydrogen production via catalytic steam reforming of fast pyrolysis bio-oil in a two-stage fixed bed reactor system. *Fuel Processing Technology,* 89**,** 1306-1316.

WU, C. & LIU, R. 2010a. Carbon deposition behavior in steam reforming of bio-oil model compound for hydrogen production. *International Journal of Hydrogen Energy,* 35**,** 7386-7398.

WU, C. & LIU, R. 2010b. Hydrogen Production from Steam Reforming ofm-Cresol, a Model Compound Derived from Bio-oil: Green Process Evaluation Based on Liquid Condensate Recycling. *Energy & Fuels,* 24**,** 5139-5147.

XIE, J., SU, D., YIN, X., WU, C. & ZHU, J. 2011. Thermodynamic analysis of aqueous phase reforming of three model compounds in bio-oil for hydrogen production. *International Journal of Hydrogen Energy,* 36**,** 15561-15572.

XIU, S. & SHAHBAZI, A. 2012. Bio-oil production and upgrading research: A review. *Renewable and Sustainable Energy Reviews,* 16**,** 4406-4414.

XU, J. & FROMENT, G. F. 1989. Methane steam reforming, methanation and water-gas shift: I. Intrinsic kinetics. *AIChE Journal,* 35**,** 88-96.

YONG, S. T., OOI, C. W., CHAI, S. P. & WU, X. S. 2013. Review of methanol reforming-Cu-based catalysts, surface reaction mechanisms, and reaction schemes. *International Journal of Hydrogen Energy,* 38**,** 9541-9552.

YOON, S., KANG, I. & BAE, J. 2008. Effects of ethylene on carbon formation in diesel autothermal reforming. *International Journal of Hydrogen Energy 3 3 (2 0 0 8) 4 7 8 0 – 4 7 8 8,* 33**,** 4780-4788.

YOON, S., KANG, I. & BAE, J. 2009. Suppression of ethylene-induced carbon deposition in diesel autothermal reforming). *International Journal of Hydrogen Energy,* 34**,** 1844-1851.

YOUN, M. H., SEO, J. G., CHO, K. M., JUNG, J. C., KIM, H., LA, K. W., PARK, D. R., PARK, S., LEE, S. H. & SONG, I. K. 2008. Effect of support on hydrogen production by auto-thermal reforming of ethanol over supported nickel catalysts. *Korean Journal of Chemical Engineering,* 25**,** 236-238.

ZAHEDI NEZHADA, M., ROWSHANZAMIRA, S. & EIKANIC, M. H. 2009. Autothermal reforming of methane to synthesis gas: Modeling and simulation. *International Journal of Hydrogen Energy,* 34**,** 1292-1300.

ZHANG, Y., BROWN, T. R., HU, G. & BROWN, R. C. 2013. Comparative techno-economic analysis of biohydrogen production via bio-oil gasification and bio-oil reforming. *Biomass and Bioenergy,* 51**,** 99-108.

ZHENGZHOU, A. M. 2016. *Biopellet Machines* [Online]. Available: http://www.biopelletmachine.com/product/sawdust-making-machine/EFB-shredder-crushing-machine.html [Accessed 28/10/2016 2016].

ZIN, R. M., LEA-LANGTON, A., DUPONT, V. & TWIGG, M. V. 2012. High hydrogen yield and purity from palm empty fruit bunch and pine pyrolysis oils. *International Journal of Hydrogen Energy,* 37**,** 10627-10638.

ZIN, R. M., ROSS, A. B., JONES, J. M. & DUPONT, V. 2015. Hydrogen from ethanol reforming with aqueous fraction of pine pyrolysis oil with and without chemical looping. *Bioresour Technol,* 176**,** 257-66.

Appendix A

A.1 Property methods

Table A. 1 Boie correlation parameters

Symbol	Value (default)
a_{1i}	151.2
a_{2i}	499.77
a_{3i}	45.0
a_{4i}	-47.7
a_{5i}	27.0
a_{6i}	-189.0

Table A. 2 Kirov equation parameters

Symbol	Value (default)
$a_{i,11}$	1.0
$a_{i,12}$	0
$a_{i,13}$	0
$a_{i,14}$	0
$a_{i,21}$	0.165
$a_{i,22}$	6.8×10^{-4}
$a_{i,23}$	-4.2×10^{-7}
$a_{i,24}$	0
$a_{i,31}$	0.395
$a_{i,32}$	8.1×10^{-4}
$a_{i,33}$	0
$a_{i,34}$	0
$a_{i,41}$	0.71
$a_{i,42}$	6.1×10^{-4}
$a_{i,43}$	0
$a_{i,44}$	0
$a_{i,51}$	0.18
$a_{i,52}$	1.4×10^{-4}
$a_{i,53}$	0
$a_{i,54}$	0

A.2 Stream results

The flowsheet and corresponding stream results for the PAPS-BT process and given in Figure A.1 and Table A.3 respectively. Figure A. 2 is the flowsheet for the PAWS-CT process and the summary stream table is listed in Table A. 4. Similar streams listed on Table A.3 are left out of the summary stream Table A. 4. Table A.3, A.5 and A.6 contain stream results for the PAWS-BT and PAWS-CT processed shown in Figure 5.22 and Figure 5.23.

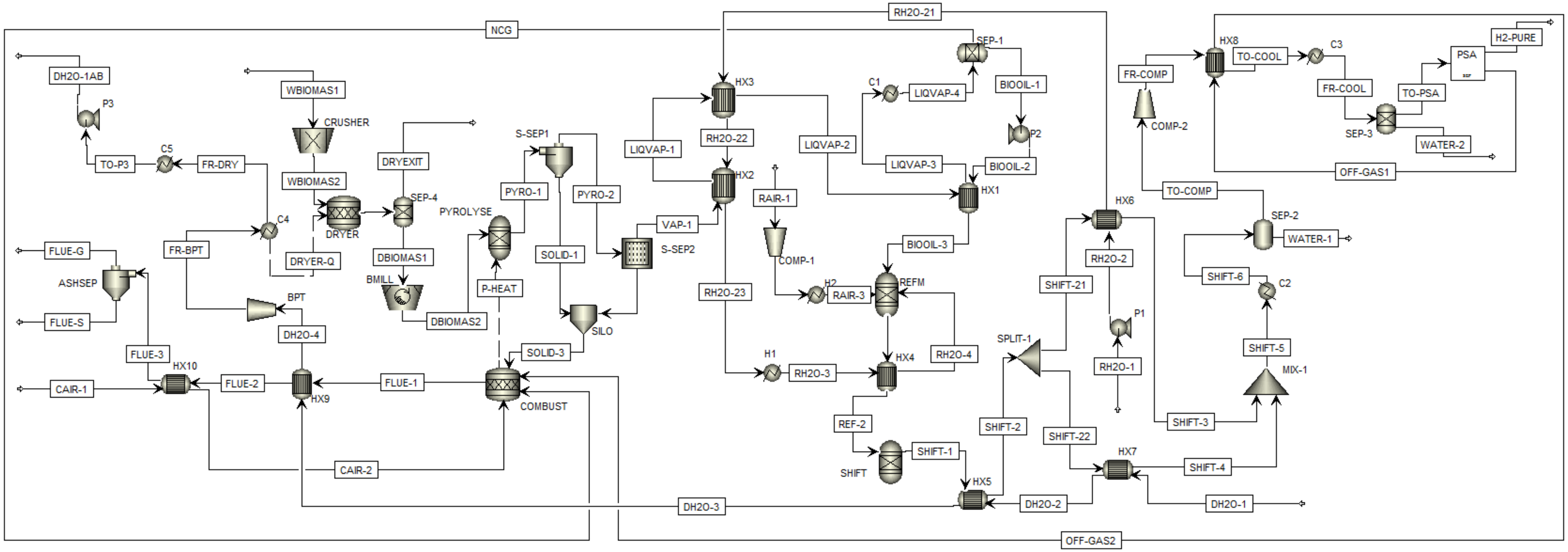

Figure A. 1 Flowsheet for a heat integrated PAPS-BT process

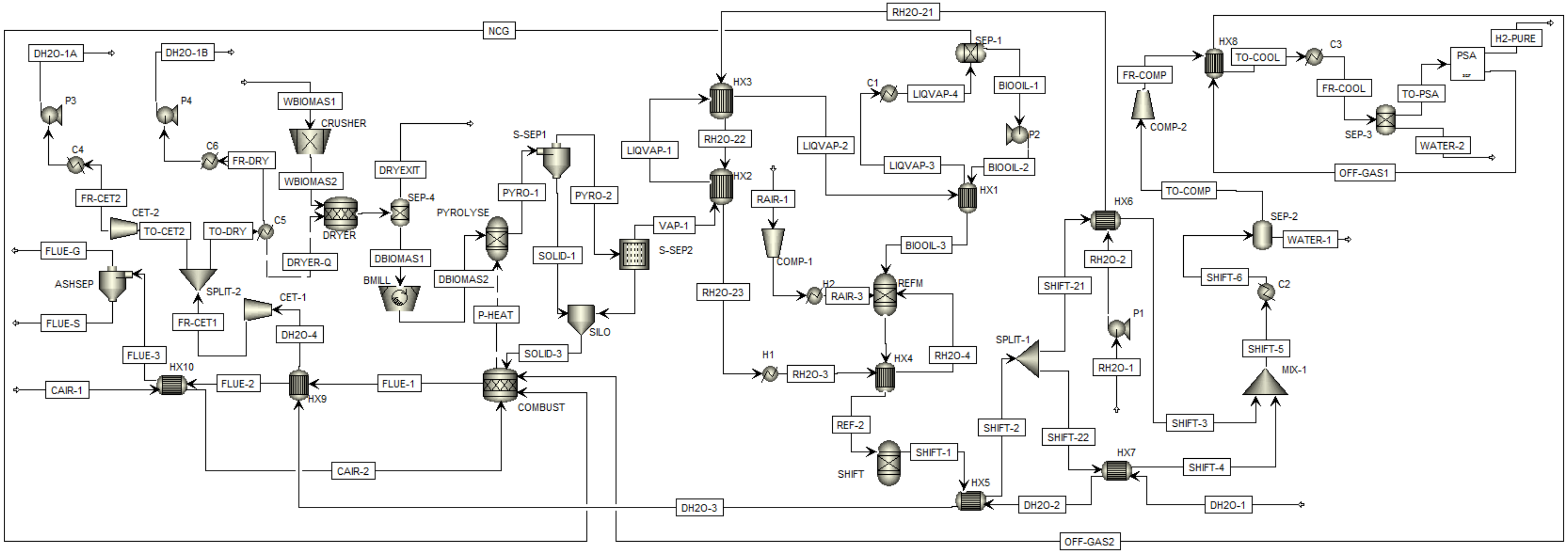

Figure A. 2 Flowsheet for a heat integrated PAPS-CT process

Table A. 3 Complete stream results for the base case PAPS-BP process

	Stream	**WBIOMAS1**	**WBIOMAS2**	**IN**	**DRYEXIT**	**DBIOMAS1**	**DBIOMAS2**	**PYRO-1**	**PYRO-2**	**SOLID-1**	**SOLID-2**	**SOLID-3**	**VAP-1**	**LIQVAP-1**	**LIQVAP-2**	**LIQVAP-3**	**LIQVAP-4**
From			CRUSHER	DRYER	SEP-4	SEP-4	BMILL	PYROLYSE	SOLIDSP1	SOLIDSP1	S-SEP2	SILO	S-SEP2	HX2	HX3	HX1	C1
To		CRUSHER	DRYER	SEP-4		BMILL	PYROLYSE	SOLIDSP1	S-SEP2	SILO	SILO	COMBUST	HX2	HX3	HX1	C1	SEP-1
Temp.	°C	25	25.25495	101.08	101.0819	101.0819	101.1974	500	500	500	500	500	500	200	153.5	84.01223	30
Pressure	bar	1	1	1	1	1	1	1	1	1	1	1	1	1	1	1	1
Mass Flow	kg/h	5000	5000	4999.9	1666.66	3333.33	3333.33	3333.33	2820.346	512.9873	27.94935	540.9366	2792.397	2792.397	2792.397	2792.397	2792.397
ACETIC		0	0	0	0	0	0	181.8135	179.9953	1.818135	0.00179995	1.819935	179.9935	179.9935	179.9935	179.9935	179.9935
PHENOL		0	0	0	0	0	0	18.18135	17.99953	0.181813	0.00017999	0.1819935	17.99935	17.99935	17.99935	17.99935	17.99935
LEVOGLU		0	0	0	0	0	0	90.90674	89.99767	0.909067	0.00089997	0.9099674	89.99677	89.99677	89.99677	89.99677	89.99677
FURFURA		0	0	0	0	0	0	327.2643	323.9916	3.272643	0.00323992	3.275882	323.9884	323.9884	323.9884	323.9884	323.9884
PALMITIC		0	0	0	0	0	0	18.18135	17.99953	0.181813	0.00017999	0.1819935	17.99935	17.99935	17.99935	17.99935	17.99935
H2		0	0	0	0	0	0	18.86755	18.67888	0.188675	0.00018678	0.1888623	18.67869	18.67869	18.67869	18.67869	18.67869
CO		0	0	0	0	0	0	208.3634	206.2798	2.083634	0.0020628	2.085697	206.2777	206.2777	206.2777	206.2777	206.2777
CO2		0	0	0	0	0	0	172.269	170.5463	1.72269	0.00170546	1.724395	170.5446	170.5446	170.5446	170.5446	170.5446
METHANE		0	0	0	0	0	0	10.2541	10.15156	0.102541	0.00010151	0.1026426	10.15146	10.15146	10.15146	10.15146	10.15146
CARBON		0	0	0	0	0	0	410.1642	22.33937	387.8248	22.33714	410.1619	0.002233	0.002233	0.002233	0.002233	0.002233
O2		0	0	0	0	0	0	0	0	0	0	0	0	0	0	0	0
N2		0	0	0	0	0	0	0	0	0	0	0	0	0	0	0	0
WATER		0	0	1666.6	1666.6	0	0	574.1478	568.4063	5.741478	0.0056840	5.747162	568.4007	568.4007	568.4007	568.4007	568.4007
AMMONIA		0	0	0	0	0	0	0.4101642	0.406062	0.004101	4.0606E-06	0.0041057	0.406058	0.406058	0.406058	0.406058	0.406058
FORMALD		0	0	0	0	0	0	199.9948	197.9949	1.999948	0.00197995	2.001928	197.9929	197.9929	197.9929	197.9929	197.9929
ACETALDE		0	0	0	0	0	0	18.18135	17.99953	0.1818135	0.00017999	0.1819935	17.99935	17.99935	17.99935	17.99935	17.99935
2-BUTA		0	0	0	0	0	0	18.18135	17.99953	0.181813	0.00017999	0.1819935	17.99935	17.99935	17.99935	17.99935	17.99935
CREOSOL		0	0	0	0	0	0	72.72539	71.99814	0.727253	0.00071998	0.7279739	71.99742	71.99742	71.99742	71.99742	71.99742
GUAIACO		0	0	0	0	0	0	290.9016	287.9925	2.909016	0.00287993	2.911896	287.9897	287.9897	287.9897	287.9897	287.9897
CATECHO		0	0	0	0	0	0	599.9845	593.9846	5.999845	0.00593985	6.005785	593.9787	593.9787	593.9787	593.9787	593.9787
BIOMASS		5000	5000	3333.3	0	3333.3	3333.3	0	0	0	0	0	0	0	0	0	0
ASH		0	0	0	0	0	0	102.541	5.584844	96.9562	5.584285	102.5405	0.000558	0.000558	0.000558	0.000558	0.000558

Table A.3 continue

	Stream	**BIOOIL-1**	**BIOOIL-2**	**BIOOIL-3**	**RH2O-1**	**RH2O-2**	**RH2O-21**	**RH2O-22**	**RH2O-23**	**RH2O-3**	**RH2O-4**	**RAIR-1**	**RAIR-2**	**RAIR-3**	**REF-1**	**REF-2**	**SHIFT-1**
From		SEP-1	P2	HX1		P1	HX6	HX3	HX2	H1	HX4		COMP-1	H2	REFM	HX4	SHIFT
To		P2	HX1	REFM	P1	HX6	HX3	HX2	H1	HX4	REFM	COMP-1	H2	REFM	HX4	SHIFT	HX5
Temperature	°C	30	46.15906	120	20	20.11721	74	113.246	133.5284	133.5284	499.8919	20	139.297	150	691.0861	250	250
Pressure	bar	1	3	3	1	3	3	3	3	3	3	1	3	3	3	3	3
Mass Flow	kg/h	2366.535	2366.535	2366.535	2954.691	2954.691	2954.691	2954.691	2954.691	2954.691	2954.691	3666.61	3666.61	3666.61	8987.837	8987.837	8987.837
ACETIC		178.1936	178.1936	178.1936	0	0	0	0	0	0	0	0	0	0	2.52978E-07	2.52978E-07	0
PHENOL		17.81936	17.81936	17.81936	0	0	0	0	0	0	0	0	0	0	3.8214E-20	3.8214E-20	0
LEVOGLU		89.0968	89.0968	89.0968	0	0	0	0	0	0	0	0	0	0	0	0	0
FURFURAL		320.7485	320.7485	320.7485	0	0	0	0	0	0	0	0	0	0	2.2883E-23	2.2883E-23	0
PALMITIC		17.81936	17.81936	17.81936	0	0	0	0	0	0	0	0	0	0	0	0	0
H2		0.1867869	0.1867869	0.1867869	0	0	0	0	0	0	0	0	0	0	214.5942	214.5942	267.3313
CO		2.062777	2.062777	2.062777	0	0	0	0	0	0	0	0	0	0	760.6822	760.6822	31.31256
CO2		1.705446	1.705446	1.705446	0	0	0	0	0	0	0	0	0	0	2664.965	2664.965	3811.754
METHANE		0.1015146	0.1015146	0.1015146	0	0	0	0	0	0	0	0	0	0	18.14996	18.14996	18.14996
CARBON		0.00223392	0.00223392	0.00223392	0	0	0	0	0	0	0	0	0	0	0	0	0
O2		0	0	0	0	0	0	0	0	0	0	854.3476	854.3476	854.3476	6.7663E-18	6.7663E-18	0
N2		0	0	0	0	0	0	0	0	0	0	2812.262	2812.262	2812.262	2811.472	2811.472	2812.266
WATER		562.7167	562.7167	562.7167	2954.691	2954.691	2954.691	2954.691	2954.691	2954.691	2954.691	0	0	0	2516.458	2516.458	2047.024
AMMONIA		0.00406059	0.00406059	0.00406059	0	0	0	0	0	0	0	0	0	0	0.9649567	0.9649567	0
FORMALDE		196.013	196.013	196.013	0	0	0	0	0	0	0	0	0	0	0.5500627	0.5500627	0
ACETALDE		17.81936	17.81936	17.81936	0	0	0	0	0	0	0	0	0	0	7.52547E-07	7.52547E-07	0
2-BUTA		17.81936	17.81936	17.81936	0	0	0	0	0	0	0	0	0	0	5.3011E-16	5.3011E-16	0
CREOSOL		71.27744	71.27744	71.27744	0	0	0	0	0	0	0	0	0	0	0	0	0
GUAIACOL		285.1098	285.1098	285.1098	0	0	0	0	0	0	0	0	0	0	0	0	0
CATECHOL		588.0389	588.0389	588.0389	0	0	0	0	0	0	0	0	0	0	1.4794E-24	1.4794E-24	0
BIOMASS		0	0	0	0	0	0	0	0	0	0	0	0	0	0	0	0
ASH		0	0	0	0	0	0	0	0	0	0	0	0	0	0	0	0

Table A.3 continue

	Stream	SHIFT-2	SHIFT-21	SHIFT-22	SHIFT-3	SHIFT-4	SHIFT-5	SHIFT-6	TO-COMP	WATER-1	FR-COMP	TO-COOL	FR-COOL	TO-PSA	WATER-2	H2-PURE	OFF-GAS1
From		HX5	SPLIT-1	SPLIT-1	HX6	HX7	MIX-1	C2	SEP-2	SEP-2	COMP-2	HX8	C3	SEP-3	SEP-3	PSA	PSA
To		SPLIT-1	HX6	HX7	MIX-1	MIX-1	C2	SEP-2	COMP-2		HX8	C3	SEP-3	PSA			HX8
Temperature	°C	94	94	94	82.58327	81.55425	81.86149	40	40	40	166.8807	85.76769	30	30	30	30	30
Pressure	bar	3	3	3	3	3	3	3	3	3	10	10	10	10	10	10	10
Mass Flow	kg/h	8987.837	2642.424	6345.412	2642.424	6345.412	8987.836	8987.836	7070.375	1917.461	7070.375	7070.375	7070.375	6940.751	129.6236	200.4984	6740.255
ACETIC		0	0	0	0	0	0	0	0	0	0	0	0	0	0	0	0
PHENOL		0	0	0	0	0	0	0	0	0	0	0	0	0	0	0	0
LEVOGLU		0	0	0	0	0	0	0	0	0	0	0	0	0	0	0	0
FURFURAL		0	0	0	0	0	0	0	0	0	0	0	0	0	0	0	0
PALMITIC		0	0	0	0	0	0	0	0	0	0	0	0	0	0	0	0
H2		267.3313	78.59541	188.7359	78.59541	188.736	267.3314	267.3314	267.3313	0.000111465	267.3313	267.3313	267.3313	267.3313	0	200.4984	66.83286
CO		31.31256	9.205892	22.10666	9.205892	22.10666	31.31255	31.31255	31.31255	4.00419E-06	31.31255	31.31255	31.31255	31.31255	0	0	31.31262
CO2		3811.754	1120.656	2691.098	1120.656	2691.097	3811.753	3811.753	3811.693	0.0599774	3811.693	3811.693	3811.693	3811.693	0	0	3811.695
METHANE		18.14996	5.336088	12.81387	5.336088	12.8135	18.14959	18.14959	18.14957	2.20525E-05	18.14957	18.14957	18.14957	18.14957	0	0	18.14939
CARBON		0	0	0	0	0	0	0	0	0	0	0	0	0	0	0	0
O2		0	0	0	0	0	0	0	0	0	0	0	0	0	0	0	0
N2		2812.266	826.8061	1985.459	826.8061	1985.459	2812.266	2812.266	2812.265	0.000339782	2812.265	2812.265	2812.265	2812.265	0	0	2812.265
WATER		2047.024	601.8251	1445.199	601.8251	1445.199	2047.024	2047.024	129.6236	1917.401	129.6236	129.6236	129.6236	0	129.6236	0	0
AMMONIA		0	0	0	0	0	0	0	0	0	0	0	0	0	0	0	0
FORMALDE		0	0	0	0	0	0	0	0	0	0	0	0	0	0	0	0
ACETALDE		0	0	0	0	0	0	0	0	0	0	0	0	0	0	0	0
2-BUTA		0	0	0	0	0	0	0	0	0	0	0	0	0	0	0	0
CREOSOL		0	0	0	0	0	0	0	0	0	0	0	0	0	0	0	0
GUAIACOL		0	0	0	0	0	0	0	0	0	0	0	0	0	0	0	0
CATECHOL		0	0	0	0	0	0	0	0	0	0	0	0	0	0	0	0
BIOMASS		0	0	0	0	0	0	0	0	0	0	0	0	0	0	0	0
ASH		0	0	0	0	0	0	0	0	0	0	0	0	0	0	0	0

Table A.3 continue

	Stream	**OFF-GAS2**	**NCG**	**CAIR-1**	**CAIR-2**	**FLUE-1**	**FLUE-2**	**FLUE-3**	**FLUE-G**	**FLUE-S**	**DH2O-1**	**DH2O-2**	**DH2O-3**	**DH2O-4**	**FR-BPT**	**FR-DRY**	**DH2O-1AB**
From		HX8	SEP-1		HX10	COMBUST	HX9	HX10	ASHSEP	ASHSEP		HX7	HX5	HX9	BPT	C4	P3
To		COMBUST	COMBUST	HX10	COMBUST	HX9	HX10	ASHSEP			HX7	HX5	HX9	BPT	C4	C5	
Temperature	°C	146	30	20	250	1100	280	146.7441	146.7441	146.7441	20	74	146.672	400.0001	133.5284	133.5284	43.41071
Pressure	bar	10	1	1	1	1	1	1	1	1	40	40	40	40	3	3	40
Mass Flow	kg/h	6740.255	425.8618	11996.15	11996.15	19703.2	19703.2	19703.2	19600.66	102.5412	7571.252	7571.252	7571.252	7571.252	7571.252	7571.252	7571.252
ACETIC		0	1.799935	0	0	0	0	0	0	0	0	0	0	0	0	0	0
PHENOL		0	0.1799935	0	0	0	0	0	0	0	0	0	0	0	0	0	0
LEVOGLU		0	0.8999677	0	0	0	0	0	0	0	0	0	0	0	0	0	0
FURFURAL		0	3.239884	0	0	0	0	0	0	0	0	0	0	0	0	0	0
PALMITIC		0	0.1799935	0	0	0	0	0	0	0	0	0	0	0	0	0	0
H2		66.83286	18.4919	0	0	0	0	0	0	0	0	0	0	0	0	0	0
CO		31.31262	204.2149	0	0	0	0	0	0	0	0	0	0	0	0	0	0
CO2		3811.695	168.8391	0	0	6015.457	6015.457	6015.457	6014.856	0.6015457	0	0	0	0	0	0	0
METHANE		18.14939	10.04995	0	0	0	0	0	0	0	0	0	0	0	0	0	0
CARBON		0	0	0	0	0	0	0	0	0	0	0	0	0	0	0	0
O2		0	0	2794.106	2794.106	711.8357	711.8357	711.8357	711.7645	0.0711835	0	0	0	0	0	0	0
N2		2812.265	0	9202.04	9202.04	12014.31	12014.31	12014.31	12013.1	1.201431	0	0	0	0	0	0	0
WATER		0	5.684007	0	0	858.6545	858.6545	858.6545	858.5686	0.0858654	7571.252	7571.252	7571.252	7571.252	7571.252	7571.252	7571.252
AMMONIA		0	0.4019979	0	0	0.4061036	0.4061036	0.4061036	0.406063	4.06104E-05	0	0	0	0	0	0	0
FORMALDE		0	1.979929	0	0	0	0	0	0	0	0	0	0	0	0	0	0
ACETALDE		0	0.1799935	0	0	0	0	0	0	0	0	0	0	0	0	0	0
2-BUTA		0	0.1799935	0	0	0	0	0	0	0	0	0	0	0	0	0	0
CREOSOL		0	0.7199742	0	0	0	0	0	0	0	0	0	0	0	0	0	0
GUAIACOL		0	2.879897	0	0	0	0	0	0	0	0	0	0	0	0	0	0
CATECHOL		0	5.939787	0	0	0	0	0	0	0	0	0	0	0	0	0	0
BIOMASS		0	0	0	0	0	0	0	0	0	0	0	0	0	0	0	0
ASH		0	0.000558479	0	0	102.541	102.541	102.541	1.95987	100.5812	0	0	0	0	0	0	0

Table A. 4 Summary stream results for PAPS-CT process

	Stream	**FR-CET1**	**TO-CET2**	**FR-CET2**	**TO-DRY**	**FR-DRY**	**DH2O-1B**
From		CET-1	SPLIT-2	CET-2	SPLIT-2	C5	P4
To		SPLIT-2	CET-2	C4	C5	C6	
Temperature	°C	164.6049	154.5525	19.75047	154.5525	151.8339	44.17058
Pressure	bar	5	5	0.023	5	5	40
Mass Flow	kg/h	7567.688	4622.688	4622.688	2945	2945	2945
ACETIC		0	0	0	0	0	0
PHENOL		0	0	0	0	0	0
LEVOGLU		0	0	0	0	0	0
FURFURAL		0	0	0	0	0	0
PALMITIC		0	0	0	0	0	0
H2		0	0	0	0	0	0
CO		0	0	0	0	0	0
CO2		0	0	0	0	0	0
METHANE		0	0	0	0	0	0
CARBON		0	0	0	0	0	0
O2		0	0	0	0	0	0
N2		0	0	0	0	0	0
WATER		7567.688	4622.688	4622.688	2945	2945	2945
AMMONIA		0	0	0	0	0	0
FORMALDE		0	0	0	0	0	0
ACETALDE		0	0	0	0	0	0
2-BUTA		0	0	0	0	0	0
CREOSOL		0	0	0	0	0	0
GUAIACOL		0	0	0	0	0	0
CATECHOL		0	0	0	0	0	0
BIOMASS		0	0	0	0	0	0
ASH		0	0	0	0	0	0

Table A. 5 Complete stream results for PWAS-BT process (excludes similar steams listed in Table A.3)

	Stream	**SHIFT-1**	**SHIFT-2**	**SHIFT-21**	**SHIFT-22**	**SHIFT-31**	**SHIFT-32**	**SHIFT-4**	**SHIFT-51**	**SHIFT-52**	**SHIFT-6**	**WATER-1**	**TO-COMP**	**FR-COMP**	**TO-SCRUB**
From		SHIFT	HX5	SPLIT-2	SPLIT-2	SPLIT-1	SPLIT-1	HX6	HX8	HX7	MIX-1	SEP-2	SEP-2	COMP-2	C2
To		HX5	SPLIT-2	HX6	SPLIT-1	HX8	HX7	MIX-1	MIX-1	MIX-1	SEP-2		COMP-2	C2	SCRUBBER
Temperature	°C	250	94	94	94	94	94	82.55351	79.02839	83.15847	82.14401	82.14401	82.14401	222.1631	30
Pressure	bar	3	3	3	3	3	3	3	3	3	3	3	3	10	10
Mass Flow	kg/h	8987.836	8987.836	2642.424	6345.412	1938.523	4406.889	2642.424	1938.523	4406.889	8987.836	921.7572	8066.079	8066.079	8066.079
ACETIC		0	0	0	0	0	0	0	0	0	0	0	0	0	0
PHENOL		0	0	0	0	0	0	0	0	0	0	0	0	0	0
LEVOGLU		0	0	0	0	0	0	0	0	0	0	0	0	0	0
FURFURAL		0	0	0	0	0	0	0	0	0	0	0	0	0	0
PALMITIC		0	0	0	0	0	0	0	0	0	0	0	0	0	0
H2		267.362	267.362	78.60442	188.7575	57.66543	131.0921	78.60442	57.66543	131.0921	267.362	0.000180918	267.3618	267.3618	267.3618
CO		31.3195	31.3195	9.207932	22.11156	6.755083	15.35648	9.207932	6.755083	15.35648	31.3195	6.50570E-06	31.31949	31.31949	31.31949
CO2		3811.912	3811.912	1120.702	2691.21	822.1645	1869.045	1120.702	822.1645	1869.045	3811.912	0.0430215	3811.869	3811.869	3811.869
METHANE		18.08776	18.08776	5.317802	12.76996	3.901222	8.868736	5.317802	3.901222	8.868737	18.08776	2.73472E-05	18.08773	18.08773	18.08773
CARBON		0	0	0	0	0	0	0	0	0	0	0	0	0	0
O2		0	0	0	0	0	0	0	0	0	0	0	0	0	0
N2		2812.266	2812.266	826.8061	1985.459	606.5579	1378.902	826.8061	606.5579	1378.902	2812.266	0.000559005	2812.265	2812.265	2812.265
WATER		2046.889	2046.889	601.7855	1445.104	441.4793	1003.625	601.7855	441.4793	1003.625	2046.889	921.7134	1125.176	1125.176	1125.176
AMMONIA		0	0	0	0	0	0	0	0	0	0	0	0	0	0
FORMALDE		0	0	0	0	0	0	0	0	0	0	0	0	0	0
ACETALDE		0	0	0	0	0	0	0	0	0	0	0	0	0	0
2-BUTA		0	0	0	0	0	0	0	0	0	0	0	0	0	0
CREOSOL		0	0	0	0	0	0	0	0	0	0	0	0	0	0
GUAIACOL		0	0	0	0	0	0	0	0	0	0	0	0	0	0
CATECHOL		0	0	0	0	0	0	0	0	0	0	0	0	0	0
BIOMASS		0	0	0	0	0	0	0	0	0	0	0	0	0	0
ASH		0	0	0	0	0	0	0	0	0	0	0	0	0	0

Table A. 5 continue

	Stream	**FWF**	**H2-RICH**	**TO-FLASH**	**F-GAS**	**F-LIQUID**	**OFFGAS**	**ST-AIR**	**RE-H2O**	**WPA-1**	**WPA-2**	**PURGE**	**CAIR-1**	**CAIR-2**	**CAIR-3**
From			SCRUBBER	SCRUBBER	SEP-3	SEP-3	STRIPPER		STRIPPER	SPLIT-3	P3	SPLIT-3		HX8	HX10
To		SCRUBBER		SEP-3		STRIPPER		STRIPPER	SPLIT-3	P3	SCRUBBER		HX8	HX10	COMBUST
Temperature	°C	20	29.08165	33.88325	49.25027	49.25027	28.88804	20	27.51398	48.94237	49.45105	48.94237	20	74	250
Pressure	bar	10	10	10	1	1	1	1	1	1	10	1	1	1	1
Mass Flow	kg/h	4500	450.9169	262115	7321.538	254794	20101.81	20000	254692	250000	250000	4691.818	10862.72	10862.72	10862.72
ACETIC		0	0	0	0	0	0	0	0	0	0	0	0	0	0
PHENOL		0	0	0	0	0	0	0	0	0	0	0	0	0	0
LEVOGLU		0	0	0	0	0	0	0	0	0	0	0	0	0	0
FURFURAL		0	0	0	0	0	0	0	0	0	0	0	0	0	0
PALMITIC		0	0	0	0	0	0	0	0	0	0	0	0	0	0
H2		0	267.3612	0.000575779	0.000575757	2.2143E-08	2.2143E-08	0	0	0	0	0	0	0	0
CO		0	1.21186E-06	31.31949	31.31912	0.000368441	0.000368441	0	0	0	0	0	0	0	0
CO2		0	1.2876E-10	3811.869	3807.31	4.558907	4.558907	0	1.6547E-08	1.62421E-08	1.62421E-08	3.0482E-10	0	0	0
METHANE		0	1.1403E-21	18.08773	18.08583	0.00190516	0.00190516	0	0	0	0	0	0	0	0
CARBON		0	0	0	0	0	0	0	0	0	0	0	0	0	0
O2		0	21.97122	89.07307	89.05389	0.0191828	4545.231	4658.34	113.1282	111.0442	111.0442	2.083997	2530.113	2530.113	2530.113
N2		0	151.1774	2954.53	2954.497	0.0329344	15042.74	15341.66	298.9495	293.4424	293.4424	5.507114	8332.61	8332.61	8332.61
WATER		4500	10.40708	255210	421.2713	254789	509.2702	0	254280	249596	249596	4684.227	0	0	0
AMMONIA		0	0	0	0	0	0	0	0	0	0	0	0	0	0
FORMALDE		0	0	0	0	0	0	0	0	0	0	0	0	0	0
ACETALDE		0	0	0	0	0	0	0	0	0	0	0	0	0	0
2-BUTA		0	0	0	0	0	0	0	0	0	0	0	0	0	0
CREOSOL		0	0	0	0	0	0	0	0	0	0	0	0	0	0
GUAIACOL		0	0	0	0	0	0	0	0	0	0	0	0	0	0
CATECHOL		0	0	0	0	0	0	0	0	0	0	0	0	0	0
BIOMASS		0	0	0	0	0	0	0	0	0	0	0	0	0	0
ASH		0	0	0	0	0	0	0	0	0	0	0	0	0	0

Table A.5 continue

	Stream	FLUE-1	FLUE-2	FLUE-3	FLUE-G	FLUE-S	DH2O-1	DH2O-2	DH2O-3	DH2O-4	FR-BPT	FR-DRY	DH2O-1A
From		COMBUST	HX9	HX10	ASHSEP	ASHSEP		HX7	HX5	H3	BPT	C3	P4
To		HX9	HX10	ASHSEP			HX7	HX5	H3	HX9	C3	C4	
Temperature	°C	1100	280	122.1326	122.1326	122.1326	20	74	188.8322	188.8322	133.5284	133.5284	43.95496
Pressure	bar	1	1	1	1	1	40	40	40	40	3	3	40
Mass Flow	kg/h	11829.52	11829.52	11829.52	11726.98	102.5412	4736.625	4736.625	4736.625	4736.625	4715.307	4715.307	4715.307
ACETIC		0	0	0	0	0	0	0	0	0	0	0	0
PHENOL		0	0	0	0	0	0	0	0	0	0	0	0
LEVOGLU		0	0	0	0	0	0	0	0	0	0	0	0
FURFURAL		0	0	0	0	0	0	0	0	0	0	0	0
PALMITIC		0	0	0	0	0	0	0	0	0	0	0	0
H2		0	0	0	0	0	0	0	0	0	0	0	0
CO		0	0	0	0	0	0	0	0	0	0	0	0
CO2		2104.775	2104.775	2104.775	2104.565	0.2104775	0	0	0	0	0	0	0
METHANE		0	0	0	0	0	0	0	0	0	0	0	0
CARBON		0	0	0	0	0	0	0	0	0	0	0	0
O2		1068.56	1068.56	1068.56	1068.454	0.106856	0	0	0	0	0	0	0
N2		8332.61	8332.61	8332.61	8331.777	0.833261	0	0	0	0	0	0	0
WATER		220.6285	220.6285	220.6285	220.6065	0.0220628	4736.625	4736.625	4736.625	4736.625	4715.307	4715.307	4715.307
AMMONIA		0.4061036	0.4061036	0.4061036	0.406063	4.06104E-05	0	0	0	0	0	0	0
FORMALDE		0	0	0	0	0	0	0	0	0	0	0	0
ACETALDE		0	0	0	0	0	0	0	0	0	0	0	0
2-BUTA		0	0	0	0	0	0	0	0	0	0	0	0
CREOSOL		0	0	0	0	0	0	0	0	0	0	0	0
GUAIACOL		0	0	0	0	0	0	0	0	0	0	0	0
CATECHOL		0	0	0	0	0	0	0	0	0	0	0	0
BIOMASS		0	0	0	0	0	0	0	0	0	0	0	0
ASH		102.541	102.541	102.541	1.172581	101.3685	0	0	0	0	0	0	0

Table A. 6 Summary stream results for PAWS-CT process

	Units	**FR-CET1**	**TO-CET2**	**FR-CET2**	**DH2O-1A**	**TO-DRY**	**FR-DRY**	**DH2O-1B**
From		CET-1	SPLIT-4	CET-2	P5	SPLIT-4	B3A	P4
To		SPLIT-4	CET-2	C4		B3A	C5	
Temperature	°C	164.6247	154.5753	19.75047	22.92952	154.5753	151.8339	44.17058
Pressure	bar	5	5	0.023	40	5	5	40
Mass Flow	kg/h	4735.368	1790.368	1790.368	1790.368	2945	2945	2945
ACETIC		0	0	0	0	0	0	0
PHENOL		0	0	0	0	0	0	0
LEVOGLU		0	0	0	0	0	0	0
FURFURAL		0	0	0	0	0	0	0
PALMITIC		0	0	0	0	0	0	0
H2		0	0	0	0	0	0	0
CO		0	0	0	0	0	0	0
CO2		0	0	0	0	0	0	0
METHANE		0	0	0	0	0	0	0
CARBON		0	0	0	0	0	0	0
O2		0	0	0	0	0	0	0
N2		0	0	0	0	0	0	0
WATER		4735.368	1790.368	1790.368	1790.368	2945	2945	2945
AMMONIA		0	0	0	0	0	0	0
FORMALDE		0	0	0	0	0	0	0
ACETALDE		0	0	0	0	0	0	0
2-BUTA		0	0	0	0	0	0	0
CREOSOL		0	0	0	0	0	0	0
GUAIACOL		0	0	0	0	0	0	0
CATECHOL		0	0	0	0	0	0	0
BIOMASS		0	0	0	0	0	0	0
ASH		0	0	0	0	0	0	0
Volume flow rate, mixture		1839.206	685.5222	85933.01	2.10585	1127.624	289.0426	3.513899
Mass vapor fraction		1	1	0.8175579	0	1	0.25973	0
Mass solid fraction		0	0	0	0	0	0	0
Density, mixture		2.57468	2.611686	0.0208344	850.1881	2.611686	10.18881	838.1004
Temperature		164.6247	154.5753	19.75047	22.92952	154.5753	151.8339	44.17058
Pressure		5	5	0.023	40	5	5	40

A.3 Calculator blocks

Pyrolysis yield (PYROLYSE BLOCK)

```
C     DECLARE PHASE YIELD OF BIOOIL.

      SOLID = 0.15 * FLOW
      LIQUID = 0.70 * FLOW
      GAS = 0.12 * FLOW
      ASH = 0.03 * FLOW
C    PYROLYSIS PRODUCT YIELDS
      CHAR = SOLID - ASH
      MOISTURE = 0.24 * LIQUID
      ORGANICS = (1 - 0.24) * LIQUID
      ACETIC = 0.1 * ORGANICS
      PHENOL = 0.01 * ORGANICS
      LEVO = 0.05 * ORGANICS
      PALMI = 0.01 * ORGANICS
      FURFURAL = 0.18 * ORGANICS
      FORMAL = 0.11 * ORGANICS
      ACETAL = 0.01 * ORGANICS
      BUTANONE = 0.01 * ORGANICS
      CREOSOL = 0.04 * ORGANICS
      GUAIACOL = 0.16 * ORGANICS
      CATECHOL = 0.33 * ORGANICS
      CO2 = GAS * 42 / 100
      CO = GAS * 50.8 / 100
      CH4 = GAS * 2.5 / 100
      H2 = GAS * 4.6 / 100
      NH3 = GAS * 0.1 / 100
```

Amount of ATR air ($\lambda = 0.28$)

```
      C1 = ACETIC * 2 + PHENOL * 6 + LEVO * 6
      C2 = FURFURAL * 5 + PALMI * 16
      C3 = FORMAL * 1 + ACETAL * 2
      C4 = BUTANONE * 4 + CREOSOL * 8
      C5 = GUAIACOL * 7 + CATECHOL * 6
      H1 = ACETIC * 4 + PHENOL * 6 + LEVO * 10
      H2 = FURFURAL * 4 + PALMI * 32
      H3 = FORMAL * 2 + ACETAL * 4
      H4 = BUTANONE * 8 + CREOSOL * 10
      H5 = GUAIACOL * 8 + CATECHOL * 6
      O1 = ACETIC * 2 + PHENOL * 1 + LEVO * 5
      O2 = FURFURAL * 2 + PALMI * 2
      O3 = FORMAL * 1 + ACETAL * 1
      O4 = BUTANONE * 1 + CREOSOL * 4
      O5 = GUAIACOL * 2 + CATECHOL * 2
      c = C1 + C2 + C3 + C4 + C5 + METH + CHAR
      h = H1 + H2 + H3 + H4 + H5 + METH * 4
      o = O1 + O2 + O3 + O4 + O5
      total = c + h + o
      frac_c = c / total
      frac_h = h / total
      frac_o = o / total
      POX = (c / 2) - (o / 2)
      OXYGEN = POX * 1.1
      NITROGEN = 3.76 * OXYGEN
```

Amount of ATR steam (S/C = 2.2)

```
CARB1 = ACETIC * 2 + PHENOL * 6 + LEVO * 6
CARB2 = FURFURAL * 5 + PALMI * 16
CARB3 = FORMAL * 1 + ACETAL * 2
CARB4 = BUTANONE * 4 + CREOSOL * 8
CARB5 = GUAIACOL * 7 + CATECHOL * 6
TOTALC = CARB1 + CARB2 + CARB3 + CARB4 + CARB5 + METH
STOC = 2.2
WATNEED = STOC * TOTALC
STEAM = WATNEED - MOISTURE
```

Appendix B

B.1 Equilibrium plots

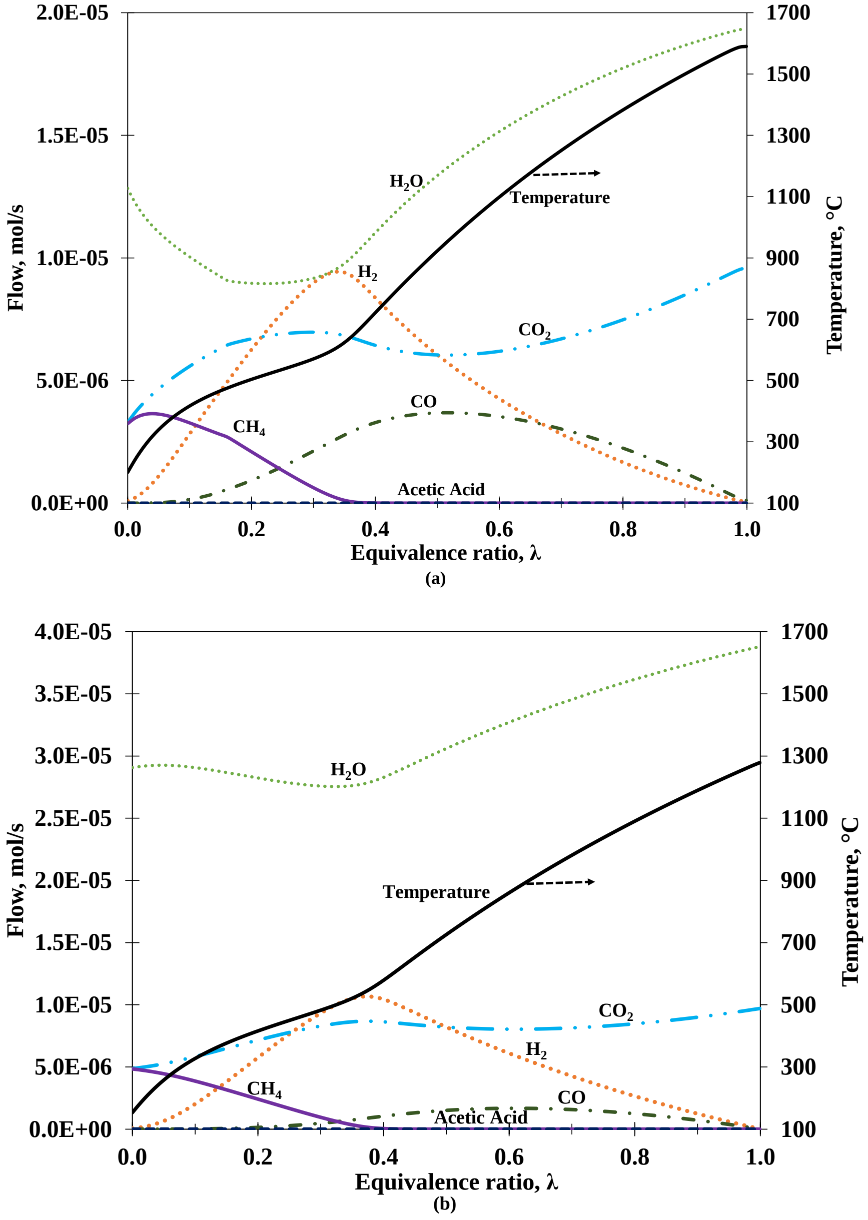

Figure B. 1 Thermodynamic equilibrium plots showing syngas composition and temperature obtained while varying λ from 0 to 1 for acetic acid flowing at 1ml/h. a) S/C = 1. b) S/C = 3

B.2 Calibration curves

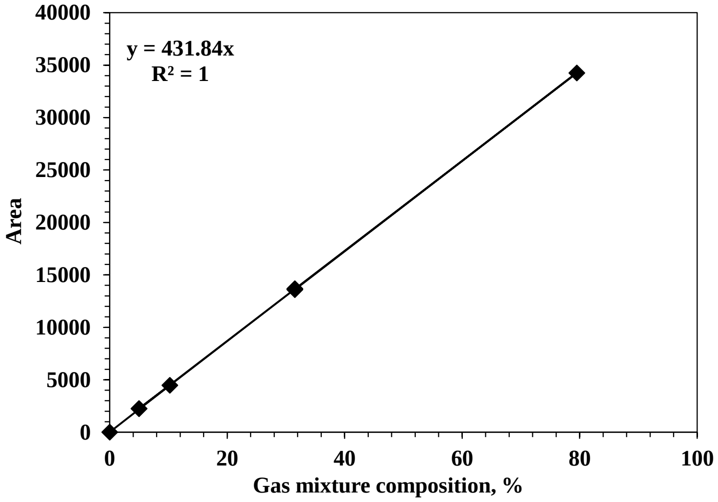

Figure B. 2 Hydrogen calibration for the micro GC (channel 1)

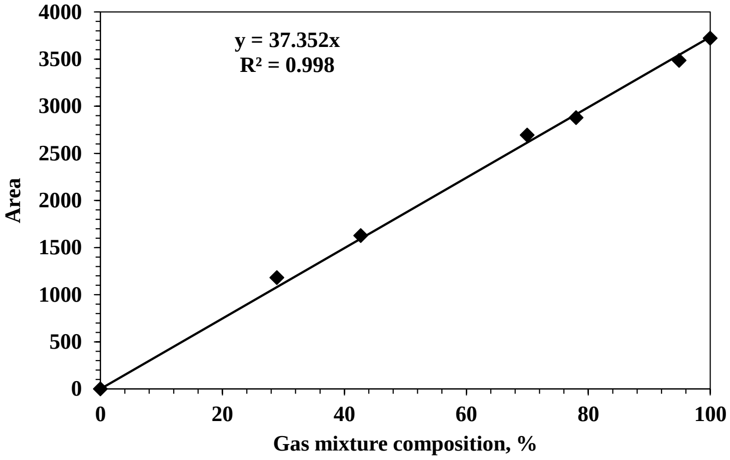

Figure B. 3 Nitrogen calibration for the micro GC (channel 1)

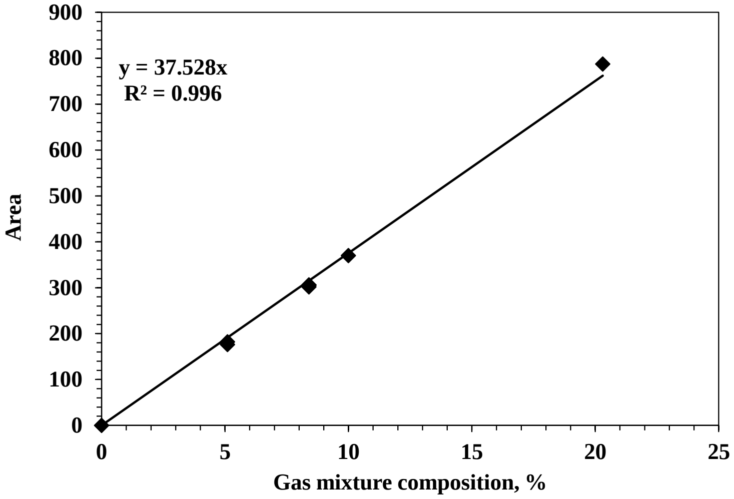

Figure B. 4 Carbon monoxide calibration for micro GC (channel 1)

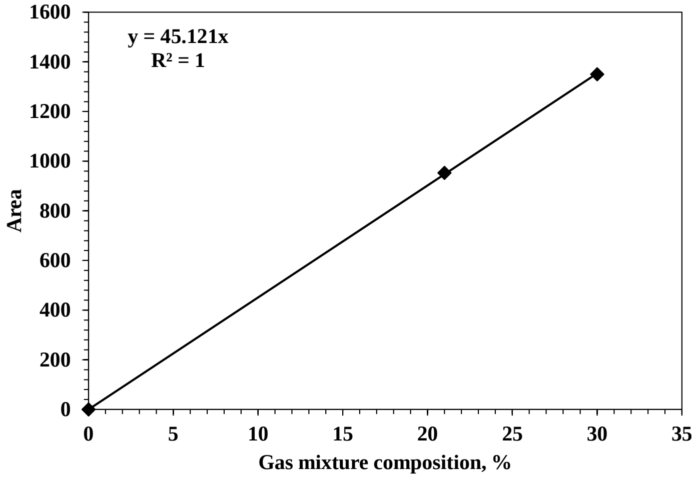

Figure B. 5 Oxygen calibration curve for the micro GC (channel 1)

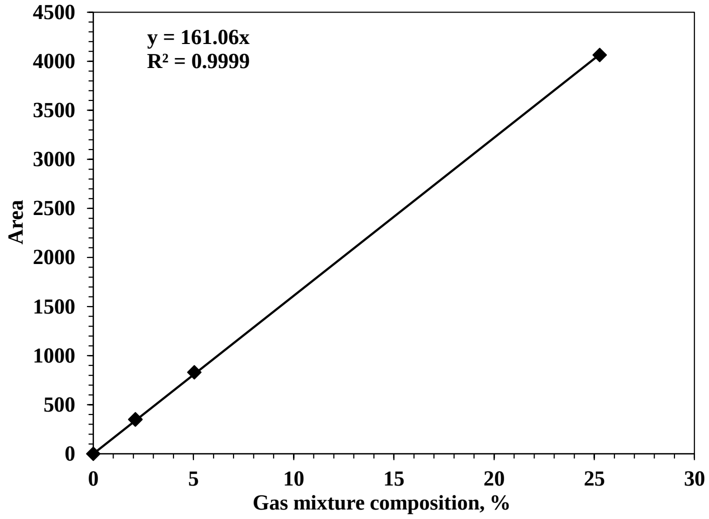

Figure B. 6 Methane calibration curve for the micro GC (channel 2)

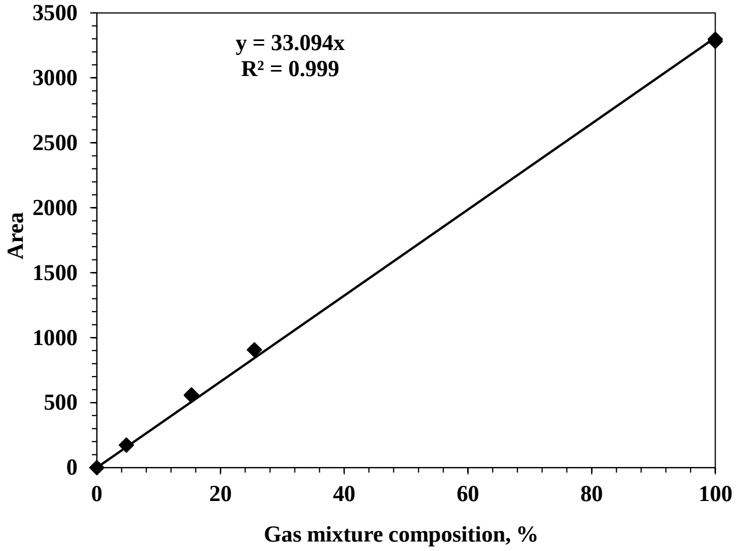

Figure B. 7 Carbon dioxide calibration curve for the micro GC (channel 2)

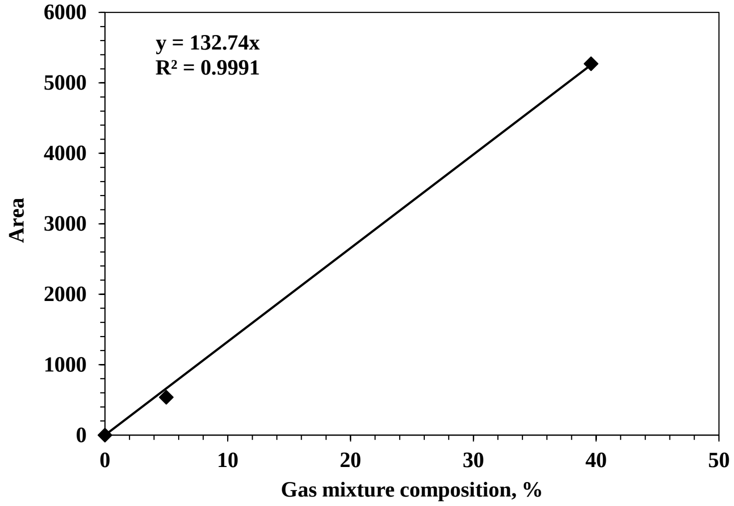

Figure B. 8 Ethane calibration curve for the micro GC (channel 2)

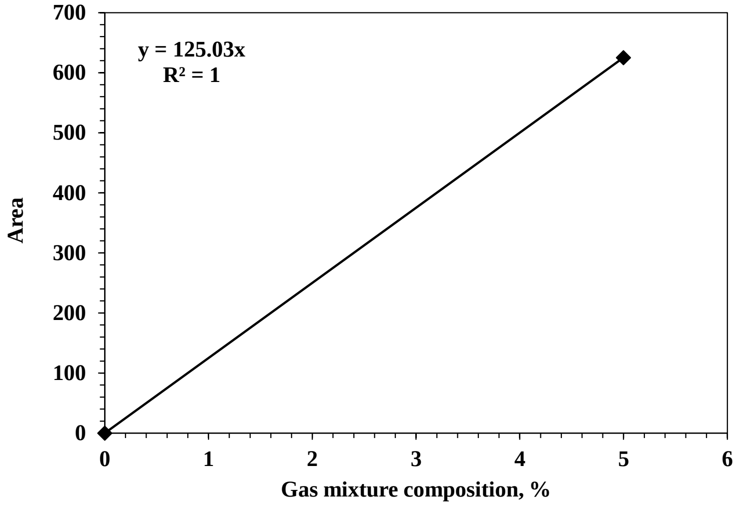

Figure B. 9 Ethylene calibration curve for the micro GC (channel 2)

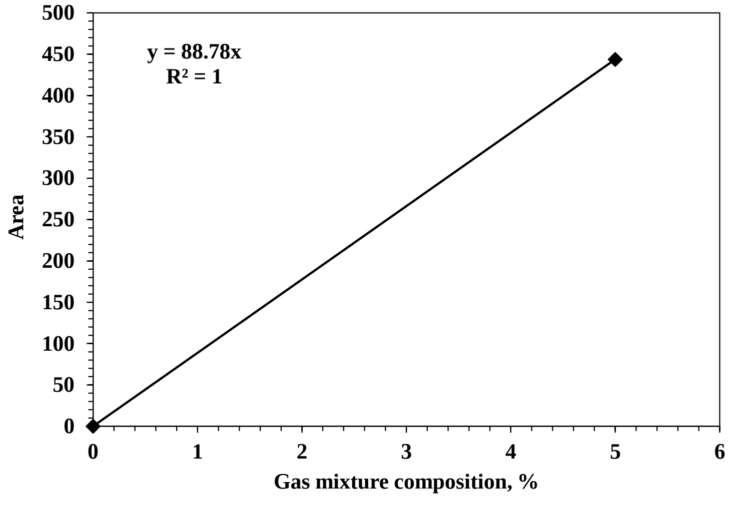

Figure B. 10 Propane calibration curve for the micro GC

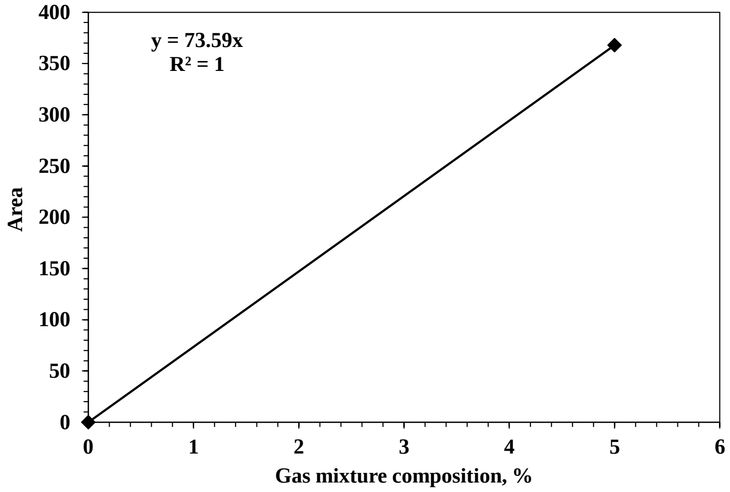

Figure B. 11 Propylene calibration curve for the micro GC (channel 2)

B.3 Carbon balance

This section contains information on how the carbon balance was determined for experiments described in Chapter 6.

Table B. 1 Carbon balance calculations for the ATR of Acetic acid with Ni catalysts

	Catalyst	**Ni-Al**	**Ni-Al**	**Ni-CaAl**
Experimental conditions	Form	Fresh	Reduced	Fresh
	Fuel in, ml/h	1.0	1.0	1.0
	C in, mol/s	9.71E-06	9.71E-06	9.71E-06
	Duration, h	2.716667	3.216667	3.416667
	Duration, s	9780	11580	12300
	Catalyst mass, g	1.000	1.002	1.001
CHNS analysis and results	Sample mass, mg	9.51	9.57	9.56
	C (%)	6.521286	14.76674	3.792101
	H (%)	0.082496	0.212048	0.31159
	C (MW), g/mol	12.012	12.012	12.012
	C on catalyst (mol)[a]	0.005809	0.014461	0.003284
	C on catalyst (mg/g(cat).h)[b]	25.70204	53.99471	11.57079
TOC analysis and results	TOC, mg/L	51.22786	29.11	2.682636
	Condensate volume, mL	3	3.40	10.3
	Dilution	10	10	100
	Total C in condensate, mol[c]	0.000128	8.24E-05	0.00023
Dry gas output (from micro GC)	C out gas, mol/s [d]	9.35E-06	9.26E-06	9.99E-06
	Total C out gas, mol [e]	0.091407	0.107178	0.122823
	Total C (out), mol[f]	0.097344	0.121721	0.126337
	Total C (in), mol[g]	0.095004	0.11249	0.119484
	% Error on C[h]	**2.47**	**8.21**	**5.74**

Table B. 2 Carbon balance calculations for the ATR of acetic acid, butanone, furfural, m-cresol and their mixture on Rh-Al catalyst

	Bio-fuel	**Acetic acid**	**Butanone**	**Furfural**	**Cresol**	**Mixture**
Experimental conditions	Fuel in, ml/h	1.0	0.781	0.781	0.523	2.806
	C in, mol/s	9.71E-06	9.71E-06	9.71E-06	9.71E-06	3.89E-05
	Duration, h	3.366667	3.283333	3.283333	3.333333	3.166667
	Duration, s	12120	11820	11820	12000	11400
	Catalyst mass, g	0.2015	0.2005	0.2005	0.1972	0.1953
CHNS analysis and results	Sample mass, mg	9.84	10.66	10.66	9.43	9.555
	C (%)	1.814413	1.993815	1.993815	8.624168	5.978826
	H (%)	0.956895	1.004005	1.004005	1.001451	1.127352
	C (MW), g/mol	12.012	12.012	12.012	12.012	12.012
	C on catalyst (mol)[a]	0.00031	0.00034	0.00034	0.001549	0.001034
	C on catalyst (mg/g(cat).h)[b]	5.542957	6.260204	6.260204	24.89404	20.32482
TOC analysis and results	TOC, mg/L	5.115274	121.41	121.41	254.2777	293.6883
	Condensate volume, mL	3.7	3.40	3.40	5.8	11.5
	Dilution	10	10.00	10.00	100	100
	Total C in condensate, mol[c]	1.58E-05	0.000344	0.000344	0.012278	0.028117
Dry gas output (from micro GC)	C out gas, mol/s [d]	1.05E-05	9.56E-06	9.56E-06	9.08E-06	3.96E-05
	Total C out gas, mol[e]	0.127686	0.113012	0.113012	0.12526	0.45112
	Total C (out), mol[f]	0.128011	0.113695	0.113695	0.139088	0.480271
	Total C (in), mol[g]	0.117735	0.114821	0.114821	0.134055	0.442964
	% Error on C[h]	**8.54**	**0.98**	**2.02**	**3.75**	**8.42**

The following equations correspond to the letter subscripts found in Table B.1 and Table B.2

a Total Carbon (C) on catalyst (mol)

$$C\ on\ catalyst = \frac{C\ mass\ fraction}{1-(C+H\ mass\ fractions)} \times \frac{mass\ of\ catalyst(g)}{molar\ mass\ of\ carbon\ (\frac{g}{mol})} \qquad \text{B.1}$$

b Carbon on catalyst, mg/g(cat).h

$$C\ on\ catalyst = \frac{C\ mass\ fraction \times mass\ of\ sample\ (mg)}{\left(1-(C+H\ mass\ fractions)\right)\times mass\ of\ sample\ (mg)} \times \frac{1000(\frac{mg}{g})}{time(h)} \qquad \text{B.1}$$

c Total carbon in condensate, mol

$$C\ in\ condensate = \frac{TOC(\frac{mg}{L})}{1000(\frac{mg}{g})} \times \frac{volume\ of\ condensate(ml)}{1000ml/L} \times \frac{dilution}{molar\ mass\ of\ C(\frac{g}{mol})} \text{ B.3}$$

d Carbon flow(average) as product gas (mol/s)

$$C\ out\ gas = CO + CO_2 + CH_4 \quad \text{B.5}$$

e Total carbon flow as gas (mol)

$$Total\ C\ out\ gas = Cout\ gas \times time\ (s) \quad \text{B.6}$$

f Total C out (mol)

$$Total\ C\ (out) = Total\ C\ on\ catalyst + Total\ C\ in\ Condensate + Total\ Cout\ gas \quad \text{B.7}$$

g Total Carbon flow into reactor during experiment (mol)

$$Total\ C\ (in) = C\ in \left(\frac{mol}{s}\right) \times\ time(s) \quad \text{B.8}$$

h Error on carbon balance as % of carbon in feed

$$Error\ on\ C\ (\%) = \frac{|Total\ C(in) - Total\ C(out)|}{Total\ C(in)} \times 100 \quad \text{B.9}$$

B.4 Oxygen balance (water conversion)

The oxygen balance was used to confirm water conversion results obtained from the H balance.

$$\dot{n}_{H_2O(out)} = 2 \times \dot{n}_{O_2(in)} + k \times \dot{n}_{BF(in)} + \dot{n}_{H_2O(in)} - (\dot{n}_{CO(out)} + 2 \times \dot{n}_{CO_2(out)} + 2 \times \dot{n}_{O_2(out)} \quad \text{B.10}$$

From which the water conversion is calculated by applying the following equation

$$X_{H_2O} = \left[\mathbf{100} \times \frac{\dot{n}_{H_2O\ (in)} - \dot{n}_{H_2O\ (out)}}{\dot{n}_{H_2O\ (in)}}\right] \quad \text{B.11}$$

Appendix C

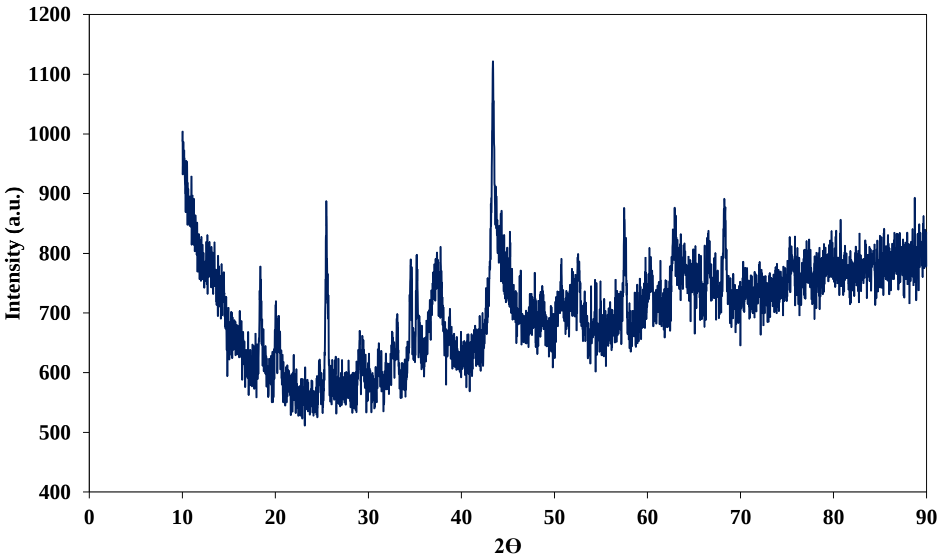

Figure C.1 XRD patterns of Ni-CaAl catalyst showing the amorphous nature of the fresh catalyst.

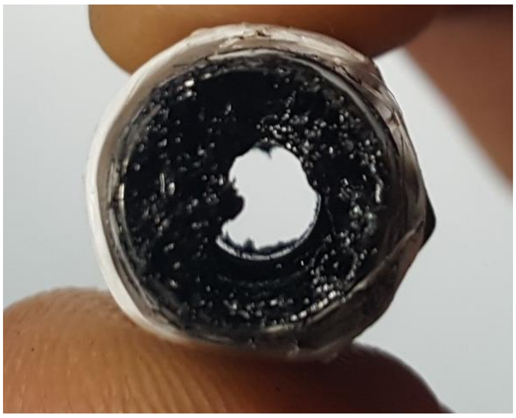

Figure C. 2 Carbon deposit formed in reactor connector pipe fitting